NUMERICAL SIMULATION OF TURBULENT AIRFLOW, TRACER GAS DIFFUSION, AND PARTICLE DISPERSION IN A MOCKUP AIRCRAFT CABIN

by

KHOSROW EBRAHIMI

B.S., University of Tehran, Tehran, Iran, 2000
M.S., K. N. Toosi University of Technology, Tehran, Iran, 2003

AN ABSTRACT OF A DISSERTATION

submitted in partial fulfillment of the requirements for the degree

DOCTOR OF PHILOSOPHY

Department of Mechanical and Nuclear Engineering
College of Engineering

KANSAS STATE UNIVERSITY
Manhattan, Kansas

2012

Abstract

In order to study the capability of computational methods in investigating the mechanisms associated with disease and contaminants transmission in aircraft cabins, the Computational Fluid Dynamics (CFD) models are used for the simulation of turbulent airflow, tracer gas diffusion, and particle dispersion in a generic aircraft cabin mockup. The CFD models are validated through comparisons of the CFD predictions with the corresponding experimental measurements. It is found that using Large Eddy Simulation (LES) with the Werner-Wengle wall function, one can predict unsteady airflow velocity field with relatively high accuracy. However in the middle region of the cabin mockup, where the recirculation of airflow takes place, the accuracy is not as good as that in other locations. By examining different k-ε models, the current study recommends the use of the RNG k-ε model with the non-equilibrium wall function as a Reynolds Averaged Navier Stokes (RANS) model for predicting the steady-state airflow velocity data. It is also found that changing the cabin air-inlet nozzle height has a significant effect on the flow behavior in the middle and upper part of the cabin, while the flow pattern in the lower part is not affected as much. Through the use of LES and species transport model in simulating tracer gas diffusion, very good agreement between predicted and measured tracer gas concentration data is observed for some monitoring locations, but the agreement level is not uniform for all the sampling point locations. The reasons for the deviations between predictions and measurements for those locations are discussed.

The Lagrange-Euler approach is invoked in the particle dispersion simulations. In this approach, the equation of motion for the discrete phase is coupled with the continuous phase governing equations through the calculation of drag and buoyancy forces acting on particles. The continuous phase flow is turbulent and RANS is employed in order to calculate the continuous phase velocity field. A complete study on grid dependence for RANS simulation is performed through a controllable regional mesh refinement scheme. The grid dependence study shows that using unstructured grid with tetrahedral and hybrid elements in the refinement region are more efficient than using structured grid with hexahedral elements. The effect of turbulence on the particle dispersion is taken into account by using a stochastic tracking method (Discrete Random Walk model). One of the significant features of this study is the investigation of the effect of the number of tries on the accuracy of particle concentration predictions when Discrete

Random Walk is used to model turbulent distribution of particles. Subsequently, the optimum number of tries to obtain the most accurate predictions is determined. In accordance with the corresponding experimental data, the effect of particle size on particle distribution is also studied and discussed through the simulation of two different sizes of mono-disperse particles in the cabin with straight injection tube, i.e., 3µm and 10µm. Due to the low particle loading, neglecting the effect of particles motion on the continuous phase flow-field seems to be a reasonable, simplifying assumption in running the simulations. However, this assumption is verified through the comparison of the results from 1-way and 2-way coupling simulations. Eventually through the simulations for the particle injection using the cone diffuser, the effects of cabin pressure gradient as well as the particle density on particles dispersion behavior are studied and discussed.

In the last part of this dissertation, the turbulent airflow in a full-scale Boeing 767 aircraft cabin mockup with eleven rows of seats and manikins is simulated using steady RANS method. The results of this simulation cannot only be used to study the airflow pattern, but also can be used as the initial condition for running the tracer gas diffusion and particle dispersion simulations in this cabin mockup.

NUMERICAL SIMULATION OF TURBULENT AIRFLOW, TRACER GAS DIFFUSION, AND PARTICLE DISPERSION IN A MOCKUP AIRCRAFT CABIN

by

KHOSROW EBRAHIMI

B.S., University of Tehran, Tehran, Iran, 2000
M.S., K. N. Toosi University of Technology, Tehran, Iran, 2003

A DISSERTATION

submitted in partial fulfillment of the requirements for the degree

DOCTOR OF PHILOSOPHY

Department of Mechanical and Nuclear Engineering
College of Engineering

KANSAS STATE UNIVERSITY
Manhattan, Kansas

2012

Approved by:

Co-Major Professor
M.H. Hosni

Approved by:

Co-Major Professor
Z.C. Zheng

Abstract

In order to study the capability of computational methods in investigating the mechanisms associated with disease and contaminants transmission in aircraft cabins, the Computational Fluid Dynamics (CFD) models are used for the simulation of turbulent airflow, tracer gas diffusion, and particle dispersion in a generic aircraft cabin mockup. The CFD models are validated through comparisons of the CFD predictions with the corresponding experimental measurements. It is found that using Large Eddy Simulation (LES) with the Werner-Wengle wall function, one can predict unsteady airflow velocity field with relatively high accuracy. However in the middle region of the cabin mockup, where the recirculation of airflow takes place, the accuracy is not as good as that in other locations. By examining different k-ε models, the current study recommends the use of the RNG k-ε model with the non-equilibrium wall function as a Reynolds Averaged Navier Stokes (RANS) model for predicting the steady-state airflow velocity data. It is also found that changing the cabin air-inlet nozzle height has a significant effect on the flow behavior in the middle and upper part of the cabin, while the flow pattern in the lower part is not affected as much. Through the use of LES and species transport model in simulating tracer gas diffusion, very good agreement between predicted and measured tracer gas concentration data is observed for some monitoring locations, but the agreement level is not uniform for all the sampling point locations. The reasons for the deviations between predictions and measurements for those locations are discussed.

The Lagrange-Euler approach is invoked in the particle dispersion simulations. In this approach, the equation of motion for the discrete phase is coupled with the continuous phase governing equations through the calculation of drag and buoyancy forces acting on particles. The continuous phase flow is turbulent and Reynolds Averaged Navier Stokes (RANS) is employed in order to calculate the continuous phase velocity field. A complete study on grid dependence for RANS simulation is performed through a controllable regional mesh refinement scheme. The grid dependence study shows that using unstructured grid with tetrahedral and hybrid elements in the refinement region are more efficient than using structured grid with hexahedral elements. The effect of turbulence on the particle dispersion is taken into account by using a stochastic tracking method (Discrete Random Walk model). One of the significant features of this study is the investigation of the effect of the number of tries on the accuracy of

particle concentration predictions when Discrete Random Walk model is used to model turbulent distribution of particles. Subsequently, the optimum number of tries to obtain the most accurate predictions is determined. In accordance with the corresponding experimental data, the effect of particle size on particle distribution is also studied and discussed through the simulation of two different sizes of mono-disperse particles in the cabin with straight injection tube, i.e., 3μm and 10μm. Due to the low particle loading, neglecting the effect of particles motion on the continuous phase flow-field seems to be a reasonable, simplifying assumption in running the simulations. However, this assumption is verified through the comparison of the results from 1-way and 2-way coupling simulations. Eventually through the simulations for the particle injection using the cone diffuser, the effects of cabin pressure gradient as well as the particle density on particles dispersion behavior are studied and discussed.

In the last part of this dissertation, the turbulent airflow in a full-scale Boeing 767 aircraft cabin mockup with eleven rows of seats and manikins is simulated using steady RANS method. The results of this simulation cannot only can be used to study the airflow pattern, but also can be used as the initial condition for running the tracer gas diffusion and particle dispersion simulations in this cabin mockup.

Table of Contents

List of Figures

List of Tables

Acknowledgements

I would like to express my sincerest appreciation and gratitude to my major advisor Professor Mohammad H. Hosni for all his support, patience, advice, and guidance throughout this course of study and research. I will always be grateful to him not only because of the very precious opportunity that I received from him to continue my education towards the highest academic level and to learn how to conduct research in a correctly efficient and productive way but also for the fatherly life lessons he taught me in the challenging situations that I experienced during the time I worked under his leadership and supervision.

I would also like to sincerely thank my co-major advisor Dr. Zhongquan C. Zheng for all his constant help and advice. I don't remember leaving a weekly meeting with him unless I had learned something new to think about. It was a great privilege for me to work with Dr. Zheng and learn Computational Fluid Dynamics (CFD) from someone who is a leader and well-known authority in this area.

This dissertation would never have been completed without the help, support, and contribution of a number of other people whose names and affiliations I would like to mention here. My sincere thanks and gratitude to Dr. C.H. Lin from Boeing Company for his invaluable inputs in CFD simulations, and also to Dr. P. A. Lebbin from the National Research Council of Canada for his kind assistance in analyzing the experimental data and test procedures. Also, I would like to thank Dr. J. Bennett from the National Institute for Occupational Safety and Health (NIOSH) for his technical assistance especially for his helpful suggestions and advice in using ANSYS FLUENT in CFD simulations.

I was much honored to have Professor Byron Jones, Professor Terry Beck, and Professor Larry Glasgow on my dissertation committee and Dr. Brian Washburn as the committee chairperson. I learned a lot through their priceless editorial and technical reviews on my dissertation. I would like to thank all of them for their unforgettable help, suggestions, and advice. Also, I would like to express my deep appreciation for the constant kind attention and encouragement I received from Professor Donald Fenton and Professor Dale Schruben during the years of my doctoral program here at Kansas State University.

I was lucky to meet and be with a number of wonderful graduate students in Mechanical and Nuclear Engineering Department of Kansas State University. More specifically, I would

like to thank Xiaofan Yang and Viet Nguyen, both from Dr. Zheng's CFD lab, for the invaluable help I got from them while learning how to utilize ANSYS FLUENT. Over the years of living in Manhattan, thousands of miles away from my family, there have been a number of marvelous friends who treated me like a member of their own families that and helped me to avoid feeling homesick or lonely. I really cannot list all of them but I wish to especially thank Shahram Shafie, Alireza Kargar and his wife Faranak, Dr. Rahim Borhani and his family, Jared Goodnight and his parents, Evraam Gorgy, Disna Samarakoon and her husband Anura, Christian Madsen and his wife Adrian, and Luis Carlos Caro-Delgado.

Also, there have been many great men and women of the past and present who taught me the most important lessons, showed me the right path, and shaped my life. I owe my success to all of them. Especially I would like to thank my late English teacher: Mr. Hooshang Bahrami, my fluid dynamics teacher at the University of Tehran: Dr. Farshad Kowsary, my BS supervisor: Dr. Karan Abrinia, my heat transfer teacher at K. N. Toosi University: Dr. Ali Keshavarz, my MS supervisor: Dr. Majid Bazargan, and my first manager in National Iranian Oil Company: Mr. Taymor Ashtari.

I was very lucky to have grown up in a family that has always valued education and provided me with any kind of support whether it is academic support, moral support, financial support, or encouragement to pursue my academic and professional goals. I always thank my esteemed father, Ali, who has been my first teacher and mentor in my life. I am deeply indebted to my great mother, Maliheh, who has been my savior in my whole life and twelve years ago when I was struggling with spinal cord tumor and almost all people had lost their hope for any treatment, she never gave up and because of her persistence and efforts I regained my health and came back to the life. I would also thank my brothers Khashayar and Sasan for their constant assistance and encouragement. Their educational success and progress have been always a source of inspiration for me. I have been and will always be grateful to my doctors and surgeons: Dr. Masoud Khadivi and Dr. Farid Kazemi. Because of their incredibly high professional skills and their unimaginably brilliant treatment and removal of my tumors I got the chance to continue my life and education.

Finally, the financial support provided in part by the Kansas State University Targeted Excellence Program is gratefully acknowledged.

Dedication

Dedicated to My Dear Mother Maliheh,
for all her love, care, affection, and attention…

Chapter 1 - Introduction

This chapter, as the opening to the dissertation, discusses the motivations and significance of the current research, statement of objectives, the applied methods to meet the desired objectives and finally the organization of the dissertation.

1.1 Motivation and Significance

The commercial airplanes cruise altitude is approximately between 30,000 and 40,000 ft. In this altitude, the ambient temperature is in the approximate range of -30^{o}F to -70^{o}F. The ambient pressure is around ~30% - ~50% of that at standard sea level and the air humidity in this altitude is almost zero (National Research Council, 2002). It is obvious that human beings cannot continue the life in this environment, therefore, the airplane passengers should be protected using a sophisticated air-conditioning system that converts the fatal environmental conditions to the standard conditions in which the passengers can breathe normally and feel safe and comfortable. In comparison with buildings, design and manufacture of air-conditioning system for aircraft cabins is much more challenging because of the limitations associated with airplanes, such as: the severe ambient environmental flight conditions, the more complex geometry, more occupant density, and a lower outside air supply rate per person (Zhang and Chen, 2007).

During the past decades, the aviation industry has experienced a dramatic increase in both the number of people traveling by commercial airplanes as well as the number of long distance commercial flights. According to the Bureau of Labor Statistics (2011) the number of commercial airline passengers experienced an average growth of 340% between the years 1970-2008. Also the statistics published by the Bureau of Transportation (2011) indicates 650-800 million passengers travel by aircrafts each year in the United States, around 20% of those are international passengers. The close proximity of this huge number of commercial airline passengers especially in long distance flights has increased the risk of spreading biological contaminants and diseases between passengers. This potential threat is the primary reason for the current study of air quality in commercial aircraft cabins.

Figure 1.1: The outside weather condition especially at cruise altitude is fatal for airliner passengers and flight crew members. (Boeing, 2011)

There are several documented cases that indicate how the global outbreak of fatal diseases happened through the transmission of diseases in the aircraft cabin environment. Here two of the most recent cases which are related to the World wide spread of Severe Acute Respiratory Syndrome (SARS) and H1N1 influenza are mentioned. On March 15th, 2003, a total of 20 passengers and two flight attendants of a three-hour flight from Hong Kong to Beijing contracted Severe Acute Respiratory Syndrome (SARS) because of exposure to an infected passenger during that flight. The infected passenger was a 72 year old man who was hospitalized after arrival in Beijing, but he died five days later (Olsen et al., 2003). Considering the total number of passengers and crew attendants in that flight which was 120, the exposure to just one infected passenger during a three-hour flight, affected around 18% of the flight occupants. Five people of the 20 infected passengers of that flight ultimately died from SARS (Olsen et al., 2003 and St. John et al., 2005). Another investigation (WHO, 2004) revealed that one of the five SARS infected passengers of the Hong Kong-Beijing flight that eventually passed away, infected two other passenger on a flight from Bangkok to Beijing on March 23rd, 2003. One of those two infected passengers also died shortly thereafter. Another documented case in which airliner passengers had a key role in transporting a fatal disease was the Global outbreak of H1N1 influenza in 2009. According to the results of an investigation conducted by Khan et al. (2009), between March and April 2009 the international flights passengers departing from Mexico transmitted a novel influenza A (H1N1) virus all around the World. A strong correlation between

the international destinations of airliner passengers departing from Mexico and confirmed H1N1 importations associated with travel to Mexico.

1.2 Commercial Aircraft Environmental Control System

In the new generation of commercial aircrafts, the cabin air-conditioning systems is designed such that to provide healthy and comfortable air at cruising altitude (the cruising altitude can reach up to ~ 40,000 ft). In order to condition the cabin environment appropriate for passengers' normal respiration the cabin must be pressurized and, according to the regulations, the cabin pressure should be greater than or equal to the outside air pressure at an altitude of 8,000 ft (Zhang and Chen, 2007 and Boeing, 2011). The cabin supply air is composed of ~50% from the compressed outside fresh air drawn off the jet engine (Figure 1.2) and ~50% from the highly filtered cabin air. The air drawn off the engine is hot and should be cooled. The first stage of cooling process is performed by the heat exchangers mounted in the engine struts. The second stage of cooling the pressurized air is done by the main air-conditioning units after flowing through the wing (to prevent injection of ozone in to the cabin, the pressurized air passes through an ozone converter before reaching the air-conditioning unit).

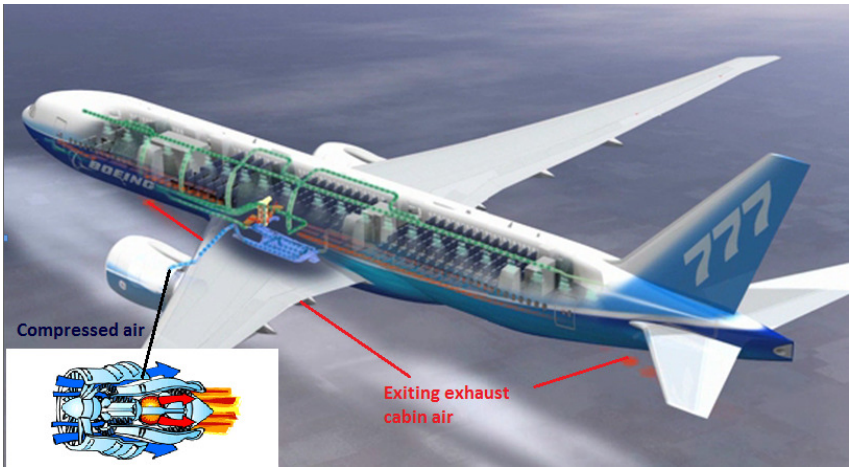

Figure 1.2: A view of a typical air-conditioning system for a commercial aircraft cabin. The picture shows how the compressed fresh air is drawn off the engine and mixes with the highly filtered cabin air in equivalent portions to provide appropriate cabin environment for normal breathing. The picture also shows the exhaust cabin air exiting the lower lobes of the fuselage (Boeing, 2011 and NASW, 2011).

The used air is exited from the cabin through the floor grills on both sides of the cabin. Around half of the exiting air is exhausted from the airplane and the remaining half is filtered by High Efficiency Particulate Air (HEPA) filters. These filters are located under the cabin floor (Boeing, 2011).

1.3 Research Background

Biological contaminants and/or diseases may spread among the airline passengers in the form of exhaled breath gases, sneeze/cough droplets and airborne pathogens. Therefore, the study of air quality, as well as evaluating the effectiveness of ventilation systems in removing contaminants in aircraft cabins, require an in depth knowledge of different transport phenomena.

There are two principal approaches in studying airflow and other transport phenomena in an aircraft cabin: (1) experimental measurements and (2) computational simulations. Because of the high expense and other operational difficulties associated with running experiments in an actual aircraft cabin during flight conditions, most of the experimental measurements have been performed on cabin mockups. However, due to the transient nature of transport phenomena, difficulties in doing measurements with reasonable spatial resolution, uncertainties and other limitations (e.g. cost, associated with experimental procedures and measuring instruments) create serious limitations in studying air quality in aircraft cabins through experimental methods. Consequently, Computational Fluid Dynamics (CFD) has been used for a few decades to evaluate the performance of air conditioning systems through the simulation of fluid flow and heat transfer for the indoor environments. Due to advances in computer technology and turbulence models, the use of CFD as a powerful and economical design tool for improving the efficiency and performance of air-conditioning systems has been increased. In aircraft industry, CFD models are used to investigate the effect of air conditioning systems on the passengers comfort as well as the dispersion of particulates and gases as part of understanding the possible spread of contaminants within an aircraft cabin (Lebbin, 2006).

Advanced computer technologies have enabled researchers to calculate airflow and contaminants distribution in a time and cost effective manner. Using a computational approach, one can study the effect of a fictitious condition that cannot be studied through experimental methods. The computational approach is divided in to two methods by itself: (1) zonal model and

(2) Computational Fluid Dynamics (CFD). Compared to CFD models, zonal models use less computing time but their results are not as accurate as those of CFD. Figure 1.3 shows two main research approaches in studying aircraft cabin environment and their corresponding sub-methods.

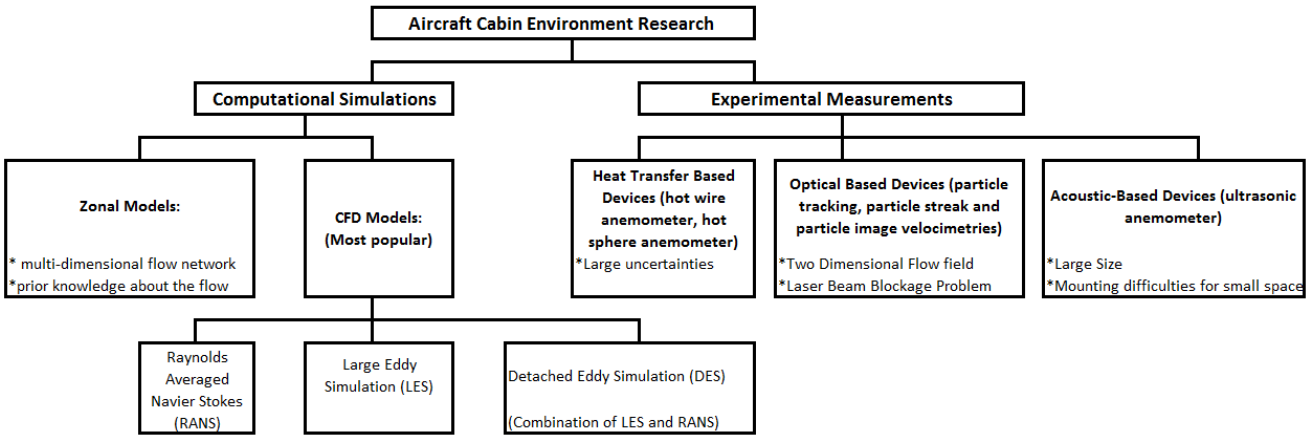

Figure 1.3: The graphical view of the main research approaches in studying aircraft cabin environment and their corresponding sub-methods.

Considering the fact that an accurate and reliable CFD simulation depends on not only the sophistication of the CFD code but also the knowledge, proficiency, and skill of the CFD user and because CFD has become a popular approach in designing and analyzing of indoor air-conditioning systems, Serbric and Chen (2002) have developed a step by step process on how to use CFD for the purpose of indoor air quality analysis. The process has the following stages:

- Case Setup
- Verification
    - basic flow pattern
    - turbulence models
    - auxiliary heat transfer and flow models
    - numerical methods
    - assessing CFD predictions
- Validation and reporting of results
    - experimental description

- flow/turbulence/auxiliary heat transfer and flow models
- boundary/initial conditions
- numerical methods
- assessing CFD prediction
- drawing conclusions

- Discussion

The above process is very close to what was followed in performing the CFD simulations presented in this dissertation. At the setup stage, the important and key parameters in designing or analyzing the indoor environment are determined. Generally these parameters are air velocity, air temperature, contaminant concentration, relative humidity, and turbulence quantities. In the verification stage, the capability of CFD code and user in predicting a roughly correct pattern for the behavior of flow, temperature, and contaminant distributions is verified. However in many cases the verification and validation stages are combined. In the validation stage the experimental setup is explained such that other people can repeat the CFD simulations. In this stage, as listed above the governing equations are formulated, the applied models for turbulence/flow/heat and mass transfer are described; the boundary and initial conditions for solving the governing partial differential equations are specified and formulated. Then the numerical method is illustrated. Before the assessment of CFD predictions through comparison with corresponding experimental measurements, a grid independence study is performed. In drawing conclusions, through the comparison between computational predictions and experimental measurements the effect of different models and numerical schemes on the accuracy of predictions is discussed and the capability of CFD code as well as the user in accurate predicting the flow velocity field, temperature field and contaminant concentration is evaluated. In the last stage which is discussion, in addition to the conclusions achieved from the simulation validation, the effect of applying different design scenarios on indoor air quality characteristics is studied through running the validated CFD codes for those scenarios and the predicted airflow velocity, and Contaminant concentration predictions are then compared with experimental results and conclusions are made based on those comparisons.

1.4 Research Objectives and Methods

The main purpose of this research, which is a continuation of a previous research conducted by Lin et al. (2006), is the understanding of the mechanisms associated with transport of diseases and contaminants transmission through the numerical simulation of turbulent airflow in an aircraft cabin mockup.

The primary objective of this project was to evaluate the CFD capabilities in simulating turbulent airflow, tracer gas diffusion, and particles dispersion in a Boeing 767 generic half-cabin as well as an 11-row full-scale cabin mockups. For this purpose, the CFD predictions for turbulent airflow velocities, tracer gas concentration, and dispersion of liquid particles were compared with the corresponding experimental measurements. For the generic cabin mockup (Figure 1.4A), the airflow and tracer gas experimental measurements used were those performed by Lebbin (2006) and the particle dispersion measurements used were those performed by Padilla (2008). All the tests associated with the generic cabin were run at Kansas State University in the Institute for the Environmental Research (IER). The measurements of airflow velocity, airflow temperature, tracer gas concentration, and particle dispersion for the 11-row full scale cabin mockup (Figure 1.4B) were performed by Beneke (2010), Shehadi (2010) and Trupka (2011) at Kansas State University in the Airliner Cabin Environmental Research (ACER) lab.

Figure 1.4: The full-size11-row Boeing 767 cabin mockup (left) and the Boeing 767 generic cabin model (right)

The CFD simulations performed in this research are divided into four phases. In the first phase the turbulent airflow in generic cabin is simulated using both Large Eddy Simulation (LES) and Reynolds Averaged Navier Stokes (RANS) models. These models are validated through comparison of the predictions for instantaneous (LES and unsteady RANS) and time averaged velocity data in specified monitoring locations inside the cabin with corresponding instantaneous Particle Image Velocimetry (PIV) data. Moreover the performance of the LES model is evaluated through the comparison of the model predictions for the velocity data with the corresponding predictions from the LES model produced by Lin et al. (2006). After the validation and evaluation of RANS and LES models the following cases are studied and discussed through the simulations:

- The effect of different k-ε models on the accuracy of RANS predictions
- The effect of using Werner-Wengle wall function on the performance of LES model
- The effect of decreasing the air inlet nozzle height on the flow circulation behavior by keeping the Reynolds number at the inlet nozzle unchanged

In the second phase, the diffusion of tracer gas (carbon dioxide-CO_2) is simulated through the numerical solution of the governing species transport equations. Both RANS and LES models are used in solving the governing Navier-Stokes equations. The simulations are validated through the comparison of time-averaged predictions for tracer gas concentration data with the corresponding measurements.

Contaminants and diseases might be transmitted between the passengers of an airliner cabin in the form of fine particles. Particles which represent viruses have a range of sizes from 0.02µm to 0.3µm. The bacteria droplets, however, cover range of sizes from 0.3µm to 12.0µm (Tang et al., 2009). Therefore in the third phase the turbulent dispersion of particles in the generic cabin is simulated. Lagrange -Euler (Discrete Phase Model, DPM) approach is used in the simulations. In accordance with the experiments, two different sizes are considered for the particles: 3µm and 10 µm. Through the validation of computational simulation using the available experimental data, the following effects on dispersion behavior of particles are also studied and discussed:

- The effect of particle size
- The effect of particle injection configuration
- The effect of particle density
- The effect of cabin inside pressure (cabin pressure gradient)

Also in grid independency studies the advantages of local mesh refinement rather than the whole mesh refinement is elaborately discussed and explained. The other important achievement of this phase of study is determination of the optimum number of tries in Discrete Phase Simulations. Figure 1.5 shows the graphical view of research in first three phases.

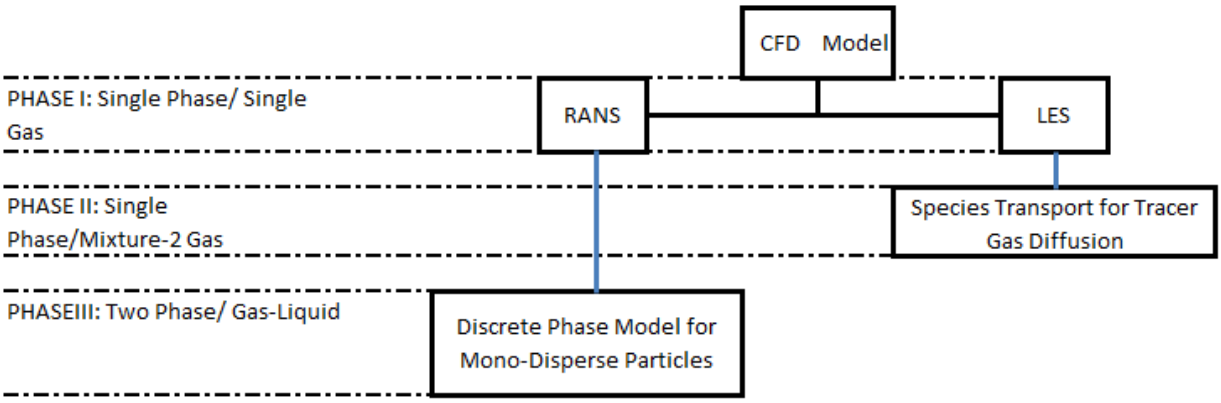

Figure 1.5: The graphical view of the current research phases

In the fifth and the last phase of the simulation the airflow is simulated in an 11-row full-scale cabin mockup using RANS. The simulations are validated through comparison with corresponding experimental measurements.

1.5 Organization of the Dissertation

This dissertation contains 8 chapters. Chapter 1 introduces the reader with the CFD area of research, scope of this work, and the applied methods. In Chapter 2 all the previous research in the area of air quality in closed enclosure is reviewed.

Since a commercial CFD software (FLUENT) is used for the simulations in this study, as an introduction to work with this software and getting familiar with its different aspects, in Chapter 3 the flow over two and three dimensional backward steps are simulated. Both turbulent and laminar flows are considered in these simulations. To ensure appropriate familiarity and application of the software, the flow over the backward step is simulated and the predicted velocity profiles before and after the step are compared with the corresponding experimental and computational data available in the literature.

In Chapter 4, the turbulent airflow in a generic cabin model with full-height and half-height nozzle is simulated. The cabin is exactly the same as one was used in Lin et al. (2006) research. The turbulent airflow characteristics are predicted by employing two widely used turbulence models: Large Eddy Simulation (LES) and Reynolds Averaged Navier Stokes. The predictions from both the LES and RANS models are validated through the comparison of the predicted velocity data with the PIV data for five monitoring areas along the cabin center plane parallel to the bulk airflow direction (Lebbin, 2006). Through these comparisons the capability of the two aforementioned turbulence models in predicting the airflow velocities is discussed and compared to each other. The effect of reducing the inlet nozzle height to one-half of its original size on turbulence level and airflow velocities in the generic cabin, while maintaining the same Reynolds number for the inlet airflow, is also studied in this Chapter.

Chapter 5 includes one of the distinctively significant objectives of this study which is simulating the diffusion of a tracer gas (carbon dioxide) injected uniformly through the circumferential surface of a 12.7 mm schedule-40 porous polythene tube installed horizontally inside the generic cabin model. The simulation is performed using the LES model for solving the governing mass, momentum and species transport equations. The computational results are validated through the comparison of time-averaged predicted concentrations of the tracer gas in specified locations in the cabin with the corresponding experimental measurements.

The other distinguishing feature of this research is presented in Chapter 6. The turbulent dispersion of 3 and 10 micron particles injected into the generic cabin is simulated using two different approaches: Euler-Euler and Lagrange-Euler. The particles are made of Di-Octyle Phthalate (DOP) and produced by a Vibrating Orifice Aerosol Generator (VOAG). Advantages of local mesh refinement comparing to the whole mesh refinement, the optimum number of tries

in Discrete Phase Model, the effects of particle density and size, cabin inside pressure and injection configuration on dispersion behavior of particles are discussed in this Chapter. Chapter 7 presents the turbulent airflow simulations in a full-scale Boeing 767 aircraft cabin using RANS method, and finally in Chapter 8 the conclusions from this study are discussed and explained.

Chapter 2 - Literature Review

The study of air quality requires the study of different transport phenomena: transport of mass, momentum, and energy. Due to the advances in computer technologies which have enabled researchers to solve the required governing partial differential equations numerically, with relatively high degree of accuracy, in a cost and time effective manner, the use of computational methods in this field of research has increased considerably in recent decades.

Numerical investigation and computational modeling of transport phenomena in aircraft cabin environments initiated since four decades ago. The earliest motivation for study of flow, heat and mass transfer in aircraft interior environments was the understanding of the mechanisms associated with the spread of fire and the diffusion behavior of resulting hot smokes and toxic gases in such environments. Emmons (1982) modeled the propagation of fire in the cabin when the source of fire is the hot gases coming into the cabin from external fire through an opening in the cabin. However, Yang et al. (1984) performed another numerical study when the fire initiated inside the cabin. For this purpose, through neglecting the lateral effects, they devised a two dimensional model by taking the effects of buoyancy, turbulence and compressibility into account. The turbulence effects were simulated through an algebraic turbulence model. For the simulation of fire, a volumetric heat and smoke source with arbitrary flame envelope and rate of local heat and smoke generation were applied. Also, the probability of igniting seat surfaces when the seat surface temperature is getting increased up to igniting levels was considered. A finite difference method was used based on the micro-control volume scheme introduced by Patankar and Spalding (1972). The calculations were based on a cabin length of 26 ft for two cases of with and without seats. In addition, several scenarios of fire location were taken into account in the simulations. The results indicated the drastic effect of seats on the flow velocities, the temperature distribution and the diffusion of smokes in the cabin. The simulations showed when the fire is located between the rows, the situation (regarding to the penetration of hot toxic gases to the other seats) would be more dangerous than the case in which the fire is located in the front of the cabin.

Horstman (1988) developed a two-dimensional computational model to simulate the airflow and contaminant (CO_2) distribution in a twine-aisle aircraft cabin. In order to solve the Navier-Stokes equations, two methods were applied: (1) Finite Difference stream functioning

equations and (2) modified Taylor series approximation of the vorticity equations. The velocity field calculated through the solution of Navier-Stokes equations was used as the basis for the simulation of contaminant propagation and distribution. Two mechanisms were considered for the transportation of contaminants: convection and diffusion.

Aboosaidi et al. (1991) used two CFD codes (FLUENT and BINS3D[1]) in order to investigate the Indoor Air Quality (IAQ) in a three-dimensional aircraft cabin mockup. Two different cases of cabin and air supply configurations were tested and the simulations validated through the comparison of predictions with corresponding experimental measurements. For one case FLUENT and for the other one BINS3D were utilized. In both cases, contaminant dispersal and transport of energy were neglected. Assuming the periodic boundary conditions allowed solving the governing Navier-Stokes equations just for one seat row instead of solving those equations for the whole cabin configuration with the large number of seat rows and consideration of end effects. While in FLUENT a two equation k-ε turbulence model was used to predict the turbulent transport of momentum, whereas in BINS3D a mixing length was implemented. In the case studied using FLUENT, a numerical analysis was performed for the flow in the nozzle and the results were applied as boundary conditions for simulating the turbulent airflow in the cabin mockup. However for the case analyzed by BIN3D, the uniform airflow condition was assumed at the inlet nozzles. The comparisons between the computational predictions and experimental measurements showed that CFD could predict the overall flow pattern, and the velocity predictions had an acceptable level of accuracy. It was also realized that the maximum errors were in the vicinity of the nozzle jet, where the computational models did not capture all the mixing characteristics. However the accuracy for the seated portion of cabin was good.

In 1992, Mizuno and Warfield developed a three dimensional model to perform airflow and thermal analysis in aircraft cabin mockup. The model was based on an incompressible Navier-Stokes code in which the Prandtl's mixing length theory was applied to model the turbulent effects. However it was found that the applied turbulence model was not successful in describing the flow characteristics sufficiently well. The effects of thermal buoyancy, the influence of cabin interior obstructions (passenger seats) and, the dispersion of contaminants

[1] This code is a three-dimensional Navier-Stokes code developed from the INS3D code of NASA Ames Research Center using the method of pseudo-compressibility (Kwak et al., 1986)

(carbon dioxide) were also considered and taken into account. The model was verified through the comparison of airflow velocity and CO_2 concentration predictions with the corresponding experimental measurements. A full-size cabin mockup was used to perform the experimental measurements. Through the verification comparisons, a relatively good correlation between the model predictions and the test results was observed.

Baker et al. (2000) used a laminar flow simulation using highly phase selective numerical simulation to calculate the ventilation flow field in an aircraft cabin at cruise condition. This approach enabled computations to be stabilized in the supply jet region in a manner that imitates a Large Eddy Simulation (LES). The results of that study indicated that CFD methodology, in a parallel computing environment, and with unstructured meshing has the capability of quantifying the existence or the lack of comfort indoor environment in aircraft cabins. Su et al. (2001) used three different sub-grid scale models of LES simulation for predicting airflow velocity, air temperature, and contaminant concentration in an air ventilated room. Validation of the simulations indicated an acceptable agreement between computational and experimental profiles of velocity, temperature, and contaminant concentration except for the near wall regions. That study demonstrated the capability of LES, as an efficient tool, in studying indoor air quality.

Through a computational study performed by Singh et al. (2002), the effect of occupants on the aircraft cabin air distribution was studied. This effect was due to flow blockage and transferred thermal energy from the passengers. The study was focused on a 5.0 m (18 ft) section of a one isle aircraft cabin. The governing Navier-Stokes and energy equations were solved for steady-state conditions and RNG k-ε model was used to calculate the effect of turbulence on airflow and heat transfer. The simulations were fulfilled for two cases of cabin with and without passengers. In order to consider the effect of passengers in blocking the flow as well as loading heat to the surrounding space, in both computations and experiments, cylinders were located on the seats with a 100 W heat generation[2]. The predictions showed the more spreading behavior of incoming air in the cabin with passengers. Also it was found that the window passenger receives the least amount of conditioned air therefore providing an additional conditioned-air near the window is necessary.

[2] In accordance with the metabolic heat generation for an adult male sitting ~94.2 W (ASHRAE, 1997)

Zhao et al. (2003) developed a simplified computational model to simulate the airflow in ventilated rooms more time and cost effectively, which was easier to work with especially for design engineers. They used the N-point Air Supply Opening Model (ASOM) technique to overcome the difficulties associated with specifying the boundary conditions at the air supply diffuser and also to reduce the number of mesh elements.

Since the particulate matters are the main infectious contents of the cough or sneeze of a sick person, an effective way to investigate the pattern of airborne disease transmission in aircraft cabins or generally in any indoor places, is to use tracer particles and study their dispersion behavior in indoor environments. Zhao et al. (2004a) investigated the air movement and aerosol particle concentration and deposition in a ventilated room numerically. Two different ventilation systems were considered: displacement and mixing. In order to simulate airflow and particle dispersion, a Lagrangian approach was adopted. This study showed the strong effect of the room ventilation type on the airflow pattern, the particle concentration and deposition rate. As a very important outcome of this research, it was found that under the same air supply rate and particle property conditions, using the displacement ventilation type, leads to less deposition rate and larger number of escaped particles comparing to the mixing type of ventilation. However, the average concentration of particles is higher in the displacement type of ventilation system.

In another effort conducted by Zhao et al. (2004b), an Euler-Euler approach was taken to study the effects of air ventilation type as well as the particle size on the behavior of particle dispersion in a ventilated room. A three dimensional drift flux model was used combined with deposition boundary conditions for the wall surfaces. Through this computational research it was found that the deposited particle mass or flux is strongly dependent on the ventilation type. More particle depositions were observed in the mixing ventilated room for a certain size of particles.

Garner et al. (2004) presented a CFD model which was developed to simulate the airflow field characteristics in a Boeing 747 aircraft cabin. The applied CFD model was described by the unsteady, time-accurate, buoyant ventilation flow field in an aircraft cabin at cruise conditions. The simulation was conducted using a finite element implementation of an augmented laminar Taylor stabilized finite turbulent kinetic energy (TKE) model. Lin et al. (2005) published the

results of their numerical investigation of airflow and airborne pathogen transport in a commercial aircraft cabin (in a two-row section of a Boeing 767-300 aircraft cabin) in couple of papers. Two different turbulence models were used in their study; LES and Reynolds Averaged Navier Stokes (RANS) models. It was observed while RANS simulation substantially under-predicted turbulent intensity, the LES predicted values were in good agreement with the test data. Based on the LES results, the k-ε equations in the RANS model were modified and then used in simulating the disease transmission using less than 1/100 of the computing resources required for the equivalent LES simulation of particle transport in the same cabin. In order to track the airborne pathogens, due to less computational requirements, a multi-species analysis was used instead of multiphase analyses. Also in simulating the dispersion of measles viruses, it was assumed that they are made of water.

As a continuation of the study performed by Garner et al. (2004), Baker et al. (2006) conducted a CFD study of turbulent airflow and contaminant distribution in a Boeing 747 aircraft cabin. The simulations were validated through the comparison of predicted velocity data with the high-quality, time-accurate, three-dimensional experimental velocity data measured in a Boeing 747-100 cabin mockup and a Boeing 747-400 in flight. The experimental data indicated the existence of a large-cabin proper circulation pattern and a second smaller circulation, energized by the unsteady Coanda- effect wall jet separation, in the upper region of the cabin between the luggage compartments. Although there was a good agreement between the predicted velocity data and the corresponding experimental measurements, the validation of CFD predictions for contaminant transport was less conclusive. The weak agreement between the calculations and measurements was attributed to the inherent limitations associated with the measurement devices. It was also found that the steady RANS codes could properly produce initial conditions for the simulation of contaminant transport in enclosures like aircraft cabins.

Lin et al. (2006) performed another study in which the CFD predicted velocity data for turbulent airflow in a generic cabin model were compared with corresponding Particle Image Velocimetry (PIV) experimental data. The main focus of that study was using LES simulation to compare the temporal variations in the experimental data. The good agreement between the simulation results and measured data validated the LES predictions. Also it was observed that

the energy-spectrum function calculated from the LES velocity prediction had excellent correlation with the Kolmogrov spectrum law in the universal equilibrium range.

Wang et al. (2006) studied the transient airborne transmission of diseases in a Boeing 767-300 aircraft cabin, numerically. In their study, the dependence of airborne transmission on different factors including the distance between the release source and the receptors, the location of the release source and the total air supply rates were investigated. By completing the research, it was figured out that the location of the release source is an important factor that affects the pattern of the airborne transmission in aircraft cabins. Accordingly, it was recommended to move the release source (sick passenger) from the center of the cabin to the sides or from the back seats to the front seats in order to decrease the disease exposure risk. The other outcome of the research was the direct proportionality between the total air supply rate and the disease exposure risk.

Zhang and Chen (2007) used a commercial CFD software to study the effects of using under-floor and personalized air distribution systems in improving the performance of air distribution systems in aircraft cabins. They used the RNG k-ε model for solving the Navier-Stokes equations. Their CFD model was first validated through the comparisons of the predictions for airflow velocity, air temperature, and tracer gas (SF_6) concentration with the corresponding measurements for the mixing type air distribution system. The comparisons indicated that while there was a good agreement between predictions and measurements for airflow velocity and air temperature data, there was a large discrepancy for the SF_6 concentration data for some locations. After the validation, the CFD model was used in studying and analyzing the performance of three types of air distribution systems: mixing, displacement and personalized, through the simulation of transport phenomena in a 4-row section of a Boeing 767-300 aircraft cabin.

There are some limitations in the number of contaminant detection sensors that can be used in aircraft cabins. These limitations are coming from the expense, weight and volume of the sensors. Zhang et al. (2007) performed a validated numerical study using a CFD program to find how a limited number of sensors should be placed in an aircraft cabin, optimally. They focused their study on a nine-row section of a Boeing 767 aircraft cabin. In their computational model, the RANS method was used with a RNG k-ε turbulence model to solve the governing

Navier-Stokes equations. Also, SF_6 was used as the tracer gas in both experiments and computations. The study revealed the uniform distribution of contaminants in the cross sections of the cabin. The optimal sensor placement location in a cross-section was found to be in the middle ceiling, if one sensor was used.

The virus transport after coughing or sneezing can be described in two steps: the intruding multi-phase jet as the first step and the global environment effect due to the air ventilation system as the second step. In an effort to study the second step of the virus transport, Zhang et al. (2008) conducted an experimental and a computational research, using the tracer gas method, to study the global transport process of contaminated air within a full-scale Boeing 767-300 mockup. Through the simulations and the experiments performed in this research, the significance of the air ventilation system and the release source location in controlling the airborne pollutants in aircraft cabin was realized. As one of the important conclusions of this research, it can be pointed out that most pollutants are transported within the half where the release source is located and seldom cross the cabin middle line. This research also confirmed the recommendation given by Wang et al. (2006) in moving the release source from the middle to the sides in order to have less air quality problems. Another interesting result of this work was the contribution of longitudinal airflow in the pollutant transportation within the aircraft cabin. Although based on the Wang et al. (2006) research work it was recommended to increase the air supply rate to decrease the disease exposure risk, the investigation performed by Zhang et al. (2008) showed that increasing the ventilation rates is not necessarily helpful for the receptors close to the pollutant source. This study demonstrated the capability of CFD in investigating the mechanism associated with disease transmission in aircraft cabin. It was also experienced how CFD can provide more comprehensive and detailed information rather than experiments.

Mazumdar and Chen (2008) studied the effect of seating patterns and contaminant source locations on the placement and contaminant detection sensors in a twin-aisle commercial aircraft cabin using a commercial CFD code. The RANS method was used in order to solve the governing Navier-Stokes equations, and the RNG k-ε model was used as the turbulence model. The convergence criteria were set to 1.0×10^{-5} for the normalized residuals. The experimental data was obtained from the tests performed in a twine-aisle cabin mockup. Through this study, it was found that the release location and seating patterns had little impact on longitudinal

contaminant distribution. They recommended the center of the cabin ceiling as the best place for mounting contaminant detection sensor when only one sensor is available.

Abdilghanie et al. (2009) investigated the effect of using laminar and turbulent inlet velocity profiles on the behavior of turbulent flow inside a simple room through LES. They also compared the performances of LES and k-ε models in predicting the flow characteristics in the same room. Their study showed that the standard k-ε model is less sensitive to the level of turbulence at the inlet than the LES model. It was also found that when the flow at inlet is laminar, the standard k-ε model fails to capture the slow development of the jet which is realized by LES.

In order to investigate the effects of using two different air distribution systems on the contaminants propagation patterns in the aircraft cabin and in between passengers, Tang et al. (2009) used a Finite Volume method to produce a three-dimensional contaminant dispersion model for a four-row section of a Boeing 767-300 aircraft cabin. They assumed the cabin was pressurized and that heat transfer effects were negligible. The standard k-ε turbulence model was used to solve the governing momentum equations. Comparisons of simulation results for CO_2 concentration and droplets residence times between two air distribution systems indicated that using the Under Floor Air Distribution (UFAD) system, because of producing better flow circulation, leads to lower levels of carbon dioxide and shorter residence times for the contaminant droplets compared to the Ceiling Air Distribution (CAD) system.

Through the experiments and CFD simulations by Yan et al. (2009), it was found that the contaminant source location has a significant effect on pollutant transport within the cabin. In that research, the contaminant dispersion in a five-row section of a Boeing 767-300 aircraft cabin was simulated through modeling tracer gas diffusion. It was also realized that increasing the ventilation rate is not necessarily useful for the receptors close to the source.

Since coughing is one of the primary sources of airborne diseases, especially in aircraft cabin environments, Gupta et al. (2009) performed a study to find a mathematical expression for the exhaled flow rate from a cough and to quantify the mass flow rate as well as size of exhaled particles. They figured out that the cough exhaled flow rate can be formulated by a combination of gamma probability distribution functions. Some medical parameters which can be obtained from the physiological details of a person were recognized to be required in order to define the

gamma probability distribution functions. However it was found that the jet direction and the mouth opening area during a cough are not a function of physiological details of person.

Mazumdar and Chen (2009) developed a one-dimensional analytical model to estimate the longitudinal transmission of disease and contaminants inside an aircraft cabin. It was not trivial because a quick and rough evaluation of disease transmission is absolutely necessary in taking actions to reduce the risk of infection of passengers and crew members. The principal assumption in that study was a uniform distribution of contaminants in the cross-section of the cabin. Both convection and diffusion transport of contaminants were considered in analyzing the contaminants distribution along the cabin aisle. The effects of air exchange rate, recirculation, efficiency of HEPA[3] filters, and longitudinal airflow were taken into consideration.

Zhang et al. (2009) performed an experimental and numerical study to investigate the airflow and contaminant transport in a section of a half-occupied twin-aisle aircraft cabin mockup. In order to simulate the gaseous contaminant, a tracer gas (SF_6) was used and for simulating the particulate contaminants, 0.7 μm Di-Ethyl-Hexyl-Sebacat (DEHS) particles were used. In solving the Navier-Stokes equations, a RANS method using a RNG k-ε model was used and to calculate the particle dispersion and, a Lagrangian approach was employed. Remarkable discrepancies between predicted and measure airflow patterns were observed which were due to the difficulties in measuring accurate flow boundary conditions from the air supply diffusers. Through the comparisons between the distribution behavior of gaseous and particulate contaminants, it was also realized that the sub-micron-sized heavy particles behave similar to the passive gas contaminant except in the region near the source position where the diffusivity is different.

Pousso et al. (2010) performed experimental and computational studies to investigate the effect of a moving human body on the airflow and the contaminant distribution in an aircraft cabin environment. Both cases of ventilated and unventilated cabin environments were considered in that investigation. In establishing the CFD model, a second-order upwind scheme and the SIMPLE algorithm were applied. The RNG k-ε model was also used as the turbulence model. Comparing to the PIV experimental measurements, CFD model predicted a higher

[3] High-Efficiency Particulate Air

longitudinal flow behind the moving body. Validation of the CFD model for contaminant transport indicated its capability to estimate the change of contaminant concentration both qualitatively and quantitatively.

Chen, X. and Chen, Q (2010) proposed a CFD method to study the decontamination process in a Boeing 747 aircraft cabin. The RANS method with RNG k-ε model was employed in the CFD model. For the validation of the proposed model, the measured air-velocity and tracer gas concentration in a cabin mockup and the tested decontamination efficacy in another cabin section were used. Reasonable agreement between the calculations and two sets of measurements proved the viability of CFD model in studying the decontamination process in airliner cabins. The validated CFD model was used to study the performance and effectiveness of different decontamination scenarios in a single-aisle and a twin-aisle cabin.

One of the serious challenges in establishing CFD models for the occupied airliner cabins is setting up the boundary conditions for the mouth and nose of the occupants which should contain information about the exhaled and inhaled air composition, flow rate, and flow direction. Gupta et al. (2010) developed a source model to provide thermo-fluid conditions of the exhaled air from breathing and talking. The model was a set of equations obtained from the measurements of the flow rate, flow direction, and area of human mouth and nose opening. It was found that the breathing flow rate variation with time is sinusoidal. The amplitude of the sine function was related to body height, weight, and gender. It was also concluded that considering a constant mean value for the breathing areas (nose and mouth) is a reasonably good assumption. Since the talking flow rate was observed to be irregular, an average flow rate was defined in order to specify the boundary condition corresponding to the talking scenario.

Through a validated computational study, Mazumdar et al. (2011) realized that the seats and passengers tended to block the contaminant transport in the lateral direction inside the aircraft cabin. In other words, it was found that the longitudinal direction along the aisle of the cabin is the dominant direction for spreading the contaminants. The other important outcome of their investigation was revealing the significant role of crews and passengers walking along the aisle in carrying the contaminant in their wake to as many rows as they passed. The CFD model in this study was established using a second-order upwind scheme and the SIMPLE algorithm with RNG k-ε as the turbulence model.

Gupta et al. (2011a) used a commercial CFD code to simulate the transport of droplets exhaled by an index patient seated in the center of a seven-row, twine-aisle, fully occupied aircraft cabin. A Lagrangian method was applied to track the droplets and calculate their trajectories. The evaporation effects were also taken into account. Three scenarios of a single cough, single breath, and a 15-s talk were considered for the injection of infectious droplets from a patient into the cabin. In order to define and set the boundary conditions for the considered scenarios of droplet injection, they used the results of their previous studies (Gupta et al. , 2009 and 2010). The steady-state airflow pattern in the cabin was used as the initial condition for the simulation of mono-dispersed droplets. The simulations were executed for four minutes of real time. The results indicated that the exhaled droplets from the cough followed mainly the bulk airflow. Although the number of droplets was much smaller, a similar pattern of propagation and dispersion was also observed for the droplets exhaled from the single breath. Since the index patient turned the head to the left, the droplets generated due to talking of the patient were mainly moved to the left side of the cabin.

In another study performed by Gupta et al. (2011b), the spatial and temporal distribution of expiratory droplets and their inhalation in an aircraft cabin environment was investigated, numerically. They developed a method to predict the amount of expiratory droplets inhaled by the susceptible passengers over a 4-hour flight under three common scenarios of the exhalation of droplets: breathing only, coughing with breathing, and talking with breathing. The first three minutes after the exhalation of particles from the index passenger was considered as the transient time in the propagation and distribution of particles. For the transient time, CFD was used to simulate the dispersion of particles. Beyond the first three minutes after the exhalation, a perfectly mixed model was used. The simulations were performed using a CFD commercial code (FLUENT) for a seven-row section of a two-aisle aircraft cabin. They used a RNG k-ε model to predict the turbulent airflow in the cabin. The effects of buoyancy and droplets density changes due to the temperature variations were also taken into account. The distribution of mono-dispersed particles was calculated using a Lagrangian approach. Based on the results of the experimental studies previously performed by Yang et al. (2007), Fabian et al. (2008), and Duguid (1946), coughing, breathing, and talking exhalations were assumed to be 8.5, 0.4, and 30μm, respectively.

Liu et al. (2012) reviewed all the experimental and computational investigations performed in studying the airflow distribution and contaminant dispersion in aircraft cabins in the past two decades. They classified the experimental research into three categories: heat transfer-based devices (hotwire and hot-sphere anemometers), optical-based devices (particle tracking, particle streak and particle image velocimetries), and acoustic-based devices (ultrasonic anemometer). They also categorized the computational research in two groups of models: Zonal models and CFD models.

Chapter 3- Flow over Backward-Facing Step

3.1. Introduction and Research Background

As explained in chapter 1, in order to fulfill the objectives of this study, a commercial CFD code was used to simulate the different transport phenomena existing in aircraft cabin environment. To learn the code, which was FLUENT, and getting familiar with its capabilities and features, especially in simulating turbulent flows, the flow over two and three-dimensional backward-facing steps was simulated and validated through the comparison of predictions with available experimental measurements**.**

Although a backward-facing step has a very simple geometry, depending on the flow Reynolds number and the geometrical characteristics of the step, the flow over a backward-facing step shows the features of more complex geometry flows such as separation, recirculation, and reattachment. Therefore backward-facing step flows have provided a favorable case for testing newly developed CFD methods during the past few decades (De Stefano et al., 1998). Hackman et al. (1984) attributed the discrepancies in the accuracy of their numerical solutions to the inadequacy of the standard k-ε turbulence model used in their computations. Kim and Moin (1985) applied a Fractional-Step model to simulate an incompressible backward-facing step flow. Yoo et al. (1989) concluded that the Reynolds stress models are more accurate than standard k-ε model in predicting the flow characteristics in the recirculation region. Fredrich and Arnal (1990) used Large Eddy Simulation (LES) to solve the continuity and momentum equations governing the turbulent flow over a backward-facing step. In that study, although there was a generally good agreement between predictions and measurements, scatter in the experimental data was proposed as the main reason for some observed disagreements. Mesh refinement was also suggested as a way to improve the accuracy of results. Kaiktsis et al. (1991) developed a Direct Numerical Simulation (DNS) to study the onset of three-dimensionality, equilibrium, and early transition flow over a backward-facing step. Le et al. (1997) studied the periodic behavior of a free shear layer in a backward-facing step turbulent flow using a DNS method. Through the simulation of flow over a backward-facing step, Keating et al. (2004) tested two sub-grid scale models: dynamic eddy-viscosity, eddy-diffusivity model and the dynamic mixed model. Nie and Armaly (2004) conducted an experimental and a computational study to investigate the reverse flow regions in three-dimensional backward-facing step flow.

Kim et al. (2005) compared the performance of different k-ε models as well as different near-wall treatments through the validation of CFD simulations for the turbulent flow passing over backward facing step. Rani et al. (2007) employed a Finite-Volume method to simulate the transient flow over a backward-facing step. Lan et al. (2008) simulated the three-dimensional forced convection heat transfer in a duct with backward-facing step. Ishiko et al. (2008 and 2009) applied an implicit LES to study the supersonic flow field over both two-dimensional and three-dimensional backward-facing steps.

3.2. Governing Equations and Numerical Solution Method

In this chapter, the governing Navier-Stokes equations for the incompressible flow over two and three-dimensional backward-facing steps, are solved numerically for steady conditions. The RANS method was used to simulate the turbulence effects. k-ε turbulence models were used to calculate the effect of turbulence. The effects of heat transfer and gravity assumed to be negligible and air is considered as the working fluid (ρ=1.225 kg/m^{3}and μ=1.7894x10^{-5}kg/m.s). For the two-dimensional backward-facing step, just the turbulent flow regime is investigated, however, for the three-dimensional one, all the flow regimes including laminar, transient, and turbulent are taken into consideration and simulated. FLUENT 6.3.26 used as the commercial CFD code in performing the simulations presented in this chapter.

The governing equations for the instantaneous flow field in the cabin are listed as follows:

Continuity:

$$\frac{\partial u_i}{\partial x_i} = 0 \tag{3.1}$$

Momentum:

$$\frac{\partial u_i}{\partial t} + u_j \frac{\partial u_i}{\partial x_j} = -\frac{1}{\rho}\frac{\partial p}{\partial x_i} + \frac{1}{\rho}\frac{\partial}{\partial x_j}(\mu \frac{\partial u_i}{\partial x_j}) \tag{3.2}$$

where, u_i (m/s) denotes the velocity components, x_i (m) represents the positions along each of the coordinate system principal directions, t (sec) is time, μ (kg/m.s) and ρ (kg/m^3) are the kinematic viscosity and density of air, respectively. Also, p (Pa) is the static pressure.

When the RANS method is used to simulate the turbulent flow, the instantaneous flow variables are decomposed into the mean value (time-averaged) and the fluctuating components:

$$u_i = \overline{u}_i + u_i' \tag{3.3}$$

$$p = \overline{p} + p' \tag{3.4}$$

where $\overline{u}_i$, $\overline{p}$ and u_i', p' denote the mean and fluctuating components of the flow velocity and pressure, respectively. Substituting the decomposed form of the flow variables into the instantaneous governing equations (3.1) and (3.2) and taking a time-average of those equations, accompanied with the Boussinesq hypothesis (Wilcox, 1998), gives the following time-averaged governing equations for the steady incompressible flow:

$$\frac{\partial \overline{u}_i}{\partial x_i} = 0 \tag{3.5}$$

$$\frac{\partial \overline{u}_j \overline{u}_i}{\partial x_i} = \frac{\partial}{\partial x_i}\left(-\overline{p}\delta_{ij} + (\mu + \mu_t)(\frac{\partial \overline{u}_i}{\partial x_j} + \frac{\partial \overline{u}_j}{\partial x_i}) \right) \tag{3.6}$$

where μ_t (kg/m.s) is the turbulent or eddy viscosity which using the Bossinesq hypothesis, is defined as:

$$\mu_t = \frac{-\rho \overline{u_i' u_j'}}{\frac{\partial \overline{u}_i}{\partial x_j} + \frac{\partial \overline{u}_j}{\partial x_i}} \tag{3.7}$$

In this study, in order to calculate the above defined turbulent viscosity, the k-ε model which is a typical two equation turbulence model employed. Using this model, the turbulent viscosity calculated through the following equation (Tu et al., 2008):

$$\mu_t = \frac{C_\mu \rho k^2}{\varepsilon} \tag{3.8}$$

where k (m^2/s^2) is the turbulent kinetic energy and ε (m^2/s^3) is the turbulent dissipation rate. While C_μ is an empirical constant for standard k-ε ($C_\mu = 0.09$) and RNG k-ε ($C_\mu = 0.0845$) models (Tu et al., 2008 and Yakhot, 1992), C_μ in realizable k-ε model is not a constant value and is calculated from (Tu et al., 2008):

$$C_\mu = \frac{1}{A_0 + A_s \dfrac{kU^*}{\varepsilon}} \tag{3.9}$$

where A_0 and A_S are constants. A_0=4.04 and A_S is determined through the following equations:

$$\begin{aligned} A_S &= \sqrt{6}\cos\varphi \\ \varphi &= \frac{1}{3}\cos^{-1}(\sqrt{6}W) \\ W &= \frac{S_{ij}S_{jk}S_{ki}}{\tilde{S}^3} \\ \tilde{S} &= \sqrt{S_{ij}^{\,2}} \\ S_{ij} &= \frac{1}{2}\left(\frac{\partial \overline{u}_i}{\partial x_j} + \frac{\partial \overline{u}_j}{\partial x_i}\right) \end{aligned} \tag{3.10}$$

where S_{ij} is the mean strain tensor. U^* in Eq. (3.9) is calculated through the following equations:

$$U^* \equiv \sqrt{S_{ij}{}^2 + \tilde{\Omega}_{ij}{}^2}$$
$$\tilde{\Omega}_{ij} = \Omega_{ij} - 2\varepsilon_{ijk}\omega_k \tag{3.11}$$
$$\Omega_{ij} = \bar{\Omega}_{ij} - \varepsilon_{ijk}\omega_k$$

where ε_{ijk} is the permutation tensor, ω_k (1/sec) is the angular velocity, and Ω_{ij} is the mean rate of rotation tensor.

In order to discretize the spatial derivatives in the governing equations, the second order upwind scheme used. Velocity and pressure are coupled through the SIMPLE algorithm. For the two-dimensional backward-facing step, three near-wall approaches, including: the Standard wall functions, Non-equilibrium wall functions, and Enhanced wall treatment, examined. However, for the three-dimensional backward-facing step, just the Non-equilibrium wall function applied. The convergence criteria set to be 10^{-5} for all the residuals. The grids for both cases structured consisting of orthogonal quadrilateral Map-type mesh elements for the two-dimensional and orthogonal hexahedral Map-type mesh elements for the three-dimensional backward facing step.

Solving the governing equations requires the boundary conditions to be specified. The boundary conditions are: velocity-inlet for the flow at the inlet, no slip stationary wall for the top and bottom walls and outflow for the flow at the outlet. In setting the boundary conditions at the inlet, the flow velocity as well as the turbulent kinetic energy and dissipation rate is specified. In the simulations performed in this study, it is assumed that the velocity at the inlet is uniform. In order to calculate the turbulence intensity at the inlet, the airflow Reynolds number based on the inlet hydraulic diameter is determined. Following the calculation of the Reynolds number, the turbulent intensity, turbulent kinetic energy, and turbulent dissipation rate at the inlet can be calculated through the equations listed below (FLUENT 6.3 Manual, 2011):

$$I = 0.16(\mathrm{Re}_{D_H})^{-1/8} \tag{3.12}$$

$$k = \frac{3}{2}(U.I)^2 \tag{3.13}$$

$$\varepsilon = C_{\mu}^{3/4} \frac{k^{3/2}}{\ell} \tag{3.14}$$

where I is the turbulence intensity, Re_{D_H} is the Reynolds number based on the hydraulic diameter, D_H (m) is the hydraulic diameter (for three-dimensional backward-facing step, the hydraulic diameter is calculated through $D_H = 4A/P$, where A is the cross-section area and P is the wetted perimeter of the cross-section. However, for two-dimensional backward-facing step, D_H is defined as two times of the duct height at the inlet, k (m^2/s^2) is the turbulent kinetic energy, ε (m^2/s^3) is the turbulent dissipation rate, U (m/s) is the uniform velocity at the inlet, ℓ is the turbulence length scale ($\ell = 0.07 D_H$), and C_μ was explained elaborately in Eq. (3.8).

3.3. Results and Discussion for the Flow over a Two-dimensional (2D) Backward-Facing Step

A schematic of the 2D backward-facing step, which is studied in this section, and the respective dimensions for the regions before and after the step are shown in Fig. 3.1. The computational domain before the step has a length of 12*h* and a height of *h*. However, the length and the height of the computational domain after the step are 50*h* and 2*h*, respectively. The Reynolds number based on the free stream velocity *U* of 40 m/s and step height *h* is evaluated as 64,000 (Tu et al., 2008). For the turbulent flow in such geometry, there is only one recirculation zone. It is also believed that the reattachment length is solely a function of the Expansion Ratio (ER) which is the ratio of inlet height to outlet height (Jongebloed, 2008).

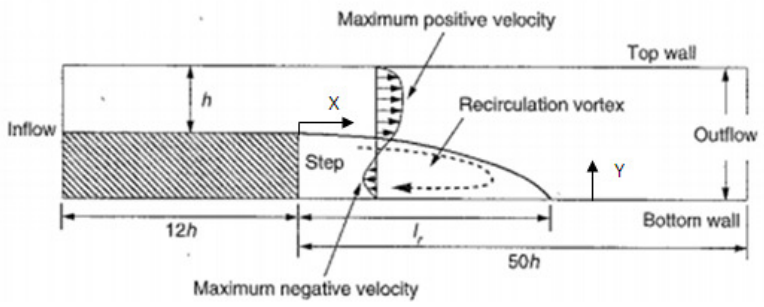

Figure 3.1 Schematic of the 2D backward-facing step flow. The step height is denoted by *h*. (Tu et al., 2008).

In simulating the turbulent flow over a 2D backward-facing step, the verification of the simulations are performed through the comparison of non-dimensionalized velocity profiles at different locations behind the step with the corresponding experimental measurements. Through the CFD simulations, the following cases are investigated and discussed:

- Study the effect of applying different k-ε turbulence models including: standard, RNG, and realizable on the quality of predictions.
- Study the effect of applying different near-wall approaches including: Standard wall functions, Non-equilibrium wall functions, and Enhanced near-wall treatment on the quality of predictions.
- Study the effect of using different estimations of the turbulent intensity in setting up the inlet boundary condition on the quality and behavior of predictions.
- Study the effect of changing the inlet Reynolds number, such that the flow remains turbulent, on the dimensionless recirculation length.

3.3.1 Uncertainty Study (Grid Independency)

Before the validation of any CFD simulation, the computational model needs to be tested for grid independency. In order to perform the grid indecency study for 2D backward-facing step, the standard k-ε is used as the turbulence model, and the standard wall functions are also used for near-wall approach. Three grids with different number of mesh cells are examined. The numbers of mesh cells in the tested grids are: 1550, 6200, and 24800. In all the grids the meshes are structured, Map-type, and made of orthogonal quadrilateral elements. Figure 3.2 shows the distribution of grids for this problem.

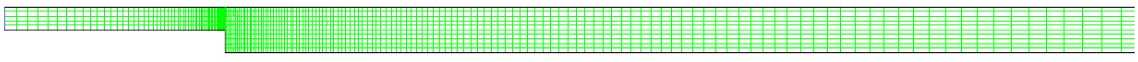

Figure 3.2 The generated grid for the 2D backward facing step flow

Figure 3.3 shows a comparison between the computational results for the x-component of the flow velocity profile corresponding to x/h=1 behind the step**.** It can be seen that the

calculated velocity profile is more sensitive to the grid size in the recirculation region (lower part of the profile). Therefore local grid refinement is recommended in order to get more accurate results in recirculation region. Also, Fig. 3.3 indicates that by increasing the number of mesh cells, the results for velocity data are converged and consequently the grid independency criteria are satisfied.

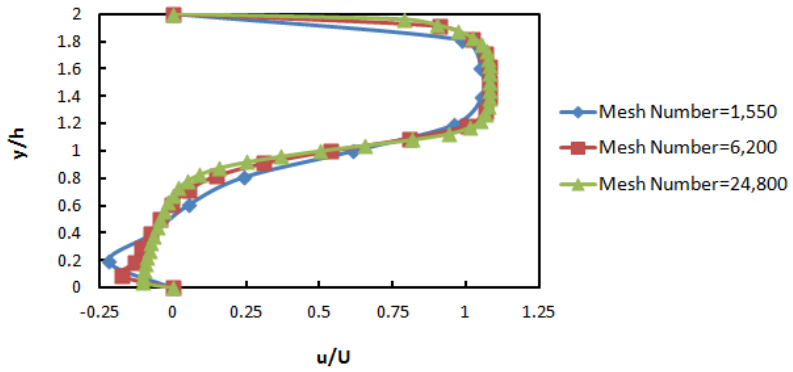

Figure 3.3 The results of uncertainty study. The predicted velocity profiles correspond to x/h=1.

3.3.2 Validation and Discussion

For the simulations presented hereafter for the 2D backward-facing step, the fine grid with 24,800 mesh cells is used. Figure 3.4 shows a validation of CFD simulations through the comparison of predicted velocity data at different locations behind the step with the corresponding experimental measurements (reported by Tu et al., 2008). The figure also shows the gradual change of velocity profile in the downstream of the flow. Similar to the simulations performed for grid independency, for the simulations presented in Fig. 3.4, standard k-ε model was used as the turbulence model and standard wall functions were used as near-wall approach.

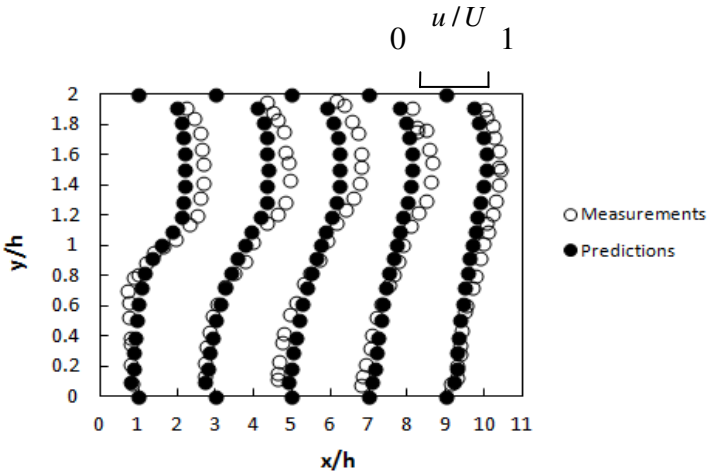

Figure 3.4 Validation of CFD simulations through the comparison of predicted x-component of velocity data at different locations behind the step (x/h=1, 3, 5, 7, and 9) with corresponding experimental measurements (reported by Tu et al., 2008).

Figure 3.5 shows the velocity contours for the flow in a duct passing over the 2D backward facing step colored by the values of stream function. The recirculation region and reattachment length are observable from this figure.

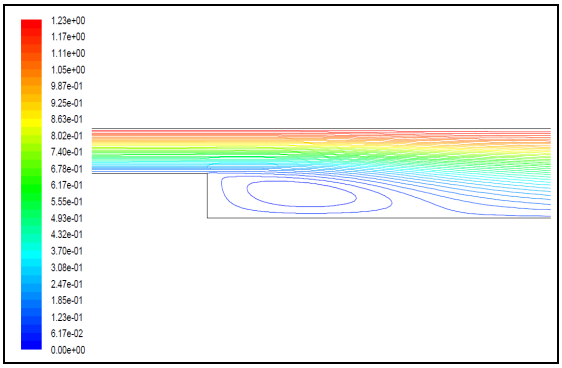

Figure 3.5 Contours of velocity based on stream function values (kg/s) for Re_{inlet}=64000

The comparisons of dimensionless velocity profiles predicted using different k-ε models (Standard, RNG, and Realizable) are shown in Fig. 3.6. It indicates that although the differences between the predictions are very small, the predictions from RNG k-ε model are slightly closer

to the measurements rather than the results from standard and realizable k-ε models. In all the simulations for studying the effect of the type of k-ε model on the quality of predictions, the standard wall functions are applied as the near-wall approach.

Figure 3.7 shows the comparisons between the predictions from RNG k-ε model accompanied with different near-wall approaches and the corresponding measurements. It reveals that, for this geometry and flow conditions, the near-wall approach has a negligible effect on the behavior of flow or the accuracy of predictions. However, the results from Non-equilibrium wall functions shows a little better agreement with experimental data comparing to the results from Standard wall functions and Enhanced wall treatment.

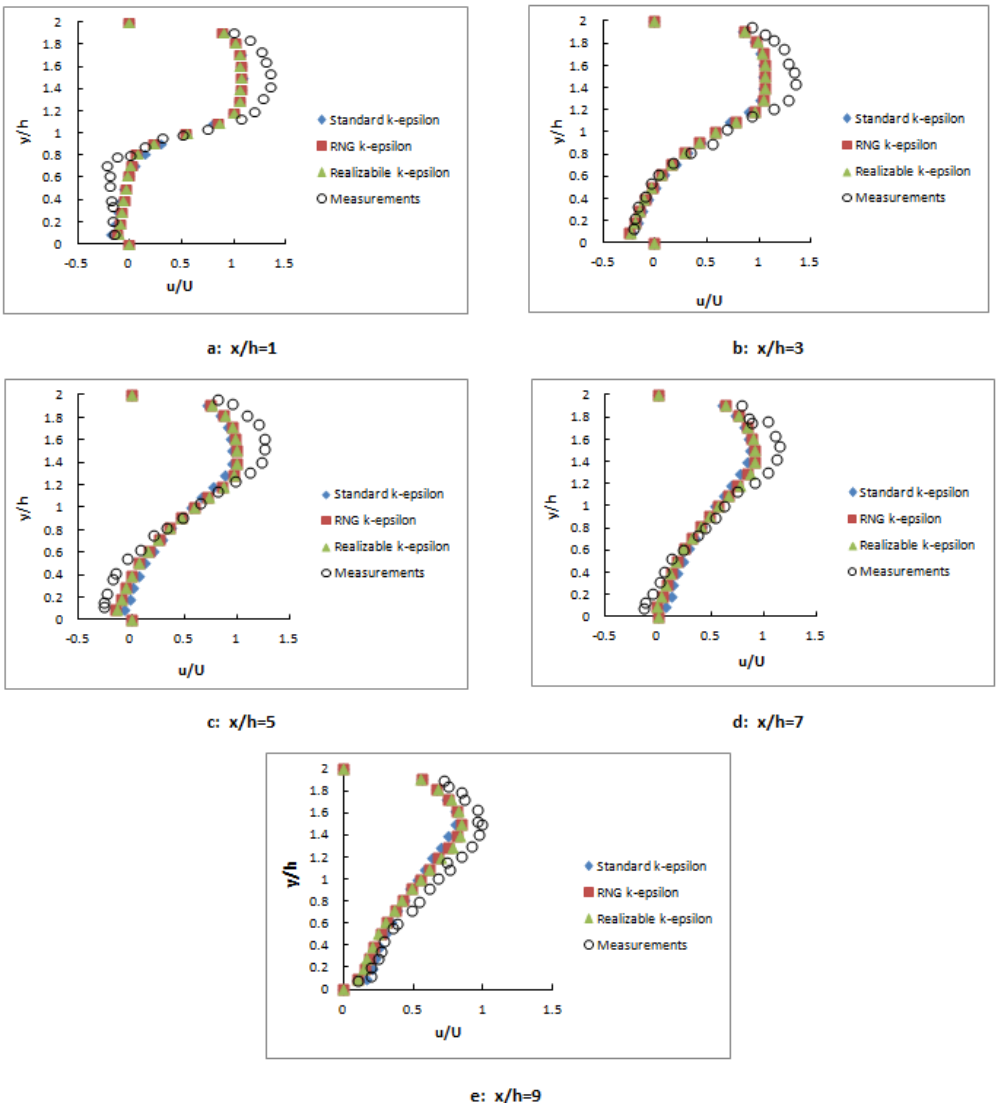

Figure 3.6 Study the effect of using different k-ε models by comparing the predictions and measurements at different locations behind the step.

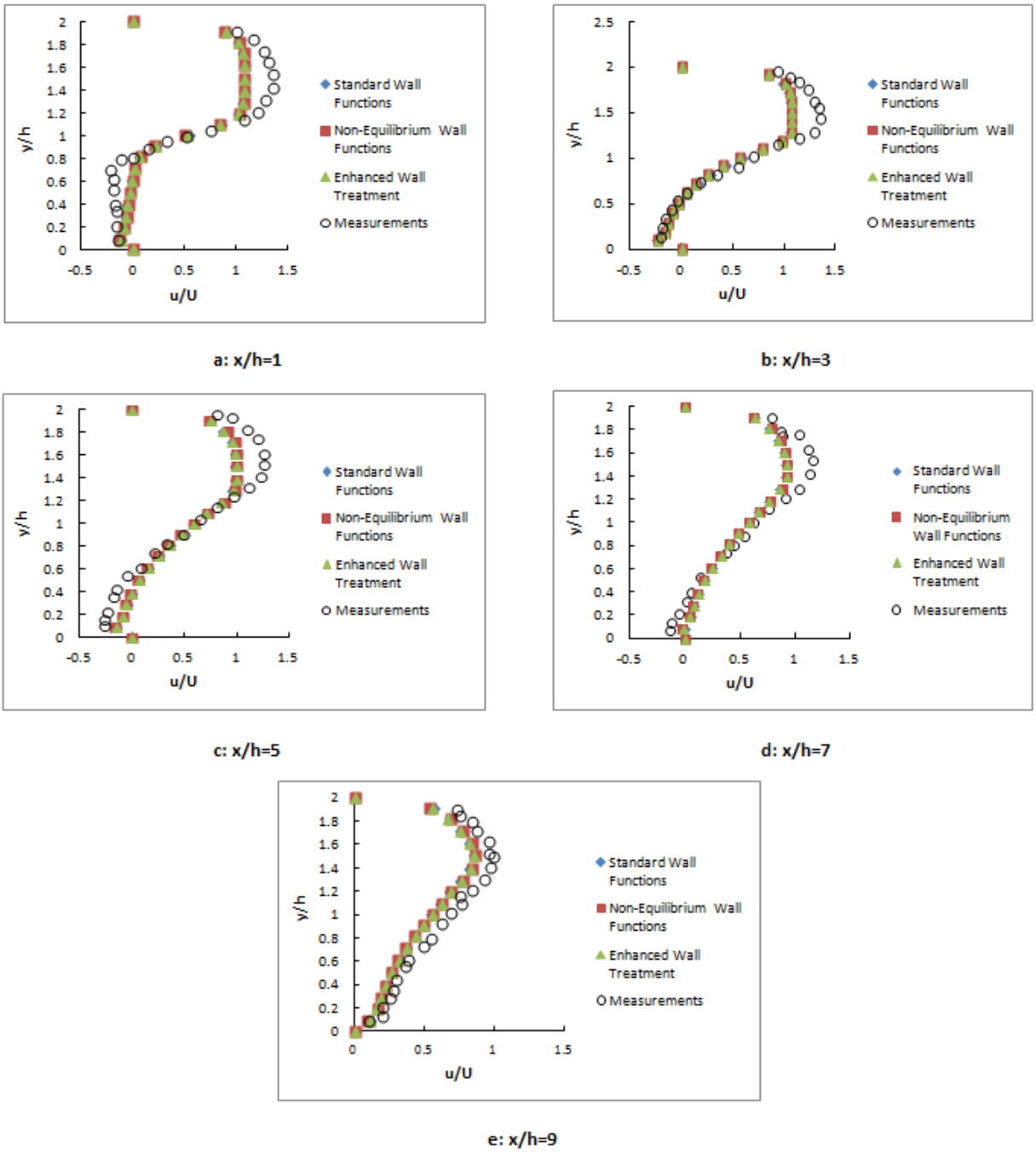

Figure 3.7 Study the effect of using different near-wall approaches through the comparison of the predictions and measurements at different locations behind the step.

As explained earlier in section 3.2 of this chapter, Eq. (3.12) was introduced for the estimation of turbulence intensity at the inlet. However, this equation was originally recommended for the calculation of turbulence intensity at the core of a fully developed turbulent duct-flow (FLUENT 6.3 Manual, 2011) which is considerably different from the flow condition at the inlet of 2D backward-facing step studied herein. Therefore, there is a lack of confidence in the accuracy and validity of the calculated inlet boundary conditions for k and ε using the turbulence intensity estimated by Eq. (3.12).

Using Eq. (3.12) led to an estimated value of ~4% for the turbulence intensity at the inlet. Now, in order to investigate the effect of estimation quality for the turbulence intensity at the inlet on the accuracy of predictions, the simulations are repeated by assuming another value for that. We assume the new value of 20% for the turbulence intensity at the inlet. This value is the maximum value that the turbulence intensity gains in the high-speed turbulent flow inside complex geometries like heat-exchangers and the flow inside rotating machinery such as turbines and compressors (CFD online, 2011). By increasing the turbulence intensity from 4% to 20%, an increase of 3200% and 17800% will be experienced for the inlet turbulent kinetic energy the dissipation rate, respectively. Comparisons of the predictions between two cases indicate that although the inlet boundary conditions for k and ε experience a drastic increase, the changes in predictions are very slight and not more than 5%.

Figure 3.8 shows the comparisons between predictions from the two different estimations of the inlet turbulence intensity and the experimental measurements corresponding to different locations behind the step. These comparisons indicate that changing the turbulence intensity at the inlet has a negligible effect on the computational results**.** For all the simulations presented in Fig. 3.8, RNG k-ε was used as the turbulence model and Non-equilibrium wall functions were used as near-wall approach.

In the last part of investigating turbulent flow over the 2D backward-facing step, the effect of the inlet Reynolds number on the recirculation length is studied. The Reynolds number is changed in a range in which the flow in duct remains turbulent. Figure 3.9 presents a comparison of the predicted maximum negative dimensionless velocities at different locations assuming two different inlet Reynolds numbers (64,000 and 80,000) with corresponding experimental data. We know that the reattachment takes place at the location where the minimum velocity (or the maximum negative velocity) is zero. Therefore, this graph is helpful

in estimating the location where the flow is reattached to the bottom wall behind the step. The RNG k-ε model is used with Non-equilibrium wall functions in the simulations. The simulations confirm this belief that as long as the flow is turbulent, changing the Reynolds number at the inlet has no effect on the recirculation length. Indeed the behavior of turbulent flow over the backward-facing step only depends on the Expansion Ratio of the backward-facing step. Figure 3.9 also indicates that although both computations and experiments estimate the same values for the recirculation length, the simulations predict less maximum for the negative velocities than experiments for all locations with x/h>3.

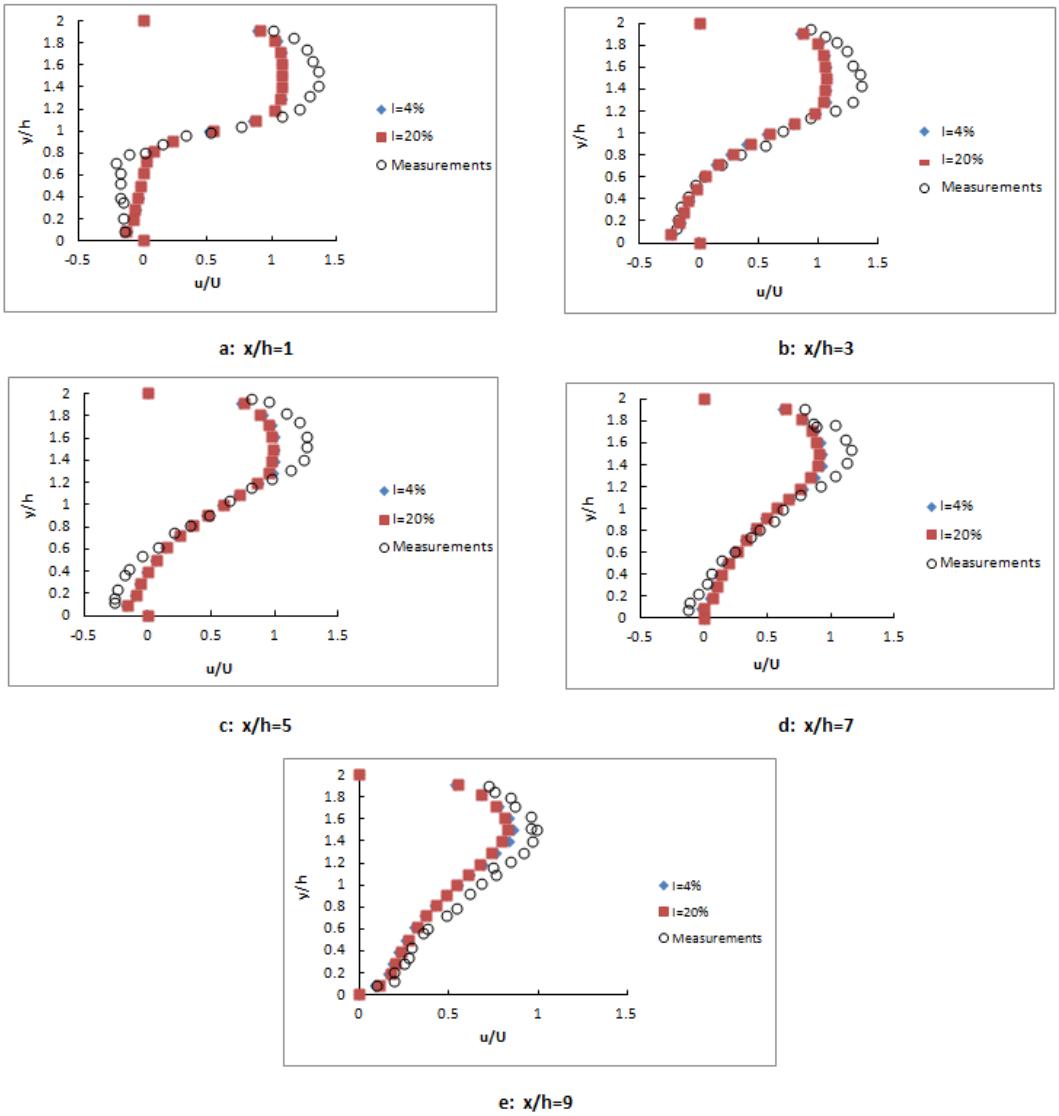

Figure 3.8 Comparison of predictions (from two estimations for turbulence intensity at the inlet) with corresponding experimental data

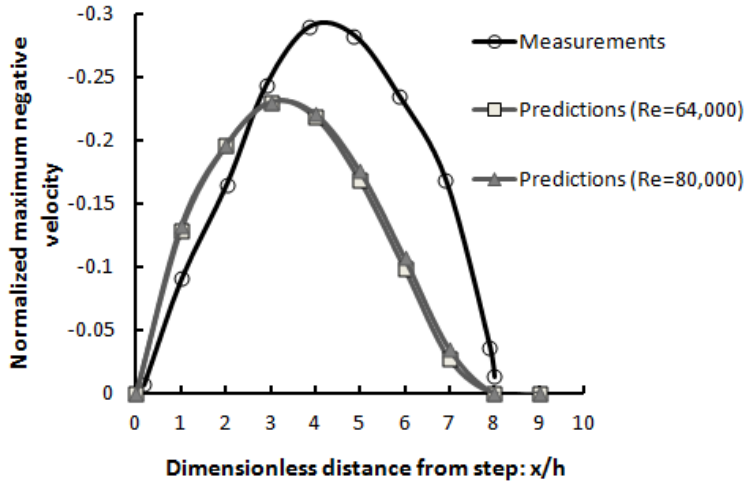

Figure 3.9 Comparison between the predictions for the maximum negative velocities and corresponding experimental data

3.4. Results and Discussion for the Flow over a Three-dimensional (3D) Backward-Facing Step

In the numerical study of the flow over 3D backward-facing step, the Reynolds number at the inlet of the tunnel is changing in a range that covers laminar, transition and turbulent flow regimes Using the outcomes of simulating 2D backward-facing step flow in the previous section, RNG k-ε is employed for modeling the turbulent flow and the Non-equilibrium wall functions are used as the near-wall approach. In order to validate the model, the velocity profile, at a specified location, on the central plane of the tunnel, is predicted and compared with the corresponding experimental measurements from the research conducted by Nie and Armaly (2004). Figure 3.10 shows the configuration of the 3D backward-facing step which is studied in this section. The geometry of the step and the flow conditions are the same as those studied by Nie and Armaly (2004) experimentally. The upstream section has the height of 0.98 cm (h) and the width of 8.00 cm (W). The downstream section has 1.98 cm height (H) and 8.00 cm width

(*W*). Therefore the Expansion Ratio for this case is ~1.49. The upstream section of the tunnel has 200.00 cm long to ensure the flow at the inlet of backward-facing step is fully developed.

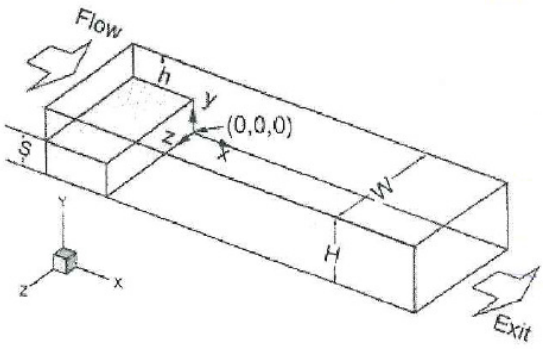

Figure 3.10 Schematic of the 3D backward-facing step (Nie and Armaly, 2004)

In order to perform the grid independency study, three different grids with different number of mesh cells are examined. All the tested grids are structured, consisting of Map-type orthogonal hexahedral mesh elements. The number of mesh cells in the grids was 25000, 294000, and 500000. (Figure 3.11 shows a view of the grid generated in the present study for the above described backward-facing step. As can be seen, in order to generate the grid, the whole volume of the tunnel divided into three cubic sub-volumes. The sub-volumes were connected through interior faces. Although the grids are distributed uniformly in span-wise direction the grids in x and y directions are denser in the flow recirculation region.

The results of grid independency study and model validation are shown in the same figure (see Fig. 3.12), where predictions from the grids with different number of mesh cells are compared with the corresponding experimental measurements at a specific location defined by x/S=-1 and z/W=0.5. The comparisons made for three different Reynolds numbers that covers laminar, transient, and turbulent flow regimes.

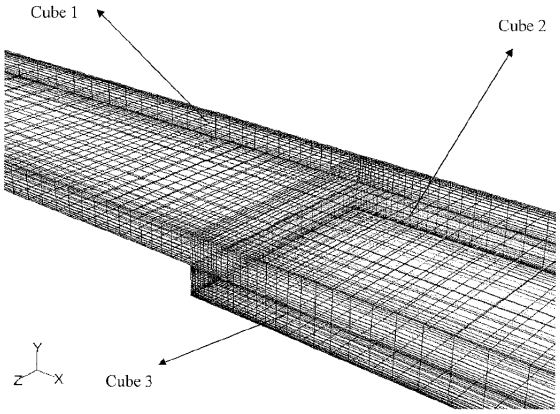

Figure 3.11 3D view of the grid generated in this study for Nie and Armaly (2004) backward-facing step

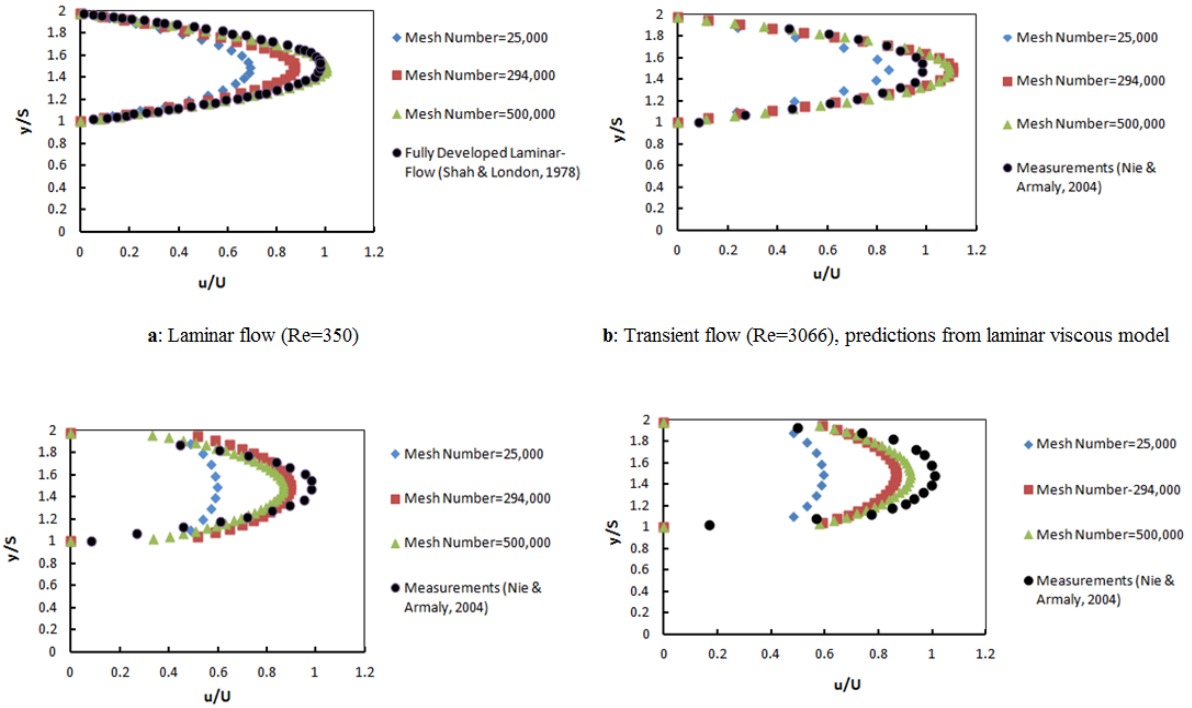

a: Laminar flow (Re=350)

b: Transient flow (Re=3066), predictions from laminar viscous model

c: Transient flow (Re=3066), predictions from RNG k-ε Turbulence Model

d: Turbulent flow (Re=7665), predictions from RNG k-ε Turbulence Model

Figure 3.12 Graphical presentation of grid independency study and model validation for 3D backward-facing step flow.

Results presented in Fig. 3.11 indicate the model is grid independent for all the flow regimes. For the laminar flow (see Fig. 3.11a), there is a very good agreement between predictions and measurements when the finest grid is used. For the transition flow, both laminar and k-ε turbulence models are used. Figure 3.10 b & c indicate that for transient flow, while the laminar viscous model over-predicts (~10%, for the finest grid) the flow velocity data in the core region, the RNG k-ε model under-predicts the flow velocity data in the same region (~10%, for the finest grid). For fully turbulent flow (see Fig. 3.11d), the comparisons between predictions and measurements indicate that the computational results from the finest grid has the best agreement with measurement; however, the largest deviations observed for the core region of the tunnel flow where, comparing to measurements, the k-ε turbulence model estimates lower values for the velocity peak values (~10% lower).

3.5. Summary

The main purpose of this chapter was to establish proficiency in using the commercial CFD code which is used in the simulations presented in this dissertation. For this reason, and to get familiar with different features of the CFD code, the flow over 2D and 3D backward-facing steps was simulated and the simulations were validated through the comparison of the computational predictions and corresponding experimental measurements for the flow velocity data at specified locations. In studying the flow over the 2D backward-facing step, the Reynolds number at the inlet changed in a range in such a way that the flow remains turbulent. The RANS method was used to solve the governing Navier-Stokes equations and the k-ε model was applied to calculate the turbulent stresses. As the first step in any CFD simulation, the model was examined for grid independency. Three structured grids with different number of orthogonal quadrilateral Map-type mesh elements were tested. Then the model was validated through the comparison of predicted velocity data at several locations behind the step with the corresponding measurements reported by Tu et al. (2008). Through the validation of the 2D computational model, an attempt was made to find an optimum combination of k-ε model and near-wall approach to get the most accurate results. Three types of k-ε models (Standard, RNG, and Realizable) accompanied with three different near-wall approaches (Standard wall functions, Non-equilibrium wall functions, and Enhanced wall treatment) were tested for this purpose.

Although it was seen that the changes in the predictions due to applying different combinations of k-ε models and near-wall approaches were almost negligible, the results from the combination of RNG k- ε model and Non-equilibrium wall functions were slightly more accurate. Through the investigation about the effect of turbulence intensity and Reynolds number at the inlet on the flow structure in the duct, it was realized that for the turbulent flow over backward-facing step, the downstream flow behavior is independent of the flow condition at the inlet. It confirmed that the behavior of turbulent flow over the backward-facing step is only a function of the Expansion Ratio, which is the ratio of the inlet height to the outlet height of the duct. In studying the flow over 3D backward-facing step, the simulations were validated through the comparison of computational predictions with the experimental measurements performed by Nie and Armaly (2004). All the flow regimes were considered in the simulations. Through the validation of the CFD model, it was found that for the laminar flow, the viscous laminar model is able to predict the flow velocity in complete agreement with measurements and theoretical solutions. For the transient flow, while the laminar viscous model over-predicts the flow velocity in the core region of the tunnel, the turbulence model under-predicts the flow velocity in the same region. For the fully turbulent flow regime, it was seen that, similar to what was experienced in modeling the transient flow, the turbulence model under-predicts the flow velocity in the core region. In modeling the turbulent flow for both transient and turbulent flow regimes, RNG k-ε turbulence model with Non-equilibrium wall functions were used.

Chapter 4 - Study of Turbulent Airflow in Generic Aircraft Cabin

4.1. Introduction

The present chapter is designed to simulate the turbulent airflow in a generic aircraft half-cabin mockup model. Since the geometry of the cabin as well as the flow conditions at the boundaries are symmetric with respect to the aircraft cabin's longitudinal plane of symmetry, it can be expected that the mean flow characteristics show a symmetric behavior with respect to that plane. Due to the stochastic nature of turbulent flow fluctuations, the instantaneous flow characteristics are not symmetric. However, in this study, the mean quantities are of the interest and therefore studying the flow in one half of the cabin is sufficient and decreases the costs associated with building the whole cabin and performing the required experiments in a larger space. Gambit is used as the grid generation tool and FLUENT is used as the CFD solver for the simulations presented herein. In order to investigate the airflow characteristics two types of turbulence models are employed: LES and RANS. The LES model provides the temporal velocity variations while the RANS model is used to simulate the airflow for steady conditions. The predictions from both LES and RANS models are compared with the PIV measured data for five monitoring surfaces on the cabin center plane parallel to the bulk airflow direction (Lebbin, 2006). Throughout these comparisons the capability of the two types of aforementioned turbulence models in predicting the airflow velocities are discussed and compared. The effects of applying different k-ε models on the accuracy of steady RANS simulations are also studied. Then the effect of reducing the inlet nozzle height to one-half of its original size, while maintaining the Reynolds number for inlet airflow at the same value, on turbulence level and airflow velocities is examined. In this part, the predictions are validated by comparing them with corresponding PIV measurements.

4.2. The Generic Cabin Mockup Model

The generic cabin mockup model (Figs.4.1 and 4.2) has the key features of one-half of a twin-aisle Boeing 767 aircraft cabin. The upper left and upper right corners represent the overhead bins. The slit right below the upper left corner represents the nozzle port through which

the fresh, conditioned air comes into the cabin and the slit in the lower right corner represents the outlet port for exiting exhaust air.

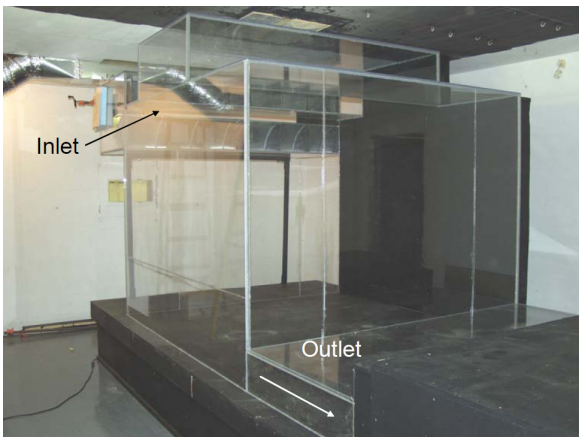

Figure 4.1 Full scale generic aircraft half-cabin mockup model (Lebbin, 2006).

The PIV measurements were taken at the five measurement locations (Figs. 4.2 and 4.3) when the airflow inside the cabin was fully developed (Lebbin, 2006). Although the velocity measurements were made for two different inlet nozzle heights: 53 mm (full-height) and 26.5 mm (half-height), the average airflow rate coming into the cabin was maintained at the constant value of 4.2 m^3/min in all the airflow velocities measurements.

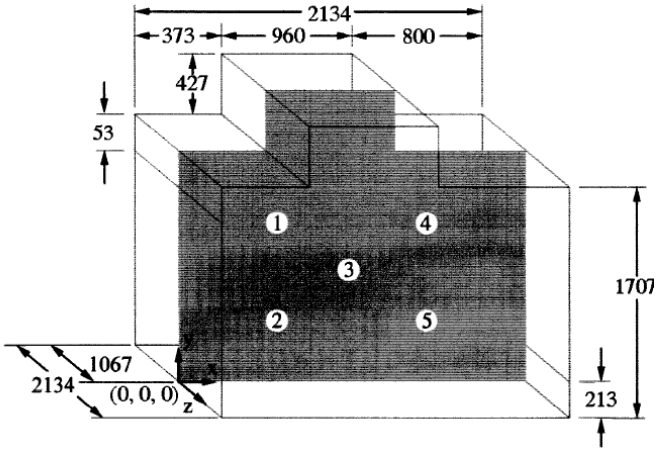

Figure 4.2 Dimensions of the generic cabin model and the location of PIV monitoring windows on the cabin central plane. All the units are in mm (Lebbin, 2006).

.

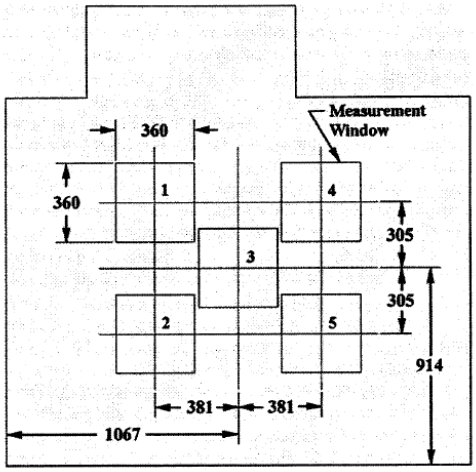

Figure 4.3 The exact locations of five PIV measurement windows on the central plane. All units are in mm (Lin et al., 2006).

4.3. Governing Equations and Numerical Solution Method

In this study the following assumptions are employed for the numerical simulation of three-dimensional turbulent airflow in the cabin. The following assumptions are consistent with the existing conditions in the experiments:

1. In the LES model, the flow is considered unsteady while the RANS model employs steady flow conditions.
2. In all the cases the flow is assumed to be incompressible.
3. The heat transfer in the cabin is neglected. The inlet airflow is at the temperature of 27 ^{o}C.
4. The effects of buoyancy are taken into consideration.

The governing equations for the instantaneous turbulent flow field and species transport in the cabin are:

Continuity:

$$\frac{\partial u_i}{\partial x_i} = 0 \tag{4.1}$$

Momentum:

$$\frac{\partial u_i}{\partial t} + u_j \frac{\partial u_i}{\partial x_j} = -\frac{1}{\rho}\frac{\partial p}{\partial x_i} + \frac{1}{\rho}\frac{\partial}{\partial x_j}(\mu \frac{\partial u_i}{\partial x_j}) + g_i \tag{4.2}$$

where, u_i (m/s) denotes the velocity components, x_i (m) represents the position along the coordinate directions, t (s) is the time, and μ (Pa.s) and ρ (kg/m^3) are the dynamic viscosity and density of air. Also p (Pa) is the static pressure, and g_i (m/s^2) is the gravity acceleration. To solve the governing Navier-Stokes equations for the turbulent flow inside the cabin, two turbulence models are applied: LES and RANS.

4.3.1 LES Turbulence Model

In solving the above governing Navier-Stokes equations using LES, just the large scale motions of the flow are solved by filtering out the small and universal eddies. In other words, in this approach the velocity field is separated into resolved and sub-grid domains. The resolved domain of the velocity field represents the large eddies which are dependent on the geometry while the sub-grid domain represents the small scale eddies which are not dependent on the geometry of flow and have a universal behavior such that their effect on the resolved domain is included through the sub-grid scale (SGS) model. Therefore, in this method the instantaneous velocity and pressure are considered as the summation of resolvable scale velocity and pressure ($\tilde{u}_i$, $\tilde{p}$) and sub-grid scale velocity and pressure (u_i'', p''):

$$\begin{aligned} u_i &= \tilde{u}_i + u_i'' \\ p &= \tilde{p} + p'' \end{aligned} \tag{4.3}$$

It should be mentioned that in the most commercial CFD packages, the grid size is used to filter out sub-grid scale eddies. Substituting the decomposition forms of u_i and p from Eq.

(4.3) in the instantaneous governing Navier-Stokes equations, and then filtering the resulting equations, gives the following filtered equations for the flow field:

$$\frac{\partial \tilde{u}_i}{\partial x_i} = 0 \tag{4.4}$$

$$\frac{\partial \tilde{u}_i}{\partial t} + \tilde{u}_j \frac{\partial \tilde{u}_i}{\partial x_j} = -\frac{1}{\rho}\frac{\partial \tilde{p}}{\partial x_i} + \frac{1}{\rho}\frac{\partial}{\partial x_j}\left([\mu + \mu_t]\frac{\partial \tilde{u}_i}{\partial x_j} \right) + g_i \tag{4.5}$$

where μ_t in Eq. (4.5) is the sub-grid scale turbulent viscosity. In this study, the Smagorinsky-Lilly SGS model (Smagorinsky, 1963 and Lilly, 1966) is used to calculate μ_t:

$$\mu_t = \frac{\rho}{\sqrt{2}}(C_s\Delta)^2 \left| \frac{\partial \tilde{u}_i}{\partial x_j} + \frac{\partial \tilde{u}_j}{\partial x_i} \right| \tag{4.6}$$

where Δ is the filter width and can be calculated using the following equation:

$$\Delta = (\text{Volume of the grid element})^{1/3} \tag{4.7}$$

and C_s is the Smagorinsky constant which varies between 0.1 and 0.2. In this study the selected value for C_s is 0.14. As it was mentioned earlier, the heat transfer is assumed to be negligible in the cabin therefore the energy or heat equation is not taken into consideration. Needless to say, the governing equations are second order with respect to space and first order with respect to time, so that in solving the governing equations we need to have two boundary conditions in each direction and one initial condition. The time step size is 0.05 sec and the second order implicit method is used as time marching scheme. The second order central differencing is used to discretize the spatial derivatives. The convergence criteria for the continuity and the momentum equations are 10^{-4} and 10^{-5}, respectively. The Werner-Wengle wall function

(Werner and Wengle, 1991 & FLUENT 6.3 Manual, 2011) is used for the near-wall solution. The reason for using the Werner-Wengle wall function, as explained elaborately by Werner and Wengle (1991), is its simplicity as well as its accuracy in comparison with the other near wall functions. While other functions are multi-domain functions based on non-dimensionalized velocity and distance from the wall, the Werner-Wengle wall function defines unique relationships between shear stress and velocity that enhances accuracy and reduces the computational time.

4.3.2 RANS Turbulence Model

When the RANS model is used to solve the Navier-Stokes equations governing the turbulent flow, the instantaneous flow variables are decomposed into the mean value (time-averaged) and fluctuating components:

$$\begin{aligned} u_i &= \overline{u}_i + u_i' \\ p &= \overline{p} + p' \end{aligned} \tag{4.8}$$

where $\overline{u}_i$, $\overline{p}$ and u_i', p' denote the mean and fluctuating components for the flow velocity and pressure, respectively. Substituting the decomposed form of the flow variables in the instantaneous governing equations (Eq. (4.1) and Eq. (4.2)) and taking a time-average of those equations gives the following time-averaged governing equations for the steady incompressible flow:

$$\frac{\partial \overline{u}_i}{\partial x_i} = 0 \tag{4.9}$$

$$\frac{\partial \overline{u}_j \overline{u}_i}{\partial x_i} = \frac{\partial}{\partial x_i}\left(-\overline{p}\delta_{ij} + (\mu + \mu_t)\left(\frac{\partial \overline{u}_i}{\partial x_j} + \frac{\partial \overline{u}_j}{\partial x_i}\right)\right) + \rho g_i \tag{4.10}$$

where μ_t is the turbulent or eddy viscosity and using the Boussinesq hypothesis (Wilcox, 1998), is defined as:

$$\mu_t = \frac{-\rho\overline{u_i' u_j'}}{\frac{\partial \overline{u}_i}{\partial x_j} + \frac{\partial \overline{u}_j}{\partial x_i}} \tag{4.11}$$

In this study, in order to calculate the above defined turbulent viscosity, the k-ε model which is a typical two equation turbulence model is employed. Using this model, the turbulent viscosity is calculated through the following equation (Tu et al., 2008):

$$\mu_t = \frac{C_\mu \rho k^2}{\varepsilon} \tag{4.12}$$

where k (m^2/s^2) is the turbulent kinetic energy and ε (m^2/s^3) is the turbulent dissipation rate. Therefore, in addition to the time-averaged governing equations, two additional differential transport equations should to be solved (along with required boundary conditions) at the same time to calculate k and ε. As explained elaborately in chapter 3, in Eq. (4.12), while C_μ is an empirical constant for standard k-ε ($C_\mu = 0.09$) and RNG k-ε ($C_\mu = 0.0845$) models (Tu et al., 2008 and Yakhot, 1992), C_μ in realizable k-ε model is not a constant value and is calculated from Eq. (3.9).

In the RANS models, three types of k-ε model are employed: Standard, Renormalization Group (RNG) and Realizable. The non-equilibrium wall function is used as the near wall treatment. The second order upwind scheme is used to discretize spatial derivatives in the governing equations. The same convergence criteria as in the LES model are used for the continuity and the momentum equations in the steady RANS simulations. For the k and ε equations, the convergence criteria are both 10^{-5}.

4.4. Results and Discussion

4.4.1. Uncertainty Study (Check for the Grid-Independent Solutions)

Uncertainty studies were done for the cabin in both cases of full-height and half-height air inlet nozzles. However, in this section the results of the uncertainty study for the cabin with full-height nozzle is presented. LES and RANS were used for solving the turbulent flow governing equations. In order to solve the governing equations, the boundary conditions (for both LES and RANS) and initial conditions (for LES only) need to be specified. The boundary conditions are: velocity-inlet for the flow at the inlet of the cabin mockup, no slip stationary wall for the cabin mockup walls and outflow for the flow at the outlet of the cabin mockup. In setting the boundary conditions at the inlet, for both LES and RANS (for all k-ε models), the flow velocity as well as the turbulent kinetic energy and dissipation rate are specified at the inlet. Knowing the air kinematic viscosity and airflow rate at the inlet, the average airflow velocity at the inlet can be calculated. In the simulations performed in this study, it is assumed that the velocity at the inlet is uniform and equal to the calculated average velocity. In order to calculate the turbulence intensity at the inlet, the airflow Reynolds number based on the inlet hydraulic diameter is determined. Following the calculation of the Reynolds number, the turbulent intensity, turbulent kinetic energy, and turbulent dissipation rate at the inlet can be calculated through the equations listed below (FLUENT 6.3 Manual, 2011):

$$I = 0.16(\mathrm{Re}_{D_H})^{-1/8} \tag{4.16}$$

$$k = \frac{3}{2}(UI)^2 \tag{4.17}$$

$$\varepsilon = C_\mu^{3/4}\frac{k^{3/2}}{\ell} \tag{4.18}$$

where I is the turbulence intensity, Re_{D_H} is the Reynolds number based on the hydraulic diameter, D_H (m) is the hydraulic diameter, k (m^2/s^2) is the turbulent kinetic energy, ε (m^2/s^3)

is the turbulent dissipation rate, U(m/s) is the average velocity at the inlet, C_μ was explained in Eq. (4.12), and ℓ is the turbulence length scale ($\ell = 0.07 D_H$). The calculated turbulent kinetic energy and dissipation rate from the above equations are used in setting the boundary conditions at the inlet for LES as well as all the *k*-ε models used in RANS. Since the velocity at the cabin inlet nozzle has its maximum magnitude throughout the flow field in the cabin, from Eqs. (4.16)-(4.18) it can be seen that, at the inlet, the turbulent kinetic energy and dissipation rate can possibly have their maximum magnitudes through in the cabin. We studied the contours of turbulent kinetic energy and dissipation rate calculated through the simulations and confirmed the above postulation. Following the calculation of turbulent kinetic energy and dissipation rate, the Kolmogorov length (η) and time (τ) scales were determined as 9.28×10^{-4} m and 0.0589 s, respectively, through the following equations (FLUENT 6.3 Manual, 2011 & Landahl, 1992):

$$\eta = \left(\frac{\nu^3}{\varepsilon} \right)^{1/4} \tag{4.19}$$

$$\tau = \left(\frac{\nu}{\varepsilon} \right)^{1/2} \tag{4.20}$$

where η (m) is the Kolmogorov length scale, τ (sec) is the Kolmogorov time scale and ν (m^2 /s) is the kinematic viscosity. As discussed earlier, the turbulent dissipation rate has its maximum magnitude at the inlet, therefore through Eqs. (4.19) and (4.20) it can be realized that the Kolmogorov length and time scales experience their minimum values at the inlet of the cabin, i.e. for the entire flow field in the cabin $\eta \geq 9.28\times10^{-4} m$ and $\tau \geq 0.0589 s$. The numbers of mesh cells in the tested four different grids in this study are: 306900, 576000, 1024000 and 2340000. In all cases the meshes are structured, Map type, and made of orthogonal hexahedral elements. Through the comparison of mesh spacing range with the Kolmogorov length scale, the grid spacing corresponding to the finest mesh (2,340,000 mesh elements) varies in the range of 7η-34η. Since the predicted data from LES have temporal behavior, the time mean values as well as

the root-mean-squared (RMS) data are used in the calculation of variations in the velocity predictions as the grid size changes.

Figure 4.4 shows a comparison between the LES predictions for the x-component of airflow velocity using different grid sizes and the corresponding PIV measurements corresponding to the location 5 of the PIV measuring windows. Figures 4.5 (a, b) and 4.6 show the converging behavior of the LES and RANS predicted x-component of velocity data as the number of grid is increased. The deviation for every grid size was calculated based on the relative difference between the predictions corresponding to that grid size and the finest grid (2,340,000). As typically shown in Fig. 4.4, the LES predictions from the finest mesh have the closest RMS and mean values to those of PIV measurements. Also, as shown in Fig. 4.5, the LES predictions demonstrate better converging behavior in locations 1 and 4 in the upper region of the cabin comparing to the middle and lower regions. Figure 4.6 indicates that in the steady RANS simulations, the location 3 at the middle of the cabin is associated with the highest grid uncertainties comparing to the other locations. It means that the flow in the middle region of the cabin has more complex structure and in order to predict the flow behavior more accurately, the regional mesh refinement is required.

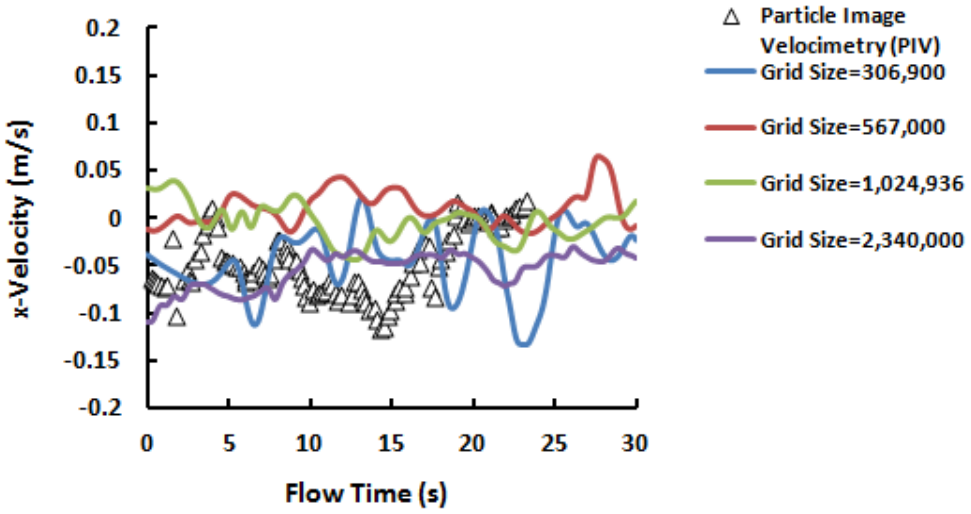

Figure 4.4 The results of uncertainty study for the cabin with full height nozzle when x component of velocity data are predicted for the location 5 of the PIV measuring windows. The PIV data were produced by Lebbin (2006).

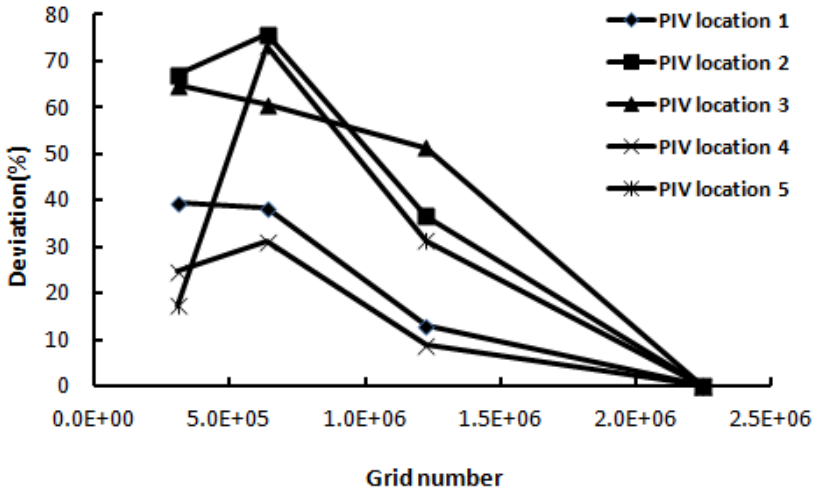

(a) Deviations based on mean values (time averaged values)

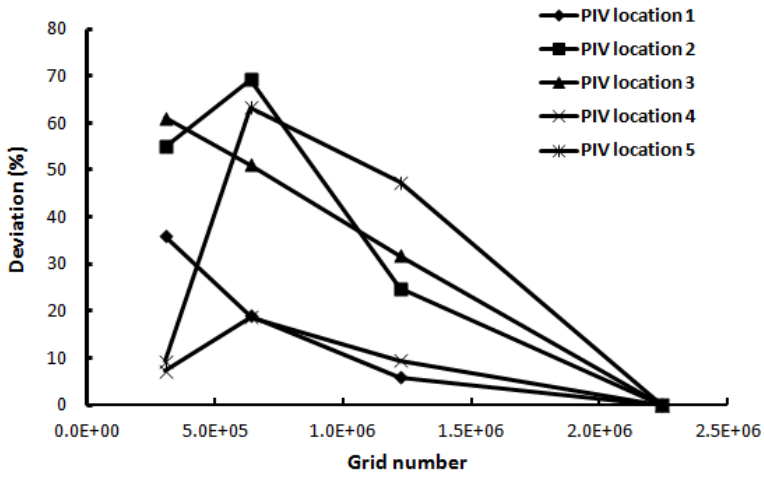

(b) Deviations based on RMS values

Figure 4.5 The converging behavior of x-component of velocity deviations with respect to the corresponding prediction from the finest grid for all the PIV measuring windows.

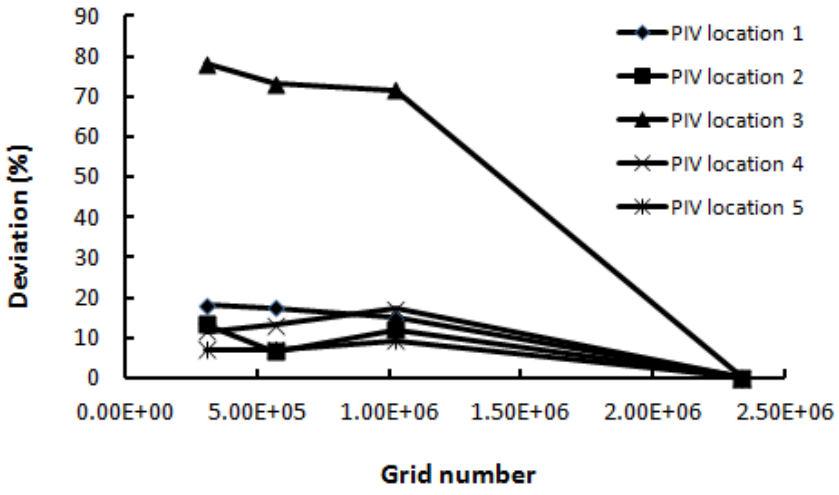

Figure 4.6 The converging behavior of x-component of velocity deviations with respect to the corresponding prediction from the finest grid from steady RANS solution for all the PIV measuring windows.

4.4.2 Study of Airflow in Cabin: Full-Height and Half-Height Nozzle Cases

a. Airflow Simulation in Cabin with Full-Height Nozzle

This section starts with the LES simulation of turbulent airflow in the generic cabin with full-height inlet nozzle. The CFD grid used in this part of the study consists of 2,340,000 hexahedral cells with the grid spacing varied in the range of 7η- 34η (through the comparison of edge grid spacing with the Kolmogorov length scale). Also the time step size of 0.05 s is used in all LES simulations presented in this paper. In order to validate the simulation, the LES predictions are compared with the PIV measurement data as well as the CFD predictions by Lin et al. (2006) at each of the five PIV measuring locations. The time interval between the each of two succeeding PIV sampling data was 0.2 s (Lin, 2006 & Lebbin, 2006). A comparison between the corresponding LES parameters used in this study and those used by Lin et al. (2006) is shown in Table 4.1. As seen in Fig. 4.7, there is a good agreement among the simulation results of this study, PIV measurements, and those of Lin et al. (2006) CFD simulations for location 1 of the PIV measuring window. The predictions and measurements for other PIV

measuring window locations are similarly compared well. Especially, the comparisons indicate that the simulations predict the ranges of variations of instantaneous velocities fairly close to the variation ranges of the measurements. Since the PIV measuring window locations are on the central plane (z=0) the magnitude of z-components of velocity data are very small and close to zero and that's the reason they are not presented here.

Table 4.1 Comparison between the important parameters in the simulations

LES Code	Lin et al. [6] (Using FLUENT)	Lin et al.[6] (Using Fire Dynamic Simulator, FDS)	Present Study (FLUENT)
Number of mesh elements	2,533,744	2,580,480	2,340,000
Mesh elements type	All hexahedral cells, Unstructured mesh	All hexahedral cells, Cartesian mesh	All hexahedral cells, Structured mesh
Grid Spacing (η)	5-20	5-20	7-34
Time step (sec)	0.05	0.01 ± 0.002	0.05
Sub-Grid Scale (SGS) model	Smagorinsky Lilly	Smagorinsky Lilly	Smagorinsky Lilly
Smagorinsky constant, Cs	0.14	0.14	0.14
Near wall treatment	Law of the wall approach	Standard wall function	Werner-Wengle
Numerical Scheme	Spatial: Second order central differencing Temporal: Implicit second order predictor corrector scheme	Spatial: Second order central differencing Temporal: Implicit second order predictor corrector scheme	Spatial: Second order central differencing Temporal: Implicit second order predictor corrector scheme

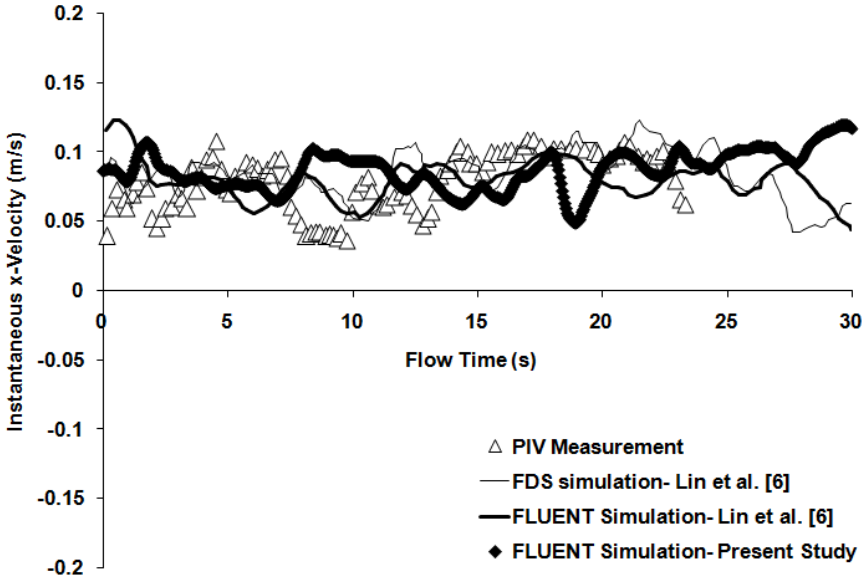

(a) x-component of velocity data at PIV location1

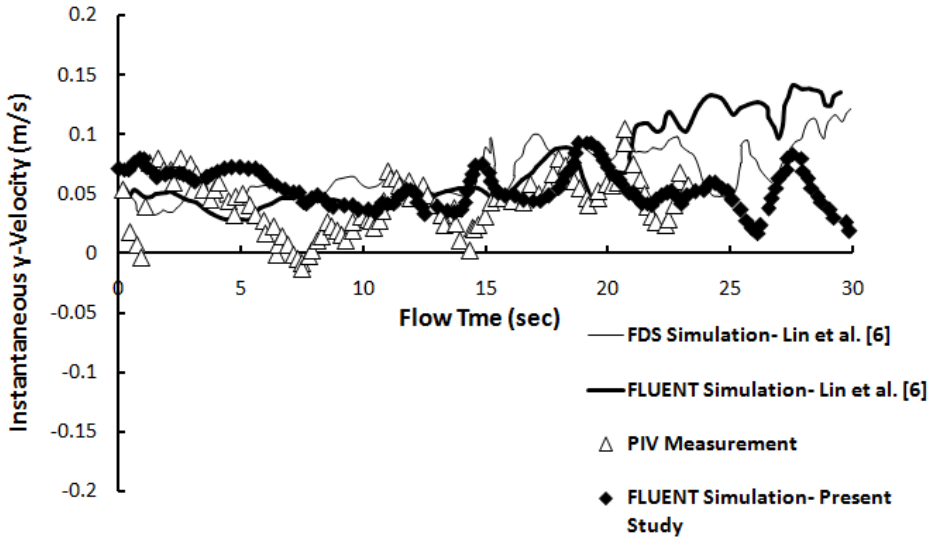

(b) y-component of velocity data at PIV location1

Figure 4.7 Comparison of the predicted values (this study), PIV measurements (Lebbin, 2006) and predictions produced by Lin et al. (2006) for the airflow velocity data corresponding to the location 1 of the cabin with full height nozzle.

In the above comparisons, the center point of each PIV measuring window was selected to monitor the predicted velocity data. However, in the experiments the PIV velocity data were averaged over the area of each measuring window. In order to study the effect of changing the monitoring surfaces from the center points to the whole area of the PIV measuring windows on the predicted velocity data, the simulation results were reprocessed based on the area weighted average values of velocities over the measuring windows areas. Figure 4.8 shows the comparisons between the predictions from two differently processed velocity values and the corresponding experimental data for location 2 of the PIV window. In Fig. 4.8, it is observed that although the mean temporal behaviors of the predictions are almost the same between the two different simulation data sets, the area-averaged data set shows a smoother curve, which means the area-averaged velocity experiences less fluctuations than the local velocity at the center point of the window.

Figure 4.9 shows the turbulent airflow patterns in the cabin at four different time levels predicted using LES. This sequence also shows the development of the flow field inside the cabin, such as formation of boundary layers and large eddies.

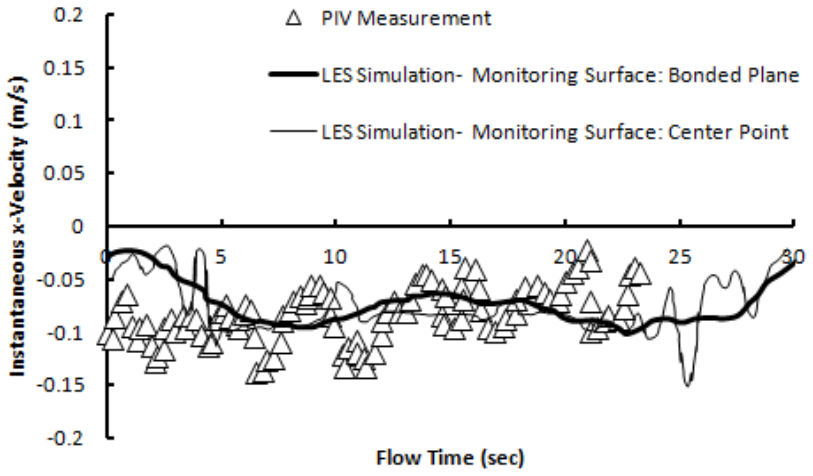

(a) x- component of velocity data at PIV location 2

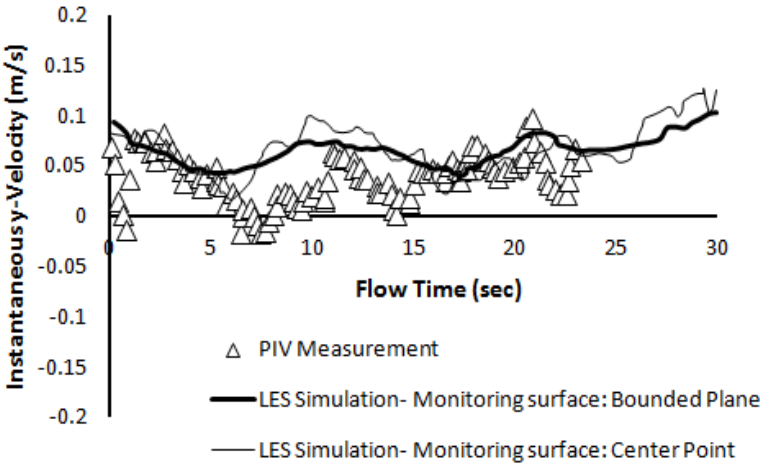

(b) y- component of velocity data at PIV location 2

Figure 4.8 Study the effect of choosing monitoring surface on the predicted velocities, corresponding to location 2 of the cabin with full-height nozzle, through comparison with PIV measurements (Lebbin, 2006)

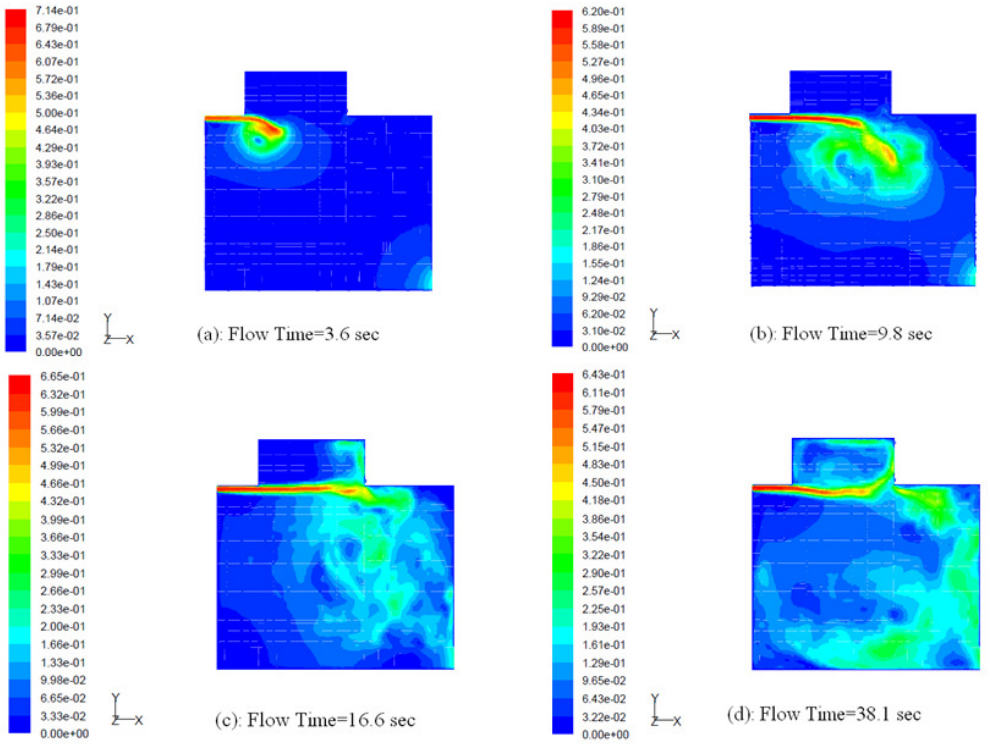

Figure 4.9 The turbulent airflow patterns (The contour representations of airflow velocity magnitudes) predicted by LES at different flow times: (a) flow time=3.6 s, (b) flow time=9.8 s, (c) flow time=16.579 s and (d) flow time=38.1 s.

Figure 4.10 represent the comparisons between the predictions for the x-component of airflow velocity data in locations 3 and 5 of the PIV measuring windows from the steady RANS simulations using three types of the k-ε turbulence models and the corresponding time-dependent PIV data. In the RANS simulations, the non-equilibrium wall function is used as the near wall treatment and also the finest mesh (with the grid number of 2,340,000) that previously used for the LES simulations is used for RANS simulations as well. Although the accuracy of RANS predictions is considerably less than LES, the computation time and cost associated with LES simulations are much more than RANS. Among the three examined RANS models: the standard k-ε (Launder and Spalding, 1972) the RNG k-ε (Yakhot and Orszag, 1986) and the realizable k-ε (Shih et al., 1995), the RNG predicted value is closer to the mean value of the experimental data. The predictions from all the

examined types of the k-ε turbulence models are greater than the mean values of PIV measurements and LES predictions. Based on the simulations performed in this study, the RNG is the most accurate model.

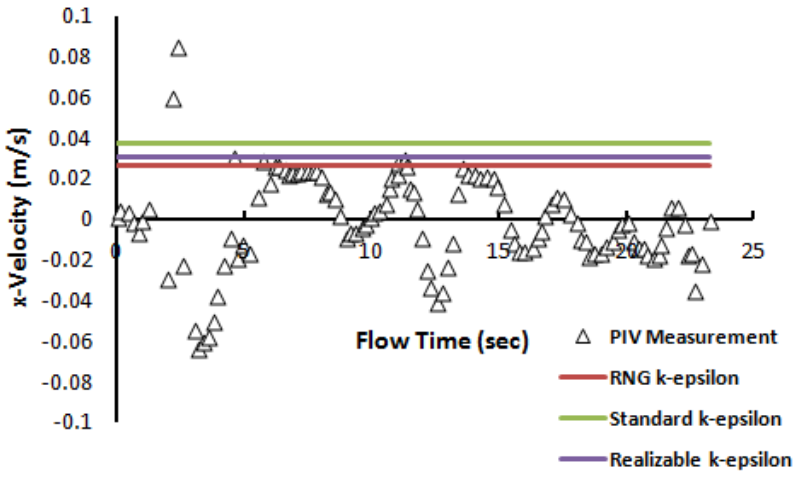

(a) Location 3

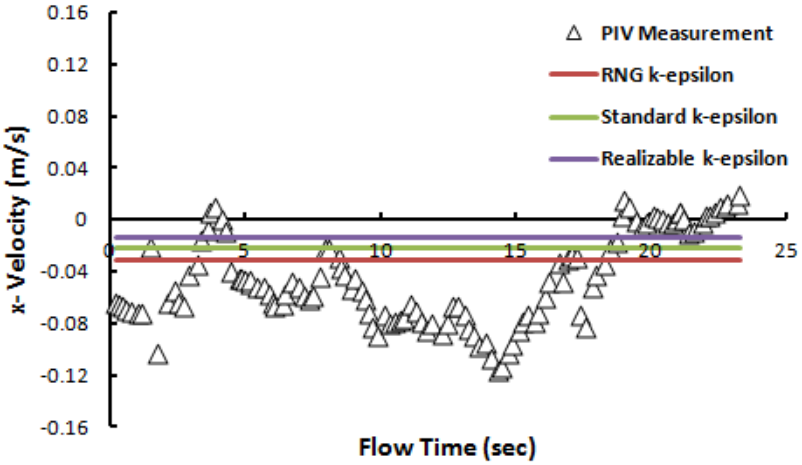

(b) Location 5

Figure 4.10 Comparison of the steady RANS predictions for the x-component of velocity data with the corresponding time dependent PIV data (Lebbin, 2006) at locations 3 and 5 of PIV measuring window.

b. Airflow Simulations in Cabin with Half-Height Nozzle

This section presents the study of flow characteristics when the cabin nozzle height is reduced to one-half of its original size. As the flow rate of the incoming air to the cabin remains the same, by halving the nozzle height, the magnitude of the airflow velocity at the inlet is doubled. So it is expected that the magnitude of each airflow velocity component in the cabin experiences an increase. Figures 4.11 and 4.12 compare the PIV measurements (Lebbin, 2006) with the LES predictions from this study for the airflow x and y velocity components in locations 1 and 3 of the PIV measuring windows (The predictions and measurements corresponding to locations 2 and 5 are also well compared similar to location 1). As explained previously, the comparisons for z-component of velocity data is not presented here. The sampling frequency in PIV measurements is 7.5 Hz. A structured grid consisting of 2,225,000 hexahedral mesh cells with the grid spacing in the range of 4η-43η is used in LES simulations for this part of study. Similar to the simulations done for the cabin with full-height nozzle, the time-step size of 0.05 sec is used in LES simulations for the cabin with half-height nozzle as well. The comparisons indicate that, except for the location 3 of the PIV measuring windows, LES predicts the range of flow velocity variations fairly well. In location 3, however, due to the complexities associated with the flow in this region, the agreement between the LES predictions and PIV measurements is not as good for all flow times. For example, in Fig. 4.12, for the times between ~12 s to ~30 s and also greater than ~35 s there is not an acceptable agreement between LES and PIV data. It seems in order to get better predictions for such regions in which the airflow patterns are more complicated, local grid refinements are needed.

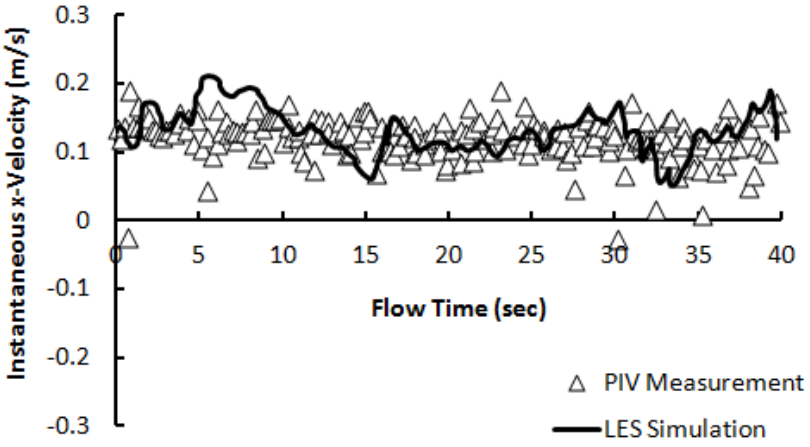

(a) x-component of velocity data

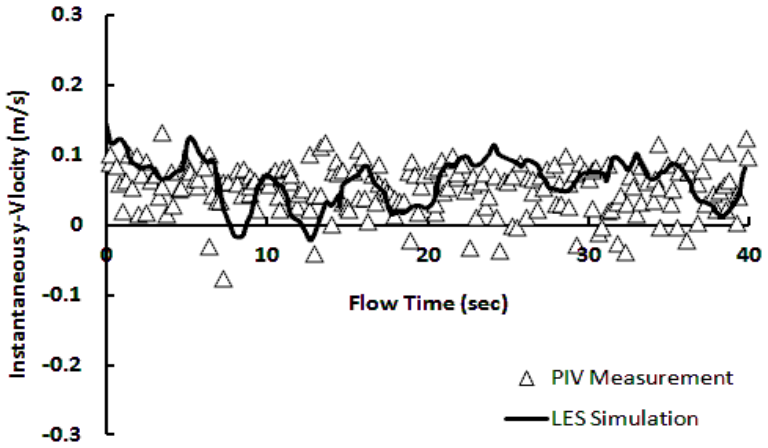

(b) y-component of velocity data

Figure 4.11 Comparison of the LES predictions and PIV measurements (Lebbin, 2006) for the x-component of velocity data corresponding to the location 1 of the cabin with half-height nozzle.

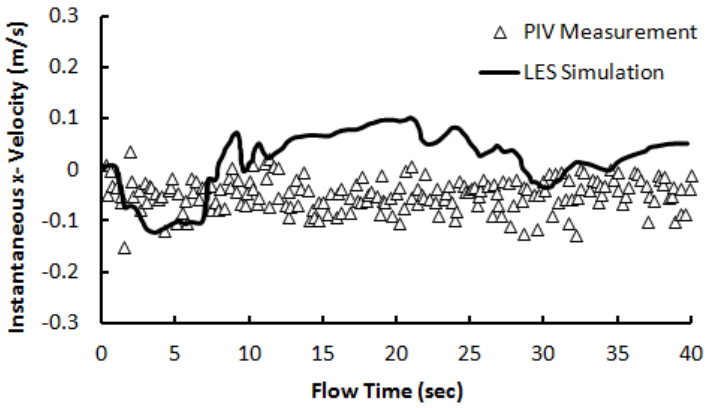

(a) x-component of velocity data

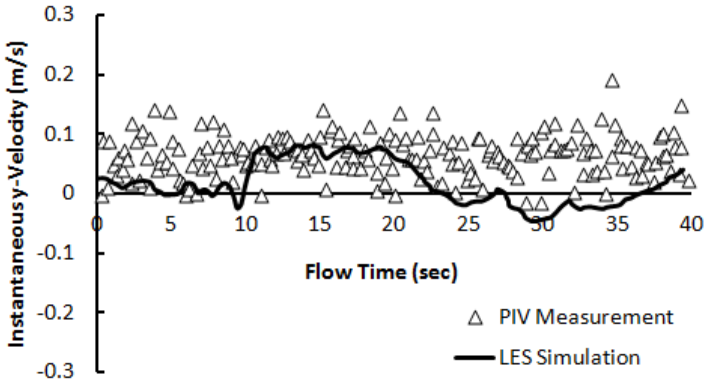

(b) y-component of velocity data

Figure 4.12 Comparison of the LES predictions and PIV measurements (Lebbin, 2006) for velocity data corresponding to the location 3 of the cabin with half-height nozzle.

Comparisons of the velocity data between the full and half-height nozzle cases indicate that by halving the nozzle height, the mean value of the predicted as well as measured flow velocity data corresponding to locations 1 and 2 of the PIV measuring windows are approximately doubled (compare Fig. 4.7 with Fig. 4.11). However for the locations 4 and 5, the expected increase in the velocity is slight and not as much as that experienced in the locations 1 and 2 (Fig. 4.13). In addition, comparison of the PIV

measurements for the velocity data corresponding to location 3 (as shown in Fig. 4.14) implies that by halving the nozzle height and consequently doubling the inlet airflow velocity, the flow in location 3, which used to be almost stationary in the full-height nozzle case, takes the tendency of moving to the upper left corner of the cabin.

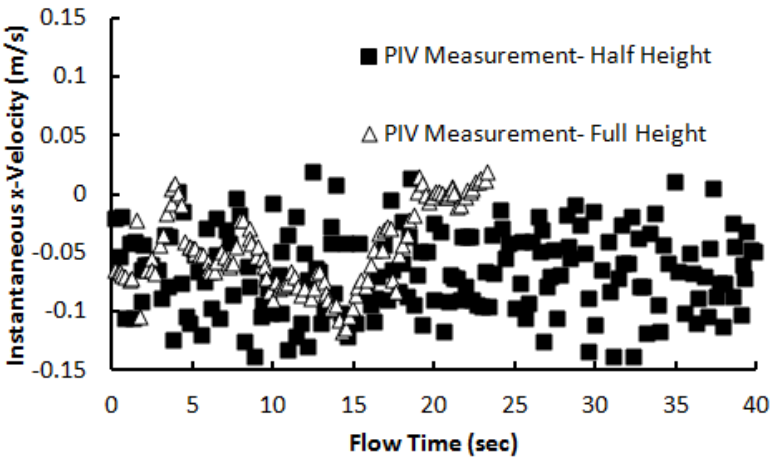

(a): x-component of velocity data

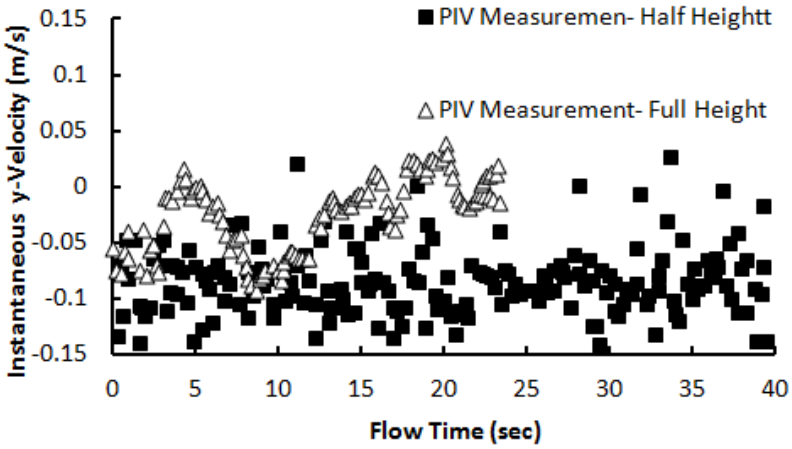

(b): y-component of velocity data

Figure 4.13 Study the effect of decreasing the cabin nozzle height through a comparison between the PIV measured velocity data (Lebbin, 2006) corresponding to the location 5 of the PIV measuring windows for two cases of full and half-height nozzle.

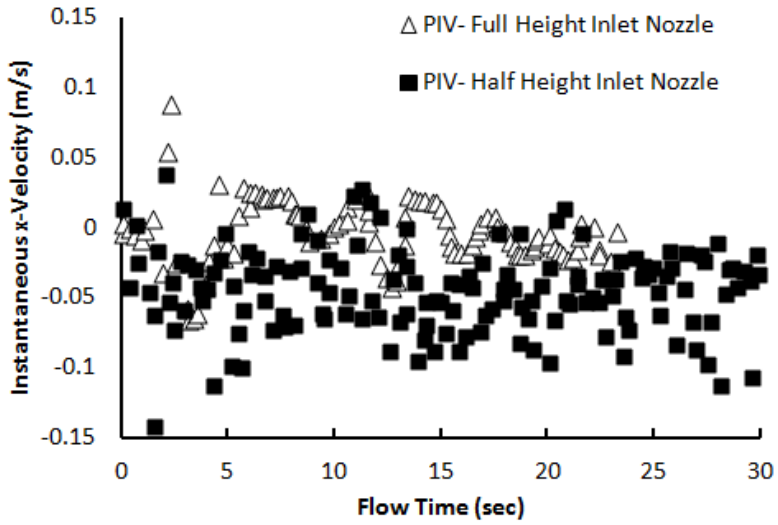

(a): x-component of velocity data

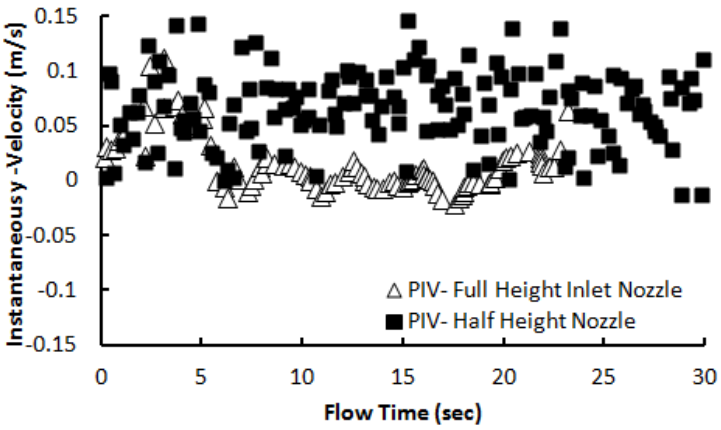

(b): y-component of velocity data

Figure 4.14 Study the effect of decreasing the cabin nozzle height through a comparison between the PIV measured velocity data (Lebbin, 2006) corresponding to the location 3 of the PIV measuring windows for two cases of full and half-height nozzle.

4.5. Summary

In this chapter, the capability of a CFD commercial software in simulating turbulent airflow in a generic half-cabin was evaluated. Two different types of turbulence models were used to find the turbulent viscosity in the governing equations: (1) unsteady Large Eddy Simulation (LES), and (2) steady Reynolds Averaged Navier Stokes (RANS) models. While the LES model predicts the temporal variations of airflow velocity, the steady RANS method predicts a steady value for the velocity. Through the comparisons, it was concluded that the LES at least is able to predict the range of velocity variations fairly well. Examining the three different k-ε (standard, RNG and Realizable) models indicated that, as expected, the errors associated with the RANS method are much more than that of LES. It was also recognized that among the above mentioned k-ε models, the RNG k-ε leads to the most accurate predictions.

In order to monitor the velocity data in PIV measuring windows, two different approaches were employed. The first approach used velocity data at the center points of the PIV windows and the second approach used the area-averaged velocity values of the PIV windows. The comparisons indicated that the area-averaged velocity value decreased the fluctuations in the velocity but the general behavior of predicted velocities did not change. Comparisons with the experimental data showed that the center point values had a better agreement with experimental measurements.

The effect of halving the cabin inlet nozzle height with the same airflow rate was studied. It was observed that, although LES method gave a good estimation of the velocity data in locations 1, 2, 4 and 5 of measuring windows, the agreement between the simulations and measurements was not as good in location 3 at the middle of the cabin. A local refinement in grid size is recommended to get more accurate results in this region in the future study. Comparing to the cabin with the full-height nozzle, it was seen that by halving the nozzle height and consequently doubling the inlet velocity, the magnitude of flow velocities in locations 1 and 4 increased dramatically (by 100%). However, in locations 2 and 5, the increase in the velocity value was slight and not as much. It was also realized that the airflow located in location 3 that used to be almost stationary in the full-height nozzle case had the tendency of moving to the upper left corner of the cabin model.

Chapter 5 - Study of Tracer Gas Diffusion in the Generic Cabin Mockup with Half-height Inlet Air Nozzle

5.1. Introduction

One of the methods of understanding mechanisms associated with airflow recirculation and contaminant spread in indoor environments such as aircraft cabins is studying diffusion of a tracer gas injected into this kind of enclosures. In this chapter, the turbulent diffusion of a tracer gas, which is carbon dioxide, injected from the circumferential surface of a horizontal tube installed inside the generic cabin mockup, is simulated by solving the species transport equation along with other governing Navier-Stokes equations. The Large Eddy Simulation (LES) method is used in solving the time-dependent equations governing the turbulent flow of air-CO_2 mixture in the cabin. The supply air is injected into the cabin through the half-height inlet air nozzle. The LES quasi-steady solution for the airflow field in the cabin with half-height nozzle, which was presented in chapter 4, is used as the initial condition for running the simulations. The computational model is validated through the comparison of time-averaged predicted concentration of the tracer gas in specified monitoring locations in the cabin, with the corresponding experimental measurements.

5.2. Experiments

In the tracer gas measurements (Lebbin, 2006), carbon dioxide was used as the tracer gas. A 12.7 mm schedule- 40 porous polythene tube was installed horizontally inside the cabin perpendicular to the xy plane. One end of the tube was connected to a CO_2 tank through the back wall (corresponding to z=-1.067m) of the cabin while the other end was capped and positioned 134 mm from the opposite wall. The tube passed through the central point of the location 2 of the PIV measuring windows as shown in Fig. 5.1. A pressurized CO_2 tank (p~5500 kPa) containing CO_2 with the purity of more than 99.6% was used to supply the carbon dioxide required for the experiments. The volumetric flow-rate of CO_2 exiting from the tank is 7.6 lpm. By passing through an expansion valve, the pressure of carbon dioxide was regulated down from ~5500 kPa to an atmospheric pressure. Since the density of CO_2 at the atmospheric pressure is

higher than the air density at the same pressure and temperature, in order to maintain the neutral buoyancy condition, before flowing into the injection tube, CO_2 was blended with Nitrogen such that the density of the diluted CO_2 in the injection tube reached approximately the density of air. Carbon dioxide was injected through small holes uniformly distributed over the circumferential surface of the injection tube. Figure 3 shows a schematic representation of the generic cabin model with the installed injection tube. In specifying the boundary conditions required for solving the species transport equation, the concentration of the carbon dioxide in the incoming air, which is in the range of ~300 - 400 ppm, is taken into account. In the experiments, the CO_2 was injected after quasi-steady conditions were achieved for the turbulent airflow in the cabin. Also, the measurement of the carbon dioxide concentration was performed when the flow of air-CO_2 mixture showed a quasi-steady behavior. In tracer gas experiments, the inlet nozzle height was 26.5 mm (half-height nozzle).

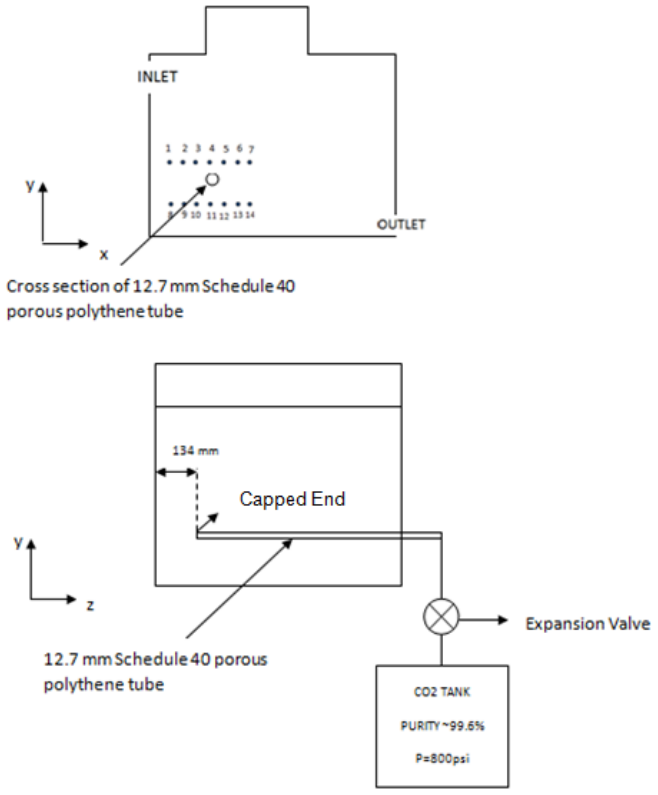

Figure 5.1 A schematic view of the experimental setup for tracer gas measurements. The xy view of the setup shows the tracer gas sampling points above and below the injection tube.

After the turbulent flow of the air-CO_2 mixture reached the quasi-steady conditions, the measurement of the time-dependent values of carbon dioxide concentration at specified sampling points, as shown in Figs. 5.1 and 5.4, was started and continued for about 10 minutes.

The measured data, denoted by C(t), were non-dimensionalized using the concentration of CO_2 at the inlet of the cabin and the average value of the CO_2 concentrations at the outlet between two times: at the beginning of the measurement and at the end of the measurement through the following equation:

$$y(t) = \frac{C(t) - \overline{C}_{inlet}}{\overline{C}_{outlet} - \overline{C}_{inlet}} \tag{5.1}$$

where;

$y(t)$: dimensionless concentration of carbon dioxide

$C(t)$: temporal data of CO_2 concentration at different sampling points

$\overline{C}_{inlet}$: the CO_2 concentration at the inlet measured one time and assumed to be constant during the experiment

$\overline{C}_{outlet}$: the average of the two measured values for the CO_2 concentration at the outlet (the measured values are corresponded to the beginning and the end of measurement duration).

5.3. Governing Equations and Numerical Solution Method

To simulate the tracer gas (carbon dioxide) diffusion in the cabin, the following assumptions are taken into account in addition to the assumptions presented in chapter 4:

1. The flow of air-CO_2 mixture is incompressible.
2. The heat transfer in the cabin is neglected. The temperature is assumed to be constant and equal to 27^{o}C.
3. The effects of buoyancy are taken into account.
4. No chemical reaction takes place in tracer gas diffusion.

In this part of study, compared to what was discussed in chapter 4, not only the geometry of the cabin is changed due to locating the carbon dioxide injection tube in the cabin, but also the equation for transport of species is added to the governing equations. The governing equation for the instantaneous species transport equation is:

$$\frac{\partial}{\partial t}(\rho Y)+\frac{\partial}{\partial x_i}(\rho u_i Y)=\frac{\partial}{\partial x_i}(\rho D)\frac{\partial Y}{\partial x_i} \tag{5.2}$$

where, u_i (m/s) denotes the velocity components, x_i (m) represents the position along the coordinate directions, t (sec) is the time, ρ (kg/m^3) is the density of air-CO_2 mixture, Y is the species mass fraction, and D (m^2/s) is the molecular diffusion coefficient of carbon dioxide in air-CO_2 mixture. In this study, it is assumed that D takes the estimated value of 1.57×10^{-5} m^2/s and is constant throughout the simulations (Bird el al., 2001).

When LES is used to solve Eq. (5.2) for turbulent flow regime, as explained in chapter 4, just the large scale motions of the flow are solved by filtering out the small and universal eddies. In other words, in this approach similar to the velocity and pressure fields, the species concentration field is also separated into resolved and sub-grid domains. Therefore, the instantaneous species mass fraction is considered as the summation of resolvable scale mass fraction ($\tilde{Y}$) and sub-grid scale mass fraction (Y''):

$$Y=\tilde{Y}+Y'' \tag{5.3}$$

The grid size is used to filter out sub-grid scale eddies (see Eq. (4.7)). Substituting the decomposition forms of u_i from Eq. (4.3) and Y from Eq. (5.3), and then filtering the resulting equation, gives the following filtered equation for the species transport equation:

$$\frac{\partial(\rho\tilde{Y})}{\partial t}+\frac{\partial}{\partial x_i}\left(\rho\tilde{u}_i\tilde{Y}\right)=-\frac{\partial}{\partial x_i}\left(-(\rho D+D_t)\frac{\partial\tilde{Y}}{\partial x_i}\right) \tag{5.4}$$

In the above equation, μ_t (Pa.s) is the sub-grid scale turbulent viscosity and calculated through Eq.(4.6). D_t (m^2/s) is the turbulent diffusion coefficient and is calculated through the definition of turbulent Schmidt number and selecting a value for that. The turbulent Schmidt number is defined as:

$$Sc_t = \frac{\mu_t}{\rho D_t} \tag{5.5}$$

In the simulations, the turbulent Schmidt number is selected as 0.7. Since Eq. (5.4) is second order with respect to space and first order with respect to time, we need to determine two boundary conditions for $\tilde{Y}$ in each direction and one initial condition. Similar to discretization schemes applied for the Navier-Stokes equations (explained in chapter 4), the time step size is selected as 0.05 sec and the second order implicit method is used as time marching scheme. The second order central differencing is used to discretize the spatial derivatives.

Another important point is that the viscosity and density of the air-carbon dioxide mixture are not uniformly constant in the cabin and their values in each location in the cabin are dependent on the concentration of constituents at that location. There are a number of methods in the commercial software to calculate the density and viscosity in a mixture. In this study the "volumetric-weighted mixing law" and "mass weighted mixing law" are used to calculate the mixture density and viscosity, respectively, as presented below:

Volumetric Weighted Mixing law:

$$\frac{1}{\rho} = \frac{\tilde{Y}}{\rho_{CO_2}} + \frac{1-\tilde{Y}}{\rho_{air}} \tag{5.6}$$

Mass Weighted Mixing law:

$$\mu = \tilde{Y}\mu_{CO_2} + (1-\tilde{Y})\mu_{air} \tag{5.7}$$

From the above explanations, it can be seen that in order to simulate the tracer gas diffusion in the cabin, five equations are to be solved simultaneously with the given boundary and initial conditions.

In order to generate grid for this geometry, as shown in Fig. 5.2, the whole volume of the cabin model is divided into 10 sub-volumes. Each of these 10 sub-volumes is meshed separately. In the simulations presented in this chapter for tracer gas diffusion, the generated grid is unstructured and contains 1,728,000 mesh elements of tetrahedral, hexahedral and wedge shapes. A schematic of this grid is shown in Fig. 5.3.

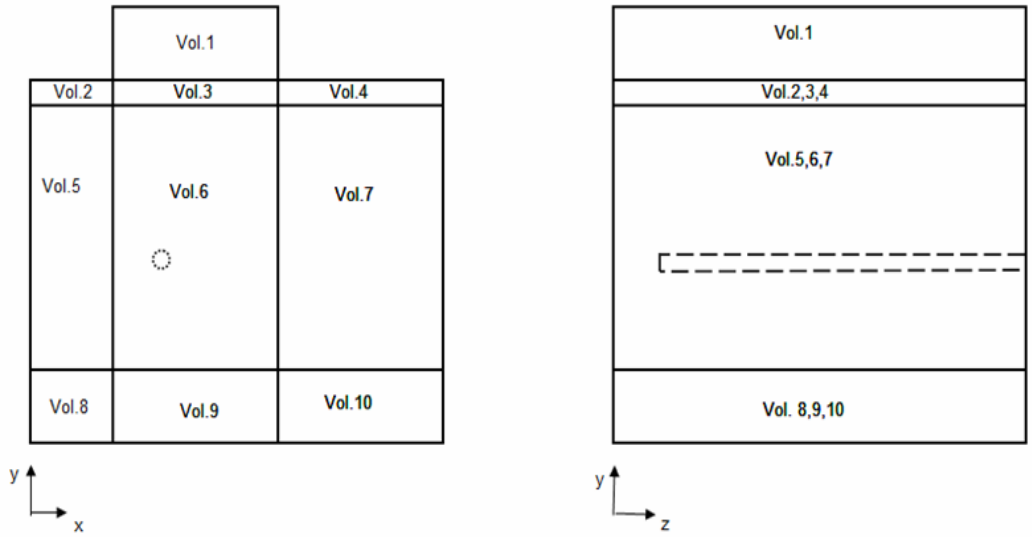

Figure 5.2 Rough graphical representation of the configuration of the generic cabin model and installed injection tube. The numbered volumes indicated the sub-volumes used for grid generation. The grids in sub-volumes: 5, 6, and 7 are unstructured containing tetrahedral, hexahedral and wedge- shape mesh elements. For the rest of sub-volumes, the grids are structured containing orthogonal hexahedral mesh elements.

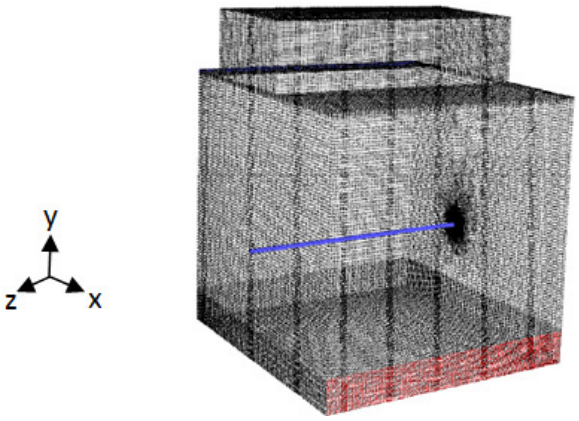

Figure 5.3 A 3D schematic of the unstructured grid (for the generic cabin with the injection tube) used in CFD simulation of the carbon dioxide diffusion in the generic cabin model.

5.4. Results and Discussion

5.4.1. Uncertainty Study (Check for the Grid-Independent Solutions)

In order to study the effect of grid size on the behavior of predictions for tracer gas concentration, the simulations are performed using two grids with different number of mesh cells: 1,728,000 and 2,630,000. Using two different grids, the CO_2 mass fraction at several specified sampling points is calculated, and compared to each other. The location of sampling points above and below the injection tube, points 1-14 are shown in Fig. 5.4.

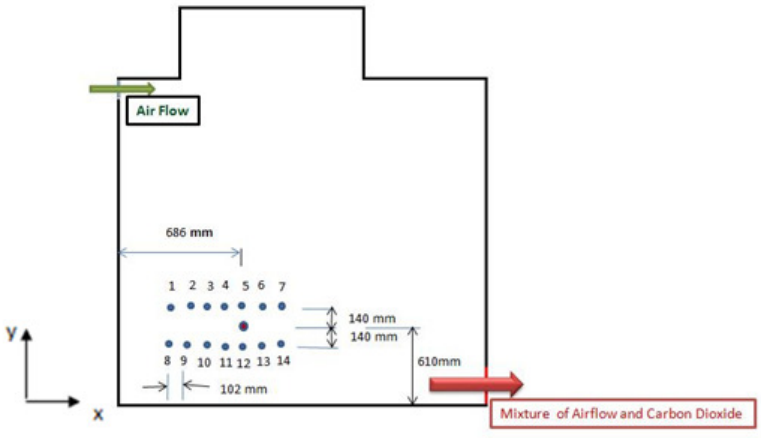

Figure 5.4 Location of tracer gas sampling points on the central plane of the cabin mockup (All dimensions are in mm)

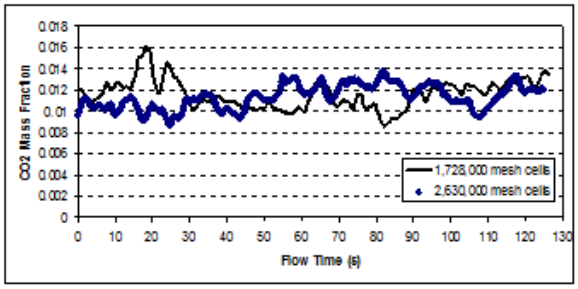

(a) Sampling point 1

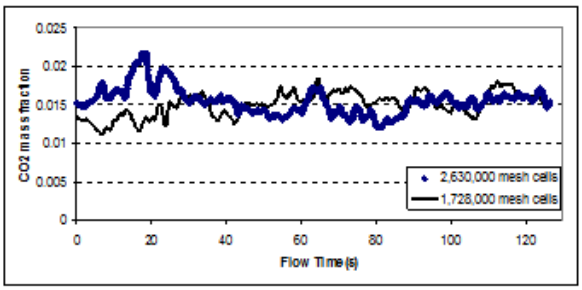

(b) Sampling point 2

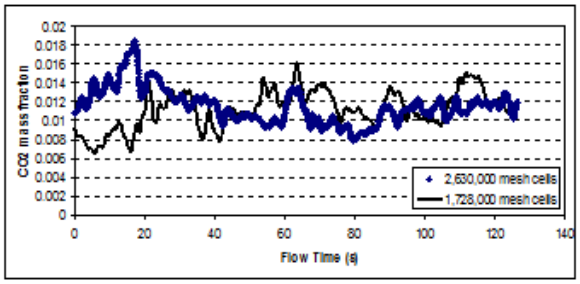

(c) Sampling point 3

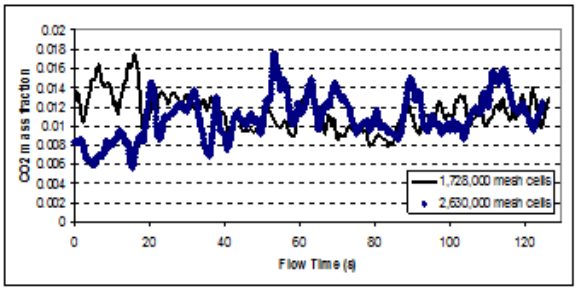

(d) Sampling point 4

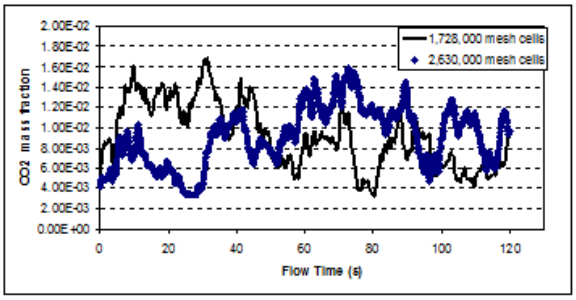

(e) Sampling point 5

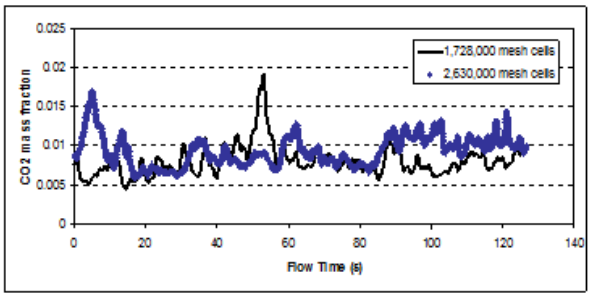

(f) Sampling point 6

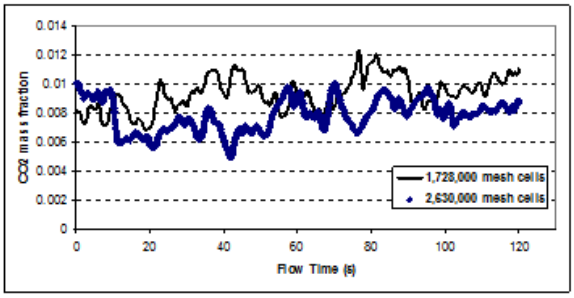

(g) Sampling point 7

Figure 5.5 Uncertainty (mesh error) study for simulating tracer gas injection through monitoring the CO_2 concentration at different sampling points above the injection tube.

A comparison of the RMS values of computed data from two different grids is shown in Table 1. As it is seen, by increasing the number of mesh cells, the computed CO_2 concentration data varies between 2% to 16%. Table 2 shows the comparisons between the mean values of computed CO_2 concentration data from two different grid sizes. As it is seen, by increasing the number of mesh cells, the computed deviation of CO_2 concentration data varies between 2% to 17%.

As seen from the prediction data presented in Tables 1 and 2, the relative difference between the predicted CO_2 concentration data using two grid sizes is greater for the sampling points located in the upper right of the injection tube. In order to explain the reason for this behavior, recall the study of the airflow in the cabin presented earlier in chapter 4. It was observed that the airflow in the location 3 of the PIV windows (see Figs. 4.2 and 4.3) demonstrates more complexity than other locations. Since the sampling points located in the upper right of the injection tube are very close to that region, changing the grid size has a considerable effect on computational accuracy. Therefore, one expects higher computational uncertainties for the sampling points located in regions with more complex airflow structure.

Table 5.1. Comparison of RMS values for computed CO_2 concentrations using two different grid sizes.

Sampling point Number	2,630,000 mesh cells	1,728,000 Mesh cells	Deviation (%)
1	0.0114	0.0116	2.38
2	0.0151	0.0155	2.87
3	0.0117	0.0114	2.85
4	0.0111	0.0116	4.16
5	0.0097	0.0088	10.22
6	0.0095	0.0082	16.06
7	0.0079	0.0094	15.9

Table 5.2. Comparison of mean values for computed CO_2 concentrations using two different grid sizes.

Sampling point Number	2,630,000 mesh cells	1,728,000 Mesh cells	Deviation %
1	0.0113	0.0116	2.08
2	0.0155	0.0151	2.89
3	0.0115	0.0112	2.85
4	0.0109	0.0114	4.86
5	0.0083	0.0092	9.78
6	0.0095	0.0082	17.1
7	0.0078	0.0093	16.13

5.4.2. Model Validation

The computational model is validated through the comparison of model predictions and experimental measurements. In Fig. 5.6 and Fig. 5.7, the time-averaged predicted and measured values of the CO_2 concentration are compared to each other. For the sampling points above the tube (Fig. 5.6), it is observed that there is an excellent agreement between predictions and measurements at sampling points 3, 5 and 6. However, the agreement for the sampling point 4 is not as good. There is an error between 11-30% in predicting the concentration data for the sampling points 1, 2 and 7.

Figure 5.7 shows a graphical comparison between the time-averaged predictions and measurements for CO_2 concentration corresponding to the sampling point located along the x-axis below the injection tube. As can be seen, the best agreements have been achieved for point 12 (right below the tube) and point 14. The worst results correspond to the points 8, 9 and 10. The error in computations for this case varies from ~4% (point 12) to ~40% (point 9).

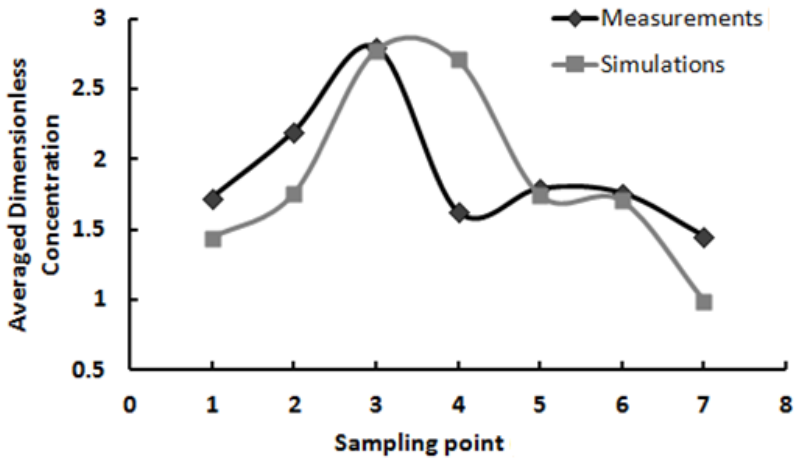

Figure 5.6 Comparison between the time-averaged predictions and measurement of dimensionless CO_2 concentration data (Lebbin, 2006) for the sampling points located along the x-axis above the injection tube (see Fig. 5.4).

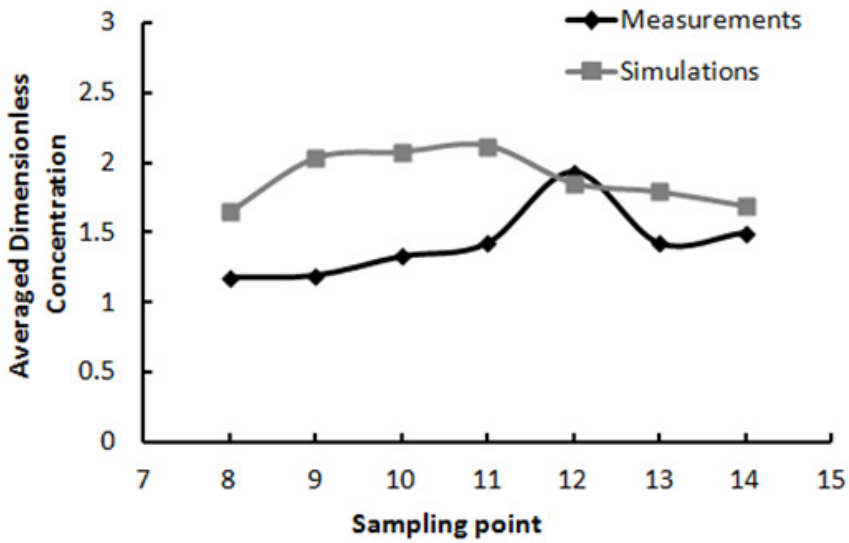

Figure 5.7 Comparison between the time-averaged predictions and measurement of dimensionless CO_2 concentration data (Lebbin, 2006) for the sampling points located along the x-axis below the injection tube (see Fig. 5.4).

5.5. Summary

In this chapter, the capability of commercial CFD software with LES in simulating the tracer gas diffusion in the generic cabin model was examined. The effects of heat transfer were neglected and no chemical reaction was assumed to take place. Carbon dioxide was chosen as the tracer gas which was injected into the cabin through the circumferential surface of a horizontal tube. Using LES, the temporal variations in tracer gas concentration in the specified sampling points were predicted. Following the same procedure as used in the experiments the predicted values were non-dimensionalized and compared with the corresponding experimental data. Although excellent agreement was observed in some sampling points, the predictions had an average error of 23%. Through performing the uncertainty study, it was realized that since the flow in the middle of the cabin has more complex structure than that in other locations, the predictions in that region is more affected by the mesh size. Therefore, it was implied that using regional mesh refinement for the location 3 of the PIV measuring windows may lead to more reliable and accurate predictions.

Chapter 6 - Study of Particle Dispersion in Generic Cabin with Full-Height Inlet Air Nozzle

6.1. Introduction and Research Background

Biological contaminants and/or viruses may spread among aircraft cabin passengers in the form of fine particles or droplets. Particles which represent viruses have a range of sizes from 0.02µm to 0.3µm. The bacteria droplets, however, cover range of sizes from 0.3µm to 12.0µm (Tang et al., 2009). In this chapter, the primary objective is to develop an understanding of the particle dispersion patterns in such enclosures through performing computational simulations. Furthermore, a number of relevant research articles in the literature that use the computational methods in order to study the particle dispersions in indoor environments are reviewed.

In order to simulate particle dispersion in a mechanically ventilated airspace, Reynolds (1997) used Thomson's (1987) Lagrangian stochastic model. The turbulent airflow was three-dimensional and strongly inhomogeneous. The standard k-ε model was used to calculate the airflow velocity data. The model worked well in predicting the locations of maximum mean concentrations of tracer-particles as well as the shape of contours of tracer-particles mean concentrations. Holmberg and Li (1998) presented a three-dimensional drift-flux model in order to study the turbulent dispersion of aerosols in a test room. Both mixed and homogeneous air supply conditions were considered in the simulations. Due to low solid loading and comparatively small particle settling velocities, the effect of particles on air turbulence was neglected (one-way coupling). Standard k-ε model was used to calculate the turbulence effects and wall functions were used for near wall treatment. Also the simulations were performed for several sizes of particles. Through the simulations it was realized that the particle distribution pattern is strongly dependent on the ventilation air supply rate. Considering the effects of Brownian and turbulent diffusion as well as gravitational settling, Lai and Nazaroff (2000) developed a mathematical model to calculate particle deposition on indoor surfaces. The results of the previous studies of near-surface turbulence were applied to the model. The developed model was able to predict the particle deposition to the smooth surfaces as a function of particle

size and density. The model equations were derived for enclosures with vertical and horizontal surfaces.

Zhao et al. (2003) investigated the air movement and aerosol particle distribution and deposition in a ventilated room numerically. Two different ventilation systems were considered: displacement and mixing. In order to simulate airflow and particle dispersion, a Lagrangian approach was adopted. This study showed the strong effect of the room ventilation type on the airflow pattern, the particle concentration distribution, and deposition rate. It was found that under the same air supply rate and particle property conditions, the displacement ventilation type leads to smaller deposition rate as well as larger particle removal rate than the mixing ventilation type. However the average particle concentration is higher in a displacement type system.

In a couple of other studies conducted by Zhao et al. (2004 a, b), both Eulerian and Lagrangian approaches were used to understand the effects of air ventilation type and particle size on the behavior of particle dispersion in a ventilated room. In the Eulerian approach a three dimensional drift-flux model was used combined with deposition boundary conditions for the wall surfaces. Through these numerical investigations it was found that the deposited particle mass or flux is strongly dependent upon the ventilation type. From the Eulerian approach (Zhao et al., 2004 a), more particle depositions were observed in the mixing-type ventilated room for a certain size of particles. From the Lagrangian approach (Zhao et al., 2004 b), it was concluded that for the same particle properties, the rate of particle deposition is lower for a displacement ventilated room comparing to that of the mixing type ventilated room. However, the rate of particle escape was higher for the room with displacement ventilation type. Through the consideration of different sizes for particles (1, 2.5, 5 and 10μm) in their numerical investigation, it was also realized that different sizes of particles have different dispersion patterns in two types of ventilated rooms. Chen and Lai (2004) proposed a simplified semi-empirical three-layer model to investigate the dispersion and deposition of aerosol particles under the influence of electrostatic forces. A modified Fick's law equation was applied to calculate Brownian and turbulent diffusion, spatially-independent external forces (gravitational and Columbic), and spatially-dependent external forces (image).

Chen et al. (2006) developed a new drift–flux model to simulate particle distribution and deposition in indoor environments. The model was applied to simulate particle distribution and deposition in a ventilated model room. Gravitational settling and deposition were considered

within the model. RNG k-ε model was used as the turbulence model in order to solve the governing Navier-Stokes equations for the continuous flow-field. The discrete-phase concentration field was divided into two regions, the core region and the concentration boundary layer. The concentration distribution in the core region was obtained by solving a three-dimensional particle transport equation. Deposition flux towards the wall was determined with a semi-empirical particle deposition model. Through the model validations, a good agreement between predictions and measurements was found.

Lain and Grillo (2007) conducted a study to compare the performance of two Lagrangian turbulent particle dispersion models: (1) the standard model reported by Sommerfeld et al. (1993) in which the fluctuating fluid velocity experienced by the particle is composed of two components, one correlated with the previous time-step and a second one randomly sampled from a Wiener process, and (2) the model proposed by Minier and Peirano (2001), which is based on the Probability Distribution Function (PDF) approach and a Langevin model for the acceleration of the fluid velocity. Through this investigation it was found that the Minier and Peirano model provides better results than the standard model because its construction better reflects the underlying physics of particle dispersion for general turbulent flows, but at the expense of a higher computational cost. Liu and Zhai (2007) proposed two particle indices: the Stokes number and the evaporation effectiveness number that can be used as simple criteria in order to determine what CFD model is appropriate for indoor particle and droplet prediction. They classified the CFD models into three classes: lazy particle model, isothermal particle model, and vaporizing droplet model. The lazy particle model was defined as a model in which the particle trajectories are not calculated. It is simply assumed that particle follows the continuous phase streamline at each point of flow-field. In this model, which is also called the tracer model, the concentration distribution of particles can be calculated through the solution of species transport equation which basically governs the transport of gas-phase contaminants. The model is appropriate for small particles with quasi-gaseous compounds. The isothermal particle model was defined as a model in which the particle trajectories are calculated, but without considering thermal effects. It means that in this type of models the particle size doesn't change and there is no exchange of heat and mass between particle and continuous phase. Finally, the vaporizing droplet model was defined as a model which is used when, due to evaporation, there

are both heat and mass exchanges between particle and continuous phase, and as a result the size of liquid particle or droplet is subject to change.

Dehbi (2008) used a modified particle-turbulence interaction in Lagrangian particle dispersion modeling. The model was basically developed through the consideration of turbulence anisotropy, especially for near-wall flows in the stochastic particle-tracking model employed in FLUENT 6.2. In this investigation, the fluid velocities in the boundary layer were computed using fits of DNS data obtained in channel flow. Zhao et al. (2009) developed their drift-flux model by considering the effects of both thermal and gravitational forces in calculating the particles slippage velocity for non-isothermal cases. After the validation of the modified model, it was used to study the effect of the indoor ventilation type and particle size on the dispersion pattern of ultrafine particles (particles with sub-100nm diameter) in a test room. Through this study, it was determined that, although using the mixing ventilation type leads to lower concentration of micron particles in the zone below one meter high, it will cause higher concentration of ultrafine particles in the mixing zone in comparison with the displacement ventilation type. It was also concluded that both ventilation types are not sensitive to the particle size when the particles diameters are in the range of 0.01 to 0.1μm. Considering the variations with height in the horizontally homogeneous turbulence kinetic energy, Gorle et al (2009) simulated the turbulent dispersion of small particles in the lower part of the atmospheric boundary layer. They used the RANS method to find the velocity profiles. The validation of simulations showed an improvement in the prediction of particle distribution compared to the simulations in which a uniform vertical distribution was assumed for the turbulent kinetic energy.

Zhang et al. (2010) used an Eulerian approach to study the deposition of particles which were tens of microns in size. The particles were created due to aggregation of nano-particles injected through an injection port to the test chamber. The transient deposition of particles caused by gravitational settling was simulated. For this purpose the mass conservation equation for the discrete phase was modified to include the gravitational settling effect as well as convection and diffusion effects. The simulations were verified through the comparisons between predictions and measurements for the particles deposition-rate data. The comparisons indicated best agreement between experimental measurements and computational predictions for the intermediate particle-size range.

This chapter is the continuation of the research presented in chapters 4 and 5 of this dissertation in the numerical investigation of turbulent transport phenomena in the generic cabin mockup model. The simulations presented in this chapter are for the turbulent dispersion of mono-disperse liquid particles in the same generic cabin mockup as studied in the previous two chapters. Two different particle injection configurations are considered in the simulations herein, while the carrier air volumetric flow rate and the particles mass flow remain at the same values for both cases of injection configurations. In the first configuration, in which the particles are injected through the top end surface of a straight tube mounted vertically on the cabin floor, the velocity of carrier air and particles at the injection port is about 3.5 times greater than the velocity of supply air injected into the cabin through the cabin inlet nozzle. However in the second configuration, in order to eliminate the effect of particle injection velocity on the distribution pattern of mono-disperse particles, the straight tube was replaced by a cone diffuser such that the injection velocity of particles is decreased down to almost zero. A Lagrangian approach was mainly used to predict the particle concentration in specified monitoring location inside the cabin as well as at the outlet of the cabin. Although the continuous phase flow-field within the cabin is simulated using both RANS and LES methods, the quasi-steady and steady RANS solutions for the airflow velocity data are used to initialize the particle-tracking calculations through the Discrete Phase Model (DPM). To calculate the effects of turbulence on the dispersion behavior of particles, a Discrete Random Walk (DRW) model was employed. Using the steady RANS method, a comprehensive grid independency study was performed by concentrating on regional mesh refinement using both structured and unstructured grids. The effectiveness of both grid refining approaches in producing the converged velocity data is investigated and discussed. The optimum mesh size and type is then used to simulate the dispersion of micron particles. The particles are made of Di-Octyle Phthalate (DOP) and injected continuously into the cabin through either a straight tube or a cone diffuser. The computational model is validated through the comparison of the predicted particle concentration data with the corresponding experimental measurements reported by Padilla (2008). One of the significant features of this study is the investigation of the effect of the number of tries on the accuracy of particle concentration predictions when stochastic particle tracking is used to model turbulent distribution of particles. Subsequently, the optimum number of tries to obtain the most accurate predictions is determined. In accordance with the corresponding experiments (Padilla,

2008), the effect of particle size on the predicted concentration distribution of particles is studied and discussed through the simulation of two different sizes of mono-disperse particles: 3μm and 10μm in the cabin with straight injection tube. Due to the low particle loading, neglecting the effect of particles motion on the continuous phase flow-field seems to be a reasonable, simplifying assumption. However, in order to verify this assumption, through the simulations performed for the cabin with straight injection tube, the effect of using one-way instead of two-way coupling on the accuracy of computational results for particle concentration is also investigated. Eventually, through the simulations for the particle dispersion in the cabin with cone diffuser, the effects of cabin pressure gradient as well as particle density on particle concentration distribution are studied and discussed.

6.2. Experiments

The particle dispersion experiments in generic aircraft cabin mockup were conducted by Padilla (2008). Figure 6.1 shows the configuration of the experimental setup including the generic cabin mockup (which was discussed in the previous two chapters) with the particle injection tube inside it. The mockup was provided by the fresh air through a full-height inlet air nozzle (the height is 54 mm). The height of the mock-up outlet-slit was 213 mm. The length and width of the mockup were equal to 2,134mm. The lower surface of the cabin overhead bins was located at the height of 1,707 mm above the cabin's floor. The height of the cabin ceiling from the floor was 2,134mm. The fresh air was injected into the cabin with the flow rate of 4,160 lpm and the average velocity of 0.64 m/s (normal to the cabin inlet-slit surface). The experiments were performed in Standard Temperature and Pressure (STP) conditions.

In the first series of experiments, particles were injected continuously through an injection tube located at x=1447 mm, y=595 mm, and z=0 (see Figs. 6.1 and 6.2). The injection tube, installed vertically on the cabin's floor, was made of stainless steel with the inner diameter of 22.1 mm (see Fig. 6.2). The injection port was the upper end of the injection tube at the height of 595 mm from the cabin's floor. The particle measurement locations are shown in Figs 6.1 and 6.2. It should be mentioned that for the five measurement locations on the cabin central plane, the Aerodynamic Particle Sizer (APS) was used to measure concentration of the particles. However, for the eleven measurement locations at the cabin outlet, Optical Particle Counter

(OPC) was used for the concentration measurements. The measurement locations at the outlet had the height of 51mm.

Through the dimensions shown in Fig. 6.2, the coordinates of the five measurement locations on the cabin central plane can be determined as they are presented in Table 6.1. The coordinates of the outlet locations can be easily extracted from Fig. 6.1. In addition, Fig. 6.2 also presents information about the inlet volumetric airflow rate as well as the volumetric flow rate of the carrier air injected into the cabin through the particle injection tube. Particles are produced by the Vibrating Orifice Aerosol Generator (VOAG) as shown in this figure. VOAG was set to a vibrating frequency of ~49 Hz that yields a theoretical concentration of 54 particles/cm^3.

The liquid particles are made of Di-Octyl Phthalate (DOP oil) and generated using TSI VOAG Model#3450. Schematic views of this device are shown in Figs.6.3 and 6.4. According to the theory of this device (TSI Model 3450 Operating and Service Manual, 2009), the particles are initially composed of Di-octyl Phthalate (DOP) oil in their core region and Isopropyl Alcohol in their outer layer. During the motion of particles in the drying column of the device, the alcohol in the outer layer is evaporated and the final particles which are delivered to the testing enclosure are mainly composed of DOP. Using the explanations, equations, and tables in the device manual and considering the probability of existing impurities in the alcohol, a range of 953 kg/m^3- 971 kg/m^3 is calculated for the density of 10 μm particles. The calculated density range for the 3 μm particles is between 970 and 971 kg/m^3.

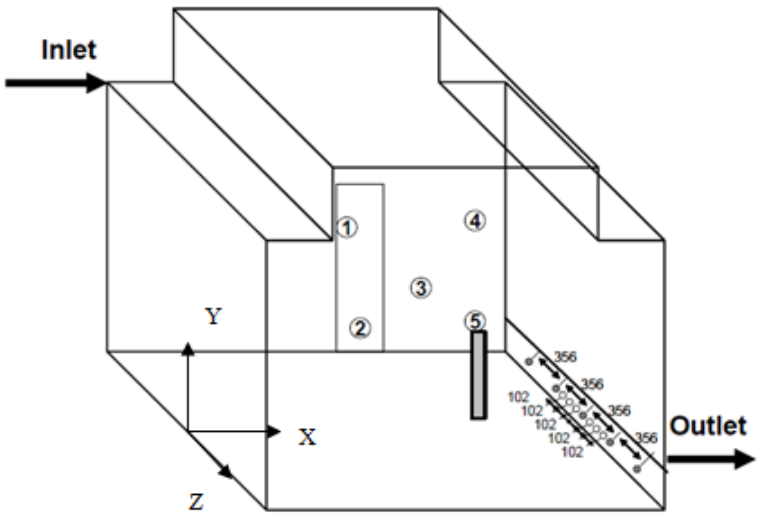

Figure 6.1 Schematic of the generic cabin, injection tube and measurement locations (units in mm). (Padilla, 2008)

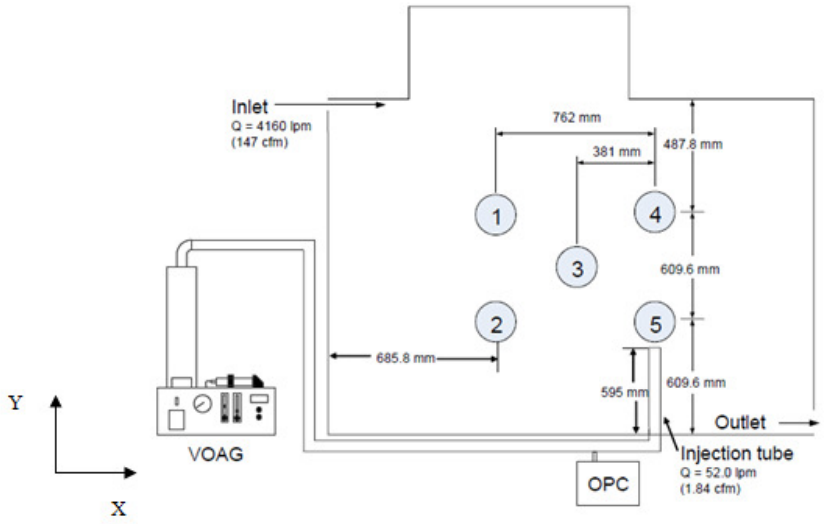

Figure 6.2 XY View of the test configuration for the straight tube injection (units in mm). (Padilla, 2008)

Table 6.1: The coordinates of APS particle measurement locations for the cabin with straight injection tube

Location #	x (mm)	y (mm)	z (mm)
1	685.5	1219.2	0
2	685.5	609.6	0
3	1066.8	914.4	0
4	1447.8	1219.2	0
5	1447.8	609.6	0

At the beginning of each experiment there was just injection of air from the inlet air nozzle and particle injection tube (or cone diffuser). The particles were not injected until the flow inside the cabin reached quasi-steady conditions. After that the VOAG was started to work and 15-30 minutes were considered as warm-up time. Then the particle count measurements were performed continuously over the period of sixty minutes. The collected data were taken time-averaged and normalized using the following equation (Padilla, 2008):

$$C = \frac{C_m \times Q_{\text{sup}}}{C_I \times Q_I} \tag{6.1}$$

where C_m is the measured sample count concentration corrected for the particle loss in the sampling tube, C_I is the calibrated injected concentration, Q_{sup} (lpm) is the supply flow (inlet and injected), and Q_I (lpm) is the injected flow of the carrier air.

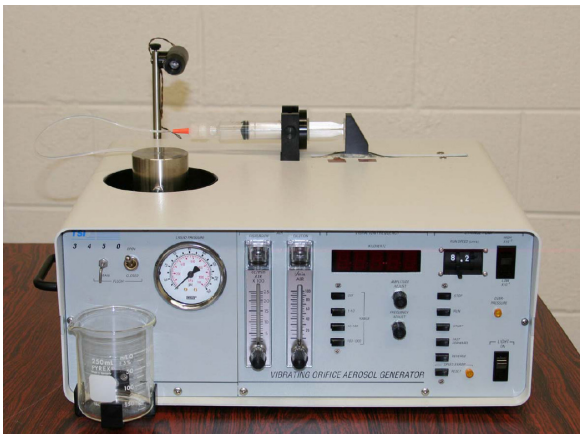

Figure 6.3 Schematic of the TSI VOAG Model#3450 (Padilla, 2008)

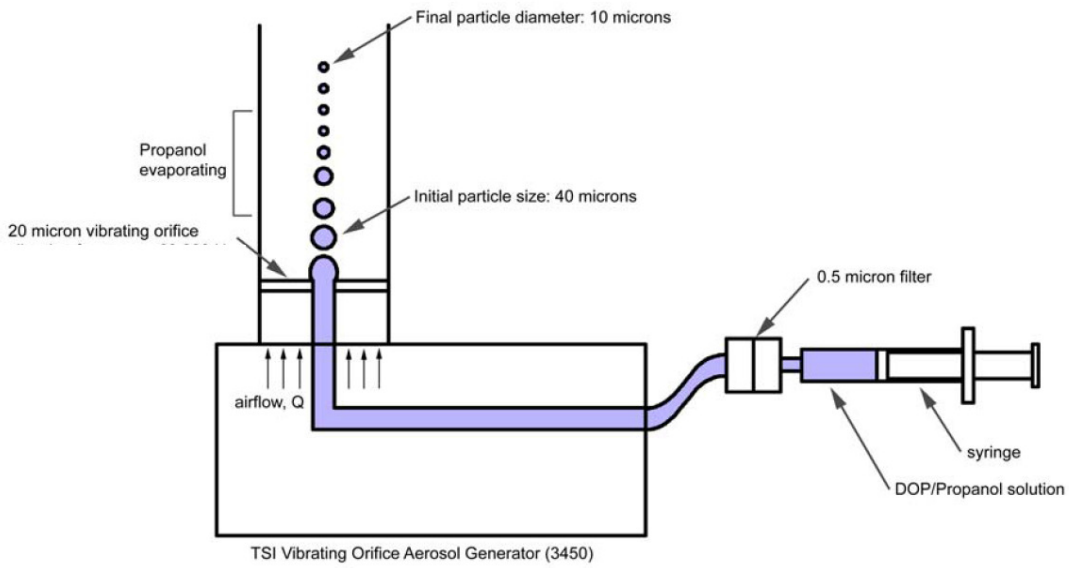

Figure 6.4 Schematic view of the process of particle generation in TSI VOAG Model#3450 (Padilla, 2008)

In the second series of the experiments, in order to eliminate the effect of particles injection velocity in studying dispersion behavior of particles, the straight injection tube was replaced by a cone diffuser. The cone dimensions as well as the test configuration for the cone injection are shown in Figs. 6.5 and 6.6, respectively. In the first series of experiments when the straight tube injection was used the cabin pressure was set to 0 gage pressure, however during the cone injection, the interior cabin gage pressure initially set to 0 gage pressure was increased from 0 in of H_2O to 0.025 in of H_2O. The carrier air volumetric flow-rate was remained at the same value as before which was 52 lpm. The cone nozzle inlet and outlet inner diameters were 22.1 mm and 152 mm, respectively.

As it is shown by Fig. 6.7, the particle count measurements for the cone diffuser injection were taken not only on the cabin central plan but also on four more planes parallel to the central plane. Measurements started from plane E and ended in plane A (see Fig. 6.7). Similar to the measurements performed for the straight tube injection, the particle count measurements were collected continuously at each sample location over the period of sixty minutes. Also, moving the sampling tube from one plane to another plane took 200 sec time in average. Table 6.2 presents the coordinates of the particle measurement locations on planes A-E.

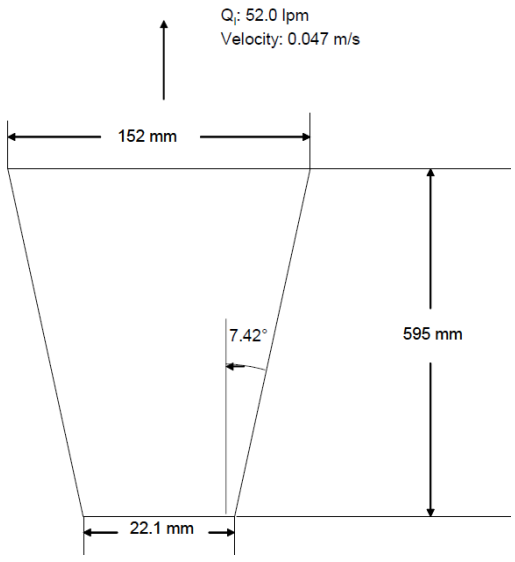

Figure 6.5 Dimensions of the cone diffuser (Padilla, 2008)

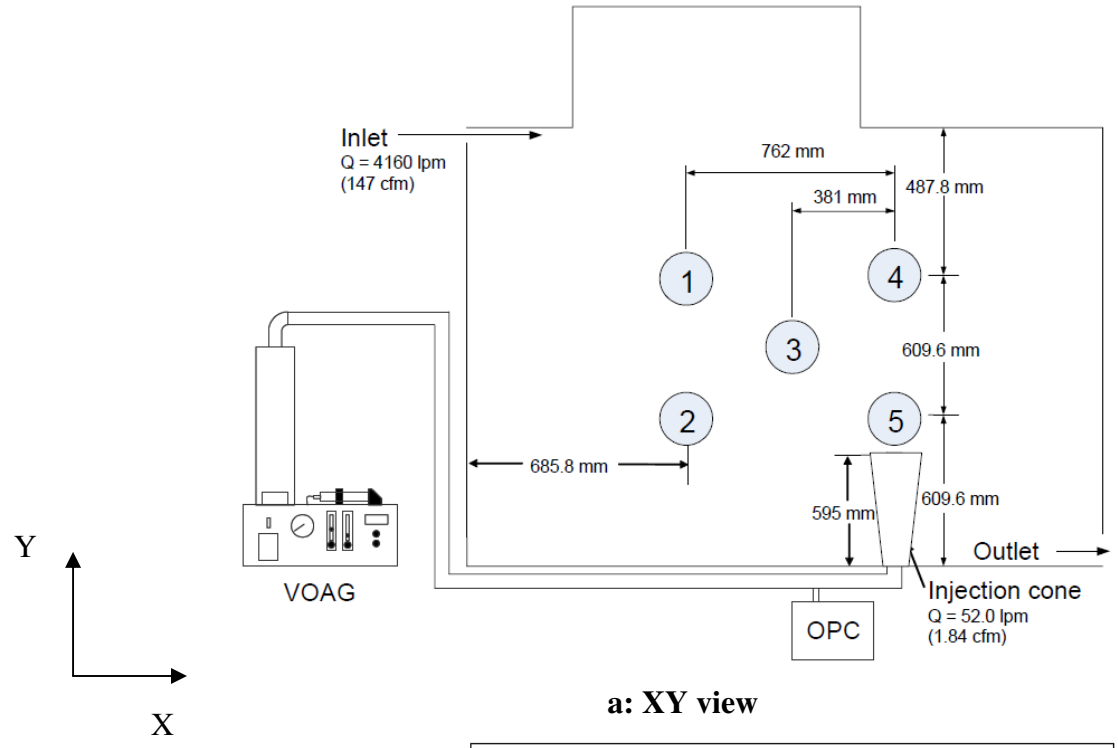

a: XY view

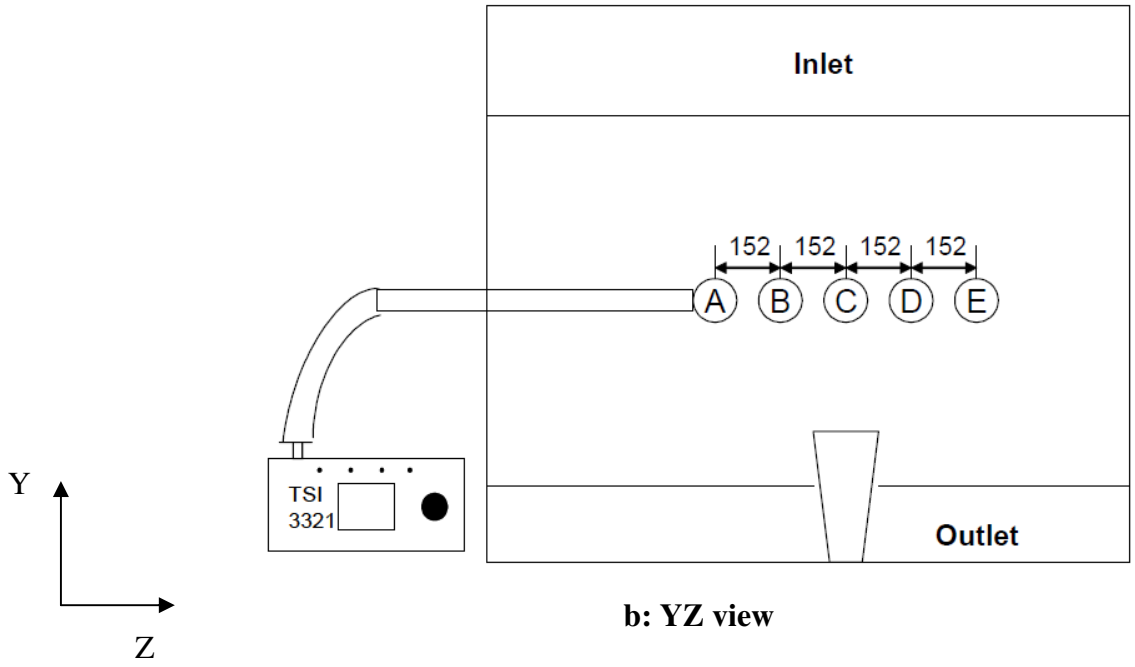

b: YZ view

Figure 6.6 XY and YZ View of the test configuration for the cone diffuser injection. All the units are in mm. (Padilla, 2008)

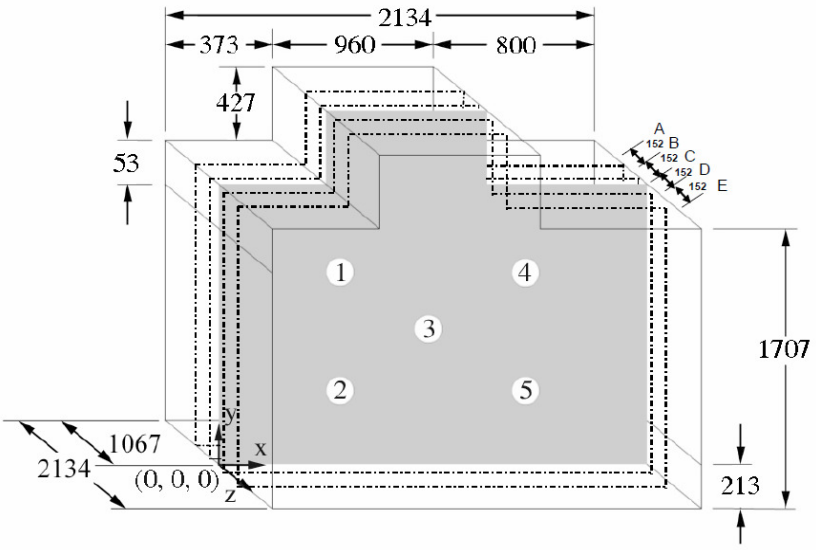

Figure 6.7 Measurement locations in the cabin mockup with cone diffuser. All the dimensions are in mm (Padilla, 2008).

Table 6.2: The coordinates of particle measurement locations in the cabin with cone diffuser (Padilla, 2008)

Location	x (mm)	y (mm)	Plane	z (mm)
1	685.8	1219.2	A	-304.8
2	685.8	609.6	B	-152.4
3	1066.8	914.4	C	0
4	1447.8	1219.2	D	152.4
5	1447.8	609.6	E	304.8

The airflow conditions at the inlet of the cabin and at the particle inject port for both cases of injection configurations were summarized by Padilla (2008) in Table 6.3.

Table 6.3: Flow parameters in the inlets and outlet of the test cabin mockup (Padilla, 2008)

Location/Device	Cross Section	Length	Q (lpm)	Q (cfm)	V_{avg} (m/s)	Reynolds Number
Cabin Inlet	53 x 2134 mm (rectangular)	-	4160	147	0.640	4200
Injection						
Straight tube	22.1 mm diameter	595 mm	52.0	1.84	2.27	3300
Diffuser cone	22.1 mm inlet, 152 mm outlet diameter	595 mm	52.0	1.84	0.047	484
APS Sample Tube	18.9 mm diameter	1000 mm	5.00	0.177	0.296	370
Outlet OPC	2 mm diameter	25.4 mm	2.83	0.1	15.0	2000

6.3. Governing Equations and Numerical Solution Method

In this part of study, the Lagrangian approach is used to model the dispersion of particles in the cabin. In this approach which is also called Discrete Phase Model (DPM), the discrete phase computations are performed in a Lagrangian frame (calculation of particles trajectories). The continuous gas phase, however, is dealt with in an Eulerian frame which has interaction with the discrete phase through the exchange of momentum, heat and mass. In this approach, the interaction between particles is not taken into account. In order to have negligible interactions between particles, the discrete phase needs to be sufficiently dilute. For this reason the application of DPM is recommended only for the two-phase flows in which the discrete phase has volume fraction (ANSYS FLUENT 12.0 Manual, 2009).

In order to simulate the distribution of mono-disperse particles, using DPM, the following assumptions have been adopted:

1. The continuous phase flow is incompressible.
2. The heat transfer is neglected in the cabin. The temperature is assumed to be constant at $27^{o}C$.
3. The particles are not cooled, heated or evaporated (inert particles).
4. The particles neither coagulate nor break.
5. The effects of buoyancy are taken into account.
6. No chemical reaction takes place between discrete and continuous phases.
7. Steady RANS model is used to solve the continuous phase governing equations.
8. Except the drag and gravity forces, other forces are assumed to be zero.
9. The particles are assumed to be trapped on the walls when they collide with the walls.
10. The injection type is surface injection.

6.3.1. Discrete Phase Equation of Motion

The trajectory of particles is computed through integrating the governing equation for the particles motion:

$$\frac{du_i^p}{dt} = \frac{F_i}{m_p} \tag{6.2}$$

where m_p(kg) is the mass of particle, u_i^p(m/s) is the velocity of particle in i direction. F_i (N) denotes all the forces acting on the particle which is a combination of viscous, pressure drags, and buoyancy force (Clayton et al. , 1998):

$$F_i = \frac{1}{2}\rho \cdot A \cdot C_D \cdot (u_i - u_i^p)\left|u_i - u_i^p\right| + m_p g_i \frac{\rho_p - \rho}{\rho_p} \tag{6.3}$$

where ρ and ρ_p (kg/m^3) are the densities of the continuous phase (air) and particles, respectively, C_D is the drag coefficient for the spherical particle, A (m^2) is the projected area for the particle, u_i (m/s) is the instantaneous velocity of continuous phase in i direction, and finally g_i (m/s^2) is the gravitational acceleration in i direction. Equations (6.2) and (6.3) indicate that the continuous phase affects the trajectory of particles through the drag and buoyancy forces.

6.3.2. Continuous Phase Governing Equations

The governing equations for the continuous phase are:

Continuity:

$$\frac{\partial u_i}{\partial x_i} = 0 \tag{6.4}$$

Momentum:

$$\frac{\partial u_i}{\partial t} + u_j \frac{\partial u_i}{\partial x_j} = -\frac{1}{\rho}\frac{\partial p}{\partial x_i} + \frac{1}{\rho}\frac{\partial}{\partial x_j}\left(\mu \frac{\partial u_i}{\partial x_j}\right) + g_i - \frac{F_i}{m_p} \tag{6.5}$$

where μ (kg/m.s) is the continuous phase viscosity, p (Pa), is the continuous phase pressure and F_i/m_p (N/kg) is the force acting on the continuous phase exerted by the discrete phase (the reaction of drag and buoyancy forces acting on the particles).

In coupled (two-way coupling) approach, the effect of discrete phase on the continuous phase calculations is taken into account by keeping the last term in Eq. (6.5). However, in the uncoupled approach (one-way coupling) the effect of discrete phase on the continuous phase is neglected by dropping the last term in the same equation. The comparison between results from these two approaches are presented and discussed later in this chapter.

6.3.3. Solution Method

The simulation begins with the quasi-steady solution of the continuous phase governing equations, i.e. Eqs. (6.4) and (6.5). At the beginning, the value of the last term in Eq. (6.5) is considered as zero. Therefore the number of unknowns (three velocity components and one pressure) matches with the number of equations (one continuity and three momentum equations). After the first 5 iterations of the continuous phase computations, using the calculated continuous phase velocity data (from the last iteration), the trajectory of particles is calculated by solving Eqs. (6.2) and (6.3). By calculating the particles trajectory, the last term in Eq. (6.5) will not be zero for the next 5 iterations of the continuous phase computations. After every 5 iterations of the continuous phase calculations, the last term of Eq.(6.5) is updated through the simultaneous solution of Eqs. (6.2) and (6.3). This computational procedure is continued until the convergence criteria (10^{-7} for velocity components as well as k and ε and 10^{-6} for continuity) for the continuous phase governing equations are satisfied.

6.3.4. Turbulence model

In solving Eqs. (6.4) and (6.5), which govern the instantaneous velocity field of the continuous phase (airflow), the Reynolds Averaged Navier Stokes (RANS) model is applied. In this study, for steady RANS:

$$\frac{\partial \overline{u}_i}{\partial x_i} = 0 \tag{6.6}$$

$$\frac{\partial \overline{u}_j \overline{u}_i}{\partial x_j} = \frac{\partial}{\partial x_j}\left(-\overline{p}\delta_{ij} + (\mu + \mu_t)(\frac{\partial \overline{u}_i}{\partial x_j} + \frac{\partial \overline{u}_j}{\partial x_i}) \right) + \rho g_i - \frac{F_i}{m_p} \tag{6.7}$$

Using the standard *k-*ε turbulence model, the turbulent viscosity is calculated through the following equation:

$$\mu_t = \frac{C_\mu \rho k^2}{\varepsilon} \tag{6.8}$$

where C_μ is an empirical constant which is equal to 0.09 for standard k-ε (Launder and Spalding, 1972) and is equal to 0.0545 for RNG k-ε (Tu et al., 2008 and Yakhot, 1992).

6.3.5. Particle-Turbulence Interactions

The major issue in the Lagrangian particle tracking is calculating the effect of turbulence on particles trajectory (Dehbi, 2008). As explained before, the trajectory of particles is computed by integrating the equation of motion (Newton's second law) of the particles. By combining Eq. (6.2) and (6.3) the following equation is derived for the spherical particles. Integrating this equation determines the path of particles.

$$\frac{du_i^{\,p}}{dt} = \frac{3C_D \rho}{8 r \rho_p}(u_i - u_i^{\,p})\left|u_i - u_i^{\,p}\right| + g_i \frac{(\rho_p - \rho)}{\rho_p} \tag{6.9}$$

In the equation above, r (m) denotes the particle radius and as the RANS method is used, the instantaneous velocity, u_i, consists of a time-averaged or mean component ($\overline{u}_i$) and a fluctuating component (u'). The continuous phase mean velocity data is computed from the

RANS method. The turbulence affects the trajectory of particles through the fluctuating velocity (u') components. In this study, in order to calculate the effect of turbulence on the trajectory of particles, the Discrete Random Walk (DRW) model was used. The main idea of this model is the interaction between the particles and turbulent eddies. In other words, in this model, it is assumed that the particle is trapped by an eddy during an eddy life time. The eddy life time (τ_e) is calculated using the equation below (Daly and Harlow, 1970):

$$\tau_e = 2.C_L \frac{k}{\varepsilon} \tag{6.10}$$

The value of C_L in Eq. (6.10) does depend on the employed turbulence model. For the k-ε model, $C_L \approx 0.15$. During lifetime of the eddy, the continuous phase velocity fluctuations are randomly distributed Gaussian variables whose Root Mean Squared (RMS) values are equal and deduced from the turbulent kinetic energy:

$$u_i' = \lambda_i \sqrt{\overline{u_i'^2}} \tag{6.11}$$

$$\sqrt{\overline{u_i'^2}} = \sqrt{2k/3} \tag{6.12}$$

In the equations above, the λ_i's are Gaussian random variables with a mean value of 0 and standard deviation of 1. In the simulations, in order to calculate the random effects of turbulence on the discrete phase dispersion, it is required to pick a sufficient number of representative particles which is called the number of tries (Dehbi, 2008 and the ANSYS FLUENT 12.0 Manual, 2009). The effect of number of tries will be discussed in the next sections.

6.3.6. Particle Tracking Parameters

In order to take the integration of Eq. (6.9), two parameters should be specified: The time step size and the maximum number of time steps. The time step size can be calculated using the following equation:

$$\Delta t = \frac{L}{\left\|\vec{u}_p\right\| + \left\|\vec{u}\right\|} \tag{6.13}$$

where L (m) is the length scale, $\left\|\vec{u}_p\right\|$ (m/s), is the magnitude of particle velocity and $\left\|\vec{u}\right\|$ (m/s), is the magnitude of continuous phase velocity. In this study the length scale, which is the length traveled by a particle between two successive particle tracking updates, is assumed to be constant and equal to 0.01m. The maximum value of Δt is such that the cell is traversed in one step. Smaller time steps leads to more accurate results. The maximum number of steps should be equal to the number of grid cells that particles traverse in a computational domain (ANSYS FLUENT 12.0 Manual, 2009).

6.3.7. Numerical Scheme

In the RANS method, the second order upwind scheme is used to discretize spatial derivatives in the governing continuity and momentum equations. Also, the standard wall function is used as the near-wall treatment. In calculating the particle trajectories, which is performed through the integration of Eq. (6.9), an automated tracking algorithm is employed. This algorithm switches between the numerically stable lower order and higher order schemes, depending on whether or not the particle is close to hydrodynamic equilibrium (ANSYS FLUENT Manual, 2009). In this study, trapezoidal integration is used in the higher order scheme; however, for the lower order scheme an implicit Euler integration is applied.

6.3.8. Setting-up the Boundary Conditions and the Injection Properties

The rate of particle counts injected into the cabin is determined using the following equation:

$$\dot{N}_{inj} = N_{inj} \cdot Q_{inj} \tag{6.14}$$

where $\dot{N}_{inj}$ (particle/sec) is the rate of particle counts injected into the cabin, N_{inj} (particle/cm^3) is the count concentration of particles at the injection port, and Q_{inj} (cm^3/sec) is the volumetric airflow-rate at the injection port. Using the information presented in Table 6.3 and Eq. (6.14), the rate of particle counts injected into the cabin is 46,800. Knowing the volumetric flow-rate of carrier air at the injection-port and assuming the particles are injected at the same velocity as the carrier air, the injection velocity of the particles can be calculated. The injection velocity of particles at the injection surface of straight tube is 2.27 m/s and at the injection surface of cone diffuser is 0.0478 m/s. Having the size of particles, the rate of particle counts injected, and the density of particles (which is assumed to be equal to the density of DOP: 971 kg/m^3) the mass flow-rate of particles can be calculated through the following equation:

$$\dot{m}_p = \rho_p \cdot (\frac{\pi d_p{}^3}{6}) \cdot \dot{N}_{inj} \tag{6.15}$$

where $\dot{m}_p$ (kg/sec) is the mass flow-rate of particles, ρ_p (kg/m^3) is the density of particles, d_p (m) is the diameter of particles, and $\dot{N}_{inj}$ (particle/sec) is the rate of particle counts injected into the cabin. It is assumed that when particles, along their trajectory, meet the cabin inlet surface, cabin outlet surface, or the injection surface, they will escape. As they collide with the solid surfaces (walls) in the cabin, since they are liquid particles, it is assumed that they will be trapped by those surfaces. In order to specify the continuous phase turbulent kinetic energy and dissipation rate at the inlet of the cabin as well as the injection port, equations (3.12)-(3.14) are used.

6.4. Results and Discussions

In the first part of this section, the results from the simulation of turbulent distribution of mono-disperse particles injected into the cabin mockup interior through the straight particle injection tube are presented and discussed. Through the simulations presented in this part, the advantages of unstructured regional mesh refinement, the effect of micron particle size on particle dispersion pattern, and the effect of number of tries on the accuracy of predictions for the particle counts are investigated and discussed. In the second part, though, the computational predictions for a different injection configuration in which the straight injection tube is replaced by the cone diffuser are presented and interpreted. In this part, the effects of micron particle constituent as well as the cabin mockup inside pressure on the particles distribution patterns are examined. In both parts of this section, the simulations are validated through comparison of predicted particle concentration data with corresponding experimental measurements.

6.4.1. Study of turbulent particle injection in generic cabin mockup with straight injection tube

6.4.1.1. Simulation of turbulent airflow and the grid independency study

In the experiments, the average airflow rate coming into the cabin was maintained at the constant value of 4.2 m^3/min, resulting in an average inlet velocity of 0.64 m/s. The corresponding Reynolds number based on the hydraulic diameter of nozzle inlet was calculated as 4,200. At the outlet of the 22.1 mm particle injection tube, the airflow rate injected into the cabin was held at a constant rate of 0.05 m^3/min, resulting in an average airflow velocity of 2.27 m/s. The corresponding Reynolds number based on the injection tube diameter was 3300.

The XY view of the grid is shown in Fig. 6.8. This figure also shows the region where the grid refinement is focused. Figure 6.9 shows the 3D view of the cabin as well as the refinement region. The volume of the refinement region is less than 3% of the whole volume of the generic cabin model. The refinement region, as shown in Fig. 6.9, consists of two sub-volumes. Locations 1, 2 and 3 are located on the interface between these two sub-volumes. At the beginning, a pseudo-structured coarse mesh is generated for the cabin. This mesh is used as the base grid for the next refinements. Two approaches are followed in the refinements. In the first

approach, an attempt was made to keep the grid inside the refinement region structured with orthogonal hexahedral mesh elements; however, in the second approach, an unstructured grid with different types of mesh elements (hexahedral, tetrahedral, wedges) is used for the refining purposes. In both of the approaches the grid in other regions and sub-volumes are kept structured.

In order to check the grid independency, the velocity data calculated using different grid sizes were compared with the corresponding results from the finest grid. If this difference(deviation) experiences decreasing as the number of mesh cells increased then the solution would meet the grid independency criteria.

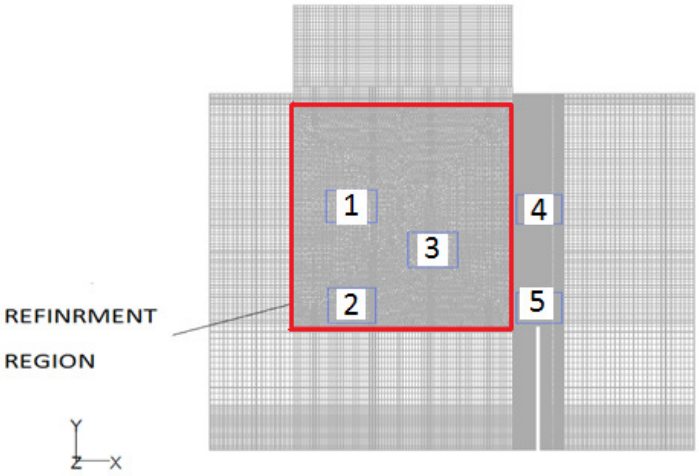

Figure 6.8 XY View of the grid. The refinement region and APS measurement locations

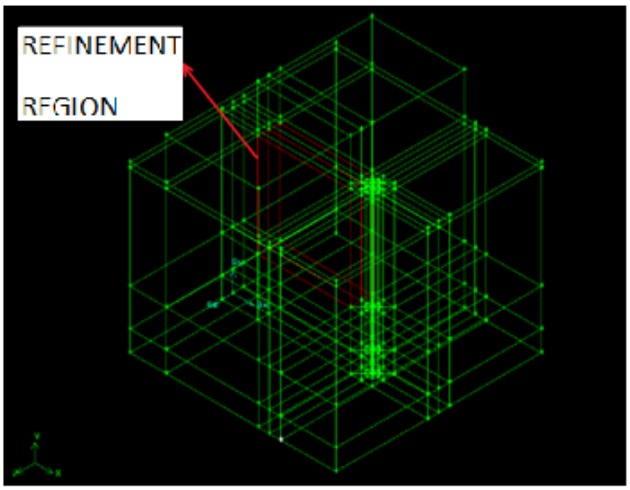

Figure 6.9 3D View of the cabin and the sub-volumes in order to create the grid. The refinement region is also marked by red edges

Figures 6.10 - 6.14 show the behavior of the results as the both approaches explained above are used in grid refining. In each figure, there are four tables and graphs. The tables and graphs in the left side of each figure show the effect of grid refinement when the structured grid refining is followed; however, the tables and graphs on the right side show the uncertainty study results when the grid is refined in the refinement region using an unstructured scheme. Each table has four columns. The first column shows the total number of mesh elements in the whole geometry. The second column shows the number of mesh cells in the refinement region. The third column shows the calculated velocity data for each grid size. And finally, the last column is the corresponding deviation percentage for each grid size which is calculated using the following equation:

$$Deviation\% = 100 \times \frac{V_{cal} - V_{cal,\,finest}}{V_{cal,\,finest}} \tag{6.16}$$

In the equation above, V_{cal} (m/s) is the calculated velocity for a specified grid size and $V_{cal,finest}$ (m/s) is the corresponding velocity calculated from the finest grid.

Figure 6.10 shows the effect of grid refinement on the behavior of x and y components of calculated velocity data corresponding to the location 1 of the APS measurement locations. It is seen that the velocity data are converged using either structured or unstructured refining scheme, however unstructured grid refinement resulted in converged velocity data for grids with smaller number of mesh cells compared to the structured refining approach.

Figure 6.11 shows the effect of grid refinement on the behavior of calculated x and y velocity data corresponding to the APS location 2. Similar to the APS location 1, it is observed that unstructured grid refining scheme is more efficient in reaching converged velocity data.

Figure 6.12 shows the effect of mesh refinement on the velocity calculations for the APS location 3. It is seen that the behavior of velocity data for this location is different from what was observed in the APS locations 1 and 2. Indeed the convergence criteria are not met for the velocities calculated for this location. In order to find a physical reason for this behavior, a special attention should be paid to the position of the APS location 3 in the cabin model (see Figs. 6.8 and 6.9). In this location, which is almost in the middle of the cabin, the flow is almost stationary and it is seen from the tables presented in this figure that the magnitude of both x and

y velocity data are very close to zero. Therefore the deviations for this location are much higher than those calculated for the locations 1 and 2.

Although the mesh refinement is focused on the refinement region that contains the APS locations 1, 2 and 3, the grid in other regions are also refined due to the mesh refinement in the refinement region. However, the refinement in other regions is not as much as that happens in the refinement region. Therefore the calculated velocity data in the APS locations 4 and 5 are also affected by the consecutive grid refinements. Figure 6.13 indicates the effect of mesh refinement on the behavior of velocity data in the APS location 4. It is seen that although this location is outside of the refinement region, using the unstructured refining scheme for the refinement region leads to reach converged velocity data for grids with less mesh element comparing to the case when the structured grid refining is used.

Figure 6.14 indicates that using unstructured grid refining in the refinement region has a very significant improvement in the convergence of the calculated x-velocity data in the APS location 5. However for y-velocity data in location 5, it shows that using either structured or unstructured grid gives results with acceptable convergence.

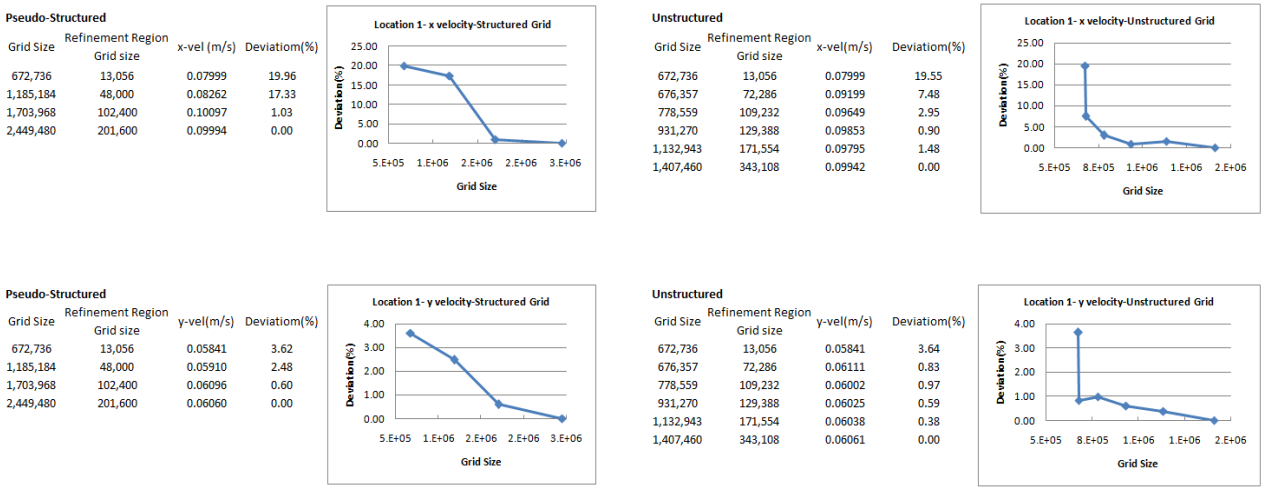

Figure 6.10 The effect of grid size on the calculated x and y components of airflow velocity corresponding to the location 1 of the APS measurement locations.

Pseudo-Structured

Grid Size	Refinement Region Grid size	x-vel(m/s)	Deviatiom(%)
672,736	13,056	-0.01282	27.16
1,185,184	48,000	-0.01425	19.03
1,703,968	102,400	-0.01482	15.80
2,449,480	201,600	-0.01760	0.00

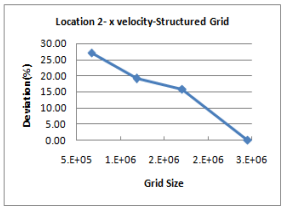

Unstructured

Grid Size	Refinement Region Grid size	x-vel(m/s)	Deviatiom(%)
672,736	13,056	-0.01282	1.75
676,357	72,286	-0.01197	8.26
778,559	109,232	-0.01235	5.35
931,270	129,388	-0.01363	4.49
1,132,943	171,554	-0.01262	3.28
1,407,460	343,108	-0.01305	0.00

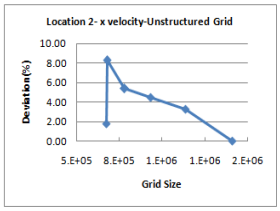

Pseudo-Structured

Grid Size	Refinement Region Grid size	y-vel(m/s)	Deviatiom(%)
672,736	13,056	0.04678	9.39
1,185,184	48,000	0.04839	6.27
1,703,968	102,400	0.05302	2.71
2,449,480	201,600	0.05163	0.00

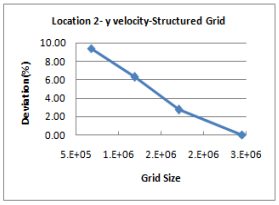

Unstructured

Grid Size	Refinement Region Grid size	y-vel(m/s)	Deviatiom(%)
672,736	13,056	0.04678	9.44
676,357	72,286	0.04798	7.11
778,559	109,232	0.05180	0.29
931,270	129,388	0.05185	0.38
1,132,943	171,554	0.05170	0.09
1,407,460	343,108	0.05165	0.00

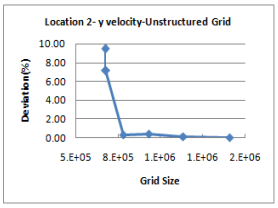

Figure 6.11 The effect of grid size on the calculated x and y components of airflow velocity corresponding to the location 2 of the APS measurement locations.

Pseudo-Structured

Grid Size	Refinement Region Grid size	x-vel (m/s)	Deviatiom(%)
672,736	13,056	0.01884	55.61
1,185,184	48,000	0.01958	53.89
1,703,968	102,400	0.03119	26.53
2,449,480	201,600	0.04246	0.00

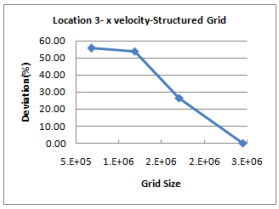

Unstructured

Grid Size	Refinement Region Grid size	y-vel(m/s)	Deviatiom(%)
672,736	13,056	0.01884	37.45
676,357	72,286	0.03047	1.13
778,559	109,232	0.02819	6.43
931,270	129,388	0.01454	51.72
1,132,943	171,554	0.02973	1.32
1,407,460	343,108	0.03013	0.00

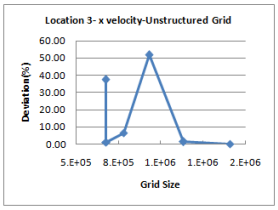

Pseudo-Structured

Grid Size	Refinement Region Grid size	y-vel(m/s)	Deviatiom(%)
672,736	13,056	-0.00266	57.50
1,185,184	48,000	-0.00681	8.63
1,703,968	102,400	0.00154	124.57
2,449,480	201,600	-0.00627	0.00

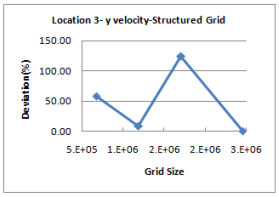

Unstructured

Grid Size	Refinement Region Grid size	y-vel(m/s)	Deviatiom(%)
672,736	13,056	-0.00266	21.18
676,357	72,286	0.00397	280.40
778,559	109,232	0.00020	108.94
931,270	129,388	-0.00246	11.76
1,132,943	171,554	-0.00351	59.59
1,407,460	343,108	-0.00220	0.00

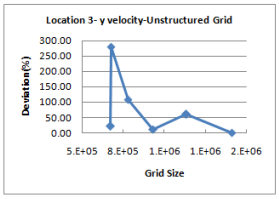

Figure 6.12 The effect of grid size on the calculated x and y components of airflow velocity corresponding to the location 3 of the APS measurement locations.

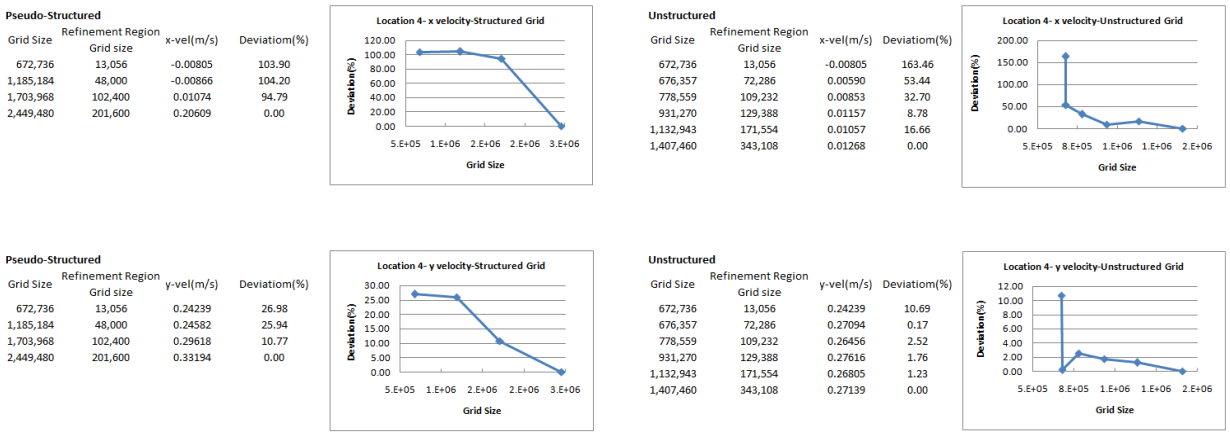

Figure 6.13 The effect of grid size on the calculated x and y components of airflow velocity corresponding to the location 4 of the APS measurement locations.

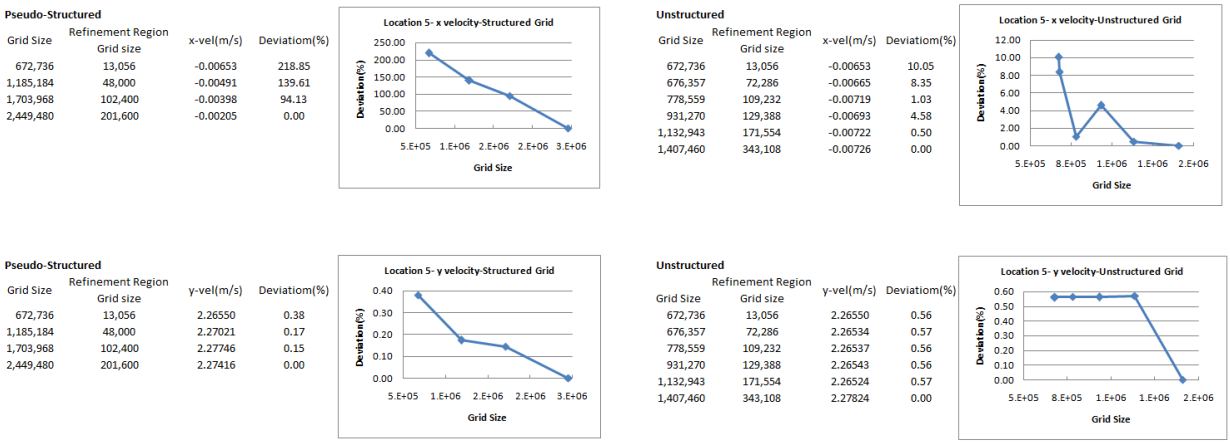

Figure 6.14 The effect of grid size on the calculated x and y components of airflow velocity corresponding to the location 5 of the APS measurement locations.

All the APS measurement locations were located on the central plane of the cabin (z=0). Due to the symmetry of the geometry as well as the boundary conditions respect to the central plane, the z-component of velocity data for the points on this plane are expected to be very close to zero and of course the computational results confirmed this expectation. Because of the very small values of z component of velocity data for the APS locations 1-5, the behavior of z-velocity data don't show a converging trend and the deviations are much larger than what were calculated for x and y components of velocity data.

From the graphs and tables presented through Fig. 6.10-6.14, the significant advantages of using the unstructured grid refining approach compared to the structured one are revealed. As shown in the above mentioned figures, in the structured grid refining approach, by 1400%

increase in the number of mesh elements in the refinement region, from 13,056 to 201, 600, the total number of mesh elements for the whole geometry is increased by 250% i.e., from 672,736 to 2,449,480. However, in the unstructured grid refining approach, the total number of mesh elements is less sensitive and by ~2500% increase in the number of mesh cells in the refinement region from 13,056 to 343,108, the total number of mesh elements experiences just a 109% growth i.e., from 672,736 to1,407,460. In the other word, the unstructured mesh refinement scheme enables us to make a high resolution grid in the refinement region with the minimum increase in the total number of mesh elements for the whole geometry. Especially when the better converging behavior of results from the unstructured grid refinement is taken into account, it can be concluded that using the unstructured grid for the local refinement purposes, not only leads to the more accurate and reliable results, but also it would be considerably more computational time and cost effective compared to the structured mesh refinement.

Figures 6.15 - 6.17 present the predictions for airflow velocity data corresponding to 5 APS measurement locations on the central plane of the cabin (see Fig. 6.2). The simulations were performed using the pseudo structured mesh with unstructured regional refinement which contains 1,407,460 mesh elements and discussed above. Both RANS (steady and unsteady) and LES methods were applied. In the RANS method, the standard k-ε was used as the turbulence model accompanied with standard wall functions as near-wall approach. Also, in these figures, the LES time-averaged predictions were compared with steady/unsteady RANS predictions. All the figures show the comparisons between predictions for the first 300 sec of the flow-time, except for x-component of velocity data in APS location 2. It can be seen that although there are differences between unsteady and steady RANS predictions in the first seconds (~100sec) of the flow time but eventually the unsteady RANS predictions merge to some value very close to the steady RANS predictions and remain constant as the flow-time progresses. It is also observable that, except for APS location 4, the LES time-averaged predictions is very close to steady/unsteady RANS predictions especially for flow-times greater than 50 sec.

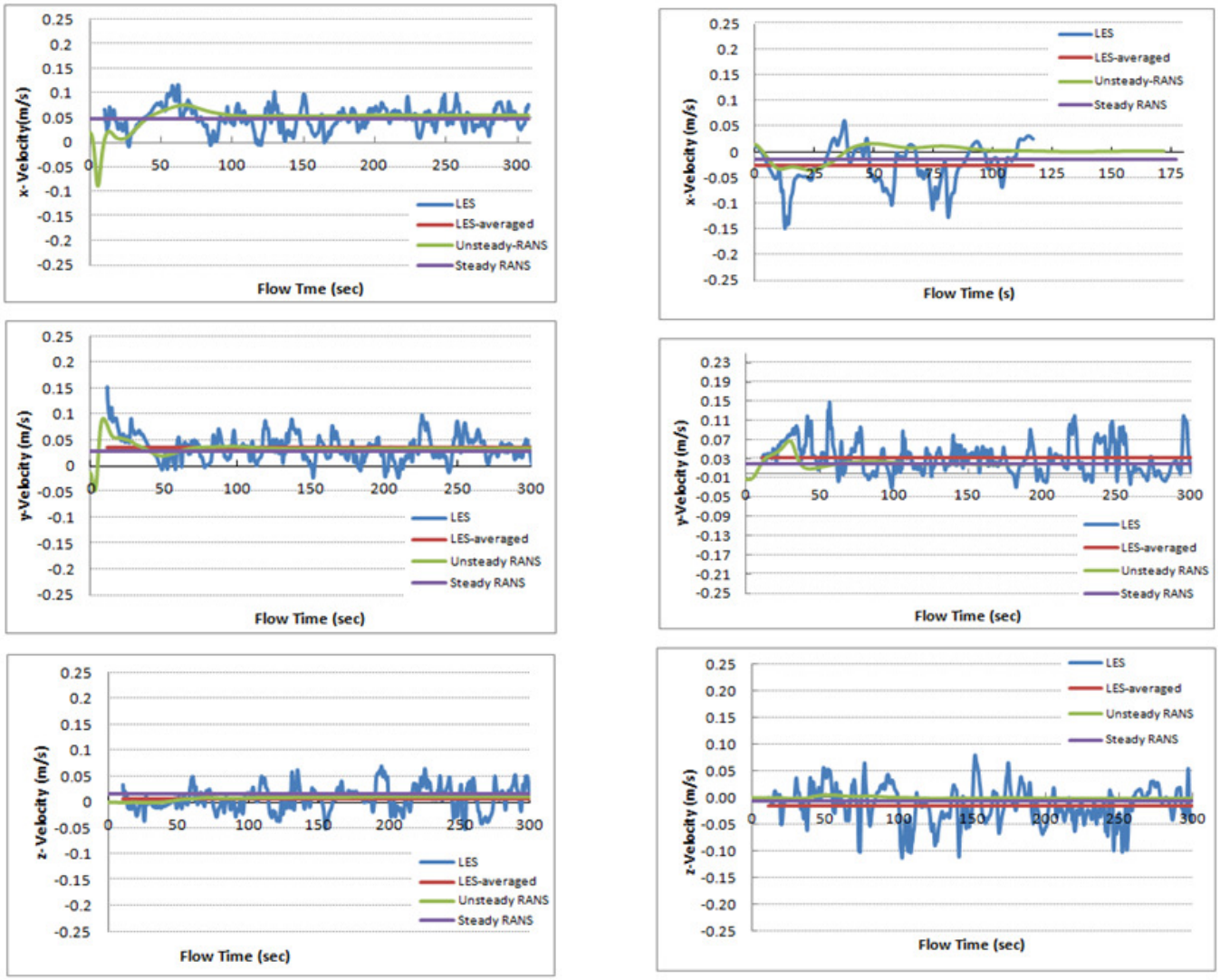

a: APS Location 1

b: APS Location 2

Figure 6.15 Prediction of airflow velocity data in APS locations 1 and 2 (see Fig. 6.2) on the central plane of the cabin with straight particle injection tube

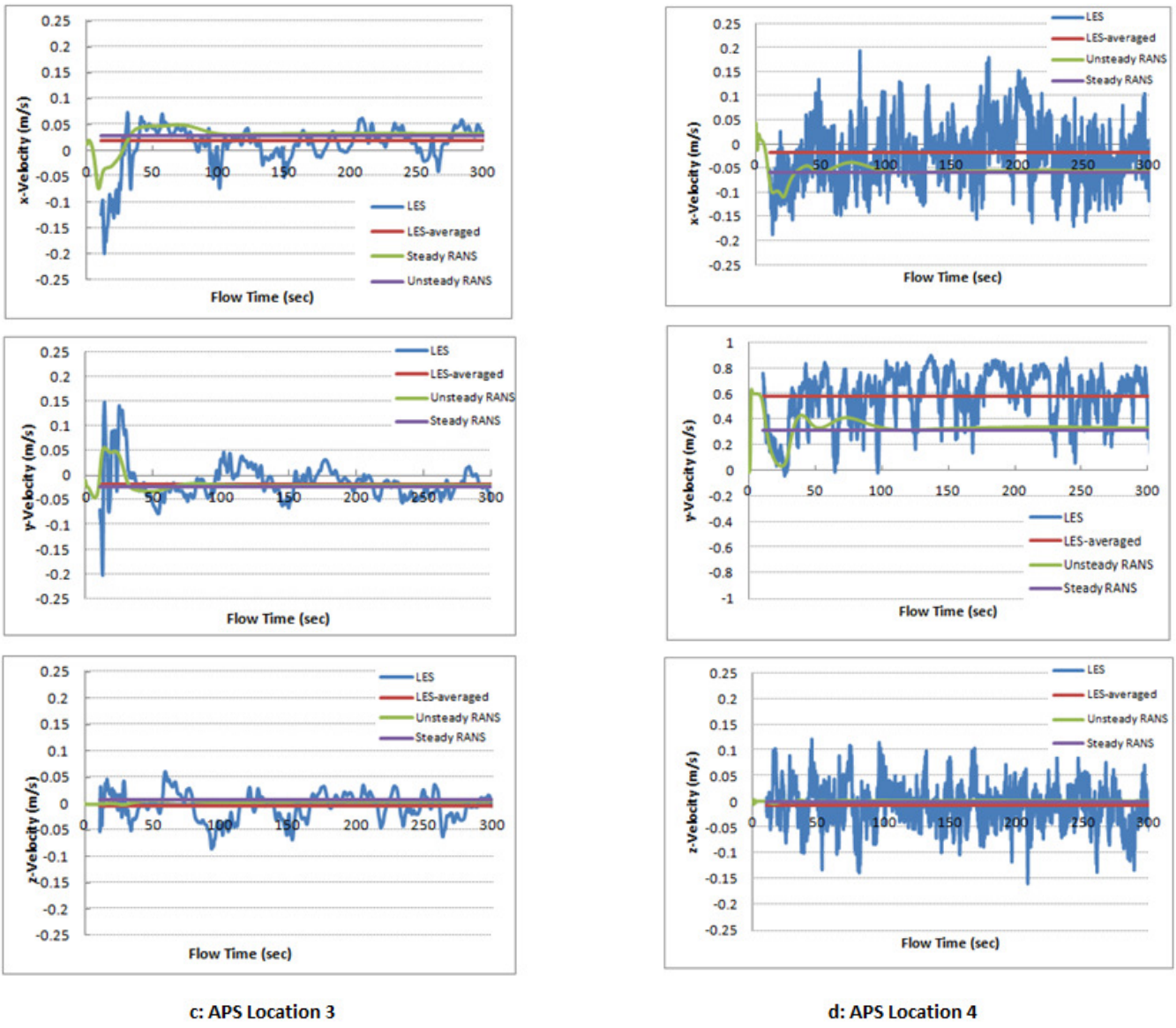

c: APS Location 3

d: APS Location 4

Figure 6.16 Prediction of airflow velocity data in APS locations 3 and 4 (see Fig. 6.2) on the central plane of the cabin with straight particle injection tube

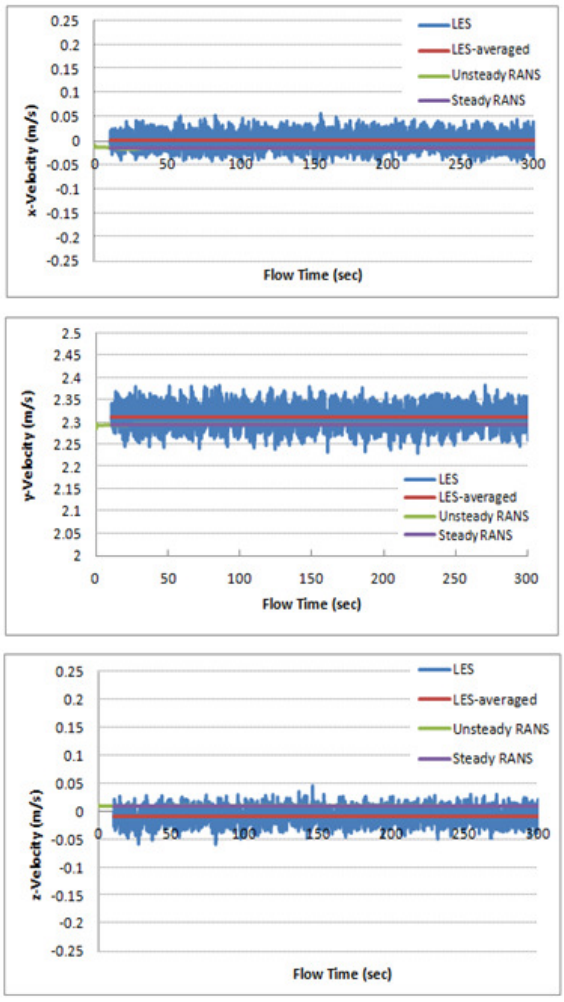

Figure 6.17 Prediction of airflow velocity data in APS location 5 (see Fig. 6.2) on the central plane of the cabin with straight particle injection tube

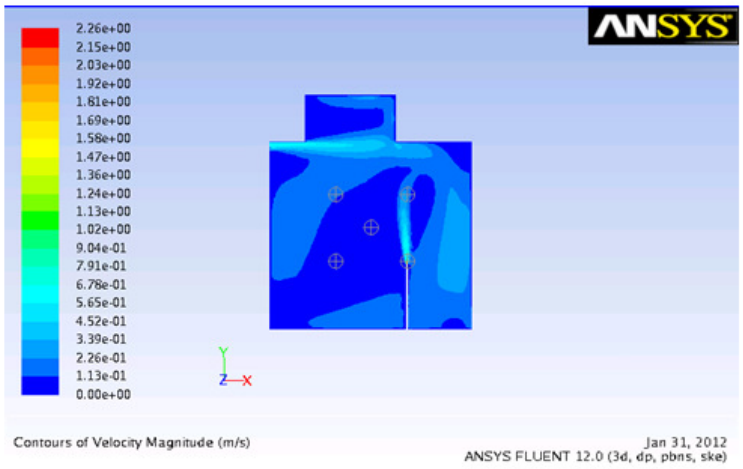

Figure 6.18 Airflow velocity magnitude (m/s) contours on the central plane (z=0) of the generic cabin model calculated using steady RANS method

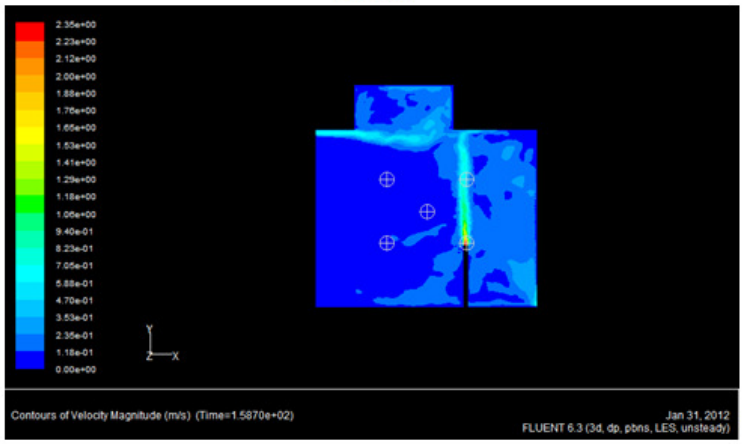

Figure 6.19 Airflow velocity magnitude (m/s) contours on the central plane (z=0) of the generic cabin model at flow-time=158.7 sec, calculated using LES method

In APS location 4, there is a considerable difference (up to ~150%) between x and y airflow velocity components predicted by steady/unsteady RANS and the corresponding LES time-averaged predictions. It is seen that comparing to LES, RANS estimates algebraically less values for x and y velocity components. This difference can also be recognized from the contours of airflow velocity magnitude on the central plane of the cabin (z=0) predicted by RANS and LES shown in Figs. 6.18 and 6.19. As can be seen from these two figures, APS location 4 is close to the region where the jet that comes from the inlet air nozzle meets the jet that comes from the particle injection tube. That makes the flow structure in that region much

more complex than other locations. Since LES, in its essence, is a more accurate and sophisticated method than RANS, it is the k-ε model that is not able to capture all the flow characteristics in the APS location 4. Although (for the DPM simulations presented herein) the quasi-steady airflow velocity data (calculated from RANS) was applied to initialize particle tracking calculations, based on what was explained above, in order to get more accurate results it is recommended to use LES quasi-steady solutions to initialize DPM calculations.

6.4.1.2. DPM Simulation results for the particles concentration data: Study the effect of number of tries

As explained earlier, the inert Di-Octyle Phthalate (DOP) spherical particles are injected continuously through the top end surface of the particle injection tube (surface injection). The vertically upward velocity of the injected particles, at the injection surface, is uniform and equals to 2.27 m/s. The concentration of particles at the injection port is 54 particle/cm^3. There are three sets of experimental measurements, entitled: test 2-APS, test 3-APS, and test 5-APS, used in order to evaluate the simulations. The uncertainty of the experimental data is around ±39%. Because of some deficiencies in measuring the particles injection at APS location 5, the comparison between the computations and measurements does not include this location and was just made for the APS locations 1, 2, 3, and 4. The finest unstructured grid with 1,407,460 mesh elements (which was discussed earlier in the grid independency study) was picked to be used in the simulations. Figure 6.20 shows an evaluation of the explained computational simulation by comparing the model predictions with the corresponding experimental measurements for the APS locations on the central plane of the cabin (see Figs. 6.2 and 6.2). In this figure the concentration data were normalized using Eq. (6.1). As discussed previously in the particle-turbulence interaction section, the accuracy of results depends on the number of tries. Different numbers of tries were examined and the corresponding simulation results were shown in Fig. 6.20. The tested numbers of tries were: 10, 50, 100, 120, 150, 175, 200, and 225. Considering the uncertainty bars for the experimental data, it is seen that the model gives results with acceptable accuracies at least for APS locations 2, 3, and 4. Table 6.4 shows the tabular outcomes of the investigation about the effect of number of tries on the accuracy of predicted particle concentration for the APS locations on the cabin's central plane. It is seen that there is

not a unique optimum value for the number of tries that leads to the most accurate results for the all APS locations.

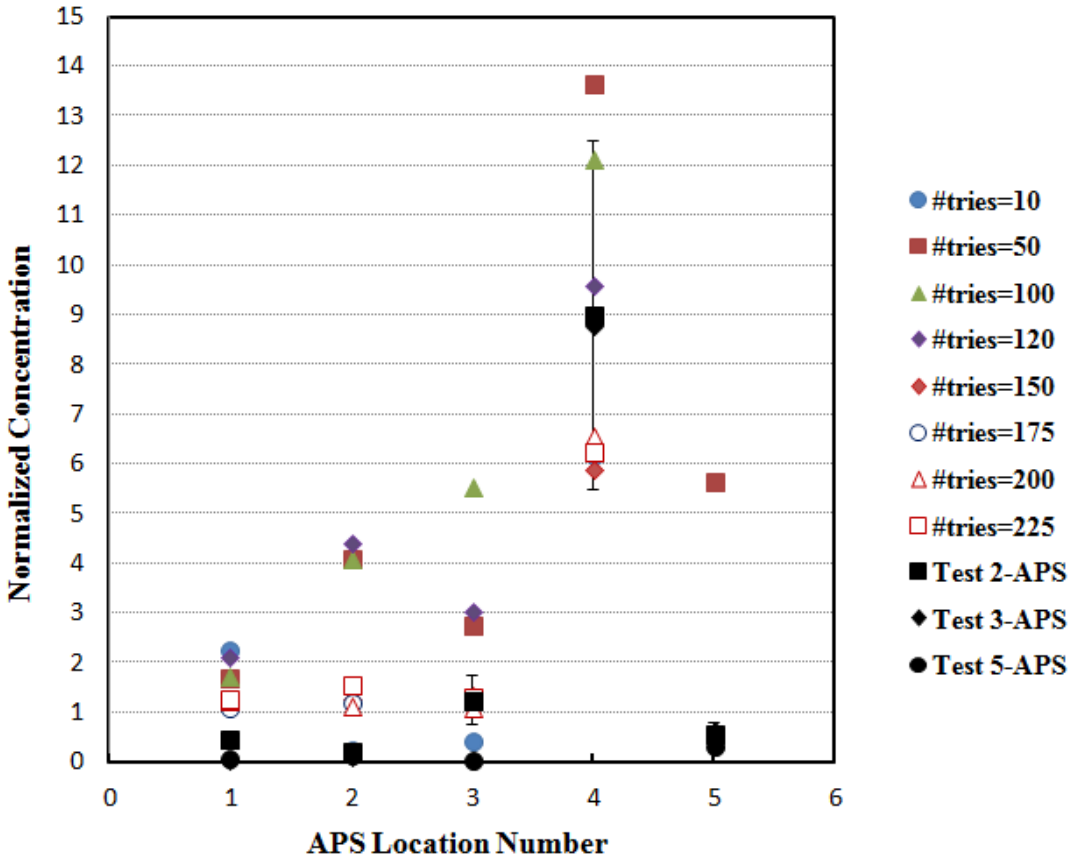

Figure 6.20 Comparisons between the computational predictions (calculated using 8 different numbers of tries) and the corresponding experimental measurements for the APS location on the cabin central plane (see Fig. 6.2).

Table 6.4 Effect of number of tries on the accuracy of predicted particle concentration data for the APS locations on the cabin central plane.

APS location number	The reference experimental test title	The number of tries corresponds to the minimum error	Minimumm error (%)
1	Test 2-APS	175	137
2	Test 2-APS	10	6.2
3	Test 2-APS	175	0.5
4	Test 2-APS	120	6.7

Another evaluation of DPM simulations is presented in Fig. 6.21 in which the predicted particle concentrations at different sampling points located at the outlet of the cabin are compared with the corresponding experimental measurement. Since the Optical Particle Counter (OPC) was used in order to measure the particle concentration at the cabin outlet, the 11 measurement locations at the outlet (see Fig. 6.1) are also called OPC locations. The same numbers of tries were tested for the APS locations, are also examined for the OPC locations. Figure 6.21 indicates that how increasing the number of tries from 10 to 150 improves the average accuracy of the predictions, however, for the numbers of tries beyond 150 no more improvement is experienced. Amongst the examined number of tries (i.e. 10, 50, 100, 120, 150, 175, 200, and 225), the least average error is achieved when 150 is selected as the number of tries. The average error corresponding to this number of tries is 169%. This figure also implies that the simulation results are closer to the measurements for the OPC sampling points located in $z>0$ region.

Figure 6.22 shows the effect of number of tries on the arithmetic average of computational errors in calculating particle concentration for APS locations, OPC location, and all the measurement locations (including both APS and OPC locations). The graph shown in this figure can give us an idea about the optimum number of tries which leads to predictions with the least arithmetic average errors for all particle measurement locations. Of course, it should be mentioned that the optimum number of tries that leads to the particle concentration predictions with the minimum average errors for all the APS and OPC locations is not necessarily equals to the number of tries which tends toward the most accurate prediction for every single APS or OPC measurement location. This figure implies selecting 150 as the number of tries gives the most accurate prediction rather than other number of tries. The average error corresponding to this number of tries is 160%.

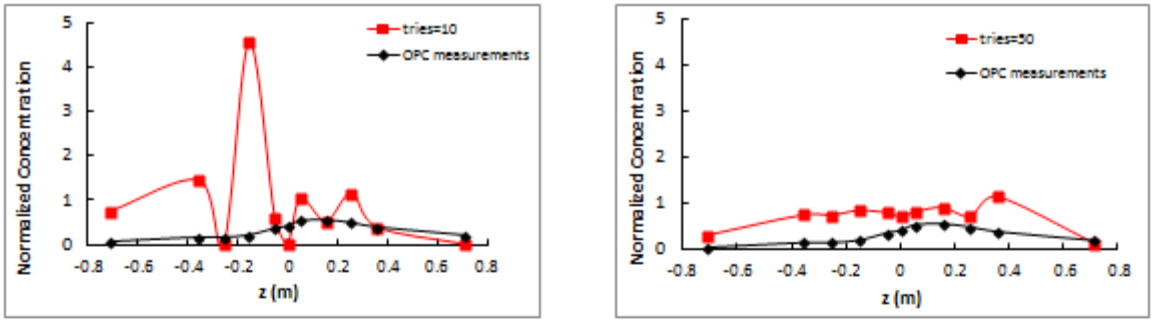

a: Number of tries=10

b: Number of tries=50

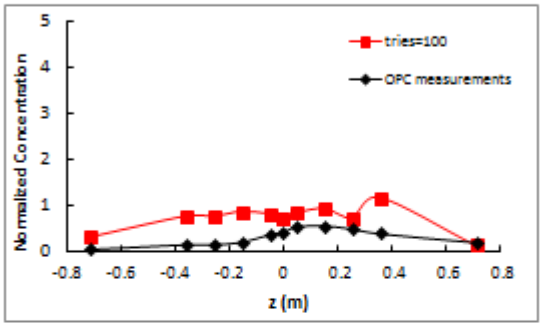

c: Number of tries=100

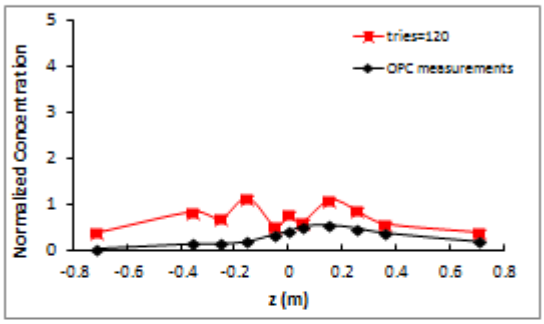

d: Number of tries=120

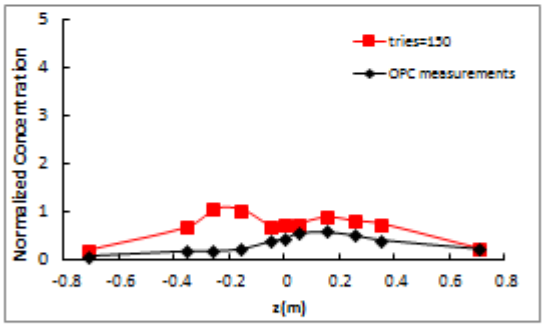

e: Number of tries=150

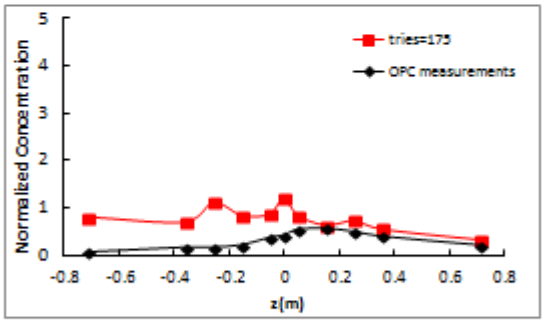

f: Number of tries=175

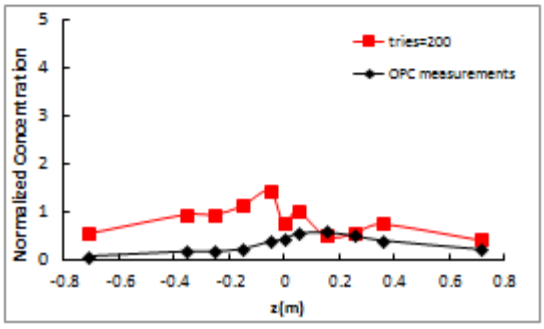

g: Number of tries=200

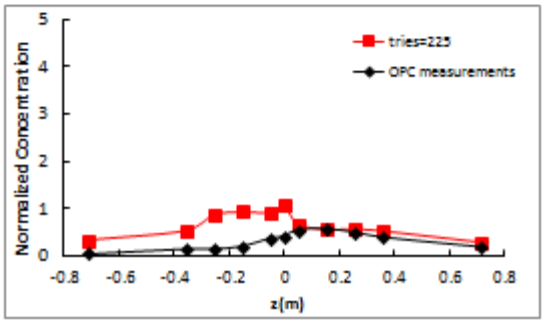

h Number of tries=225

Figure 6.21 Comparisons between the computational predictions (when different numbers of tries are examined) and the corresponding experimental measurements for the OPC location at the cabin outlet (see Fig. 6.1).

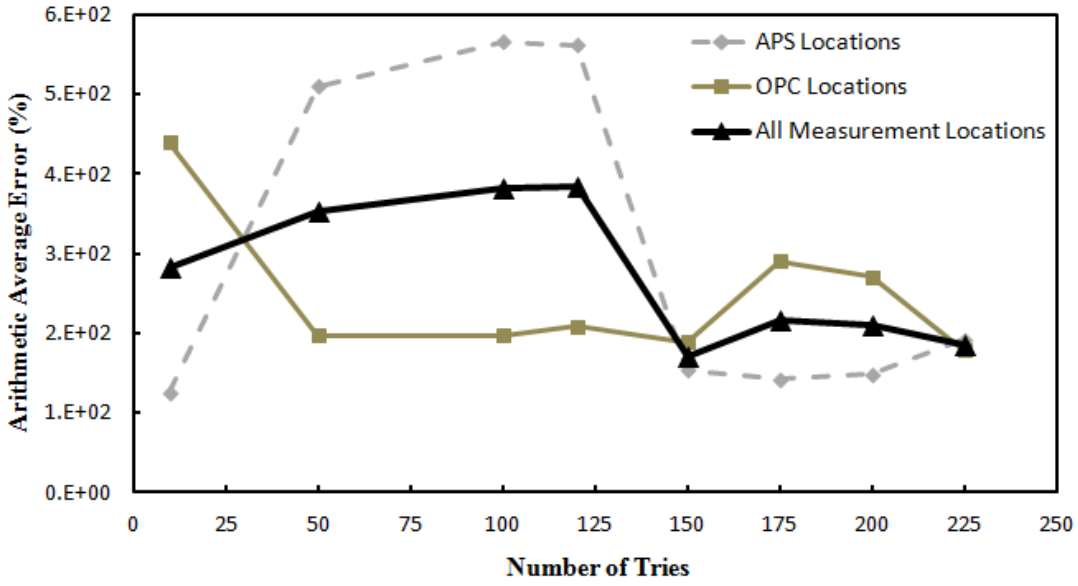

Figure 6.22 Comparisons between the arithmetic average errors for the predicted particle concentration data corresponding to the APS, OPC, and all the particle measurement locations when different numbers of tries are examined. Eight different numbers of tries were examined in this comparison: 10, 50, 100, 120, 150, 175, 200, and 225.

6.4.1.3. Study the Effect of Micron Particle Size

Padilla (2008) studied the effect of particle size on dispersion behavior of micron particles experimentally. For this purpose the particle measurement experiments, explained in section 6.2 of this chapter, were performed for two different sizes of particles: 3µm and 10µm. Except from the particle size, all the other experimental conditions and parameters were kept unchanged. Through the comparison of normalized concentration measurements, it was realized that particles with smaller size show more uniform concentration distribution and they are mixed with the airflow better than larger particles. In this part, DPM simulations are repeated for particles with 3µm diameter. The simulations are validated through the comparison of predictions with corresponding APS measurements. In order to repeat the steady RANS-steady particle tracking simulations for the dispersion of 3µm particles, all the calculations for the specified injection properties and concentration normalizations should be revised. Table 6.5 presents similar to the simulations preformed for 10µm particles. Dispersion of 3µm particles are

modeled considering particles as inert particles injected through a surface injection type, and their effects on the continuous phase are taken into account (two-way coupling).

The comparison between predictions and corresponding measurements (Test 2-APS) are presented in Fig. 6.23. The uncertainty of measurements for 3μm particles is ±20%. The best agreement between measurements and predictions was seen for location 4 (45% deviation between the predictions and measurements, see also Table 6.6). Figure 6.23 also shows a comparison of the simulation results for 10 μm particles with corresponding Test 2-APS measurements. The uncertainty of measurements for the 10μm particles is ±39%. Except for the size of particles all the other simulation parameters are the same for both cases. Similar to the 3μm particles, minimum deviations between predictions and measurement are seen for the APS location 3 (~9% deviation between the predictions and measurements, see also Table 6.6). Tables (6.6) indicate that, excluding the APS location 5, the average of errors for the 3μm particles is considerably less than that for 10μm particles. In the other word; based on the steady RANS- steady particle tracking simulations presented in this section, the agreement between predictions and measurements experienced an improvement for decreased particle size.

In addition, computational simulations shown in Fig. 6.23 confirm the outcomes of the experimental research conducted by Padilla (2008) in which, as mentioned above, it was concluded that smaller particles have better mixing behavior with the airflow circulations in the cabin and distributed more uniformly that larger particles.

Table 6.5 Comparison of injection setup parameters for 3 and 10 micron particles

Particle Size	3 micron	10 micron
Rate of the particle counts injected into the cabin (particle/sec)	46,800	46,800
Count concentration of particles at the injection-port(particle/cm^3)	54	54
Mass concentration of particles at the injection-port (kg/m3)	2.75E-05	7.41E-07
Mass flow rate of injected particles (kg/sec)	2.38E-08	6.42E-10
Injection velocity of particles(m/sec)	2.27	2.27
Volume Fraction at the injection-port	7.60E-10	2.83E-08

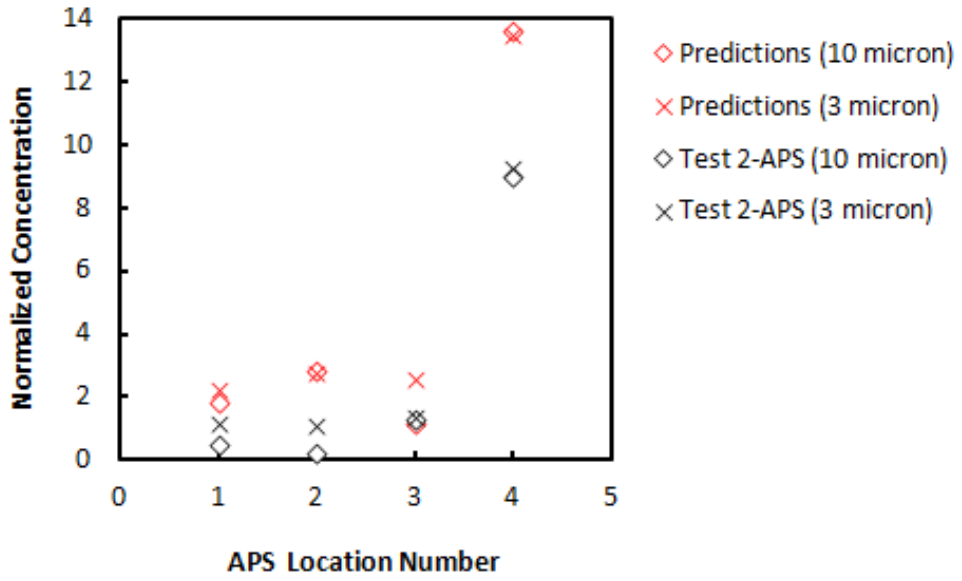

Figure 6.23 Comparison between predictions and corresponding measurements for 3 and 10 micron particles (2-way coupling, DRW model with number of tries=175, inert particles, and surface injection)

Table 6.6 Comparison between computational errors for two cases of 3 and 10 micron particles

Surface Injection
Inert particles
Two-Way
RANS: Standard ke - Standard WF
DRW: tries=175

10 micron

APS Loc	Concentration (kg/m3)	Normalized Coefficient	Normalized
1 LOCATION 1	6.20E-07	2.95E+06	1.83E+00
2 LOCATION 2	9.58E-07	2.95E+06	2.83E+00
3 LOCATION 3	3.90E-07	2.95E+06	1.15E+00
4 LOCATION 4	4.62E-06	2.95E+06	1.36E+01
5 LOCATION 5	2.13E-05	2.95E+06	6.29E+01

Normalized Measurements

test 2-APS	test 3-APS	test 5-APS
0.458438	0.0625752	0.0702411
0.2408745	0.127758	0.164796
1.26071	0.0625752	0.0567332
9.00504	8.79703	8.94493
0.589421	0.649218	0.326891

ERROR%

test 2-APS	test 3-APS	test 5-APS
2.99E+02	2.83E+03	2.51E+03
1.07E+03	2.11E+03	1.62E+03
8.83E+00	1.74E+03	1.93E+03
5.13E+01	5.49E+01	5.23E+01
1.06E+04	9.60E+03	1.92E+04
error-average **3.58E+02**	1.68E+03	1.52E+03

Exclude Loc 5

3 micron

	Computations	Normalized Coefficient	Normalized
1 LOCATION 1	2.05E-08	1.09E+08	2.24E+00
2 LOCATION 2	2.53E-08	1.09E+08	2.76E+00
3 LOCATION 3	2.35E-08	1.09E+08	2.57E+00
4 LOCATION 4	1.23E-07	1.09E+08	1.35E+01
5 LOCATION 5	5.82E-07	1.09E+08	6.36E+01

Normalized Measurements

test 1-APS	test 2-APS
1.06415	1.17736
1.08679	1.06415
1.60755	1.38113
7.76604	9.26038
3.41887	2.49057

ERROR%

test 1-APS	test 2-APS
1.11E+02	9.06E+01
1.54E+02	1.59E+02
5.98E+01	8.60E+01
7.34E+01	4.54E+01
1.76E+03	2.46E+03
error-average 9.95E+01	**9.53E+01**

Exclude Loc 5

6.4.1.4. Study the effect of discrete and continuous phase coupling

As it was discussed previously in section 6.3, the discrete phase affects the continuous phase flow through the last term of Eq. (6.5). When the effect of particle movement on the continuous phase flow is taken into account, the solution is called two-way coupling. However, in some DPM simulations, in which the discrete phase is very dilute, it is a reasonable assumption if the effect of discrete phase on the continuous phase is neglected. This simplified solution, which is performed through dropping off the last term in Eq. (6.5), is called one-way coupling. Although all the DPM simulations presented in this chapter are two-way coupling, in order to investigate the validity of the above mentioned assumption and study the effect of using one-way coupling on the quality of results comparing to two-way coupling, the one-way coupling DPM simulation was performed for 10 micron particles and the resulting predictions were compared with corresponding two-way coupling simulations as well as with the APS measurements. All the simulation parameters remained the same for the two types of simulations: one-way and two-way coupling. Figure 6.24 shows these comparisons in which no difference is recognizable between one-way and two-way coupling simulation results. Considering the volume fraction of particles at the injection surface which is ~ 3×10^{-8} (see Table 6.5), it makes sense why particles have no effect on the continuous phase flow.

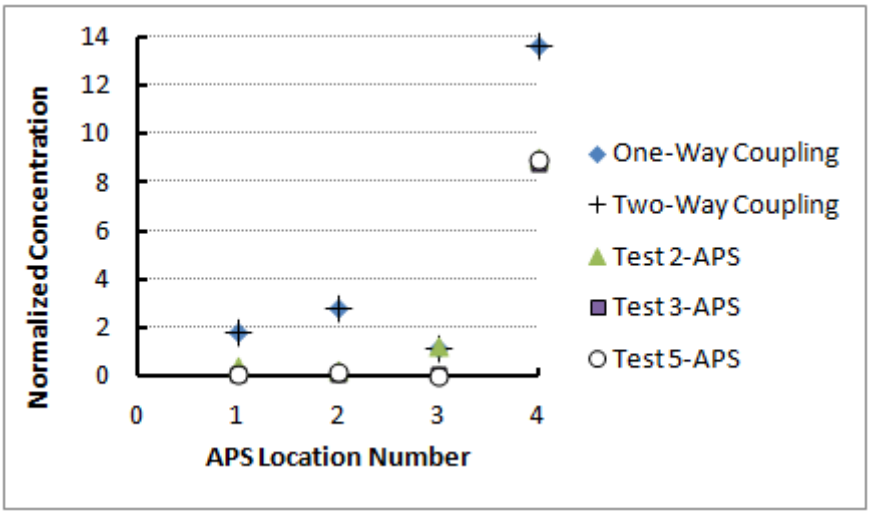

Figure 6.24 Comparisons between one-way and two-way coupling DPM simulations and their validation through the comparison with APS measurements. (DRW model with number of tries=100, inert particles, and surface injection)

6.4.2. Study of turbulent particle injection in generic cabin mockup with cone diffuser

In the first part of this section, the DPM simulation results for the mono-disperse particles injected into the cabin through the straight tube were presented and discussed. In that configuration, dispersion of particles was considerably influenced by their high injection velocity as well as the strong jet of carrier air from the straight tube. As it was elaborately discussed in section 6.3, in order to eliminate the effects of high injection velocity of particles and carrier air on dispersion mechanism of particles and focus the study on the investigation of the effect of air recirculation produced by the cabin air ventilation system on dispersion of particles, the injection tube was replaced by a cone diffuser such that the injection velocity of particles at the injection surface was decreased to very small values (the carrier air flow-rate as well as the particles mass flow-rate remained at the same values as those for the injection through the straight tube). This part, which is dedicated to the cabin with cone diffuser, starts with a grid independence study performed for the airflow velocity data. The RNG k-ε turbulence model and Non-equilibrium wall functions at the near-wall were used for the airflow simulations. Then, similar to what was carried out for the first injection configuration; a detailed study was carried out to see whether it was possible to find an optimum number for the number of tries in DRW model which would lead to the best quality predictions. For this purpose different numbers of tries were examined and the simulations were validated through comparisons between predictions and measurements for particle concentration data. Since the available measurement data correspond to two different inside cabin pressures, the simulation validations as well as the investigation about the optimum number of tries were performed for both cases of cabin inside pressures. Subsequently, the effect of cabin pressure gradient was studied through the comparison of particle concentration measurements and predictions at specified monitoring locations in the cabin between two cases of cabin inside gage pressures of 0 and 0.025 in of H_2O. Uncertainties about the exact value of the density of particles have been one of the challenges encountered in the simulation of particles motion. This necessitated the investigation of quantitative and qualitative effects of particles density on their distribution behavior for the range of particle size studied in this dissertation. The results of this study are also presented and discussed in this part through the comparison of DPM simulation results from examining different values for particle density with corresponding experimental data. The effect of particle

density in transport of particles is also investigated both numerically and theoretically through the consideration of particles as a continuous phase and application of species transport equation.

6.4.2.1. Grid independency study

In order to generate the computational grid for the cabin with the cone diffuser inside it, the whole volume was divided into 55 sub-volumes. As it is shown in Fig. 6.25, from the created 55 sub-volumes, 49 sub-volumes were just simple cubes, 2 sub-volumes located exactly above the particle injection surface were cylinders, and the remaining 4 sub-volumes which encompassed the cone diffuser side surface and the cylindrical sub-volumes had more complicated three-dimensional shapes. For the cubic sub-volumes, the Map-type structured grids with orthogonal hexahedral mesh elements were generated. For the cylindrical sub-volume located immediately above the cone diffuser (the particle injection surface was the bottom end surface of this sub-volume), a Cooper-type mesh with hexahedral and wedge elements was used as the scheme to generate the unstructured grid. For the rest of the sub-volumes, the generated grid was an unstructured TGrid-type with tetrahedral and hybrid mesh elements. Every one of the sub-volumes was connected to its neighboring sub-volumes computationally through the interior faces.

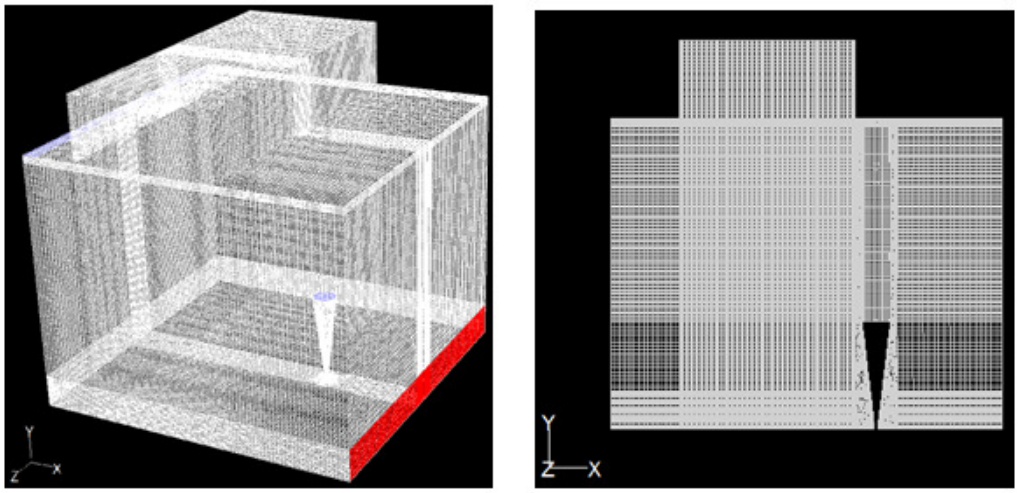

a: 3D View b: 2D XY View

Figure 6.25 3D and 2D views of the computational grid generated for CFD simulations in the generic cabin with cone diffuser

In order to evaluate the model for grid independency purposes, the airflow velocity field was calculated using four grids with different numbers of mesh elements. The numbers of mesh elements in the tested four grids were 306900, 567300, 1024936, and 2245000. The coarsest grid, which contained 306900 mesh elements, was generated first and was considered as the base-grid for the next successive grid refinements in x, y and z directions that led to producing the other tested grids. Given the facts that the velocity of carrier airflow at the injection surface of cone diffuser is very small (0.0478 m/s), and the cabin air ventilation system is exactly the same as what was discussed in chapter 4 (for the cabin with full-height nozzle), although the geometry of the flow-field in the cabin with cone diffuser is not exactly the same as that for the empty cabin (with no diffuser), one can expect that the airflow in the cabin with the cone diffuser would show a behavior similar to what was observed previously for the empty cabin with full-height inlet air nozzle. Therefore, using the outcomes of the study presented in chapter 4, in order to perform the RANS simulation of turbulent airflow in the cabin with cone diffuser, the RNG k-ε model was used along with Non-equilibrium wall functions. Figure 6.26 shows the deviations in the RANS predicted x and y components of airflow velocity data corresponding to the APS locations on the cabin central plane as the number of mesh cells increases. In order to calculate the deviations presented in this figure, Eq. (6.16) was applied. The graphs indicate the converging behavior of x and y airflow velocity components. Since the z-velocity data for the locations on the central plane are very close to zero, even a very small change in the z velocity components due to use of different grid numbers, can produce large deviations preventing the z-velocity data from showing converging behavior. For this reason the corresponding deviations graph for the z velocity data in Fig. 6.26 are not presented. The airflow velocity deviations for the APS location 3 are not shown in Fig. 6.26 due to a similar problem. As can be seen from Fig. 6.27, which shows the contours of airflow velocity magnitude on the central plane of the cabin, APS locations 3 is in a region where the flow is almost stationary and the velocity components are very close to zero which makes it very difficult to see converging behavior for the airflow velocity data in this location. Figure 6.26 also shows that the x-components of velocity data in the selected APS locations exhibit better converging behavior than the y-components of velocity data.

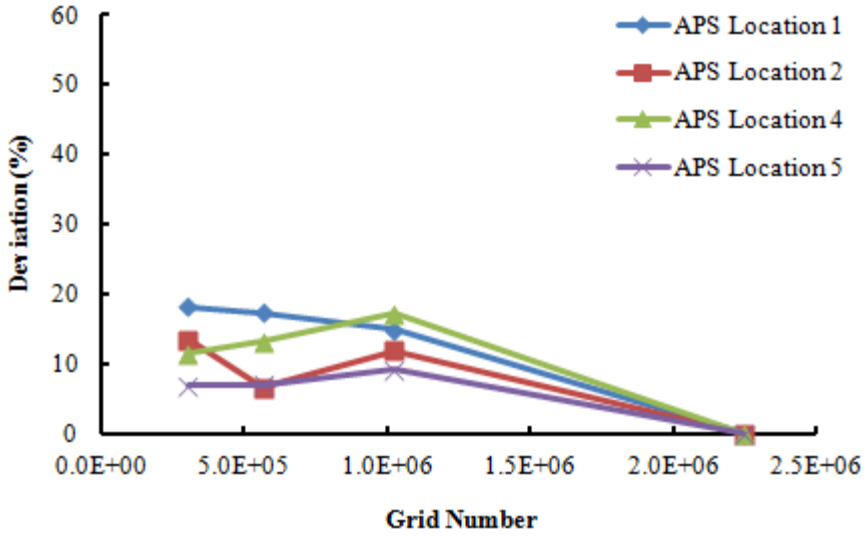

a: x-Compenent of airflow velocities

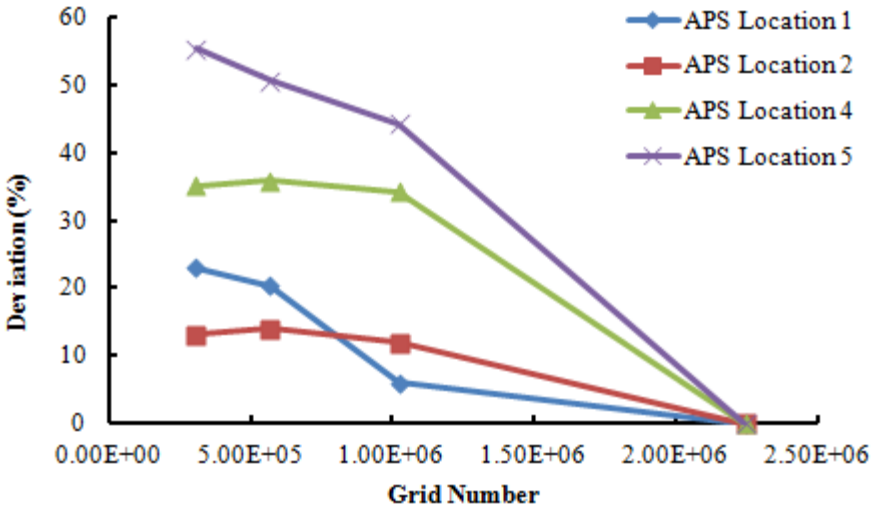

b: y-Compenent of airflow velocities

Figure 6.26 The converging behavior of x and y components of airflow velocity deviations with respect to the corresponding prediction from the finest grid for all the APS measuring locations on the cabin central plane (z=0).

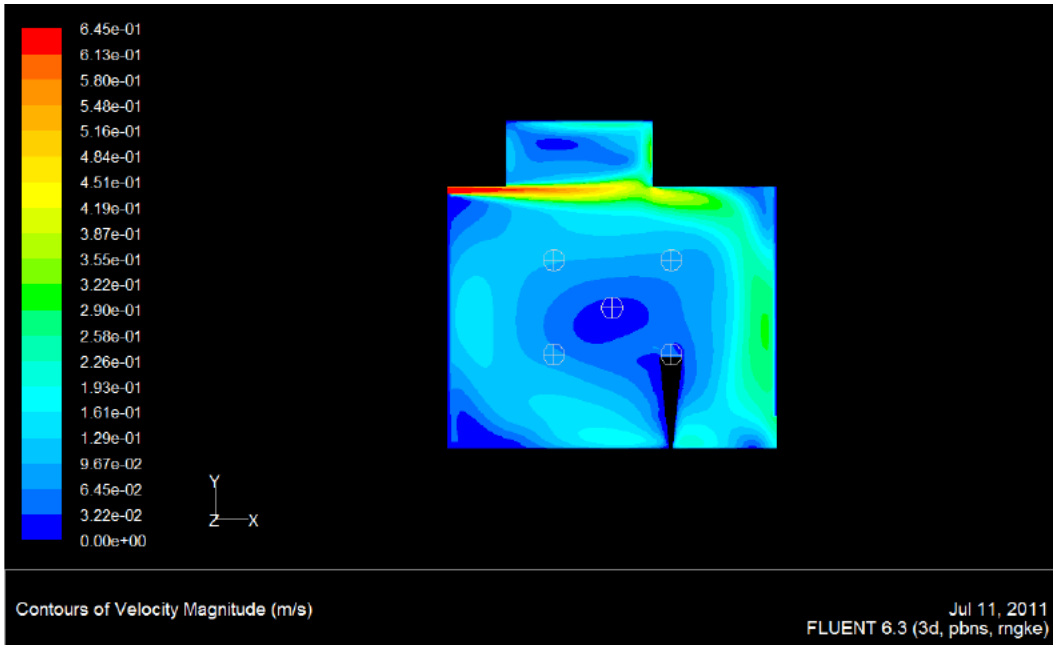

Figure 6.27 The contours of airflow velocity magnitude on the central plane of the cabin (z=0). The 5 APS locations are also shown. The wake region behind the cone diffuser can increase the instabilities in the flow structure at the middle of the cabin (around the APS location 3 on the cabin central plane).

6.4.2.2. Validation of DPM simulations for the cabin with zero pressure gradient: Exploring optimum value for the number of tries

As it was shown in Fig. 6.7, unlike the cabin with the straight particle injection tube, the APS measurements for the cabin with the cone diffuser were not limited to the locations on the central plane. Figures 6.28 and 6.29 present the comparisons between DPM predictions and APS measurements for the 25 APS measurement locations distributed among the five planes A through E (see Fig. 6.7). Seven different numbers of tries were examined in order to find an optimum number that leads to the most accurate results. The tested numbers of tries were 50, 100, 150, 175, 200, 225, and 350. In Fig. 6.28 and 6.29, for each APS location, the DPM prediction from the two numbers of tries that led to the best quality results were compared with the corresponding experimental data. In Fig. 6.30, the DPM results for the particle concentration at the cabin outlet (see Fig. 6.1) were compared with the two series of corresponding OPC

measurements. Similar to Figs. 6.28 and 6.29, the predictions shown in Fig. 6.30, were calculated using the two numbers of tries that leaded to the most accurate results.

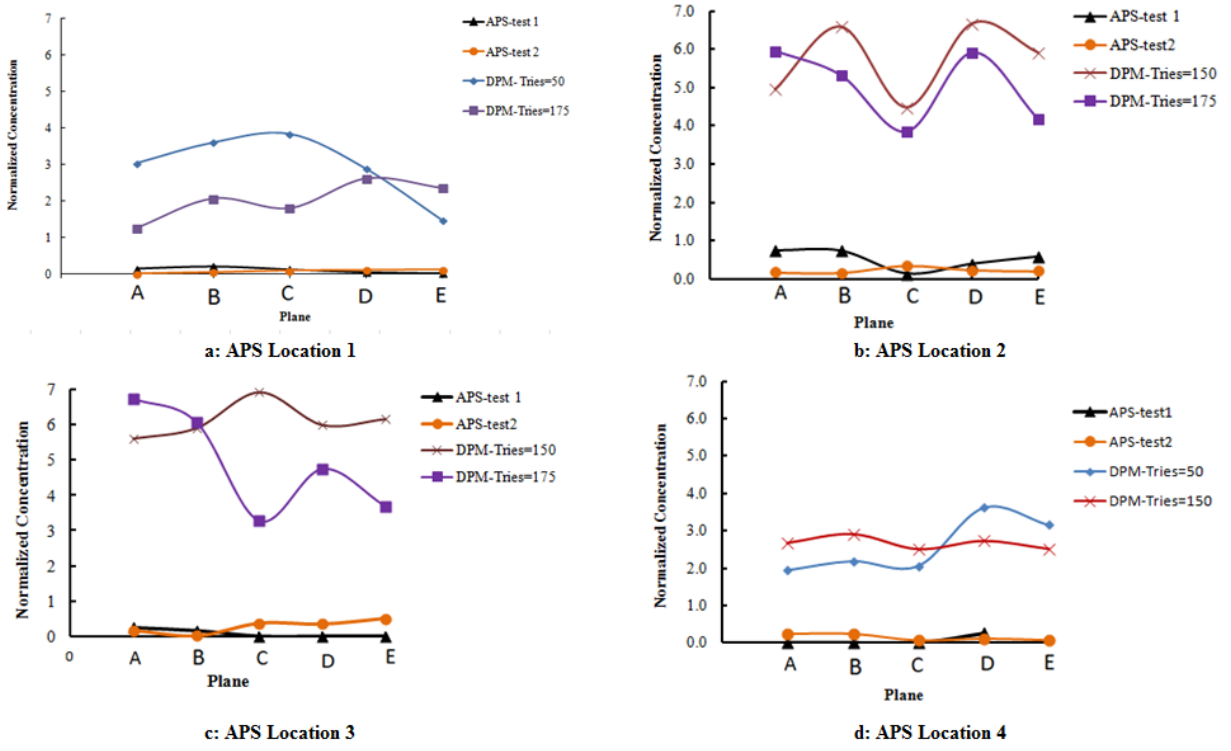

Figure 6.28 Comparison of DPM predictions and APS measurements for the APS locations 1-4. The cabin gage pressure is zero.

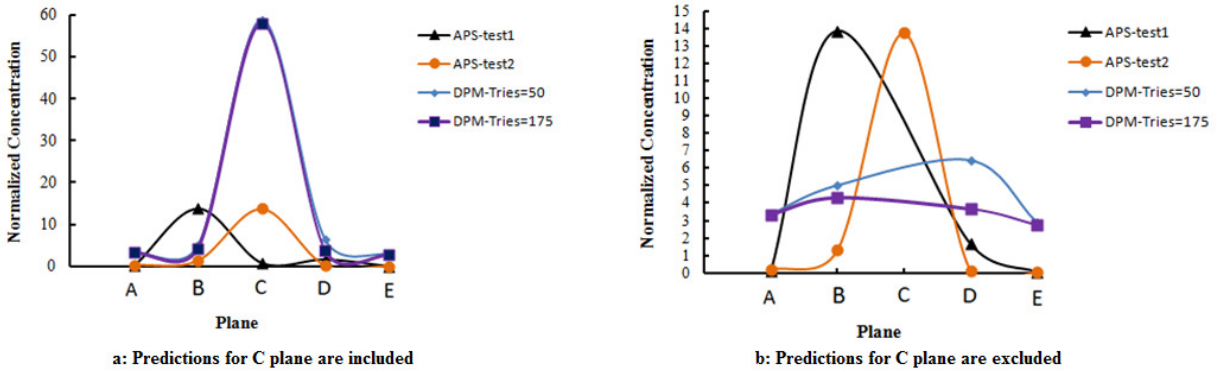

Figure 6.29 Comparison of DPM predictions and APS measurements for the APS location 5. The cabin gage pressure is zero.

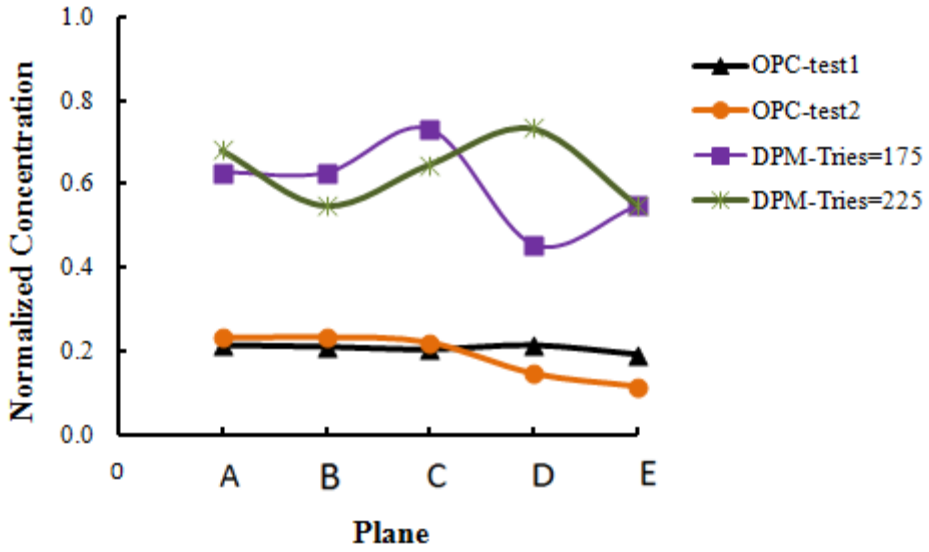

Figure 6.30 Comparison of DPM predictions and OPC measurements for the OPC locations at the cabin outlet. The cabin gage pressure is zero.

From the above figures, it can be seen that amongst the tested numbers of tries, 175 led to the best prediction for all APS and OPC locations except from APS location 4. Figures 6.28 and 6.29 also indicate that 50, 150, and 175 are the three numbers of tries that produce relatively better predictions for the particle concentration at APS locations. For OPC location the optimum numbers of tries are 175, and 225. Considering all the APS planes (A through E), the minimum average differences between DPM predictions and APS measurements were observed for the APS locations 1 and 4 (see Fig. 6.28). If we exclude plane C from our evaluations, it can be seen from Fig. 6.29b that at APS location 5, the predictions have the best agreement with the measurements. Fig. 6.30 indicates that compared to APS measurements; there is considerably better agreement between DPM predictions and OPC measurements for the locations at the outlet of the cabin. Figure 6.31 a-e, shows the contours of particle count concentration for planes A-E. These contours can help us to understand how the injected particles are propagated along the z direction of the cabin.

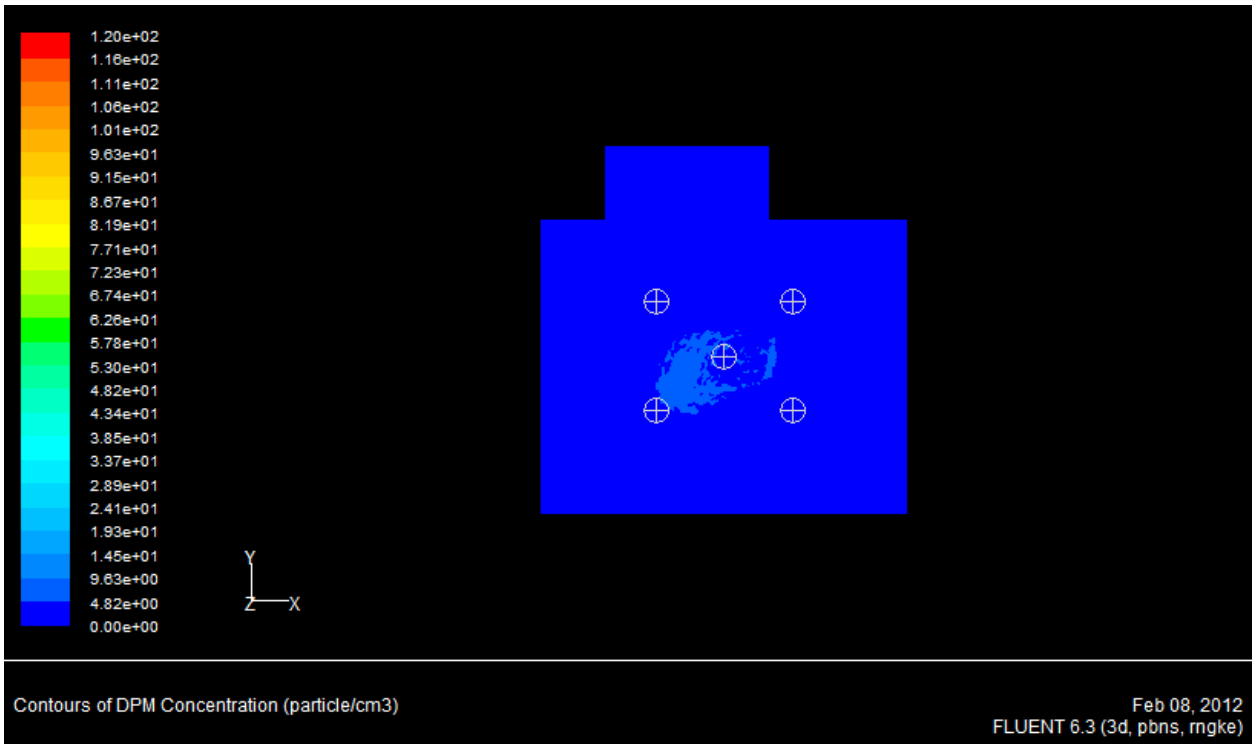

a: Contours of discrete phase concentration on plane A (z=-0.304 m)

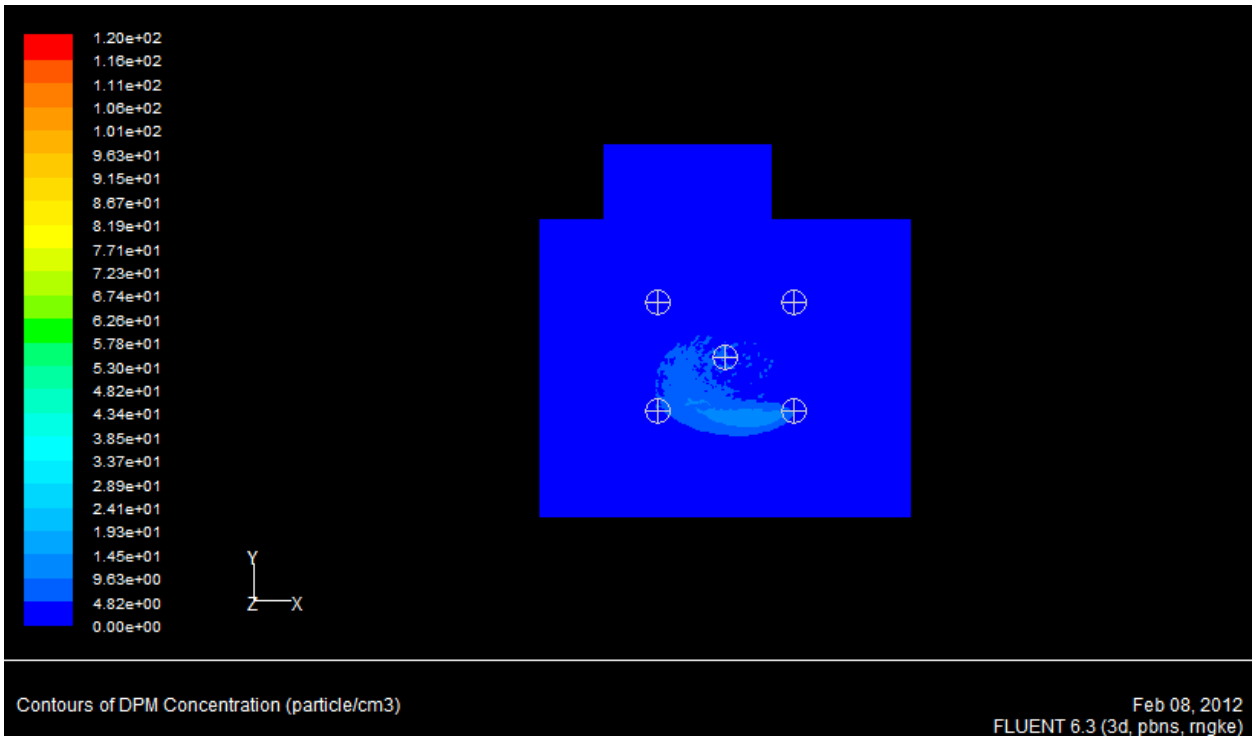

b: Contours of discrete phase concentration on plane B (z=-0.152m)

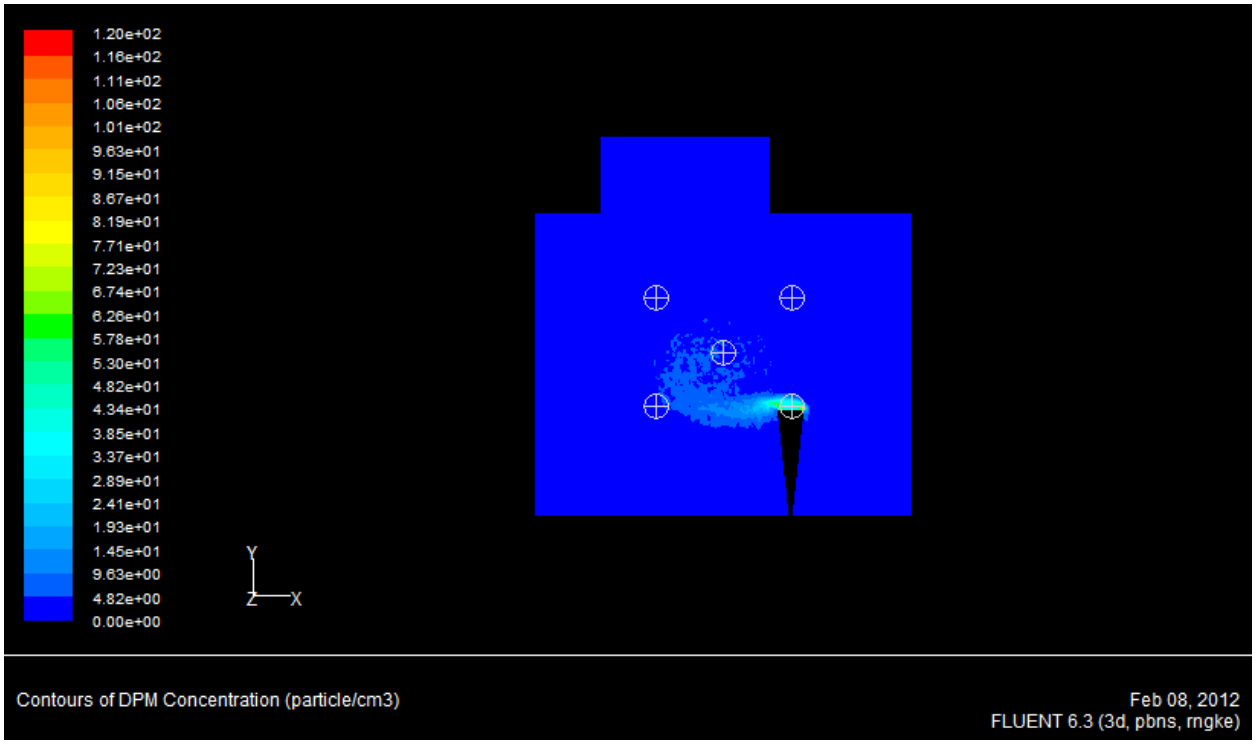

c: Contours of discrete phase concentration on plane C (z=0)

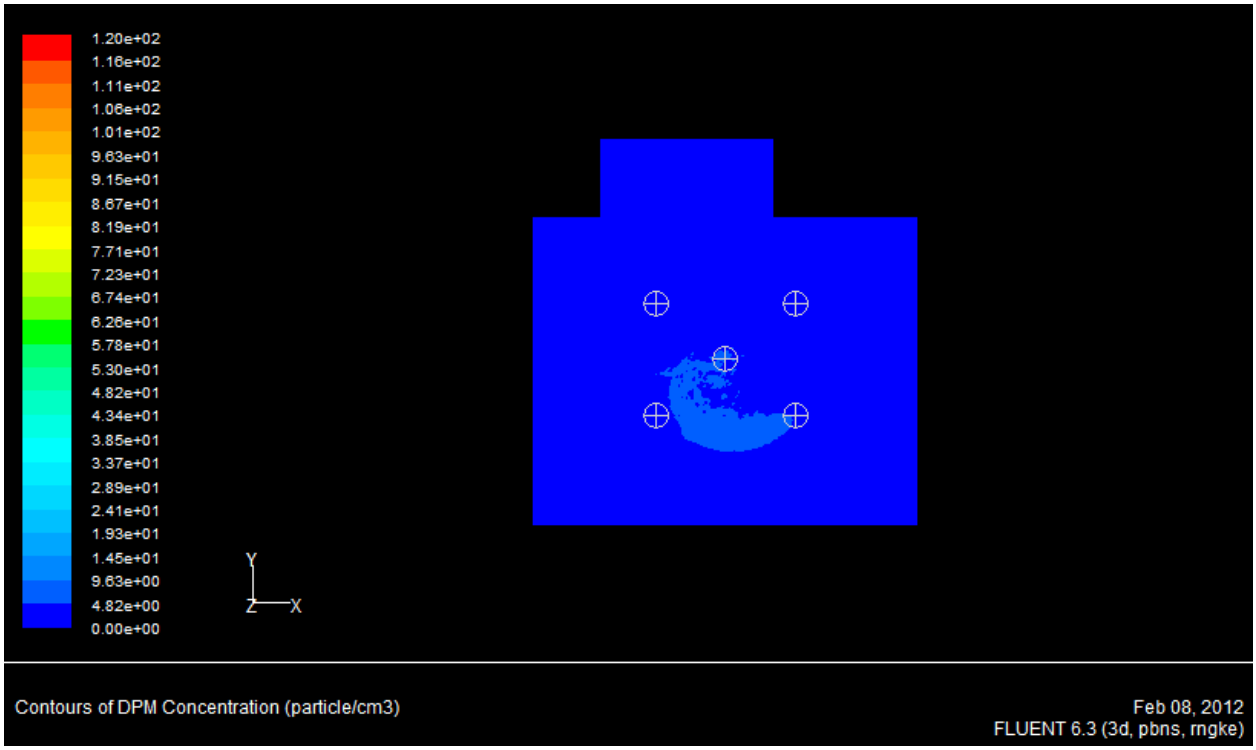

d: Contours of discrete phase concentration on plane D (z=0.152 m)

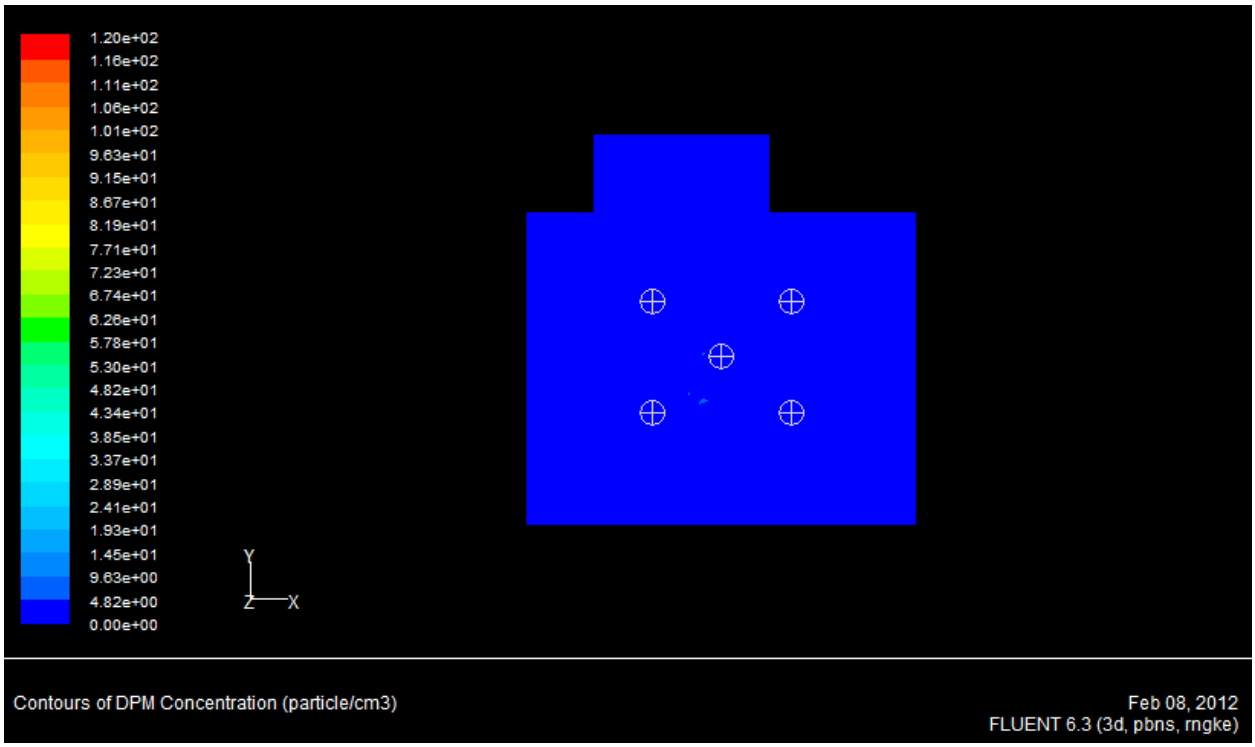

e: Contours of discrete phase concentration on plane E (z=0.304 m)

Figure 6.31 Contours of particles count concentration at APS locations on planes A-E predicted by steady RANS steady particle tracking with the number of tries=175.

6.4.2.3. Validation of DPM simulations for the cabin with positive pressure gradient: Exploring the optimum value for number of tries

As it was explained in section 6.2 of this chapter, the measurements were performed for the cabin with cone diffuser at two different gage pressures, i.e., 0 and 0.025 in H_2O. In this part the results of DPM simulations repeated for the pressurized cabin are compared with corresponding APS measurements. The available experimental data for validating the computational model for 10 micron particle dispersion in the pressurized cabin with cone diffuser included the APS measurements for locations 1-4 on planes B, C, and E (see Fig. 6.7) as well as OPC measurements for planes A through E at the outlet of the cabin. The comparisons between the predictions and measurements in Figs. 6.32 and 6.33 indicate that by pressurizing

the cabin the agreement between DPM predictions and APS/OPC measurements experienced a considerable improvement (compare Fig. 6.32 with Fig. 6.28 and Fig.6.33 with 6.30). Similar to what was observed in the cabin with zero pressure gradient, the best agreement was seen for APS locations 1 and 4. Eight different number of tries were examined for the DPM simulation in the pressurized cabin including: 50, 100, 150, 175, 200, 225, 350, and 700. Through the comparison of DPM predictions from the tested numbers of tries with the corresponding APS and OPC measurements, it was realized that 175 led to the most accurate predictions compared to the rest of tested numbers. However, as can be seen from Fig. 6.32c, number of tries equal to 700 produced slightly better predictions at APS location 3 on the plane C.

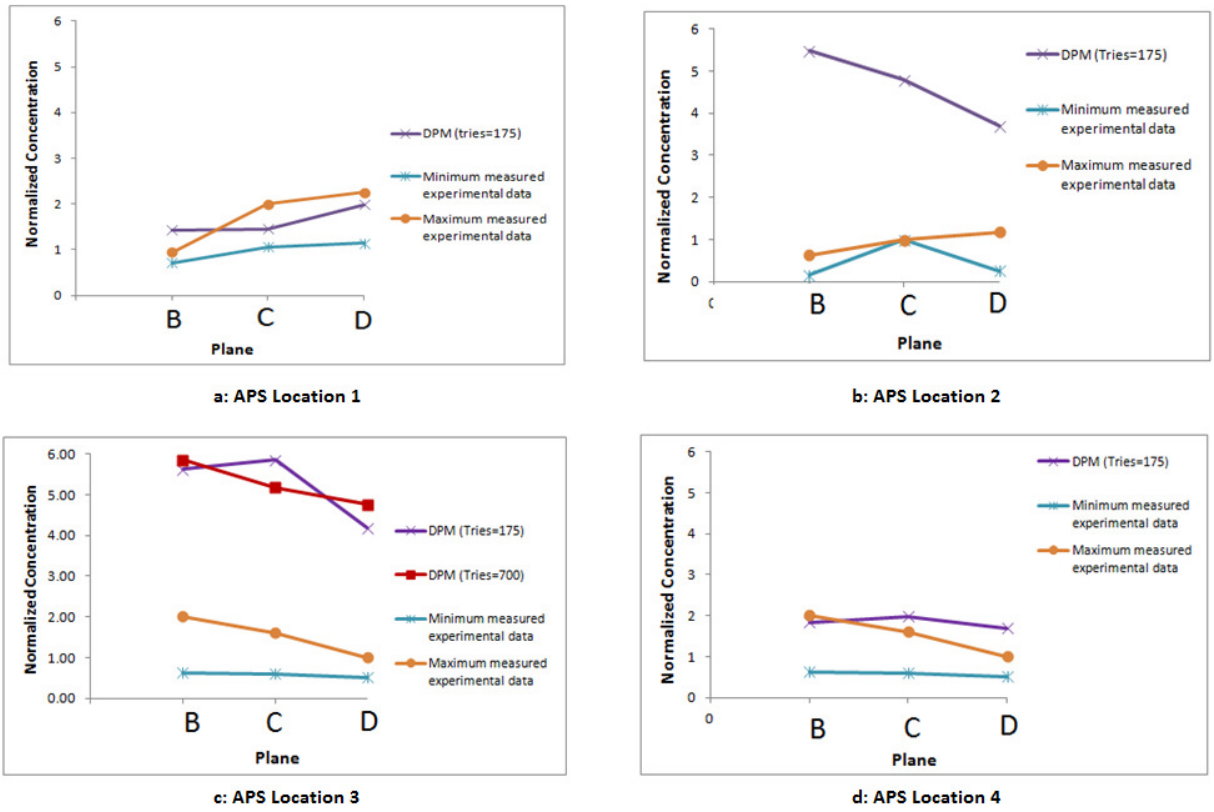

Figure 6.32 Comparison of DPM predictions and APS measurements for the APS locations 1-4 at cabin gage pressure of 0.025 in of H_2O.

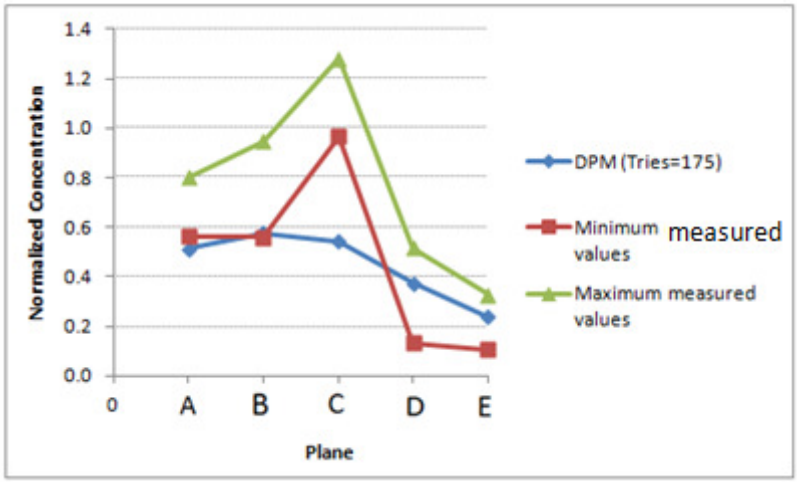

Figure 6.33 Comparison of DPM predictions and OPC measurements for the OPC locations at the cabin outlet for cabin gage pressure of 0.025 in of H_2O.

6.4.2.4. Study of the effect of particle density on dispersion behavior of micron particles

As mentioned earlier, one of the challenges encountered in the simulation of particles motion was the particle density. In the reference experiments performed by Padilla (2008), particles were generated using TSI Vibrating Orifice Generator (VOAG) model #3450. According to the technical explanations in the user's manual of this device published by TSI (2009) regarding the composition of liquid droplets produced by Model 3450 VOAG, and through the calculations performed using their equations, the density of particles is expected to be between 950-980 kg/m^3. However the visual inspection of dispersion behavior of particles created questions that the particles are probably hollow and their density might be much smaller than the above mentioned values. This issue necessitated performing an independent numerical study to understand the effect of particle density on the dispersion pattern of micron sized particles.

There are a number of published studies in which the effect of particles density on their dispersion pattern was investigated both experimentally and computationally. Toy et al. (2011) performed an experimental research to understand the effect of the density of nano-scale particle on the vessel wall deposition rate. The experiment indicated that nano-particles with lower densities have a tendency towards larger deposition rates on the vessel wall. Hulsman et al.

(1997) conducted a theoretical and experimental investigation to determine the effect of the density of the micron-sized particles on the retention time in slurry flows. Marchioli et al. (2007) used a Direct Numerical Simulation (DNS) to study the effect of solid particle density on the particle velocity and deposition rate in a turbulent boundary layer. The upward, downward, and horizontal particle-laden turbulent flows were simulated using different particle Stokes numbers. The simulation results indicated that for particles with the Stokes number of greater than 15, gravity and lift (density), do not affect the qualitative behavior of particle dispersion and deposition. In 1997, Smith et al. performed a numerical investigation to study the effect of particle size, density and impact velocity on particle depth of penetration when a solid stream is falling into a stationary liquid. An experimental study was performed by Razzak et al. (2010) to investigate the effects of particle shape, density and size on dispersion behavior in a fluidized bed riser.

In order to investigate the effect of particle density on dispersion pattern of particles, the DPM simulations were repeated for the cabin with zero pressure gradient assuming that particles are hollow from inside and therefore their density are close to air density. For the hollow particles a density of 1.3 kg/m^3 was considered in DPM simulations. Since the newly assumed density for the particles was approximately 1/1000 of its previously considered value, it was expected that simulations indicate considerably different behavior of particle dispersion comparing to what was observed through the previous simulations (for particles with the density of 971 kg/m^3). Figure 6.34 presents the comparisons between particle concentrations in different APS locations on plane A-E using two drastically different values for the particle density. From this figure it can be seen that the difference between two predictions is less than 60% (which corresponds to the APS location 3 on plane C). For the APS location 1, 2 , and 3, the predictions from two different particle density values are very close to each other. It seems that for this size of particles, the dispersion pattern of particles is not a strong function of the particle density. Since it was difficult to find out the reason of this behavior through discrete phase equations, the Euler approach and the species transport equation were used to evaluate the effect of particle density theoretically.

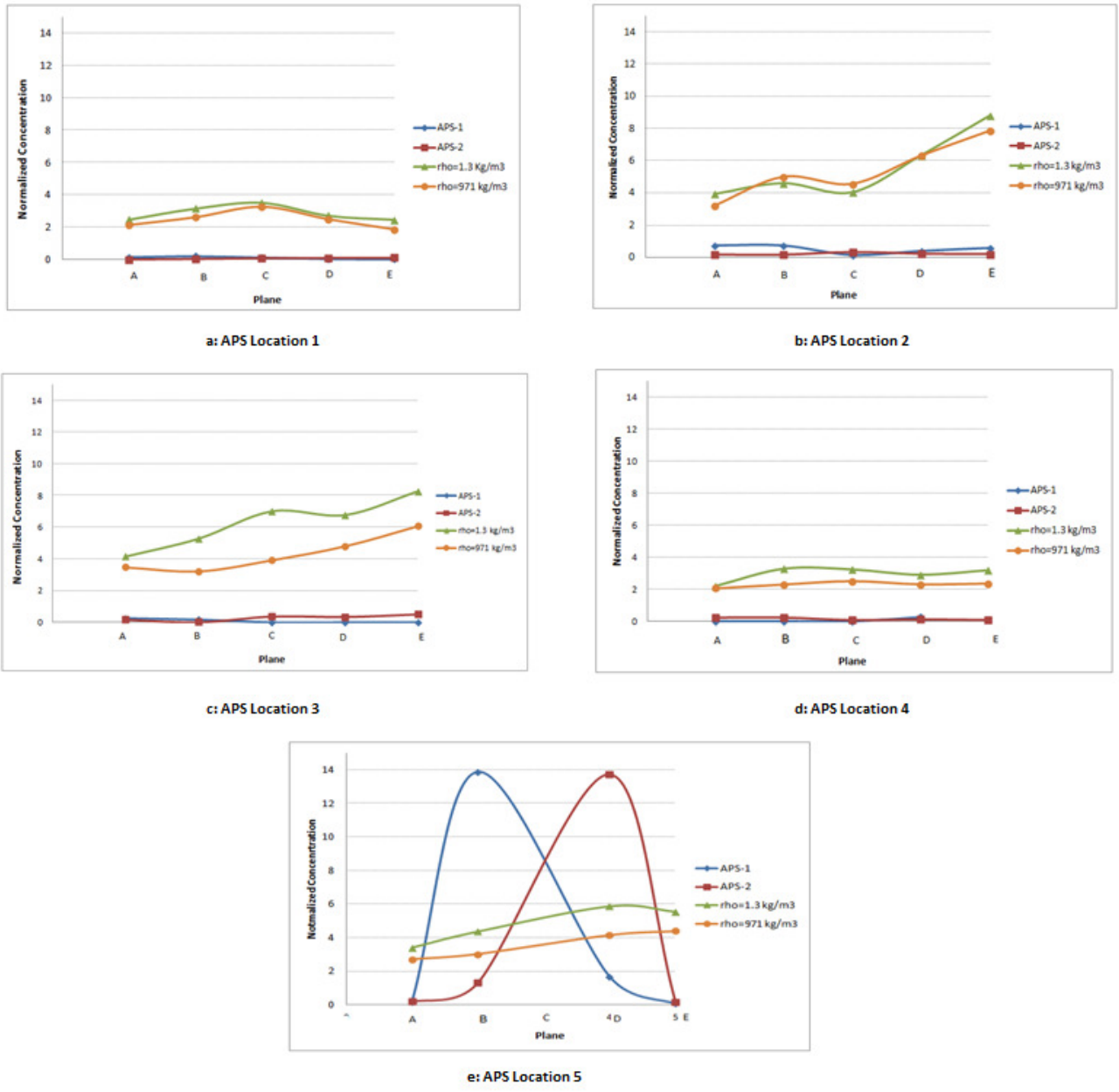

Figure 6.34 Comparison of DPM simulation using two different values for particle density: 1.3 kg/m3 and 971 kg/m3. (The cabin pressure gradient is zero).

In the Euler approach for simulating dispersion of particles, the governing species transport equation, neglecting the slippage velocity of particles, is:

$$\frac{\partial(\rho Y)}{\partial t}+\frac{\partial}{\partial x_i}(\rho u_i Y)=-\frac{\partial}{\partial x_i}\left(-(\rho D+\frac{\mu_t}{Sc_t})\frac{\partial Y}{\partial x_i}\right) \tag{6.17}$$

The equation above was elaborately explained in section 5.3 of chapter 5. The boundary conditititions for this equation are:

$$C_{injection-port}=54\,pt/cm^3$$

$$m_p=54.V_p=2.83\times10^{-14}\rho_p$$

$$m_{total}=m_p+\rho_{Air}(10^{-6}m^3)$$

$$m_{total}=2.83\times10^{-14}\rho_p+1.225\times10^{-6}$$

$$Y_{inj-port}=\frac{m_p}{m_{total}}=\frac{2.83\times10^{-14}\rho_p}{2.83\times10^{-14}\rho_p+1.225\times10^{-6}}$$

$$\frac{\partial Y_{wall}}{\partial n}=0$$

$$Y_{inlet}=0$$

$$\frac{\partial}{\partial x}(\frac{\partial Y_{outlet}}{\partial x})=0$$

Considering two different values for the particle density (1.3 and 971 kg/m^3) the following tabulated values for the species (particle) mass fraction is calculated at the injection port as presented in Table 6.7.

Table 6.7: Particle mass fraction and mixture (particle-air) density at the injection port

$\rho_{particle}$ (kg/m^3)	971	1.3
M_p (kg)	2.7454E-11	3.6757E-14
M_{total} (kg)	1.225E-06	1.225E-06
Y	2.2411E-05	3.0005E-08
$\rho_{Mixture}$	0.816308	0.816327

The APS and OPC measurements for the concentration data are presented in dimensionless form. The dimensionless concentration was defined in Eq. (6.1) which is rewritten as below:

$$C = \frac{C_m \times Q_{\sup}}{C_I \times Q_I}$$

where C_m is the measured sample concentration corrected for the particle loss in the sampling tube, C_I is the calibrated injected concentration, $Q_{\sup}$ is the supply flow (inlet and injected), and Q_I is the injected flow of the carrying air.

$$Q_{\sup} = 4212 lpm$$

$$Q_I = 52 lpm$$

Consistent with the way that experimental measurements were presented, the new mass fraction is defined as follows:

$$C = \frac{Y \times Q_{\sup}}{Y_{inj-port} \times Q_I} = 81 \frac{Y}{Y_{inj-port}} \Rightarrow Y = \frac{C.Y_{inj-port}}{81}$$

Substituting *Y* with *C* using the above equation in species transport equation we will have:

$$\frac{\partial(\rho C)}{\partial t} + \frac{\partial}{\partial x_i}(\rho u_i C) = -\frac{\partial}{\partial x_i}\left(-(\rho D + \frac{\mu_t}{Sc_t})\frac{\partial C}{\partial x_i}\right) \tag{6.18}$$

and the boundary conditions are:

$$C_{injection-port} = \frac{Y_{inj-port} \times Q_{\sup}}{Y_{inj-port} \times Q_I} = \frac{Q_{\sup}}{Q_I} = 81$$

$$\frac{\partial C_{wall}}{\partial n} = 0$$

$$C_{inlet} = 0$$

$$\frac{\partial}{\partial x}\left(\frac{\partial C_{outlet}}{\partial x}\right) = 0$$

Comparing Eqs. (6.17) and (6.18) and their boundary conditions indicate that in Eq. (6.18), boundary conditions are independent of particle density. The molecular diffusion coefficient (D_P) in Eqs. (6.17) and (6.18) is calculated using Stokes Einstein equation:

$$D_P = \frac{K_B T \cdot C_C}{6\pi \cdot \mu \cdot r} \tag{6.18}$$

where, $K_{B,}$ is the Boltzmann constant=1.3806503 × 10^{-23} m^2 kg s^{-2} K^{-1}

r (m), is the diameter of mono dispersed particles

C_C, is the slip correction coefficient and computed using the following equation:

$$C_C = 1 + 0.8715\frac{\lambda_0}{d_P}\frac{T}{p} \tag{6.19}$$

where λ_0=0.066 μm is the mean free path for air (which is carrying gas in this project) at standard condition, and d_P is the diameter of particles. In order to calculate the slip correction coefficient correctly, λ_0 and d_P are in μm, T denotes absolute temperature in K, and p is the absolute pressure in KPa.

So it is seen that the diffusion coefficient is independent of particle density. Also from Table 6.8 it can be seen that in Eq. (6.18) the density of the mixture varies between ~0.82 kg/m^3 (at the injection port) and 1.225 kg/m^3 (at the cabin inlet) for both assumed ultimate values of particle density. Therefore, we can expect that the solutions of Eq. (6.18) using two different particle density values to be close to each other.

Figure 6.35 shows a comparison between DPM predictions, species transport calculations, and APS measurements corresponding to APS location 2 on planes A-E. The DPM and Species Transport simulation parameters are compared in Table 6.8.

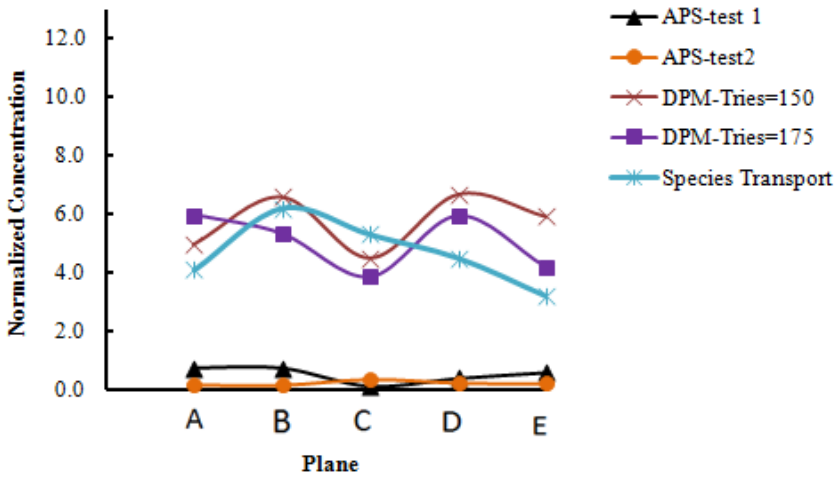

Figure 6.35 Comparison between DPM predictions, species transport calculations, and APS measurements corresponding to APS location 2 on planes A-E (Cabin with zero pressure gradient)

Table 6.8: Comparison between DPM and Species transport simulation parameters

Discrete Phase Model (DPM)	**Species Transport**
2-phase flow	1-phase flow
The continuous phase is air: ρ=1.225 kg/m^3 μ=1.7894e-5 kg/ms	The continuous phase is the mixture of air and particles $\frac{1}{\rho}=\frac{Y}{\rho_p}+\frac{1-Y}{\rho_{air}}$ $\mu = Y\rho_p + (1-Y)\rho_{air}$ $K = Y.K_p + (1-Y).K_{air}$ $C_p = Y.C_{P,p} + (1-Y).C_{P,air}$
The Governing Equations: • Trajectory equation for discrete phase (particles) • Navier Stokes Equations for the continuous gas phase	The Governing Equations: • Navier Stokes equations • Species transport equation • Energy equation • Mixture property equations • Stokes-Einstein equation for the calculation of particles diffusivity

Boundary Conditions: • At the injection port: $C_{injection-port} = 54\,pt/cm^3$ $Q_{injectio-port} = 52 lit/\min$ $\dot{N}_p = C_{injection-port} \times Q_{injection-port} = 46800\,pt/s$ $V_p = \frac{\pi.d_p^{\,3}}{6} = 5.236\times10^{-16} m^3$ $\dot{m}_p = \rho_p V_p.\dot{N}_p = 2.5404\times10^{-11}\rho_p$ Particle fate: escape Velocity of airflow=0.0478 m/s Velocity of particles=0.0478 m/s • On the walls and solid surfaces No slip wall Particles are trapped • Cabin Inlet: Boundary type: Velocity-Inlet Airflow velocity=0.64 m/s Particle fate=escape • Cabin Outlet: Boundary type: Outflow Particle fate=escape	Boundary Conditions: • At the injection port: $C_{injection-port} = 54\,pt/cm^3$ $m_p = 54.V_p = 2.83\times10^{-14}\rho_p$ $m_{total} = m_p + \rho_{Air}(10^{-6}m^3)$ $m_{total} = 2.83\times10^{-14}\rho_p + 1.225\times10^{-6}$ $Y = \frac{m_p}{m_{total}} = \frac{2.83\times10^{-14}\rho_p}{2.83\times10^{-14}\rho_p + 1.225\times10^{-6}}$ Velocity of mixture-flow=0.0478 m/s • On the walls and solid surfaces $\frac{\partial Y}{\partial n} = 0$ No slip wall • Cabin Inlet: Boundary type: Velocity-Inlet $Y = 0$ flow velocity=0.64 m/s • Cabin Outlet: Boundary type: Outflow $\frac{\partial}{\partial x}(\frac{\partial Y}{\partial x}) = 0$
• Turbulence Model: RNG K-ε • Near Wall Treatment: Non-Equilibrium wall function	• Turbulence Model: RNG K-ε Sc_t=0.7 • Near Wall Treatment: Non-Equilibrium wall function
• Operating Condition T=300 k P=101,325 pa Gravity =-9.81 m/s^2	• Operating Condition T=300 k P=101,325 pa Gravity =-9.81 m/s^2

6.5. Summary

In this chapter, the capabilities of computational approaches in predicting different transport phenomena in aircraft cabins was investigated by simulating the turbulent airflow and dispersion of inert micron-sized spherical particles injected into a generic half cabin model. Two different particle injection configurations were considered in this part of study while the carrier air volumetric flow rate and the particles mass flow were kept unchanged for both cases of injection configuration. In the first configuration, in which the particles were injected through a straight tube, the injection velocity of carrier air and particles at the injection port were almost 3.5 times greater than the injection velocity of supply air at the cabin inlet nozzle. However in the second configuration, in order to eliminate the effect of particle and carrier air injection velocity on distribution pattern of mono-disperse particles, the straight tube was replaced by the cone diffuser such that the injection velocity of particles was reduced to very small values. A Lagrangian approach was used to predict the particle concentration at specific APS and OPC measurement locations inside and at the outlet of the cabin. The steady RANS solutions for the airflow velocity data were used to initialize the particle-tracking calculations through the Discrete Phase Model (DPM). To calculate the effects of turbulence on the dispersion behavior of particles, a Discrete Random Walk (DRW) model was employed. From the simulations performed for the cabin with straight injection tube, the following summary and conclusions are reached:

1. Using the steady RANS method (standard k-ε mode), a comprehensive grid independency study was performed by concentrating on regional mesh refinement using both structured and unstructured grids. The effectiveness of both grid refining approaches in producing the converged velocity data was investigated and discussed**.** From the grid dependency, the benefits associated with the regional mesh refinement were discussed. Using the regional refinement enabled us to have more control on the number and the type of the mesh elements. The other benefit of using regional refinement was to reduce the number of mesh elements that that normally results in increased computational cost and time. Although the initial generated coarse mesh was structured, two approaches were used in refining the mesh in each selected

refinement region. After several tests, it was concluded that unstructured local grid refinement not only leads to the more accurate and reliable results , but also is considerably more computational time and cost effective than the structured local grid refinement. The optimum mesh size and type was then used to simulate the dispersion of micron-sized particles.

2. The turbulent airflow was simulated using LES and both steady /unsteady RANS (using standard k-ε). The comparisons between the steady/unsteady RANS velocity predictions indicated that although there were differences between two predictions in transient time but eventually the unsteady RANS predictions produced values very close to the steady RANS predictions. In the region where two jets of airflow from the particle injection tube and cabin inlet nozzle meet a considerable difference (up to ~150%) between LES time-averaged and RANS airflow velocity predictions was observed. One can speculate that the flow structure in that region is much more complex than other locations therefore RANS is not able to capture all the flow characteristics (e.g. APS location 4).

3. Comparison of the Steady RANS-Steady Particle Tracking (DPM) simulation results with the corresponding experimental data revealed that, considering the measurements uncertainty, there is a good agreement between the predictions and measurements for the APS locations 2, 3, and 4 (on the cabin central plane). For APS location 1, due to the fact that the experimental measurements are very small, achieving predictions with good accuracy for this location was difficult.

4. A detailed study on the effect of the number of tries on the accuracy of predicted particle concentration data was also performed. The investigation showed that although increasing the number of tries has a positive effect on improving the average accuracy, beyond a specific number of tries (which is called as the optimum number of tries in which the average error has its minimum value), any increase in the number of tries does not necessarily improve the average accuracy.

5. Through the comparison of DPM simulations from 1-way and 2-way coupling schemes, it was determined that due to very low volume fraction of particles, the effect of discrete phase on continuous phase is negligible and the particle concentration predictions from above mentioned two schemes are the same. Comparison of DPM simulation results for dispersion of two different sizes of micron-sized particles, i.e., 3 μm and 10 μm, showed that particle concentration predictions for the smaller size particles have better agreement with the corresponding experimental results. This comparison also confirmed the outcome of the previously performed experimental study in which it was observed that smaller particles distributed more uniformly than the larger particles. In other words, smaller particles have better mixing behavior with air circulation in the cabin.

For the particle injection using the cone diffusion, the findings may be summarized as the followings:

1. The RNG k-ε turbulence model and Non-equilibrium wall functions for the near-wall approach were used for the airflow simulations. A detailed study was carried out to obtain an optimum number for the number of tries in the DRW model resulting in the best quality predictions. Since the available experimental data included two different inside cabin pressures, the investigation on the optimum number of tries was performed for both cases of cabin inside pressures. It appeared that the optimum number of tries was 175 for both cases.

2. The effect of cabin pressure gradient was studied through the comparison of particle concentration measurements and predictions at specified monitoring locations in the cabin between two cases of cabin inside gage pressures of 0 and 0.025 in of H_2O. It was observed that by increasing the cabin gage pressure the agreement beween predictions and measurements were improved.

3. Through the investigation of the effects of particles density on distribution behavior of micron-sized particles, it was determined that the distribution behavior is not a strong function of particle density.

Chapter 7 - Study of Turbulent Airflow in a Full-Size Aircraft Cabin Mockup

In this chapter the turbulent airflow in a full-scale 11-row Boeing 767 aircraft cabin mockup is simulated. The full-scale 11-row aircraft cabin mockup was used by Beneke (2010), Shehadi (2010), and Trupka (2011) in running tracer gas diffusion and particle dispersion experiments. As it was discussed in details through chapters 4-6, the first step in simulating tracer gas diffusion or particle dispersion is the calculation of the airflow field. The calculated velocity data presented in this chapter can be used later as the initial condition for the tracer gas and particle dispersion simulations. Based on the outcomes of the study presented in chapter 3 regarding the evaluation of different k-ε models, the RNG k-ε model is used to calculate the airflow velocity data. In the first section of this chapter, the geometry of the cabin is explained in detail. Then the approach used for creating the geometry and generating the mesh is described, along with the adopted numerical method for solving the governing Navier-Stokes equation. In the last section the predicted velocity contours in different locations in the cabin are presented and discussed.

7.1. Cabin Mockup Description*

Figure 7.1 shows the outside and inside views of the mockup aircraft cabin which was built in the Department of Mechanical and Nuclear Engineering at Kansas State University to experiment different transport phenomena associated with air quality in aircraft cabin environment. This mockup which is amongst the largest mockup chambers in its class has 9.75 m length and 4.72 m width as shown in Fig. 7.2. The cabin consists of 11 rows of 7 seats, two seats are located in the East and West sides of the aircraft cabin and three seats are located in the center of each row. Two outboard and two centered simulated stowage bins are provided above each row of seats. The air diffusers are located between the two centered stowage bins (Fig. 7.3).

* In the preparation of this section, the "Draft Final Technical Report, Contaminant Transport in Airliner Cabins Project, Kansas State University, 2009" was used extensively as the main reference.

The remaining space between the upper parts of the inside and outside of the air craft cabin is occupied by the air conditioning and lighting systems' components.

The seats are faced towards the mockup South wall and occupied by the manikins. Two access doors to the cabin are provided in the north end which is considered as the rear of the cabin. As shown in Fig. 7.2, there are also two hallways in the eastern and the western sides of the cabin. The data acquisition system and the cabin control system are located in those hallways (Shehadi, 2010). Figure 7.3 shows the cross section of the Boeing 767 aircraft cabin. The dimensions presented in this figure will be used later in creating the geometry and generating mesh required for the computational simulations. The diffuser assembly is also shown in Fig. 7.4.

a: outside view

b: inside view

Figure 7.1 Outside and inside views of Boeing 767 11-row cabin mockup (Trupka, 2011).

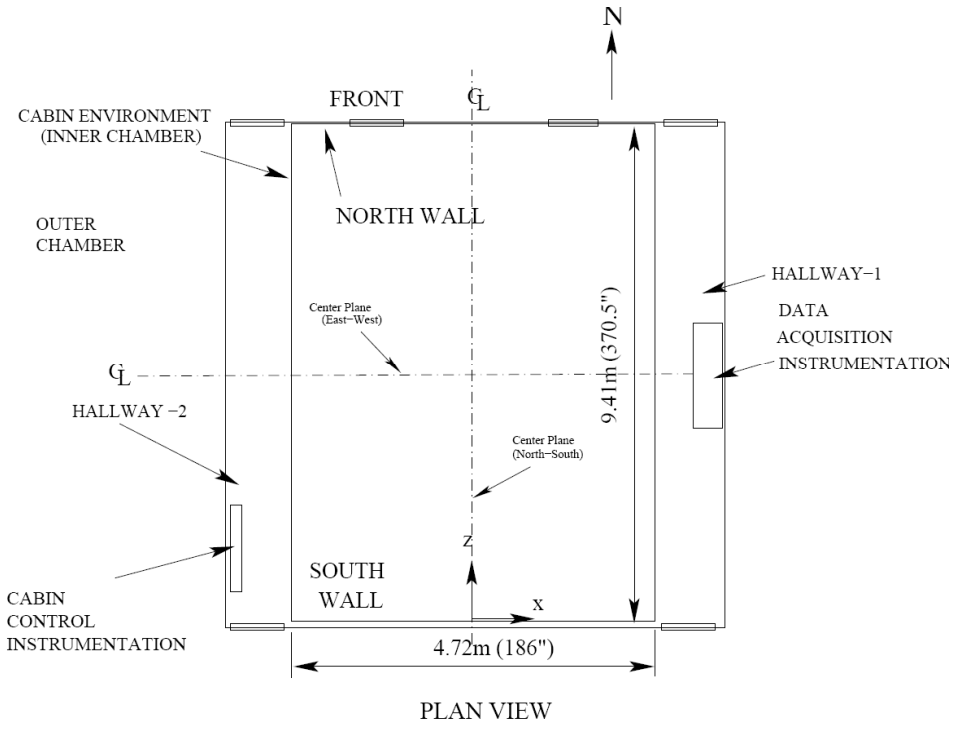

Figure 7.2 Schematic diagram of the cabin simulator (plan view and not to scale).

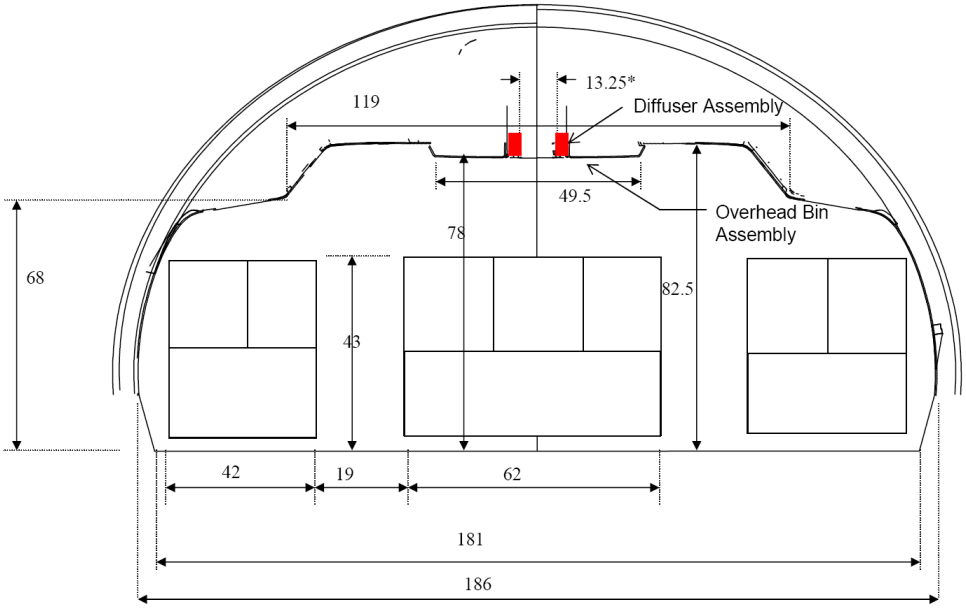

Figure 7.3 Overall cabin dimensions and air diffuser locations. All dimensions are in inches. Drawing is not to scale (All dimensions are in inches)

* 13.25 inches is the distance between the inside edges of the air inlet slots

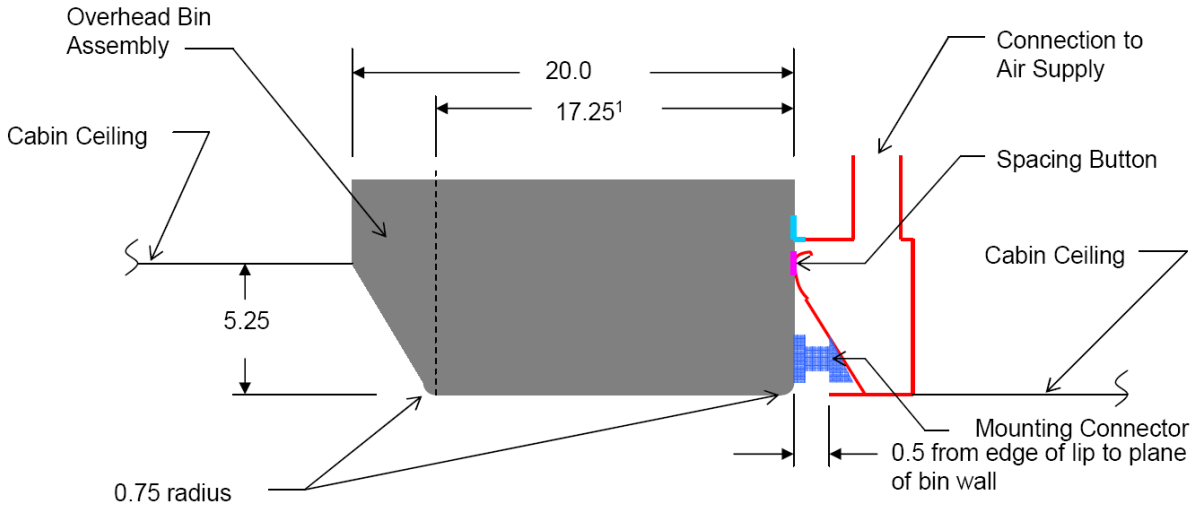

Figure 7.4 Mounting of the diffuser assembly in the cabin(All dimensions are in inches)

7.1.1 The cabin geometry and dimensions

In order to determine the geometrical specifications of the cabin's interior profile, a manual method was employed. The graph of the interior cabin profile, based on the achieved data, is shown in Fig. 7.5. This graph does not include the centered stowage bin. However, this part of the profile can be completed easily using other indicated geometrical data presented in Fig. 7.3. Since the aircraft cabin is symmetric, the cabin profile would be symmetric as well and therefore only the west portion (approximately one half) of that is shown in Fig.7.5 (The front of the aircraft towards the South). This portion of the profile consists of seven segments. These segments are either curves or straight lines which can be defined by the equations given in Table 7.1.

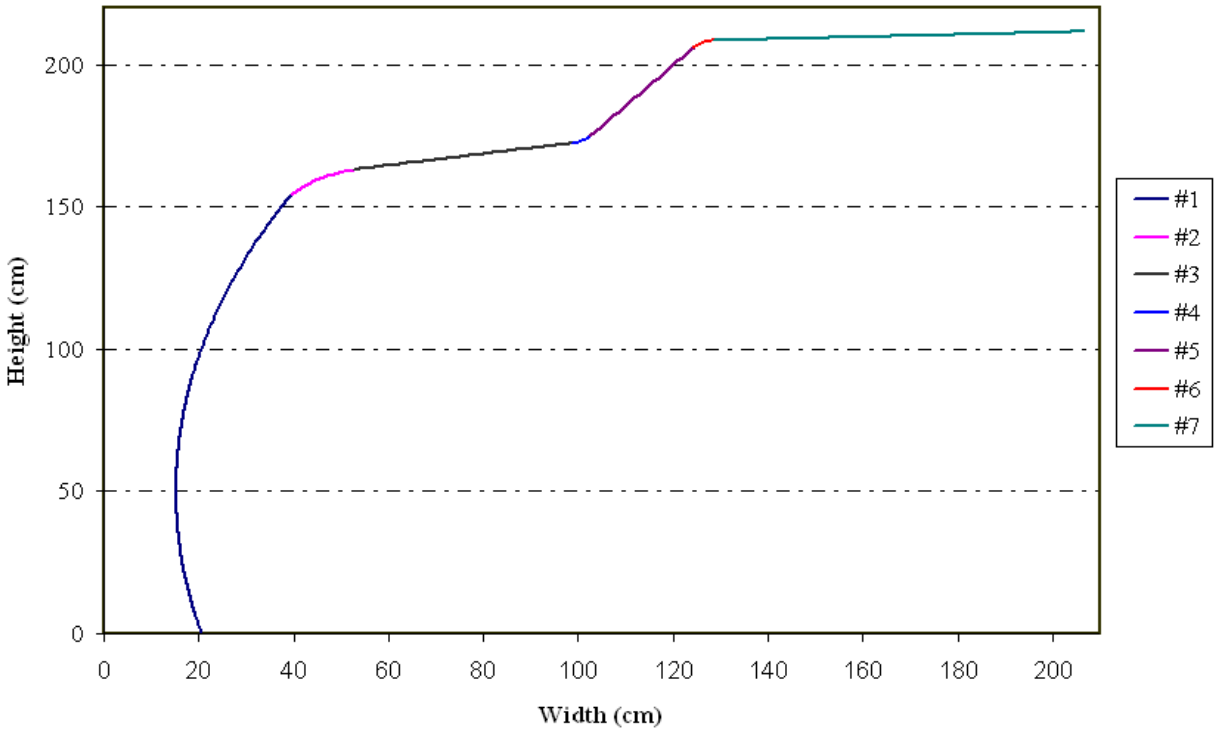

Figure 7.5 West Portion of the cabin profile (the centered stowage bin is not included)

Table 7.1 Mathematical description for different segments of cabin profile (all data are in cm).

Segment #	Start Point (width, height)	End Point (width, height)	Corresponded Mathematical Equation (y=Height, x=Width)
1	(20.661,0)	(39.485,154.419)	$(x-251.472)^2+(y-50.221)^2=(236.211)^2$
2	(39.485,154.419)	(52.46,162,975)	$y=(8\times10^{-8})x^3-0.0393x^2+4.268x+46.672$
3	(52.46,162,975)	(98.536,172.2864)	$y=0.2022x+152.3672$
4	(98.536,172.2864)	(102.48,174.8672)	$(x-97.284)^2+(y-174.872)^2=40.1956$
5	(102.48,174.8672)	(124.356,206.2)	$y=1.4319x+28.1311$
6	(124.356,206.2)	(128.35,208.3858)	$(x-128.557)^2+(y-203.27)^2=26.2144$
7	(128.35,208.3858)	(206.46,211.54)	$y=0.04043x+203.1934$

7.1.2. The seats locations

The configuration of the first row of seats is shown in Fig. 7.6. The exact location of seats are determined by measuring the distances between the seats' mounting location and south wall as well as between mounting location and cabin's floor center line. A sample of mounting location is shown in Fig. 7.7.

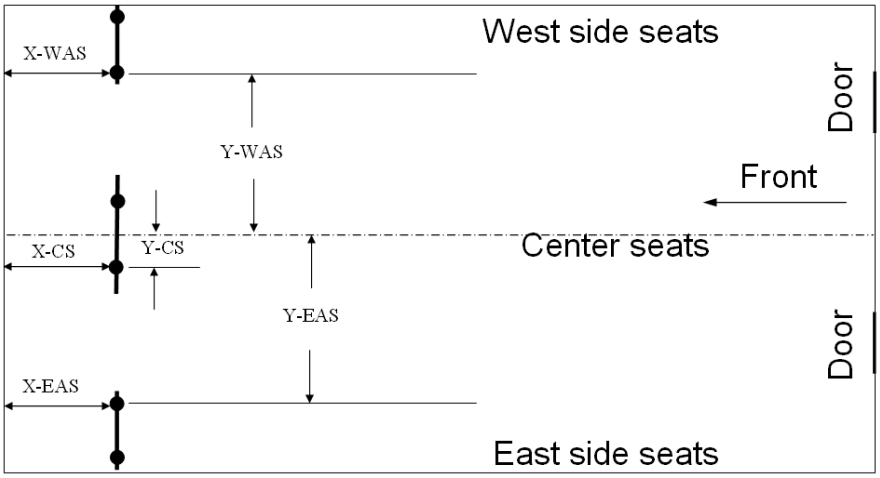

Figure 7.6 Configuration and orientations of the first row of seats and required coordinates to exact determination of seats' locations

The geometrical parameters indicated in Fig.7.6 are defined as follows:

X-EAS **X-value for the east aisle seats:** Distance between the mounting point of east isle seats and south wall

Y-EAS **Y-value for the east aisle seats:** Distance between the mounting point of east isle seats and cabin's floor centerline

X-CS **X-value for the Center seats:** Distance between the mounting point of center seats and south wall

Y-CS **Y-value for the Center seats**: Distance between the mounting point of center seats and cabin's floor centerline

Y-WAS **X-value for the west aisle seats:** Distance between the mounting point of west isle seats and south wall

Y-WAS Y-value for the west aisle seats: Distance between the mounting point of west isle seats and cabin's floor centerline

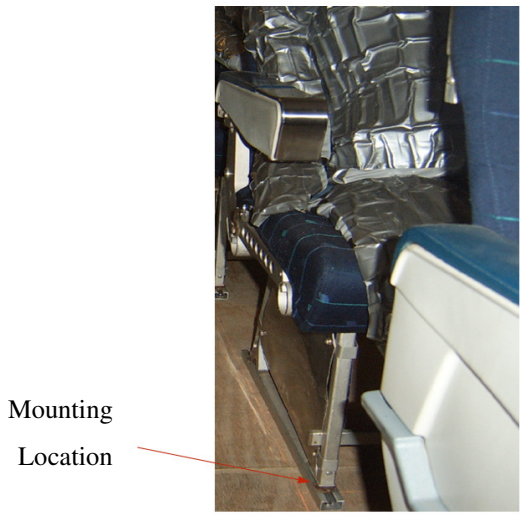

Figure 7.7 Seats 'mounting point

Based on the locations considered for mounting points (for the east aisle seats: contact point of the front right seats' leg with the floor, for the west aisle and the center seats: contact point of the front left seats' leg with the floor) the following data was achieved:

Table 7.2 Aircraft seats locations based on their mounting points locations

Row # (from front)	X-value East Aisle seats (inches)	Y-value East Aisle seats (inches)	X-value Center seats (inches)	Y-value Center seats (inches)	X-value West Aisle seats (inches)	Y-value West Aisle seats (inches)
1	14.84	54.1	14.63	11.13	15.19	53.94
2	48.13	54.35	48.13	11.25	47.63	54.34
3	81.13	53.97	82.13	11.38	80.25	54.23
4	113.63	54.06	113.94	11.5	113.44	54.5
5	147.25	54.13	148.5	11.19	146.75	54.11
6	180.32	54.3	180.25	11.16	179.88	54.14
7	213.19	54.44	213.07	11.22	212.94	55.25
8	246.32	54.5	245.88	11.27	245.63	54.37
9	279.25	54.44	280.13	11.15	278.75	54.2
10	312.44	54.08	312.38	11.29	313	54.72
11	348.5	54.63	345.13	11.02	345.44	54.32

7.1.3. The seats dimensions

In order to generate the computational grid required for running the CFD simulations, knowing the dimensions and geometry of seats are also required. Figures 7.8 -7.10 provide the geometrical data for this purpose (All dimensions are in inches).

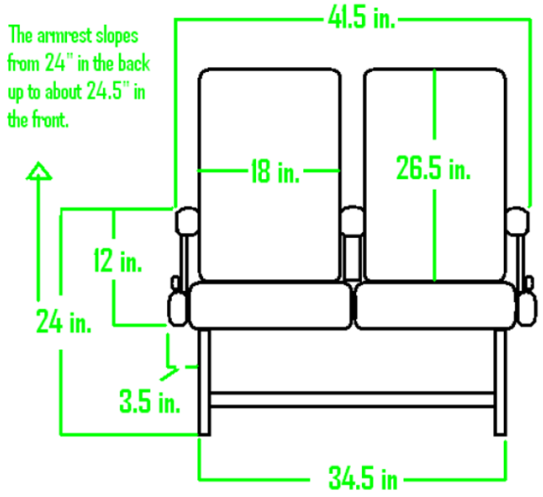

Figure 7.8 Dimension of the aisle seats from the front view

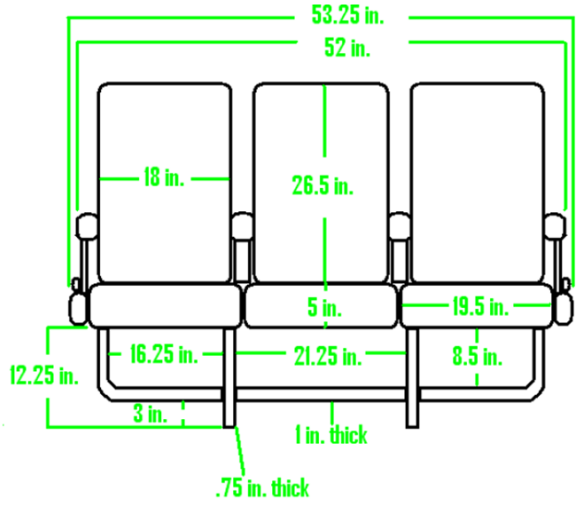

Figure 7.9 Dimension of the center seats from the front view

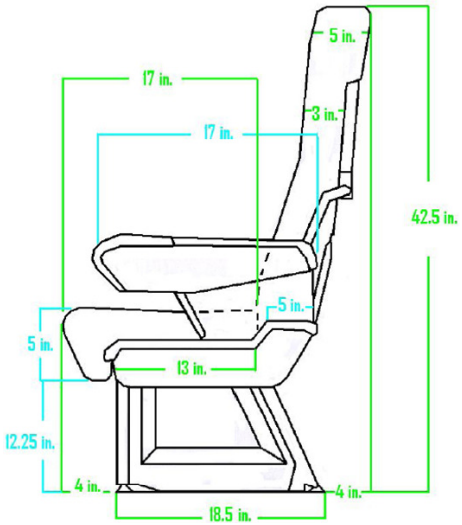

Figure 7.10 Dimension of the seats from the right view

7.1.4. The manikin dimensions

The manikins were used in the experiments to resemble the aircraft cabin passengers. The manikin dimensions are also necessary to generate the computational grid. The dimensions shown in Fig. 7.11 are used for this purpose.

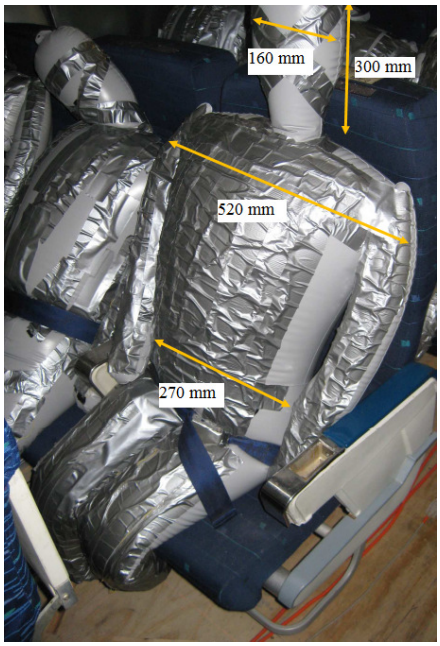

Figure 7.11 Dimensions of the manikin seated in the cabin

7.2. Grid generation and numerical solution methods

Using the information presented in section 7.1 and neglecting the curves in the seats and manikins geometry, the geometry of the cabin with seats and manikins was created in Gambit. Figures 7.12 and 7.13 indicate how the geometry of the cabin was created in Gambit. The whole volume is divided into 11 rows and 3 columns, therefore, the whole volume consists of 33 sub-volumes (see Fig. 7.12). As Fig. 7.13 shows, each row is divided into 3 sub-volumes: East and West sub-volumes which are symmetric to each other with respect to the cabin longitudinal plane of symmetry and the center sub-volume. These sub-volumes are connected to each other through interior faces.

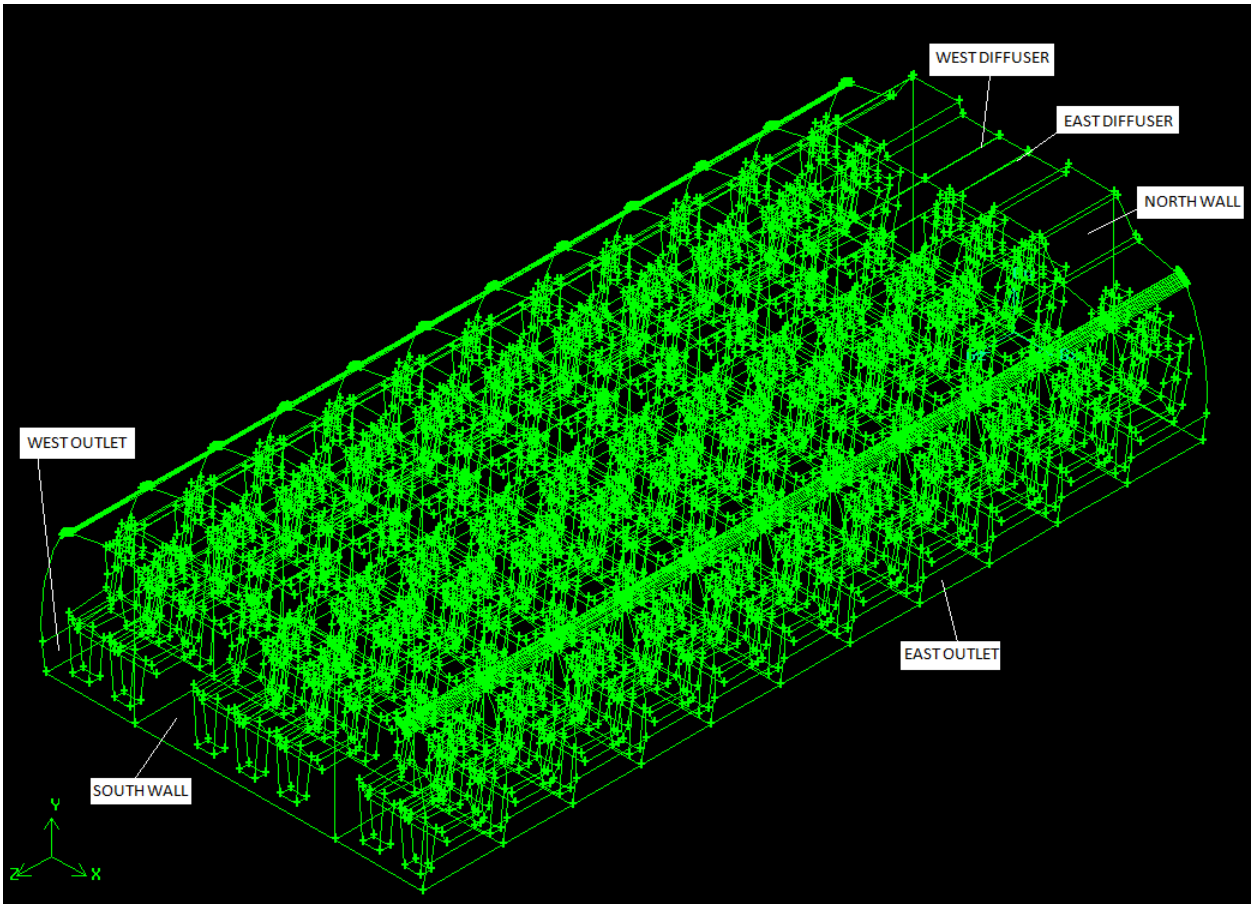

Figure 7.12 The created cabin geometry in Gambit

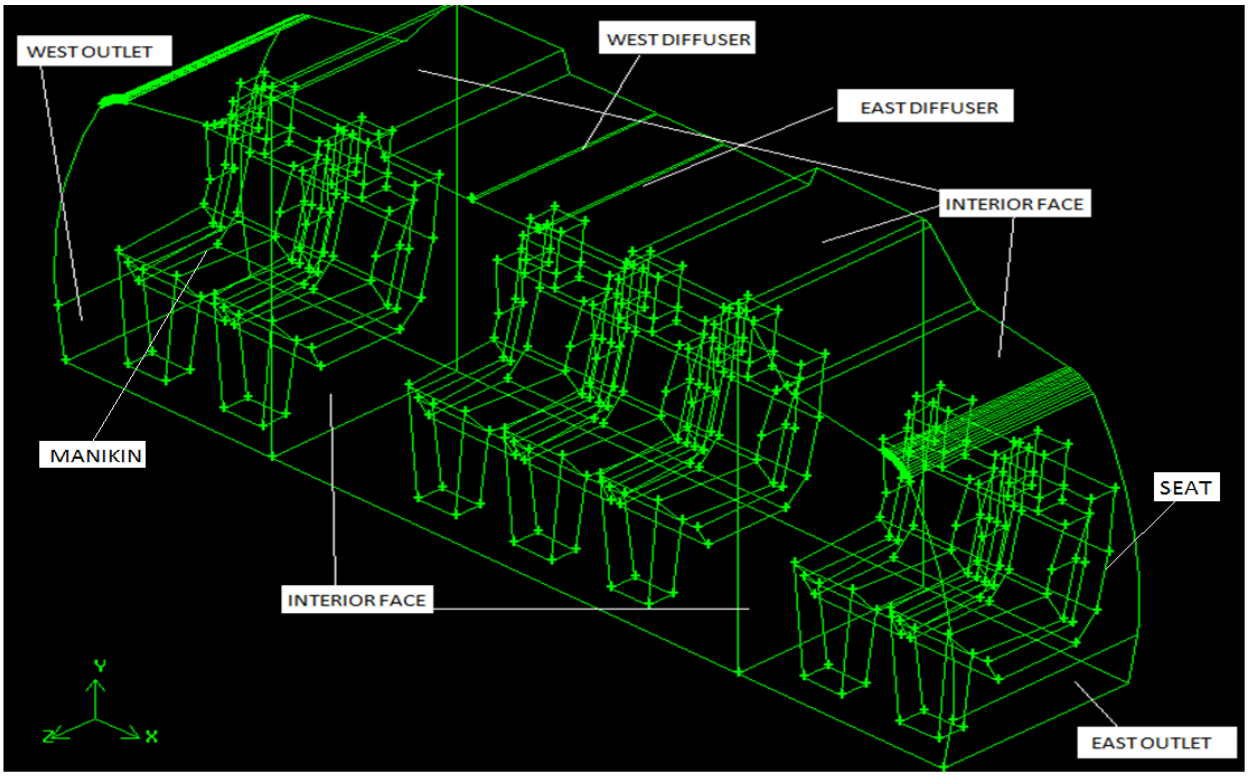

Figure 7.13 3D view of the created geometry for one row of the cabin. The three sub-volumes are recognizable. The sub-volumes are connected through interior faces.

Because of the complex geometry of the cabin, the unstructured T-Grid mesh consisting of hybrid and tetrahedral mesh elements was generated. The sub-volumes were meshed separately. Figure 7.14 shows the generated unstructured grid for one row of the cabin. The generated grid for the whole geometry is also shown in Fig. 7.15.

The initial size of the generated grid was 11,950,000 elements that led to stoppage of the calculations, since the number of mesh cells was higher than the available computational capacity of the computers used for the simulations. Therefore, the number of mesh cells was decreased. For grid uncertainty purposes, three different sizes of grid were examined, i.e., 2630000, 3667000, and 5438000.

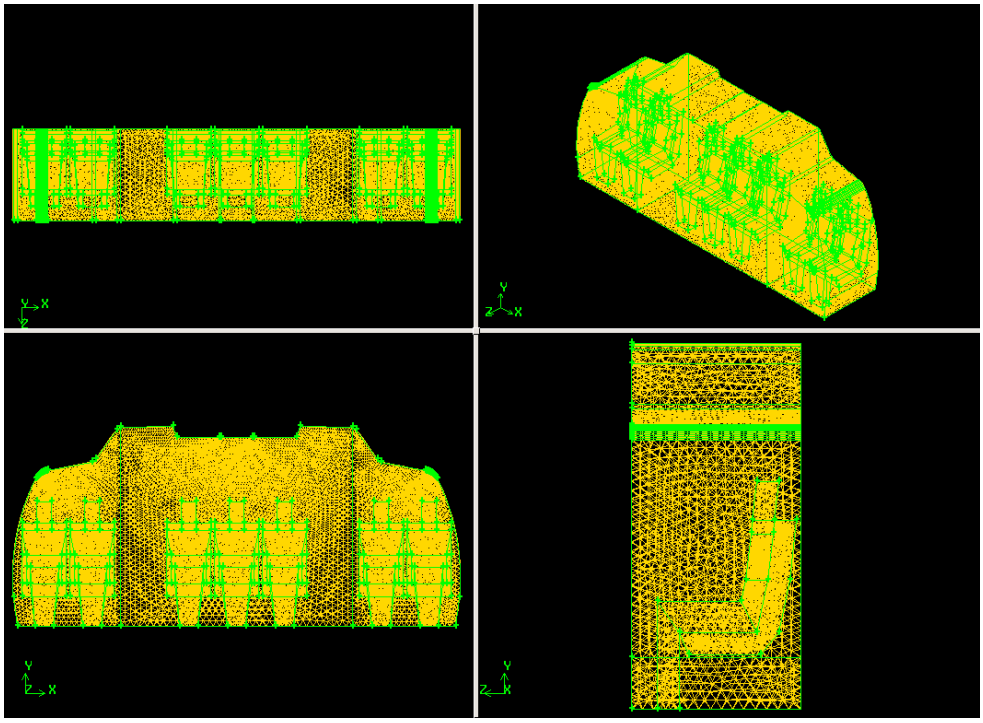

Figure 7.14 Different views of the generated unstructured grid for one row of the cabin

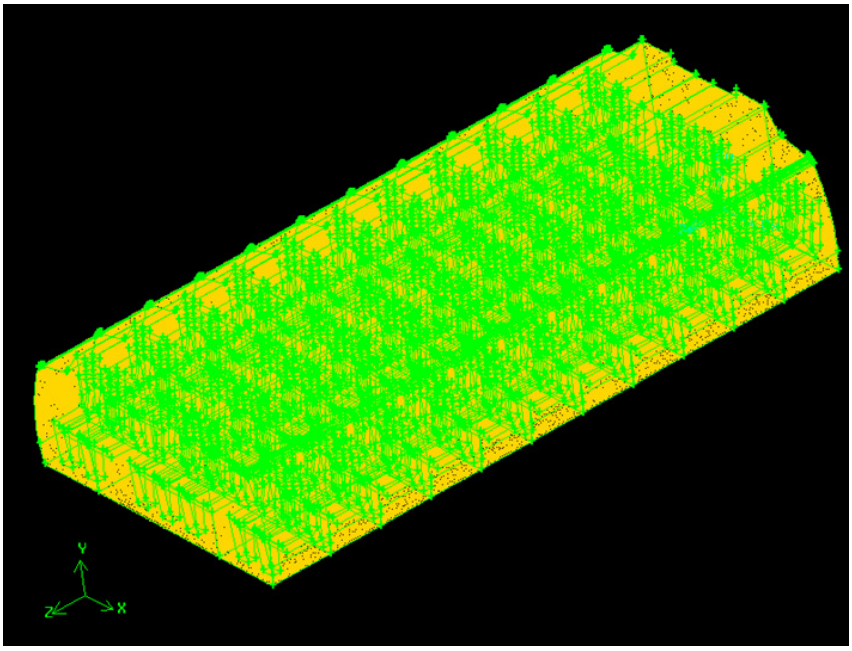

Figure 7.15 Generated unstructured grid for the whole cabin

The following assumptions were employed for the numerical simulation of three-dimensional turbulent airflow in the cabin. The assumptions are consistent with the existing conditions in the experiments:

1. The flow is assumed to be incompressible.
2. The heat transfer in the cabin is neglected. The inlet airflow is at the temperature of 27 ^{o}C.
3. The effects of buoyancy are taken into consideration.

A steady RANS method was used to solve the governing Navier-Stokes equations. The RNG k-ε model was applied as the turbulence model. The second order upwind scheme was used to discretize the spatial derivatives in the governing continuity and momentum equations. Also the non-equilibrium wall function was used as the near-wall treatment. The convergence criteria for all the continuity and momentum equations were set to 10^{-4}. In order to setup the boundary conditions at the outlet of East and West air diffusers, the airflow velocity, turbulent kinetic energy, and turbulent dissipation rate had to be specified at those locations. For this purpose, the airflow velocities measured at the outlet of the East and the West diffusers, presented in Fig. 7.17, were used. The velocity measurements were made with an omnidirectional probe. Figure 7.16 shows the position of the omnidirectional probe and the cabin air diffuser. Determination of velocity profile at the outlet of diffuser is a major challenge because, as it is obvious from Fig. 7.16, the omnidirectional probe was not located exactly at the outlet of diffuser. In this study we started the simulations assuming that the airflow velocities measured by the omnidirectional probe were the same as the airflow velocities at the diffuser outlet (or cabin inlet) and then the predicted velocity data at the position of omnidirectional probe were compared with the measurements. Based on this comparison the airflow velocity data at the diffuser outlet was corrected and the simulations were repeated. In Fig. 7.17, x-axis is the distance in meters from the south wall and y-axis is the total velocity in meter/sec (Draft Final Technical Report, Contaminant Transport in Airliner Cabins Project, Kansas State University, 2009). Figure 7.17a shows the velocity distribution for the south half of the cabin (0m – 4.75m) and Fig.7.17b shows the velocity distribution for the north half of the cabin (4.75m–9.5m). The data presented in Fig. 7.17 shows that the airflow velocity at the east diffuser varies between 0.25 and 2.5 m/s; however, for the west diffuser the mean velocity data varies between 0.25 and

2 m/s. In the simulations presented in this chapter, for each of the east and west diffusers the average velocity over the entire cabin length was calculated and then using Eqs (3.12)- (3.14) the boundary conditions for the east and west diffusers were calculated (see Table 7.3 which shows the first utilized boundary conditions). Figure 7.16 indicates that the airflow velocities at the outlet of the diffuser are in the x-direction.

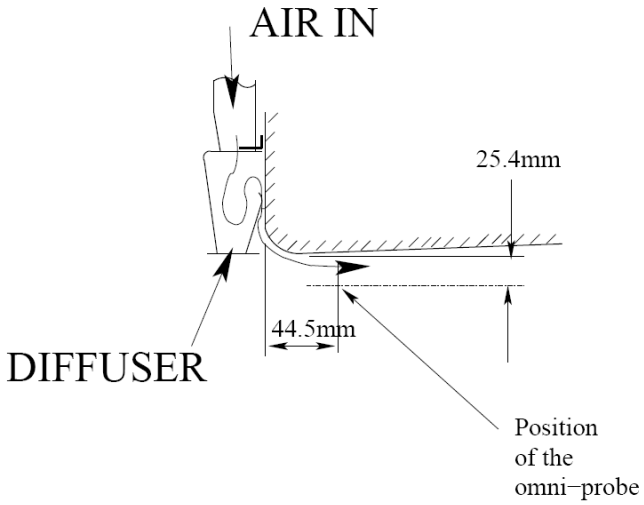

Figure 7.16 Measurement location of the omnidirectional probe. Direction of traverse is perpendicular to the paper (Draft Technical Report, 2009)

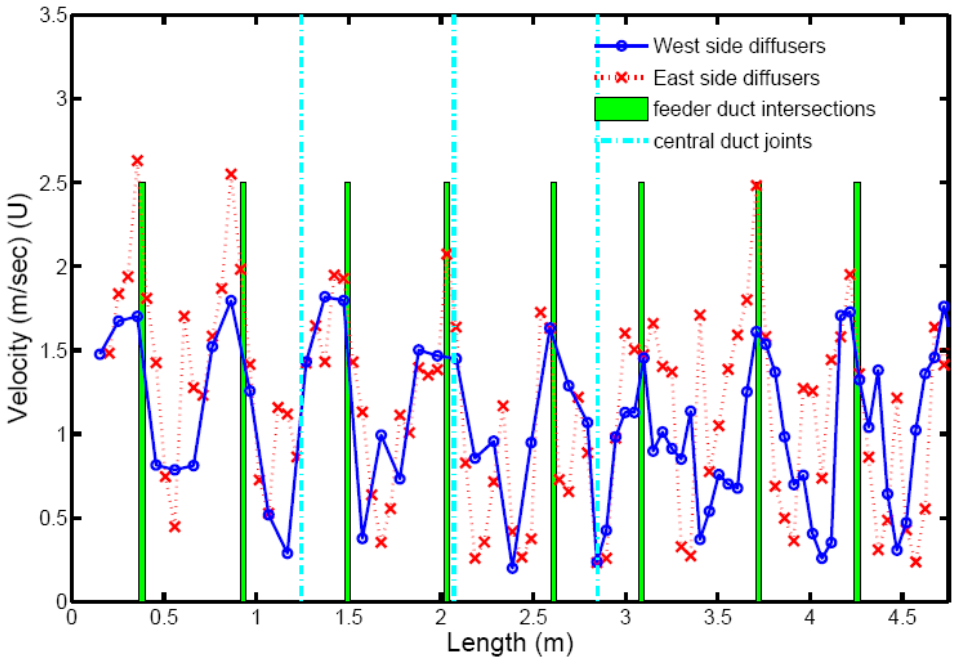

a: Comparison of span-wise mean velocity profiles between east and west side diffusers for the south half of the cabin.

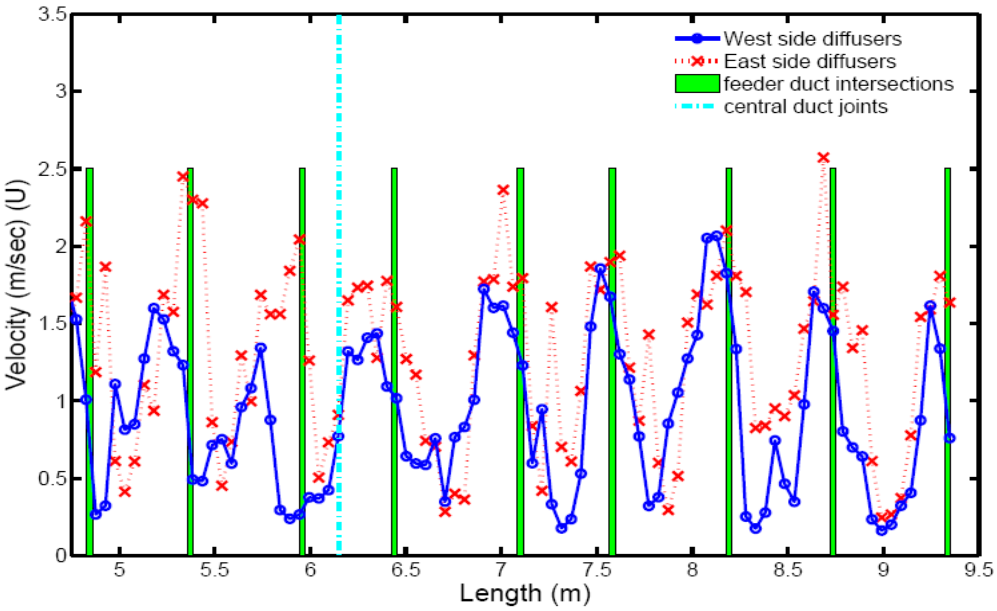

b : Comparison of span-wise mean velocity profiles between east and west side diffusers for the north half of the cabin.

Figure 7.17 Measured velocity data at the outlet of the cabin air diffusers (Draft Final Technical Report, 2009).

Table 7.3 First tried boundary conditions at the outlet of cabin air diffusers

	EAST DIFFUSER	WEST DIFFUSER
Average Velocity (m/s)	1.15	0.96
Turbulent Kinetic Energy (m^2/s^2)	0.0076	0.0055
Turbulent Dissipation Rate (m^2/s^3)	0.0614	0.0382

7.3. Airflow simulation results

As explained in details in the previous section, simulations are started using the omnidirectional probe measured velocity data and then based on the difference between the estimated and measured velocity data at the omnidirectional probe position, the boundary conditions for the diffuser outlet (or cabin inlet) are corrected. Figure 7.18 shows this comparison which corresponds to the east omnidirectional probe positions in the south of the

cabin. It is observed that the average of measured velocity data is ~ 6 times greater than the estimated velocity data. The reason of large difference is the strong influence of boundary condition created by the ceiling of the cabin.

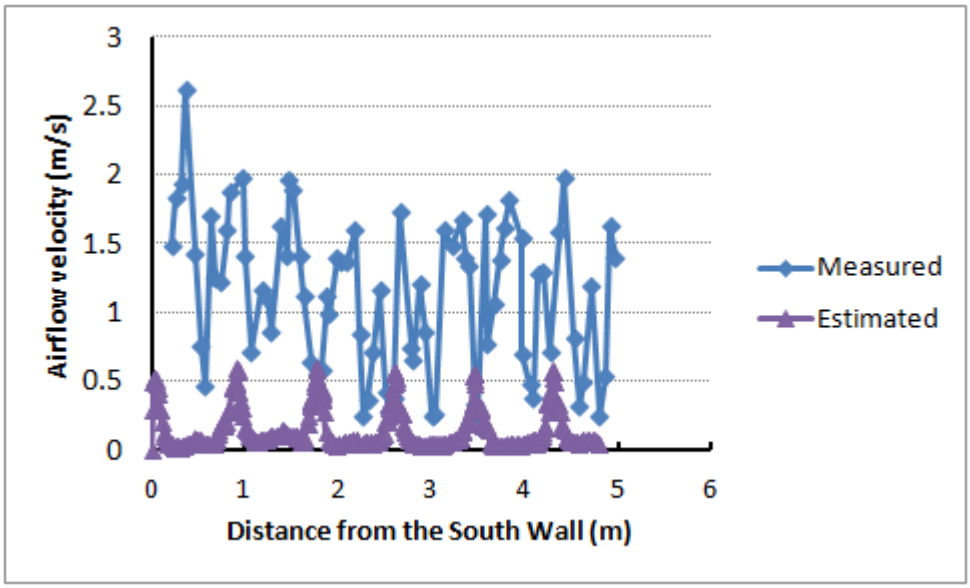

Figure 7.18 Comparison of measured and calculated velocity data at the omnidirectional probe position in the east side and south half of the cabin based on the boundary conditions presented in Table 7.3.

Based on the difference between predictions and measurements presented in Fig. 7.18, the cabin inlet velocity data were increased to the values tabulated in Table 7.4. The simulations were repeated using the new inlet boundary condition values for velocity, turbulent kinetic energy and dissipation rate.

Table 7.4 Second trial values for the inlet boundary condition

	EAST DIFFUSER	WEST DIFFUSER
Average Velocity (m/s)	7.3	6.1
Turbulent Kinetic Energy (m^2/s^2)	0.1929	7.8373
Turbulent Dissipation Rate (m^2/s^3)	0.1408	4.8914

Figure 7.19 shows the comparison between the estimated and measured velocity data corresponding to the east side position of omnidirectional probe in the south half of the cabin. For the predictions presented in this figure a grid with 5,438,000 mesh elements were used. The predictions are corresponding to two different values of the angle between jet and x-axis (0 and 45^{o}). This figure indicated that there is better agreement between predictions and measurements when an angle of 45^{o} is assumed for the jet of flow injected from the outlet of air diffusers. Therefore for the turbulent airflow simulations in the full-scale cabin mockup the angle between inlet airflow and x-axis is assumed to be 45^{o}.

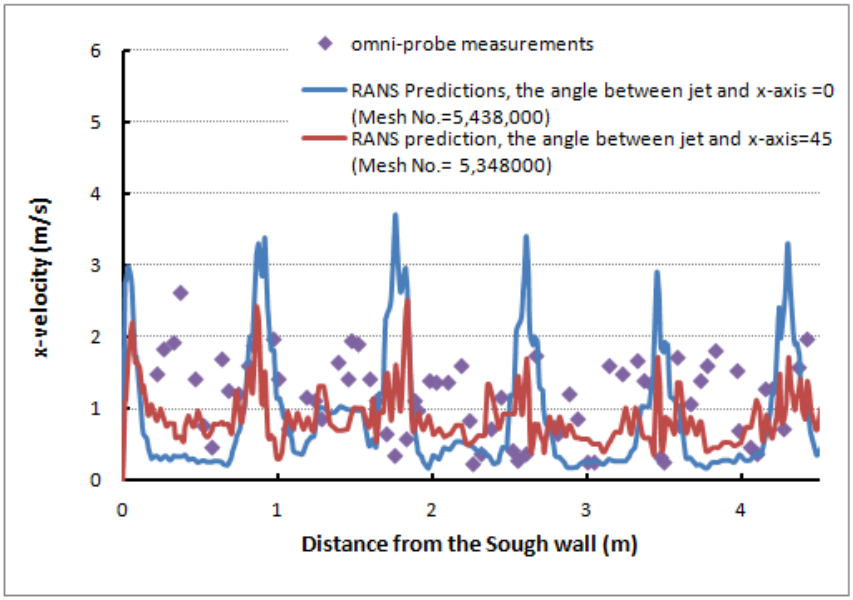

Figure 7.19 Comparison of measured and calculated velocity data at the omnidirectional probe position in the east side and south half of the cabin based on the boundary conditions presented in Table 7.4.

For the grid uncertainty analysis, the velocity distribution along a lateral line located at the height of 1.65 m and z=3 m was calculated using three different sizes of grids, i.e., 2630000, 3667000, and 5438000. Figure 7.20 shows the comparison between the predicted velocity distributions for the examined grids.

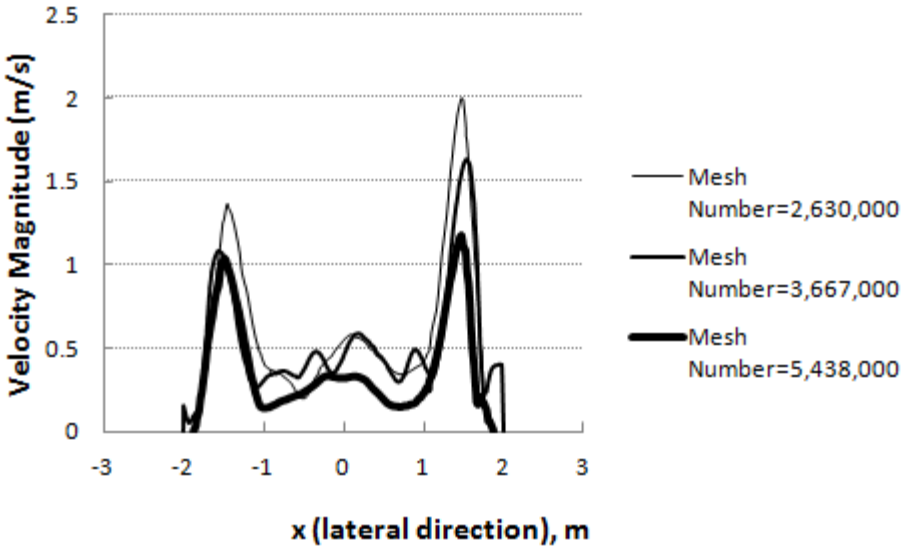

Figure 7.20 Comparison between predictions for the lateral velocity predictions from three examined grids and experimental data (y=1.65m).

Considering Fig. 7.21 which shows the experimentally determined lateral velocity distribution and comparing that to the calculated velocity distribution presented in Fig. 7.20 indicate that the RANS model was successful to predict two peaks in lateral velocity distribution.

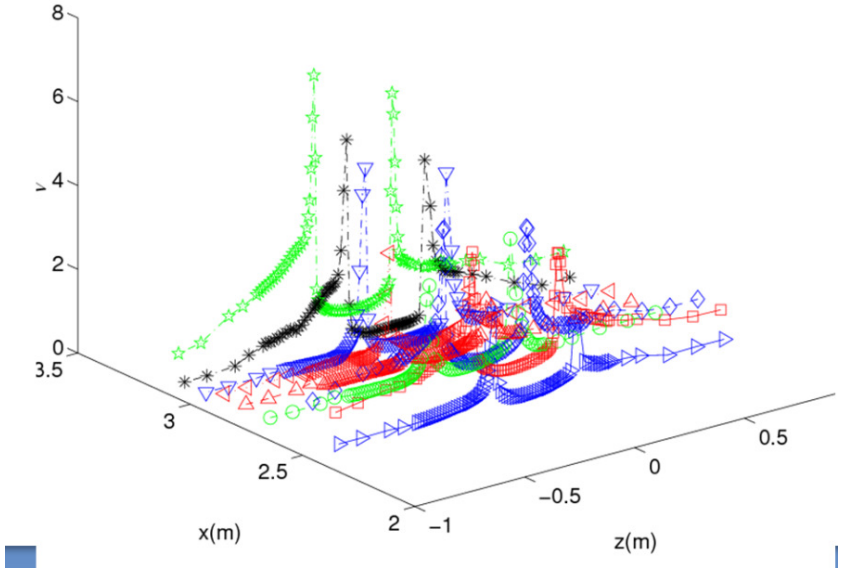

Figure 7.21 Experimentally determined lateral distribution of velocity data in full-scale cabin mockup.

Using the boundary conditions indicated by Table 7.4, and considering an angle of 45^{o} between the x-axis and the injected airflow at the inlet of the cabin, the contours of velocity magnitudes on two cross sections of the cabin are shown in Figs. 7.22 and 7.23. One of the cross sections is between rows 2 and 3 and the other is the cross section at the second row. Figs. 7.24 and 7.25 show the grid distribution corresponding to these planes.

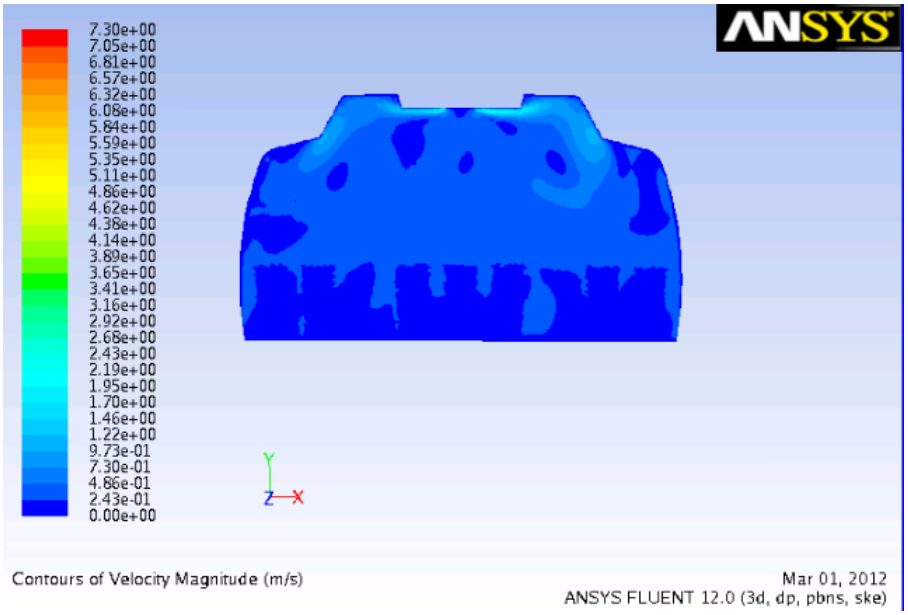

Figure 7.22 Contours of velocity magnitude on plane z=7.6715895 m (between rows 2 and 3, the distance between the plane and the sough wall is 1.828 m)

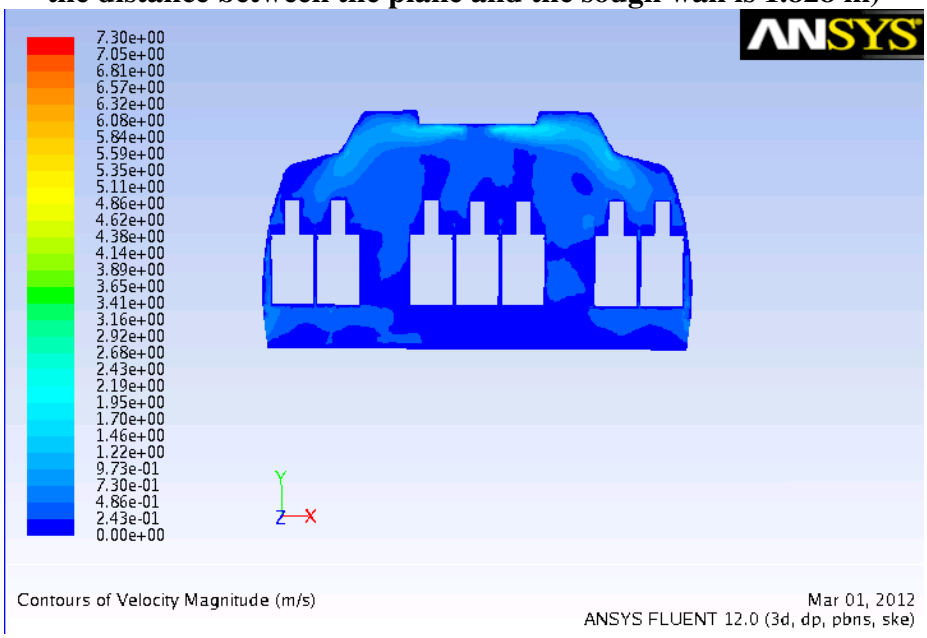

Figure 7.23 Contours of velocity magnitude on plane z=7.00 m (rows 2, the distance between the plane and the sough wall is 2.4996 m)

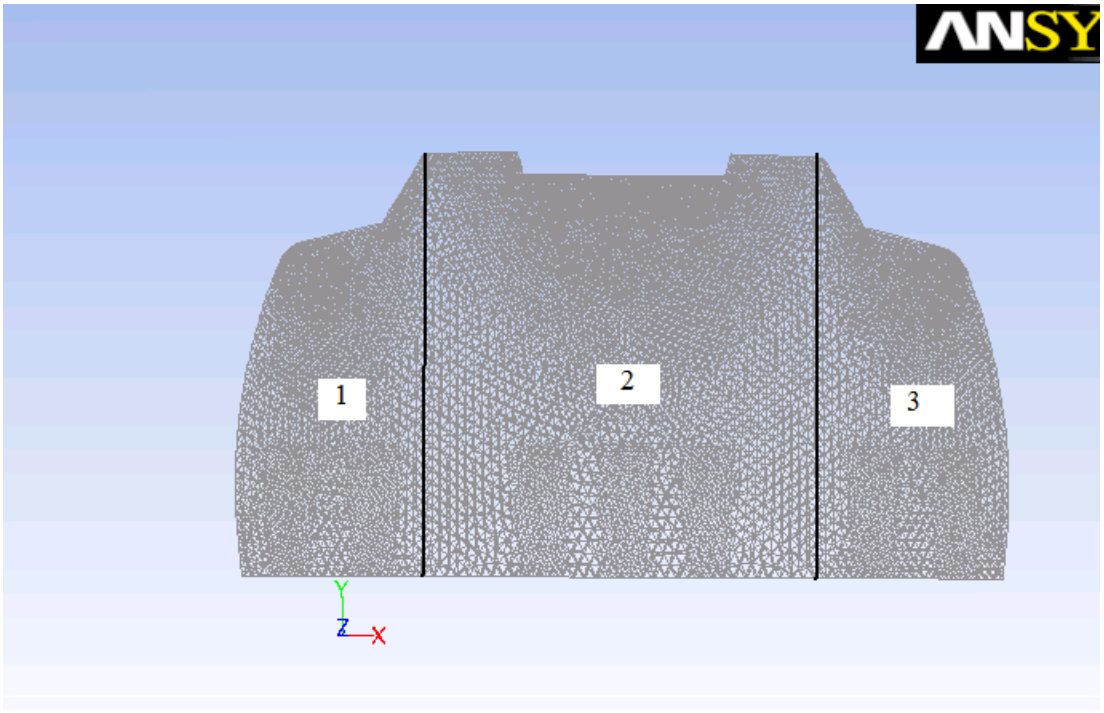

Figure 7.24 The grid distribution on plane z=7.6715895 m (between rows 2 and 3, the distance between the plane and the sough wall is 1.828 m)

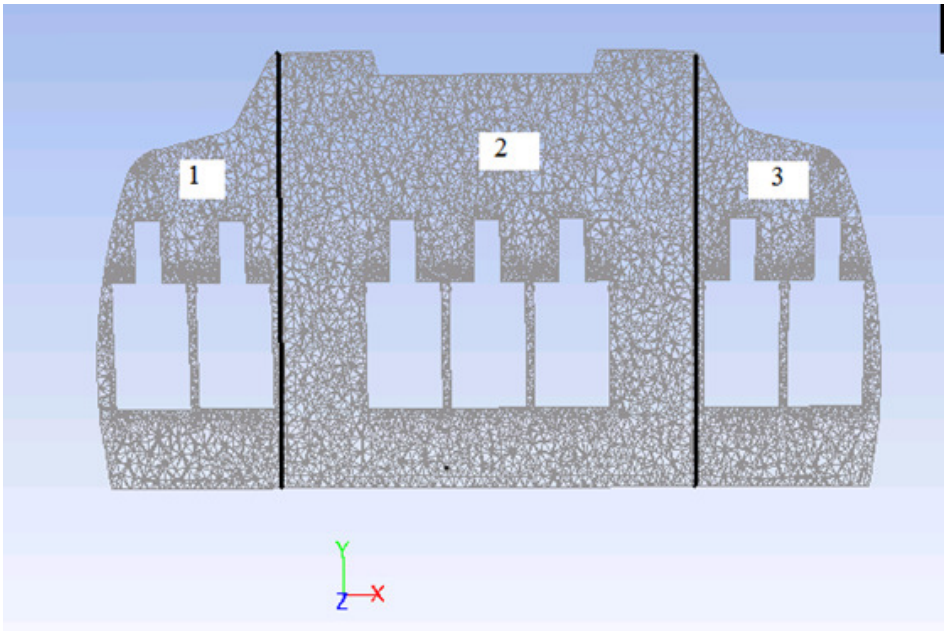

Figure 7.25 The grid distribution on plane z=7.00 m (rows 2, the distance between the plane and the sough wall is 2.4996 m)

7.4. Summary

In this chapter the details of geometry and grid generation for the full-scale aircraft cabin mockup were presented. The entire cabin volume was divided into 11 rows and each row was divided into 3 parts; therefore, the entire cabin volume was divided into 33 sub-volumes for the grid generation. The generated mesh was used for the simulation of airflow while steady RANS was applied to solve the governing Navier-Stokes equations. The simulations started with ~ 11 million hybrid/tetrahedral mesh elements of T-Grid type, but since that size of grid was beyond the computational capacity of the computers used for the simulations, the number of mesh elements was decreased. Three different sizes of grids were examined for grid uncertainly purposes. The number of mesh elements in all three examined grids was 6×10^6. Since the velocity data at the outlet of the air diffusers were not known, the mean velocity data measured by the omnidirectional probe were used to determine the boundary conditions at the inlet of the cabin initially. Then, based on the difference between measured and estimated velocity data at the omnidirectional probe position, the boundary conditions at the inlet of the cabin were corrected and the simulations were repeated.

Chapter 8 - Conclusions

The main purpose of this research was computational modeling of complex turbulent transport phenomena in aircraft cabin environments. In order to accomplish the research objectives, in the first phase, the turbulent airflow in a Boeing767 generic half-cabin was simulated using RANS and LES methods. Then, in the second phase, the diffusion of a tracer gas (CO_2) was simulated through the solution of species transport equation along with Navier-Stokes equations. In the third phase, the turbulent dispersion of micron size spherical DOP particles was modeled using DPM. Finally, in the fourth phase, the turbulent airflow inside a full-scale 11-row Boeing 767 aircraft cabin mockup was simulated using a RANS method. In this chapter, the conclusions that were derived in each phase of the research are listed, as well as recommendations for the future research in this area.

Through the validation of simulations in the first phase it was concluded that

- LES with the Werner-Wengle wall function can predict the unsteady airflow velocity field with relative high accuracy.
- The errors associated with the RANS method are much more than that of LES.
- Amongst the three different k-ε models: standard, RNG and Realizable, the RNG k-ε leads to the most accurate predictions.
- Monitoring the PIV windows' center point values of LES predictions, leads to better agreement between the LES predictions and PIV measurements for the instantaneous velocity data comparing to the case when the corresponding PIV windows' area-averaged values are monitored. However, there is no difference between the two monitoring schemes in predicting the general behavior of airflow velocities.
- Due to the more complex flow-structure in the middle of the cabin, the agreement between the LES predictions and PIV measurements is not as good as that for other PIV locations. A local refinement in grid size is recommended to get more accurate results in this region in the future.

- Studying the effect of halving the cabin inlet nozzle height on the airflow behavior, while the airflow rate remains unchanged, indicated that by halving the nozzle height and consequently doubling the inlet velocity, the magnitude of flow velocities in PIV locations 1 and 4 increased dramatically (by 100%). However, in PIV locations 2 and 5, the increase in the velocity value is slight and not as much. It was also realized that the airflow located in PIV location 3 that used to be almost stationary in the full-height nozzle case has the tendency of moving to the upper left corner of the cabin model.

In the second phase, the capability of CFD modeling in simulating the tracer gas (CO_2) diffusion was studied. For this purpose, the species transport model was used with LES to predict the instantaneous tracer gas concentration data at specified sampling locations in the cabin:

- Although the comparisons between the tracer gas concentration predictions and measurements indicated an excellent agreement at some sampling points, the average error at some other sampling locations was much higher and error values up to ~23% were observed.
- Since the flow in the middle of cabin has more complexities comparing to the flow in other locations, the predictions in that region is more sensitive to the mesh size. Therefore, regional mesh refinement for the PIV location 3 is recommended in order to get more accurate predictions.

In the third phase, dispersion of inert micron-size spherical particles was simulated using DPM. The effects of turbulence were calculated through the application of the DRW model. The RANS method was used to calculate the continuous-phase (airflow) velocity field. Through the simulations for the cabin with straight particle injection tube the following conclusions were reached:

- The regional mesh refinement enabled us to have more control on the number and the type of the mesh elements. Using the regional mesh refinement reduces the number of mesh elements that normally results in increased computational cost and time.

- Unstructured regional mesh refinement not only leads to the more accurate and reliable results , but also is considerably more computational time and cost effective than the structured regional mesh refinement.
- Considering the measurement uncertainty, good agreement between the predictions and measurements for the APS locations 2, 3, and 4 (on the cabin central plane) was observed. For the APS location 1, due to the fact that the experimental measurements are very small, achieving predictions with good accuracy for this location was difficult.
- Although increasing the number of tries in DRW model has a positive effect on improving the average accuracy, beyond a specific number of tries (which is called as the optimum number of tries in which the average error has its minimum value) an increase in the number of tries does not necessarily improve the average accuracy.
- Due to very low volume fraction of particles, the effect of the discrete phase on the continuous phase is negligible and the particle concentration predictions from 1-way and 2-way coupling schemes are the same.
- The DPM simulation results for the smaller size particles (3 μm particles compared with 10 μm particles) showed better agreement with the corresponding experimental results.
- The DPM simulations also confirmed the outcome of the previously performed experimental study in which it was observed that smaller particles distributed more uniformly than the larger particles. In other words, smaller particles have better mixing behavior with air circulation in the cabin.

In the third phase and through the simulations for the particle injection using the cone diffuser, the following conclusions were achieved:

- Through a detailed study, carried out to obtain an optimum number for the number of tries in the DRW, it was realized that the optimum number of tries was 175 for both cases of pressurized and non-pressurized cabin.
- The agreement between the DPM predictions and APS measurements experienced an improved by increasing the cabin gage pressure from 0 and 0.025 in of H_2O.
- Through the investigation of the effect of particles density on distribution behavior of micron-sized particles it was determined that the distribution behavior is not a strong function of particle density.

In the fourth and last phase, geometry of the full-scale 11-row cabin was produced and the corresponding computational grid was generated. The generated mesh was used for the simulation of airflow using steady RANS. The calculated velocity data can be used as the initial condition for future tracer gas diffusion and particle dispersion measurements.

References

Abdilghanie, A.M., & Collins, L.R., & Caughey, D.A. (2009). Comparison of Turbulence Modeling Strategies for Indoor Flows., J. Fluids Eng.-Trans. ASME, 131,.051402-1:051402-18.

Aboosaidi, F., & Warfield, M, & Choudhury, D. (1991). Computational fluid dynamics applications in airplane cabin ventilation system design. Proceedings of Society of Automotive Engineers. 246, 249-258.

ANSYS FLUENT 12.0 Manual, April 2009, ANSYS Inc.

Baker, A.J., & Taylor, M.B., & Winowich, N.S., & Heller,M.R. (2000). Prediction of the distribution of indoor air quality and comfort in aircraft cabins using computational fluid dynamics. Air Quality and Comfort in Airliner Cabins, ASTM STP 1393, N. L. Nagda, Ed., ASTM.

Baker, A.J., & Ericson S.C., & Orzechowski, J.A., & Wong, K.L., & Garner R.P. (2006). Aircraft passenger cabin ECS-generated ventilation velocity and mass transport CFD simulation: velocity field validation. Journal of the IEST. 49(2), 51-83.

Beneke, J.M (2010). Small diameter particle dispersion in a commercial aircraft cabin. MS thesis, Kansas State University. Manhattan, Kansas.

Bird, B.R., & Steward, W.E., & Lightfoot, E.N. (2001). Transport Phenomena, 2nd Edition, John Wiley and Sons, NY.

Boeing company website (http://boeing.com/ visited Nov. 13, 2011).

Chen, X., & Chen, Q. (2010). Comparison of different delivery methods for sterilizing unoccupied commercial airliner cabins. Building and Environment. 45(9), 2027-2034.

Chen, F., & Lai, A.C.K. (2004). An Eulerian model for particle deposition under electrostatic and turbulent conditions. J. Aerosol Sci., 35, 47-62.

Chen, F., & Simon C.M., & Lai, A.C.K. (2006). Modeling particle distribution and deposition in indoor environments with a new drift-flux model. Atmospheric Environment, 40, 357-367.

Clayton. C., & Sommerfeld. M., & Tsuji. Y. (1998). Multiphase Flows, CRC Press, USA.

Daly, B.J., & Harlow, F.H. (1970). Transport Equations of Turbulence. Phys. Fluids, 13, 2634-2649.

Dehbi, A. (2008). A CFD model for particle dispersion in turbulent boundary layer flows. Nuclear Engineering and Design, 238(3), 707-715.

De Stefano, G., & Denaro, F.M., & Riccardi, G. (1998). Analysis of 3D backward-facing step incompressible flows via a local averaged-based numerical procedure. Int. J. Numer. Meth. Fluids, 28, 1073-1091.

Duguid, J.P. (1946). The size and the duration of air-carriage of respiratory droplets and droplet-nuclei. Journal of Hygiene, 44(6), 471-479.

Emmons, W.H. (1982). The Ingestion of Flames and Fire Gases into a Hole in an Aircraft Cabin for Tilt Angles and Wind Speed. Technical Report Number 52.

Fabian, P., & McDevitt, J.J., & Dehaan, W.H., & Fung, R.O.P., & Cowling, B.J., & Chan, K.H., & Leung, G.M., & Milton, D.K.(2008). Influenza virus in human exhaled breath: an observational study. PLoS ONE, 3(7), e2691.

FLUENT 6.3 User's Manual, 2011, FLUENT Inc.

Friedrich, R. & Arnal, M. (1990) Analyzing turbulent backward-facing step flow with the lowpass-_ltered Navier-Stokes equations. J. Wind Engng Indust. Aerodyn, 35, 101-128.

Garner, R.P., & Wong, K. L., & Ericson, S.C., & Baker, A.J, & Orzechowaki, J.A. (2004). CFD Validation for Contaminant Transport in Aircraft Cabin Ventilation Fields. Report No. DOT/FAA/AM-04/7, U.S. Department of Transportation and Federal Aviation Administration, Office of Aerospace Medicine, Washington DC.

Gorle, C., & van Beeck, J., & Rambaud, P., & Van Tendeloo, G. (2009). CFD modeling of small particle dispersion: The influence of turbulence kinetic energy in the atmospheric boundary layer. Atmospheric Environment, 43, 673-681.

Gupta, J.K., & Lin, C.H., & Chen, Q. (2009). Flow dynamics and characterization of a cough. Indoor Air. 19, 517-525.

Gupta, J.K., & Lin, C.H., & Chen, Q. (2010). Characterizing exhaled airflow from breathing and talking. Indoor Air. 20, 31-39.

Gupta, J.K., & Lin, C.H., & Chen, Q., (2011a). Inhalation of expiratory droplets in aircraft cabin. Indoor Air. 21(4), 341-350.

Gupta, J.K., & Lin, C.H., & Chen, Q. (2011b). Transport of expiratory droplets in an aircraft cabin. Indoor Air. 21(1), 3-11.

Holmberg, S., & Li, Y. (1998). Modelling of indoor environment - particle dispersion and deposition. Indoor Air, 8, 113-122.

Horstman, R.H. (1988). Predicting velocity and contaminant distribution in ventilated volumes using Navier-Stokes equations. Proceeding of ASHRAE Conference IAQ 88. April 11-13, Atlanta, Georgia, 209-230.

Hulsman, M., & Bos, M., & van der Linden, E. (1997). Dispersion behaviour of solid particles in flow-injection analysis. Analytica Chimiza Acta, 346, 351-360.

Ishiko K., & Ueno, K., & Sawada, K. (2008). Implicit LES of compressible turbulent flow over a backward-facing step. 47th AIAA Aerospace Science Meeting Including The New Hosizons and Aerospace Exposition, Orlando, Florida.

Jongebloed, L. (2008). Numerical study using FLUENT of the separation and reattachment points for backward-facing step flow. Master of Engineering thesis. Rensselaer Polytechnic Institute, Hartford, Connecticut.

Kaiktsis, L., & Karniadakis, G. E., & Orszag, S. A. (1991). Onset of three-dimensionality, equilibria,and early transition in flow over a backward-facing step. J. Fluid Mech., 231, 501-528.

Keating, A., & Piomelli, U., Bremhorst, K., & Nesic, S. (2004). Large-eddy simulation of heat transfer downstream of a backward-facing step. J. Turbulence, 5(20), 1-28.

Khan, K., & Arino, J., & Hu, W., et al. (2009). Spread of a novel influenza A (H1N1) virus via global airline transportation. New England Journal of Medicine, 361(2), 212–214.

Kim, J., & Mion, P. (1985). Application of a fractional-step method to incompressible Navier-Stokes equations. J. Comp. Physics, 59, 308-323.

Kim, J.Y., & Ghajar, A.J., & Tang, C., & Foutch, G.L. (2005). Comparison of near wall treatment methods for high Reynolds number backward-facing step flow. Int. J. Comp. Fluid Dynamics, 19(7), 493-500.

Lai, A.C.K., & Nazaroff, W.W. *(*2000). Modeling indoor particle deposition from turbulent flow on to smooth surfaces*,* J. Aerosol Sci.*,* 31*,* 463–476.

Lain, S., & Grillo, C.A. (2007). Comparison of turbulent particle dispersion models in turbulent shear flows. Brazilian J. Chem. Eng., 24(3), 351-363.

Lan, H., & Armaly, B.F., & Drallmeier J.A. Three-dimensional simulation of turbulent forced convection in a duct with backward-facing step. Int. J. Heat & Mass Transfer, 52, 1690-1700.

Landahl, M.T. , Mollo-Christensen, M., 1992, Turbulence and Random Processes in Fluid Mechanics, 2nd Edition, Cambridge, UK.

Launder, B.E., Spalding, D.B., 1972,"Lectures in Mathematical Models of Turbulence," Academic Press, London, England.

Le, H., & Moin, P., & Kim, J. (1997). Direct numerical simulation of turbulent flow iover a backward-facing step. J. Fluid Mech., 330, 349-374.

Lebbin, P.A., 2006, “Experimental and Numerical Analysis of Air, Tracer Gas and Particulate Movement in a Large Eddy Simulation Chamber”, PhD dissertation, Kansas State University. Manhattan, Kansas.

Lilly, D.K, 1966, “On the Application of the Eddy Viscosity Concept in the Internal Sub-range of Turbulences”, National Center for Atmospheric Research, Manuscript No.123.

Lin, C.H., Horstman, R.H., Ahlers, M. F., Sedgwick, LM., Dunn, K.H., Topmiller, J.L, Bennett, J.S., Wirogo, S.,(2005), Numerical Simulation of Airflow and Airborne Pathogen Transport in Aircraft Cabins- Part I: Numerical Simulation of the Flow Field. ASHRAE Transactions, 111, pp: 755-763.

Lin, C.H., Horstman, R.H., Ahlers, M. F., Sedgwick, LM., Dunn, K.H., Topmiller, J.L, Bennett, J.S., Wirogo (2005), Numerical Simulation of Airflow and Airborne Pathogen Transport in Aircraft Cabins- Part II: Numerical Simulation of Airborne Pathogen Transport, ASHRAE Transactions, 111, pp: 764-768.

Lin, C.H., Horstman, R.H., Lebbin, P.A., Hosni, M.H., Jones, B.W, Beck, B.T., 2006, “Comparison of Large Eddy Simulation Predictions with Particle Image Velocimetry Data for the Airflow in a Generic Cabin,” HVAC&R Special Issue, 12(3c), pp: 935-951.

Liu, X., & Zhai, Z. (2007). Identification of appropriate CFD models for simulating aerosol particle and droplet indoor transport. Indoor and Built Environment, 16(4), 322-330.

Liu, W., & Mazumdar, S., & Zhang, Z., & Poussou, S.B., & Liu, J.,& Lin, C.H., Chen, Q. (2012). State-of –the-art methods for studying air distributions in commercial airliner cabins, Building and Environment. 47, 5-12.

Marchioli, C., & Picciotto, M., & Soldati, A. (2007). Influence of gravity and lift on particlevelocity statistics and transfer rates in turbulent vertical channel flow. Int. J. Multiphase Flow, 33 (3), 227–251.

Mazumdar, S., & Chen, Q. (2008). Influence of cabin conditions on placement and response of contaminant detection sensors in a commercial aircraft. Journal of Environmental Monitoring. 10, 71-81.

Mazumdar, S., & Chen, Q. (2009). A one-dimensional analytical model for airborne contaminant transport in airliner cabins. Indoor Air. 19(1), 3-13.

Mazumdar, S., & Pousso, S., & Lin, C.H., & Isukapalli, S.S., & Chen, Q. (2011). The impact of scaling and body movement on contaminant transport in airliner cabins. Atmospheric Environment. 45(33), 6019-6028.

Minier, J.P., & Peirano, E., (2001). The PDF approach to turbulent poly-dispersed two-phase flows. Physics Reports, 352, 1-214.

Mizuno, T., & Warfield M.J. (1992). Development of three-dimensional thermal airflow analysis computer program and verification test, ASHRAE Trans. 98, 329-338.

National Transportation Statistics, Bureau of Transportation, (http://www.bts.gov, visited June 10, 2011).

National Research Council, 2002 Edition (http://www.nationalacademies.org/nrc/).

Nie, J.H., & Armaly, B.F. (2004). Reverse flow regions in three-dimensional backward-facing step flow. Int. J. Heat & Mass Transfer, 47, 4713-4720.

Naval Air Station Wildwood (NASW) Aviation Museum website (http://usnasw.org/, visited Nov.13, 2011).

Occupational Outlook Handbook, Bureau of Labor Statistics, 2010-11 Edition (http://www.bls.gov/oco/ocos107.htm, visited June 10, 2011).

Olsen, S.J., & Chang, H., & Cheung, T.Y., et al. (2003). Transmission of the Severe Acute Respiratory Syndrome on Aircraft. New England Journal of Medicine, 349(25):2416-2422.

Padilla, A. (2008). Experimental analysis of particulate movement in a large eddy simulation chamber. MS thesis, Kansas State University. Manhattan, Kansas.

Patankar, S.V., & Spalding, D.B. (1972). A calculation procedure for heat, mass and momentum transfer in three-dimensional parabolic flows. Int. J . Heat Mass Transfer. 15, 1787-1806.

Pousso, S., & Mazumdar, S., & Plesniak, M.W., & Sojka, P., & Chen, Q. (2010). Flow and contaminant transport in an airliner cabin induced by a moving body: scale model experiments and CFD predictions, Atmospheric Environment, 44(24), 2830-2839.

Rani, H.P., & Tony, Sheu, T.W.H., & Tsai, E.S.F. (2007). Eddy structures in a transitional backward-facing step flow. J. Fluid Mech., 588, 43-58.

Razzak, S.A., & Zhu, J.X., & Barghi, S. (2010). Effects of particle shape, density and size on a distribution of phase holdups in a gas-liquid-solid circulating fluidized bed riser. Ind. Eng. Chem. Res., 49, 6998, 7007.

Reynolds, A.M. (1997). A Lagrangian stochastic model for particle trajectories in non-Gaussian Turbulent flows. Fluid Dynamics Research, 19(5), 277-288.

Shehadi, M. (2010). Experimental investigation of optimal particulate sensor location in an aircraft cabin. MS thesis, Kansas State University. Manhattan, Kansas.

Shih, T.H., Lieu, W.W., Shabbir, A., Yang, Z., Zhu, J., 1995, “A New k-ε Eddy-Viscosity Model for High Reynolds Number Turbulent Flows - Model Development and Validation" J. Computers & Fluids, 24(3), pp: 227-238.

Singh, A.,& Hosni, M.,& Horstman, R. (2002). Numerical simulation of airflow in an aircraft cabin section. ASRAE Transaction, 108(1) , 1005-1013.

Smith, K.M., & Davidson, M.R., & Fletcher, D.F. (1997). Dispersion of solid streams falling into a stationary liquid. Inter. Conf. on CFD in Mineral & Metal Processing Power Generation, CSIRO.

Sommerfeld, M., & Kohnen, G.,& Rüger, M. (1993). Some open questions and inconsistencies of Lagrangian particle dispersion models. Proc. 9th Symposium on Turbulent Shear Flows, Kyoto, Japan, paper 15-1.

Smagorinsky, J., 1963, "General Circulation Experiments with the Primitive Equations: I. The Basic Experiment", Monthly Weather Review, 91, pp: 99-164.

St John R K, & King A, & de Jong D, & Bodie-Collins M, & Squires S G, & Tam T W S. (2005) Border screening for SARS Emerging Infectious Diseases, 11:6–10.

Su, M., Chen, Q., & Chiang, C.M. (2001). Comparison of Different Sub-Grid-Scale Models of Large Eddy Simulation for Indoor Airflow Modeling. J. Fluids Eng.-Trans. ASME, 123, pp: 628-639.

Tang, Y., Ratko, D., Wang, X., 2009, "3D Numerical Simulation of Contaminant Distribution in an Aircraft", Proceedings of the ASME 2009 International Mechanical Engineering Congress & Exposition, Lake Buena Vista, Florida, pp: 31-36.

Thomson, D.J. (1987). Criteria of the selection of stochastic models of particle trajectories in turbulent flow. J. Fluid Mech., 180, 529-556.

Toy, R., & Hayden, E., & Shoup, C., & Baskaran, H., & Karathanasis, E. (2011). The effects of particle size, density and shape on margination of nanoparticles in microcirculation. Nanotechnology, 22(11), 1-9.

Trupka, A.T. (2011). Tracer gas mapping of beverage card wake in a twin aisle aircraft cabin simulation chamber. MS thesis, Kansas State University. Manhattan, Kansas.

TSI VOAG Model 3450 Manual. (2011). Chapter 4: Operating the aerosol generator.

Tu, J., & Yeoh, G.H., & Liu, C. (2008). Computational fluid dynamics – A practical approach. Butterworth-Heinemann, USA.

Wang, A., & Zhang, Y., & Topmiller, J., & Bennet. J, & Dunn, K. (2006). Tracer study of Airborne disease transmission in an aircraft cabin mock-up . ASHRAE Transaction, 112(2), 697-705.

Werner. H., Wengle, H., 1991, "Large Eddy Simulation of Turbulent Flow Over and Around a Cube in a Plate Channel", 8th Symposium on Turbulent Shear Flows, Munich, Germany.

WHO. (2004). Summary of probable SARS cases with onset of illness from 1 November 2002 to 31 July 2003, 21 April (http://www.who.int/csr/sars/country/table2004_04_21/en/) Accessed 20 December 2004.

Wilcox, D.C. (1998). Turbulence modeling for CFD. 2nd edition. DCW Industries, La Canada, California.

Yan, W., Zhang, Y., Sun, Y., Li, D., 2009, "Experimental and CFD Study of Unsteady Airborne Pollutant Transport within an Aircraft Cabin Mock-up", J. Building and Environment, 44, pp:34-43.

Yang, K.T., & Lloyd, J.R., & Kanury, A.M., & Satoh, K. (1984). Modeling of turbulent buoyant flows in aircraft cabins. Combustion Science and Technology. 39, 107-118

Yang, S., & Lee, GWM., & Chen, C.M., & WU, C.C., & Yu, K.P.(2007). The size and concentration of droplets generated by coughing in human subjects. Journal of Aerosol Medicine, 20(4), 484-494.

Yakhot, V., & Orszag., S.A. (1986). Renormalization group analysis of turbulence: I. Basic theory. J. Scientific Computing, 1(1), 1-51.

Yoo, J. Y., & Choi, H.C., & Han, S.M. (1989). Numerical Analysis of Turbulent Flow over a Backward-Facing Step Using Reynolds Stress Closure Model. KSME J., 3, pp. 31-37.

Zhang, T., & Chen, Q. (2007). Identification of contaminant sources in enclosed spaces by a single sensor. Indoor Air. 17(6), 439-449.

Zhang, T., & Chen, Q., & Lin. C.H. (2007) Optimal sensor placement for airborne contaminant detection in an aircraft cabin. HVAC&R Research. 13(5), 683-696.

Zhang, T., & Lee, K., & Chen, Q.(2008). A simple method to simulate complex air diffusers used for underfloor air distribution system. Proceeding of the 11th International Conference on Indoort Air Quality and Climate (Indoor Air 2008), paper 670, 8 pages, Copenhagen, Denmark.

Zhang, Z., & Chen, X., & Mazumdar, S., & Zhang, T., & Chen, Q. (2009). Experimental and numerical investigation of airflow and contaminant transport in an airliner cabin mockup. Building and Environment. 44(1), 85-94.

Zhao, B., & Li, X., & Yan, Q. (2003). A simplified system for indoor airflow simulation. Building and Environment, 38, 543-552.

Zhao, B., & Zhang, Y., & Li, X., & Yang, X., & Huang, D. (2004a). Comparison of indoor aerosol particle concentration and deposition in different ventilated rooms by numerical methods. Building and Environment, 39, 1-8.

Zhao, B., & Li, X., & Zhang, Y. (2004b). Numerical study of particle deposition in two differently ventilated rooms. Indoor and Built Environment, 13, 443-451.

Zhao, B., & Chen, C., & Tan, Z. (2009). Modeling of ultrafine particle dispersion in indoor environments with an improved drift flux model. J. Aerosol Sci.,40, 29-43.

Zhang, N., & Zheng, C., & Glasgow, L., & Braley, B. (2010). Simulation of particle deposition at the bottom surface in a room-scale chamber with particle injection. Advanced Powder Technology, 21, 256-267.

Appendix A - Peer Reviewed Article (submitted for publication)

A Computational Study of Turbulent Airflow and Tracer Gas Diffusion in a Generic Aircraft Cabin Model

Khosrow Ebrahimi[4]
ASME Student Member
e-mail: khe1976@ksu.edu
Department of Mechanical and Nuclear Engineering
Kansas State University

Zhongquan C. Zheng
ASME Fellow
e-mail:zzheng@ku.edu
Department of Aerospace Engineering
University of Kansas

Mohammad H. Hosni
ASME Fellow
e-mail: hosni@ksu.edu
Department of Mechanical and Nuclear Engineering
Kansas State University

ABSTRACT

In order to study the capability of computational methods in investigating the mechanisms associated with disease and contaminants transmission in aircraft cabins, the Computational Fluid Dynamics (CFD) models are used for the simulation of turbulent airflow and tracer gas diffusion in a generic aircraft cabin mockup. The CFD models are validated through the comparisons of the CFD predictions with corresponding experimental measurements. It is found that using Large Eddy Simulation (LES) with the Werner-Wengle wall function, one can predict unsteady airflow velocity field with relatively high accuracy. However in the middle region of the cabin mockup, where the recirculation of airflow takes place, the accuracy is not as good as that in other locations. By examining different k-ε models, the current study recommends the use of the RNG k-ε model with the non-equilibrium wall function as a RANS model for predicting the steady-state airflow velocity. It is also found that changing the nozzle height has a significant effect on the flow behavior in the middle and upper part of the cabin, while the flow pattern in the lower part is not affected as much. Through the use of LES and species transport model in simulating tracer gas diffusion, a very good agreement between predicted and measured tracer gas concentration data is observed for some monitoring locations, but the agreement level is not uniform for all locations. The reasons for the deviations between predictions and measurements for those locations are discussed in the paper.

---

[4] Current address: Department of Mechanical and Nuclear Engineering, Kansas State University, 3009 Rathbone Hall, Manhattan, KS 66506. Tel: 785-532-2321, Fax:785-532-7057

INTRODUCTION

According to the Bureau of Labor Statistics [1], the number of commercial airline passengers experienced an average growth of 340% between the years 1970 and 2008. Also the statistics published by the Bureau of Transportation [2] indicates 650-800 million passengers travel by aircrafts each year in the United States, around 20% of those are international passengers. Considering the close proximity of this huge number of passengers in aircraft cabins, the potential risk of spreading biological contaminants and diseases between passengers has been raised dramatically due to the impressive increasing trend in the number of airline passenger especially in international flights. Global outbreaks of SARS and swine flu, in the first decade of the current century, were the two instances in which airline passengers had the key role in spreading these diseases. Therefore this serious potential threat to airline passengers has been the major reason for conducting this research which deals with the air quality in commercial aircraft cabins.

Since the biological contaminants and/or diseases may spread among aircraft passengers in the form of exhaled breath gases, cough or sneeze droplets, and airborne pathogens, the study of air quality in such enclosures requires the study of different transport phenomena: transport of mass, momentum, and energy. Due to the advances in computer technologies which have enabled researchers to solve the governing partial differential equations numerically, with relatively high degree of accuracy, in a cost and time effective manner, the use of Computational Fluid Dynamics (CFD) has increased considerably in this field of research in recent decades.

There are a number of relevant research articles in the literature that have used computational methods in order to study the complex transport phenomena existing in enclosed environments such as aircraft cabins. Garner et al. [3] presented a CFD model which was developed to simulate the airflow characteristics in a Boeing 747 aircraft cabin. The applied CFD model was used to predict the unsteady buoyant ventilation flow field in an aircraft cabin at cruise condition.

Lin et al. [4, 5] performed a numerical simulation of airflow and airborne pathogen transport in a Boeing 767 commercial aircraft cabin. Two types of turbulence models were used in that study: Large Eddy Simulation (LES) and Reynolds Averaged Navier-Stokes (RANS). It was observed while RANS simulation substantially under-predicted the turbulent intensity, the LES predicted values were in good agreement with the test data. Based on the LES results, the k-ε equations in the RANS model were modified and then used in simulating the disease transmission. Less than 1/100 of the computing resources was required for the equivalent LES simulation of particle transport in the same cabin. In another research conducted by Lin et al. [6], the CFD predicted velocity data for turbulent airflow in a generic cabin model were compared with corresponding Particle Image Velocimetry (PIV) measurements. The main focus of that study was using LES simulation to compare the temporal variations in the experimental data. The good agreement between the simulation results and measured data validated the LES predictions. Also it was observed that energy-spectrum function calculated from the LES velocity prediction had an excellent correlation with the Kolmogrov spectrum law in the universal equilibrium range.

In order to investigate the effects of using two different air distribution systems on the contaminants propagation patterns in aircraft cabin and between passengers, Tang et al. [7] used a Finite Volume method to produce a three-dimensional contaminant dispersion model for a 4-

row section of a Boeing 767-300 aircraft cabin. They assumed the cabin was pressurized and the heat transfer effects were negligible. The standard k-ε turbulence model was used to solve the governing momentum equations. Comparisons of simulation results for CO_2 concentration and droplets residence times between two air distribution systems indicated that using the Under Floor Air Distribution (UFAD) system, because of producing better flow circulation, leads to lower level of carbon dioxide and shorter residence times for the contaminant droplets comparing to the Ceiling Air Distribution (CAD) system. Through the experiments and CFD simulations by Yan et al. [8], it was found that the contaminant source location has a significant effect on pollutant transport within the cabin. In that research, the contaminant dispersion in a 5-row section of a Boeing 767-300 aircraft cabin was simulated through modeling tracer gas diffusion. It was also realized that increasing the ventilation rate is not necessarily useful for the receptors close to the source.

Su et al. [9] used three different sub-grid scale models of LES simulation for predicting airflow velocity, air temperature, and contaminant concentration in an air ventilated room. Validation of the simulations indicated an acceptable agreement between computational and experimental profiles of velocity, temperature, and contaminant concentration except for the near wall regions. That study demonstrated the capability of LES, as an efficient tool, in studying indoor air quality. Zhao et al. [10] developed a simplified computational model to simulate the airflow in ventilated rooms more time and cost effectively which was easier to work with especially for design engineers. They used the N-point Air Supply Opening Model (ASOM) technique to overcome the difficulties associated with specifying the boundary conditions at the air supply diffuser and also to reduce the number of mesh elements. Zhang and Chen [11] used a commercial CFD software to study the effects of using under-floor and personalized air distribution systems in improving the performance of air distribution systems in aircraft cabins. They used the RNG k-ε model for solving the Navier-Stokes equations. Their CFD model was first validated through the comparisons of the predictions for airflow velocity, air temperature, and tracer gas (SF_6) concentration with the corresponding measurements for the mixing type air distribution system. The comparisons indicated that while there was a good agreement between predictions and measurements for airflow velocity and air temperature data, there was a large discrepancy for the SF_6 concentration data for some locations. After the validation of the CFD model, it was used in studying and analyzing the performance of three types of air distribution systems: mixing, displacement and personalized, through the simulation of transport phenomena in a 4-row section of a Boeing 767-300 aircraft cabin. Liu et al. [12] reviewed all the experimental and computational investigations performed in studying the airflow distribution and contaminant dispersion in aircraft cabins in the past two decades. They classified the experimental research into three categories: heat transfer-based devices (hotwire and hot-sphere anemometers), optical-based devices (particle tracking, particle streak and particle image velocimetries), and acoustic-based devices (ultrasonic anemometer). They also categorized the computational research in two groups of models: Zonal models and CFD models. Abdilghanie et al. [13] investigated the effect of using laminar and turbulent inlet velocity profiles on the behavior of turbulent flow inside a simple room through LES. They also compared the performances of LES and k-ε models in predicting the flow characteristics in the same room. Their study showed that the standard k-ε model is less sensitive to the level of turbulence at the inlet than the LES model. It was also found that when the flow at inlet is laminar, the standard k-ε model fails to capture the slow development of the jet which is realized by LES.

The present study is designed to simulate the turbulent airflow and tracer gas diffusion in a generic aircraft half-cabin mockup model. Since the geometry of the cabin as well as the flow conditions at the boundaries are symmetric with respect to the aircraft cabin's longitudinal plane of symmetry, it can be expected that the mean flow characteristics show a symmetric behavior with respect to that plane. Due to the stochastic nature of turbulent flow fluctuations, the instantaneous flow characteristics are not symmetric. However, in this study, the mean quantities are of the interest and therefore studying the flow in one half of the cabin is sufficient while it can decreases the costs associated with building the whole cabin and performing the required experiments in a larger space. Gambit is used as the grid generation tool and FLUENT is used as the CFD solver for the simulations presented herein. In the first part, the airflow characteristics are investigated. Two types of turbulence models are employed: LES and RANS. The LES model provides the temporal velocity variations while the RANS model is used to simulate the airflow for steady conditions. The predictions from both LES and RANS models are compared with the PIV measured data for five monitoring surfaces on the cabin center plane parallel to the bulk airflow direction [14]. Throughout these comparisons the capability of the two types of aforementioned turbulence models in predicting the airflow velocities are discussed and compared. The effects of applying different k-ε models on the accuracy of steady RANS simulations are also studied. Then the effect of reducing the inlet nozzle height to one-half of its original size, while maintaining the Reynolds number for inlet airflow at the same value, on turbulence level and airflow velocities is examined. In this part, the predictions are validated by comparing them with the corresponding PIV measurements. In the second part, the turbulent diffusion of tracer gas is simulated by solving the species transport equation. LES is used in solving the Navier-Stokes equations governing the turbulent flow of air as well as the species transport equation for tracer gas mixture. The simulations are validated through the comparison of time-averaged predicted concentration of the tracer gas in specified monitoring locations in the cabin with the corresponding experimental measurements.

EXPERIMENTS

The generic cabin mockup model (Figs.1-2) has the key features of one-half of a twin-aisle Boeing 767 aircraft cabin. The upper left and upper right corners represent the overhead bins. The slit right below the upper left corner represents the nozzle port through which the fresh, conditioned air comes into the cabin and the slit in the lower right corner represents the outlet port for exiting exhaust air.

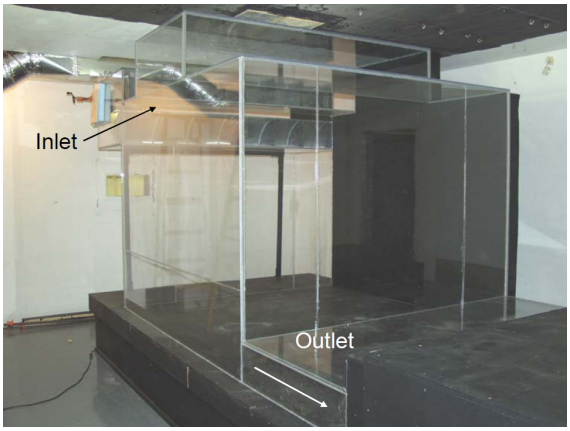

Fig. 2 Full scale generic aircraft half-cabin mockup model [14].

The PIV measurements were taken at the five measurement locations (Fig. 2) when the airflow inside the cabin was fully developed [14]. Although the velocity measurements were made for two different inlet nozzle height: 53 mm (full-height) and 26.5 mm (half-height), the average airflow rate coming into the cabin was maintained at the constant value of 4.2 m^3/min in all the airflow velocity and tracer gas concentration measurements.

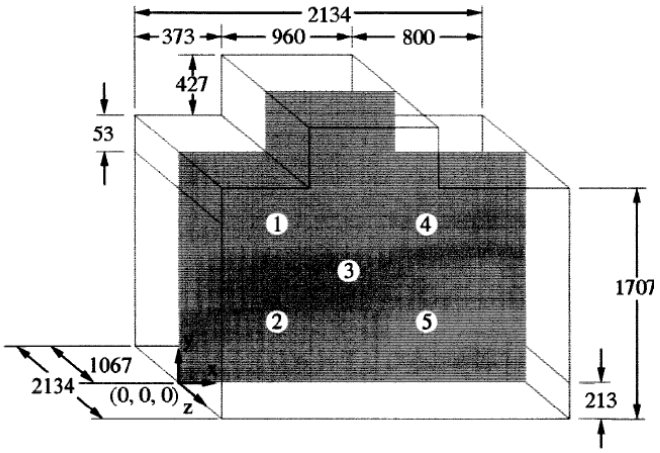

Fig. 2 Dimensions of the generic cabin model and the location of PIV monitoring windows on the cabin central plane (units in mm) [15].

In the tracer gas measurements, carbon dioxide was used as the tracer gas. A 12.7 mm schedule-40 porous polythene tube was installed horizontally inside the cabin perpendicular to the xy plane. One end of the tube was connected to a CO_2 tank through the back wall (corresponding to z=-1.067m) of the cabin while the other end was capped and positioned 134 mm from the opposite wall. The tube passed through the central point of the location 2 of the PIV measuring windows as shown in Fig. 3. A pressurized CO_2 tank (p~5500 kPa) containing CO_2 with the purity of more than 99.6% was used to supply the carbon dioxide

required for the experiments. By passing through an expansion valve, the pressure of carbon dioxide was regulated down from ~5500 kPa to an atmospheric pressure. Since the density of CO_2 at the atmospheric pressure is higher than the air density at the same pressure and temperature, in order to maintain the neutral buoyancy condition, before flowing into the injection tube, CO_2 was blended with Nitrogen such that the density of the diluted CO_2 in the injection tube reached approximately to the density of air. Carbon dioxide was injected through small holes uniformly distributed over the circumferential surface of the injection tube. Figure 3 shows a schematic representation of the generic cabin model with the installed injection tube. In specifying the boundary conditions required for solving the species transport equation, the concentration of the carbon dioxide in the incoming air, which is in the range of ~300 - 400 ppm, is taken into account. In the experiments, the CO_2 was injected after quasi-steady conditions were achieved for the turbulent airflow in the cabin. Also the measurement of the carbon dioxide concentration was performed when the flow of air-CO_2 mixture showed a quasi-steady behavior. In tracer gas experiments, the inlet nozzle height was 26.5 mm (half-height nozzle) [14].

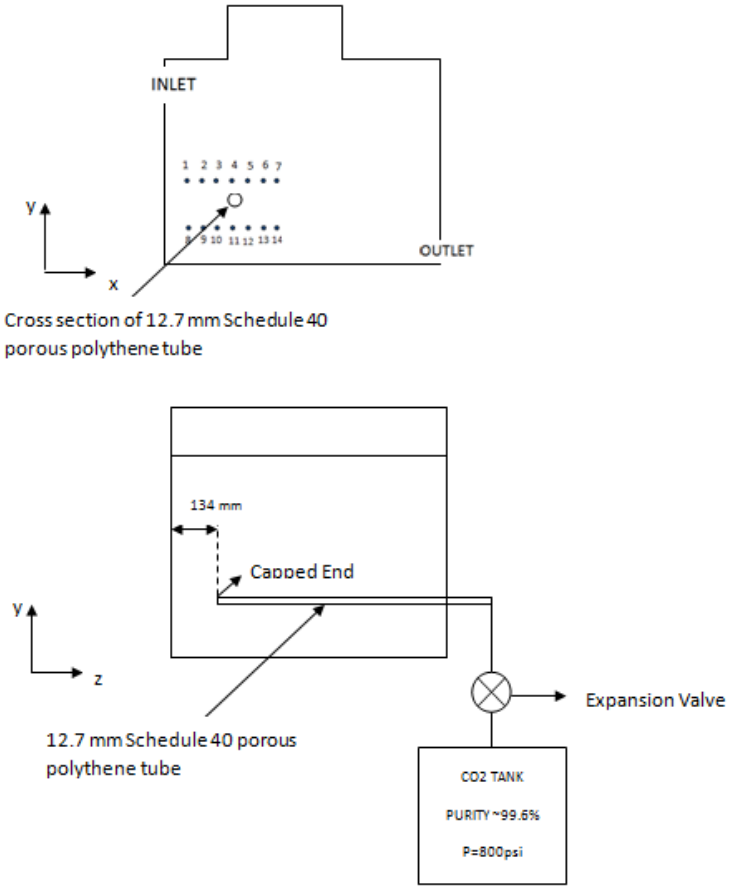

Fig. 3 A schematic view of the experimental setup for tracer gas measurements. The xy view of the setup shows the tracer gas sampling points above and below the injection tube.

NUMERICAL SOLUTION METHOD

In this study the following assumptions are employed for the numerical simulation of three-dimensional turbulent airflow and tracer gas diffusion in the cabin. The following assumptions are consistent with the existing conditions in the experiments:

5. In the LES model, the flow is considered unsteady while the RANS model employs steady flow conditions.
6. In all the cases the flow is assumed to be incompressible.
7. The heat transfer in the cabin is neglected. The inlet airflow is at the temperature of 27 ^{o}C. In simulating the carbon dioxide diffusion, the temperature of injected CO_2 is also considered to be 27 ^{o}C.
8. In simulating the turbulent flow and tracer gas injection, the effects of buoyancy are taken into consideration.
9. No chemical reaction is assumed to take place in the tracer gas diffusion calculations.

The governing equations for the instantaneous turbulent flow field and species transport in the cabin are:

Continuity:

$$\frac{\partial u_i}{\partial x_i} = 0 \tag{1}$$

Momentum:

$$\frac{\partial u_i}{\partial t} + u_j \frac{\partial u_i}{\partial x_j} = -\frac{1}{\rho}\frac{\partial p}{\partial x_i} + \frac{1}{\rho}\frac{\partial}{\partial x_j}(\mu \frac{\partial u_i}{\partial x_j}) + g_i \tag{2}$$

Species transport:

$$\frac{\partial}{\partial t}(\rho Y) + \frac{\partial}{\partial x_i}(\rho u_i Y) = \frac{\partial}{\partial x_i}(\rho D)\frac{\partial Y}{\partial x_i} \tag{3}$$

where, u_i (m/s) denotes the velocity components, x_i (m) represents the position along the coordinate directions, t (s) is the time, and μ (Pa.s) and ρ (kg/m^3) are the dynamic viscosity and density of air or air-CO_2 mixture, respectively. Also p (Pa) is the static pressure, g_i (m/s^2) is the gravity acceleration. Y is the species mass fraction, and D (m^2/s) is the molecular diffusion coefficient of carbon dioxide in air-CO_2 mixture.

To solve the governing Navier-Stokes equations for the turbulent flow inside the cabin, two turbulence models are applied: LES and RANS.

In the LES model, the Smagorinsky-Lilly SGS model [16, 17] is used to calculate the turbulent viscosity. The Smagorinsky constant is selected as 0.14. The second order central differencing is used to discretize the spatial derivatives. The time step size is 0.05 s and the second order implicit method is used as time marching scheme. The convergence criteria for the continuity and the momentum equations are 10^{-4} and 10^{-5} respectively. The Werner-Wengle wall function [18, 23] is used for the near wall solution. The reason for using the Werner-Wengle wall function, as explained elaborately by Werner and Wengle [18], is its simplicity as well as its

accuracy in comparison with the other near wall functions. While other functions are multi-domain functions based on non-dimensionalized velocity and distance from the wall, the Werner-Wengle wall function defines unique relationships between shear stress and velocity that enhances accuracy and reduces the computational time.

In the RANS models, three types of k-ε model are employed: Standard, Renormalization Group (RNG) and Realizable. The non-equilibrium wall function is used as the near wall treatment. The second order upwind scheme is used to discretize spatial derivatives in the governing equations. For the LES simulations, the time step size is 0.05 s and the second order implicit method is used as time marching scheme. The same convergence criteria as in the LES model are used for the continuity and the momentum equations in the steady RANS simulations. For the k and ε equations, the convergence criteria are both 10^{-5}.

In simulating the carbon dioxide diffusion in the cabin, the species transport model is used while LES is applied to solve the governing Navier-Stokes equations. The molecular diffusion coefficient of the carbon dioxide in the air-CO_2 mixture is assumed to be constant and have the estimated value of $1.57\times10^{-5}\,m^2/s$ [19]. The turbulent Schmidt number is taken as equal to 0.7. The volumetric-weighted mixing and mass weighted mixing laws [23] are used to calculate the mixture density and viscosity, respectively.

RESULTS AND DISCUSSION

Uncertainty Study (Check for the Grid-Independent Solutions)

The uncertainty studies were done for the cabin in both cases of full-height and half-height air inlet nozzles. However, in this section the results of uncertainty study for the cabin with full-height nozzle is presented. LES and RANS were used for solving the turbulent flow governing equations. In order to solve the governing equations, the boundary conditions (for both LES and RANS) and initial conditions (just for LES) need to be specified. The boundary conditions are: velocity-inlet for the flow at the inlet of the cabin mockup, no slip stationary wall for the cabin mockup walls and outflow for the flow at the outlet of the cabin mockup. In setting the boundary conditions at the inlet, for both LES and RANS (for all k-ε models), the flow velocity as well as the turbulent kinetic energy and dissipation rate are specified at the inlet. Knowing the air kinematic viscosity and airflow rate at the inlet, the average airflow velocity at the inlet can be calculated. In the simulations performed in this study, it is assumed that the velocity at the inlet is uniform and equal to the calculated average velocity. In order to calculate the turbulence intensity at the inlet, the airflow Reynolds number based on the inlet hydraulic diameter is determined. Following the calculation of the Reynolds number, the turbulent intensity, turbulent kinetic energy, and turbulent dissipation rate at the inlet can be calculated through the equations listed below [23]:

$$I = 0.16(\mathrm{Re}_{D_H})^{-1/8} \tag{4}$$

$$k = \frac{3}{2}(U.I)^2 \tag{5}$$

$$\varepsilon = C_\mu^{3/4} \frac{k^{3/2}}{\ell} \tag{6}$$

where I is the turbulence intensity, Re_{D_H} is the Reynolds number based on the hydraulic diameter, D_H (m) is the hydraulic diameter, k (m^2/s^2) is the turbulent kinetic energy, ε (m^2/s^3) is the turbulent dissipation rate, U(m/s) is the average velocity at the inlet, C_μ is an empirical constant which is approximately equal to 0.09, and ℓ is the turbulence length scale ($\ell = 0.07 D_H$). The calculated turbulent kinetic energy and dissipation rate from the above equations are used in setting the boundary conditions at the inlet for LES as well as all the k-ε models used in RANS. Since the velocity at the cabin inlet nozzle has its maximum magnitude throughout the flow field in the cabin, from Eqs. (4)-(6) it can be seen that, at the inlet, the turbulent kinetic energy and dissipation rate can possibly have their maximum magnitudes through in the cabin. We studied the contours of turbulent kinetic energy and dissipation rate calculated through the simulations and confirmed the above postulation. Following the calculation of turbulent kinetic energy and dissipation rate, the Kolmogorov length (η) and time (τ) scales were determined as 9.28×10^{-4} m and 0.0589 s, respectively, through the following equations [23, 24]:

$$\eta = \left(\frac{\nu^3}{\varepsilon}\right)^{1/4} \tag{7}$$

$$\tau = \left(\frac{\nu}{\varepsilon}\right)^{1/2} \tag{8}$$

where η (m) is the Kolmogorov length scale, τ (sec) is the Kolmogorov time scale and ν (m^2 /s) is the kinematic viscosity. As discussed earlier, the turbulent dissipation rate has its maximum magnitude at the inlet, therefore through Eqs. (7) and (8) it can be realized that the Kolmogorov length and time scales experience their minimum values at the inlet of the cabin, i.e. for the entire flow field in the cabin $\eta \geq 9.28\times10^{-4} m$ and $\tau \geq 0.0589 s$. The numbers of mesh cells in the tested four different grids in this study are: 306900, 576000, 1024000 and 2340000. In all the cases the meshes are structured, Map type, and made of orthogonal hexahedral elements. Through the comparison of mesh spacing range with the Kolmogorov length scale, the grid spacing corresponding to the finest mesh (2,340,000 mesh elements) varies in the range of 7η- 34η. Since the predicted data from LES have temporal

behavior, the time mean values as well as the root-mean-squared (RMS) data are used in the calculation of variations in the velocity predictions as the grid size changes. Figure 4 shows a comparison between the LES predictions for the x-component of airflow velocity using different grid sizes and the corresponding PIV measurements corresponding to the location 5 of the PIV measuring windows. Figures 5 (a, b) and 6 show the converging behavior of the LES and RANS predicted x-component of velocity data as the number of grid is increased. The deviation for every grid size was calculated based on the relative difference between the predictions corresponding to that grid size and the finest grid (2,340,000). As typically shown in Fig. 4, the LES predictions from the finest mesh have the closest RMS and mean values to those of PIV measurements. Also, as shown in Fig. 5, the LES predictions demonstrate better converging behavior in locations 1 and 4 in the upper region of the cabin comparing to the middle and lower regions. Figure 6 indicates that in the steady RANS simulations, the location 3 at the middle of the cabin is associated with the highest grid uncertainties comparing to the other locations. It means that the flow in the middle region of the cabin has more complex structure and in order to predict the flow behavior more accurately, the regional mesh refinement is required.

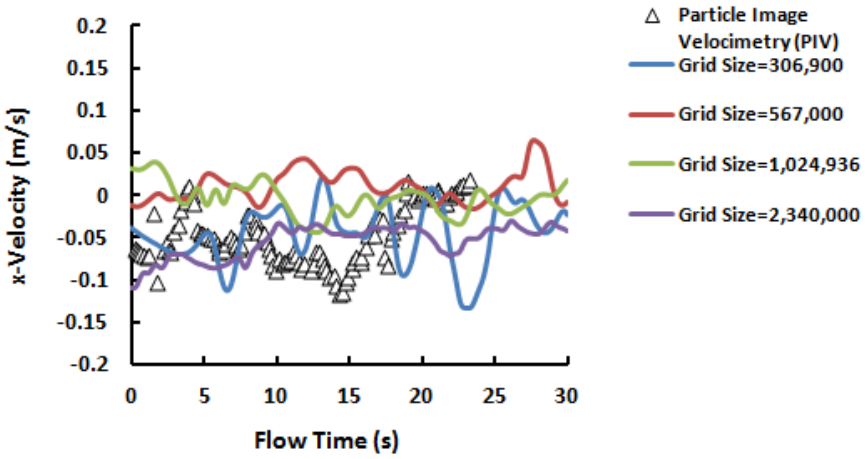

Fig. 4 The results of uncertainty study for the cabin with full height nozzle when x component of velocity data are predicted for the location 5 of the PIV measuring windows. The PIV data were produced by Lebbin [14].

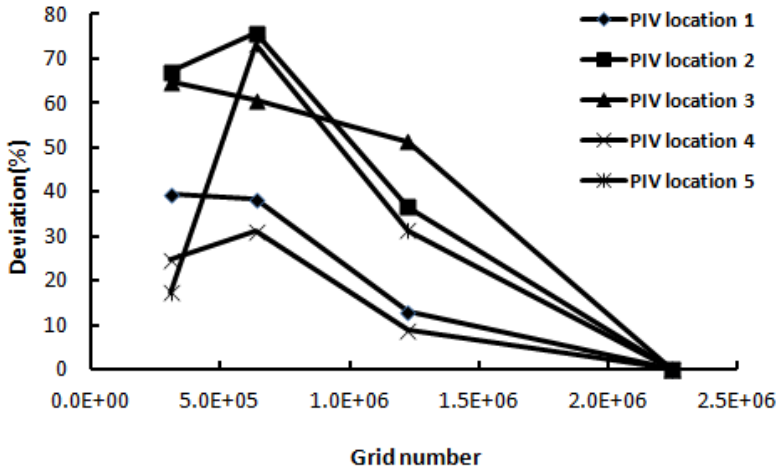

(a) Deviations based on mean values (time averaged values)

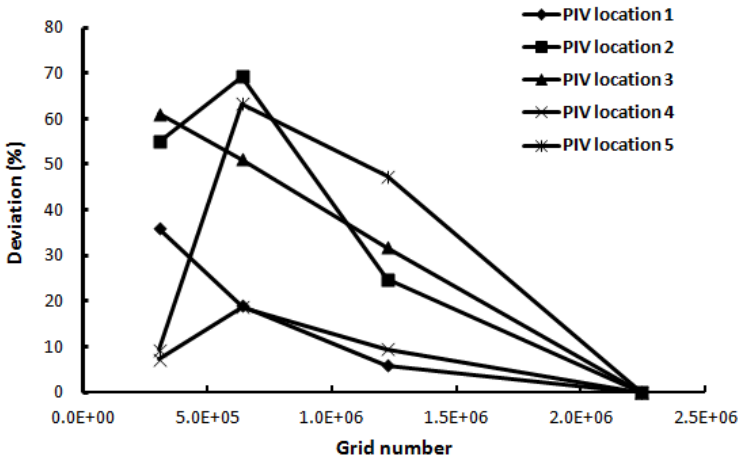

(b) Deviations based on RMS values

Fig. 5 The converging behavior of x-component of velocity deviations with respect to the corresponding prediction from the finest grid for all the PIV measuring windows.

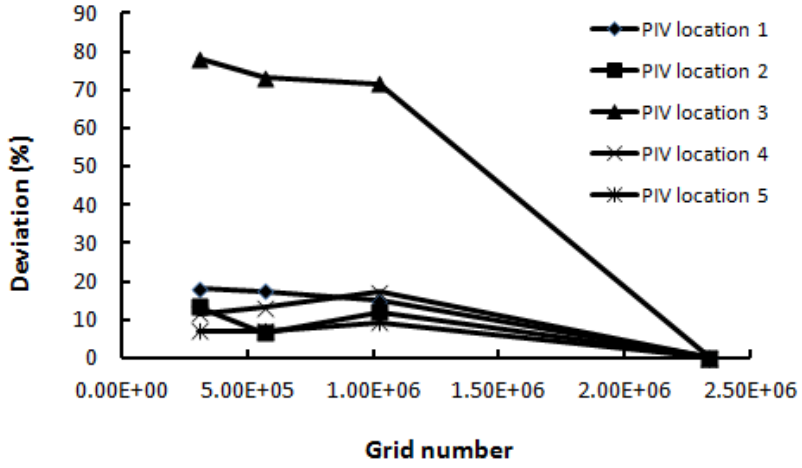

Fig. 6 The converging behavior of x-component of velocity deviations with respect to the corresponding prediction from the finest grid from steady RANS solution for all the PIV measuring windows.

Study of Airflow in Cabin: Full-Height and Half-Height Nozzle Cases

a. Airflow Simulation in Cabin with Full-Height Nozzle

This section starts with the LES simulation of turbulent airflow in the generic cabin with full-height inlet nozzle. The CFD grid used in this part of study consists of 2,340,000 hexahedral cells with the grid spacing varied in the range of 7η- 34η (through the comparison of edge grid spacing with the Kolmogorov length scale) . Also the time step size of 0.05 s is used in all LES simulations presented in this paper. In order to validate the simulation, the LES predictions are compared with the PIV measurement data as well as the CFD predictions by Lin et al.[6] at each of the five PIV measuring locations. The time interval between the each of two succeeding PIV sampling data was 0.2 s [6, 14]. A comparison between the corresponding LES parameters used in this study and those used by Lin et al. [6] is shown in Table 1. As seen in Fig. 7, there is a good agreement among the simulation results of this study, PIV measurements, and those of Lin et al. [6] CFD simulations for location 1 of the PIV measuring window. The predictions and measurements for other PIV measuring window locations are similarly compared well. Especially, the comparisons indicate that the simulations predict the ranges of variations of instantaneous velocities fairly close to the variation ranges of the measurements. Since the PIV measuring window locations are on the central plane (z=0) the magnitude of z-components of velocity data are very small and close to zero and that's the reason they are not presented here.

Table 2. Comparison between the important parameters in the simulations.

LES Code	Lin et al. [6] (Using FLUENT)	Lin et al.[6] (Using Fire Dynamic Simulator, FDS)	Present Study (FLUENT)
Number of mesh elements	2,533,744	2,580,480	2,340,000
Mesh elements type	All hexahedral cells, Unstructured mesh	All hexahedral cells, Cartesian mesh	All hexahedral cells, Structured mesh
Grid Spacing (η)	5-20	5-20	7-34
Time step (sec)	0.05	0.01 ± 0.002	0.05
Sub-Grid Scale (SGS) model	Smagorinsky Lilly	Smagorinsky Lilly	Smagorinsky Lilly
Smagorinsky constant, Cs	0.14	0.14	0.14
Near wall treatment	Law of the wall approach	Standard wall function	Werner-Wengle
Numerical Scheme	Spatial: Second order central differencing Temporal: Implicit second order predictor corrector scheme	Spatial: Second order central differencing Temporal: Implicit second order predictor corrector scheme	Spatial: Second order central differencing Temporal: Implicit second order predictor corrector scheme

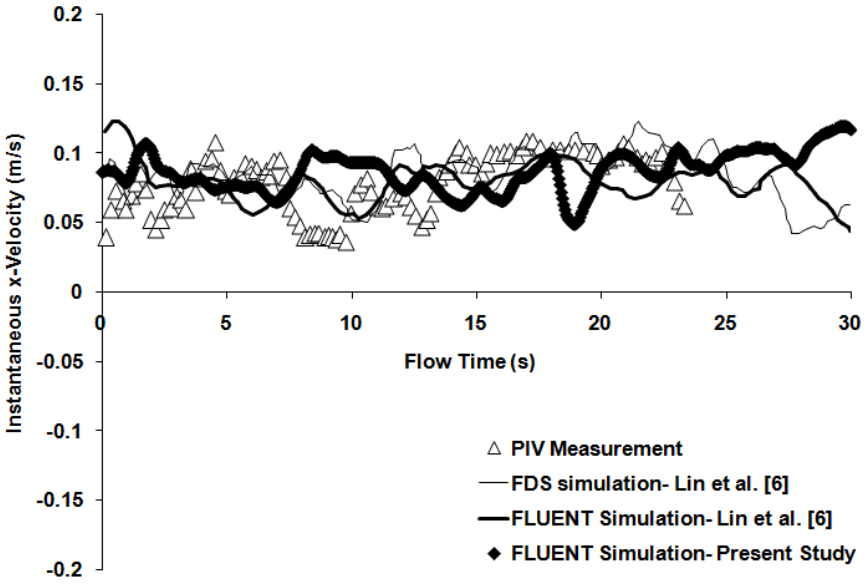

(a) x-component of velocity data at PIV location1

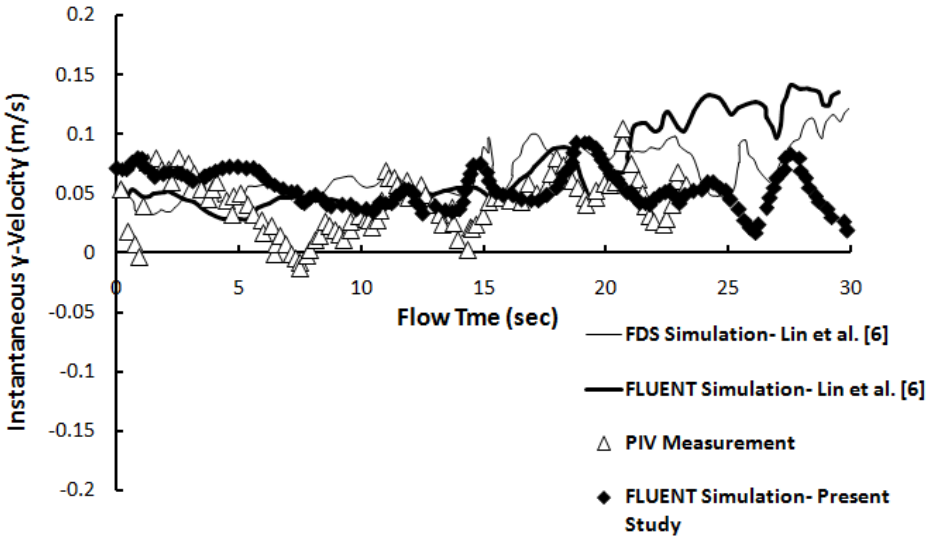

(b) y-component of velocity data at PIV location1

Fig. 7 Comparison of the predicted values (this study), PIV measurements [14] and predictions produced by Lin et al. [6] for the airflow velocity data corresponding to the location 1 of the cabin with full height nozzle.

In the above comparisons, the center point of each PIV measuring window was selected to monitor the predicted velocity data. However in the experiments, the PIV velocity data were averaged over the area of each measuring window. In order to study the effect of changing the monitoring surfaces from the center points to the whole area of the PIV measuring windows on the predicted velocity data, the simulation results were reprocessed based on the area weighted average values of velocities over the measuring windows areas. Figure 8 shows the comparisons between the predictions from two differently processed velocity values and the corresponding experimental data for location 2 of the PIV window. In Fig. 8, it is observed that although the mean temporal behaviors of the predictions are almost the same between the two different simulation data sets, the area-averaged data set shows a smoother curve, which means the area-averaged velocity experiences less fluctuations than the local velocity at the center point of the window.

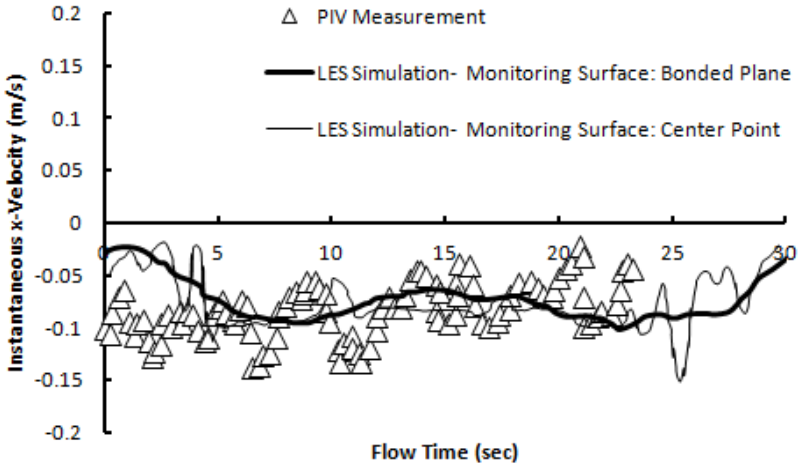

(a) x- component of velocity data at PIV location 2

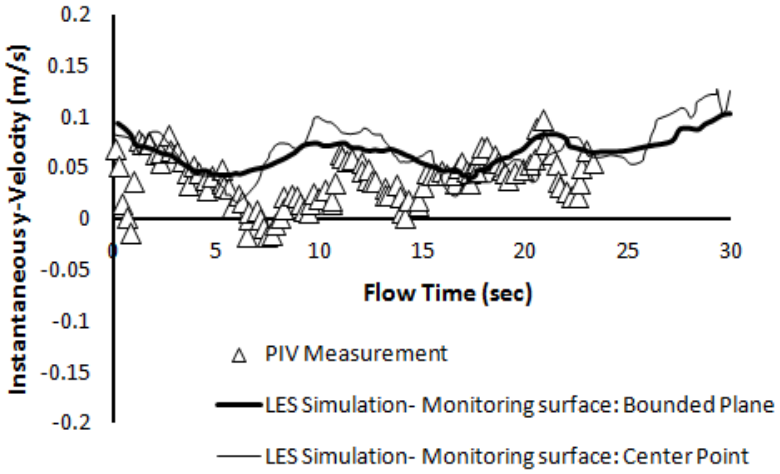

(b) y- component of velocity data at PIV location 2

Fig. 8 Study the effect of choosing monitoring surface on the predicted velocities, corresponding to location 2 of the cabin with full-height nozzle, through comparison with PIV measurements [14].

Figures 9 and 10 represent the comparisons between the predictions for the x-component of airflow velocity data in locations 3 and 5 of the PIV measuring windows from the steady RANS simulations using three types of the k-ε turbulence models and the corresponding time-dependent PIV data. In the RANS simulations, the non-equilibrium wall function is used as the near wall treatment and also the finest mesh (with the grid number of 2,340,000)

that previously used for the LES simulations is used for RANS simulations as well. Although the accuracy of RANS predictions is considerably less than LES, the computation time and cost associated with LES simulations are much more than RANS. Among the three examined RANS models: the standard k-ε [20] the RNG k-ε [21] and the realizable k-ε [22], the RNG predicted value is closer to the mean value of the experimental data. The predictions from all the examined types of the k-ε turbulence models are greater than the mean values of PIV measurements and LES predictions. Based on the simulations performed in this study, the RNG is the most accurate model.

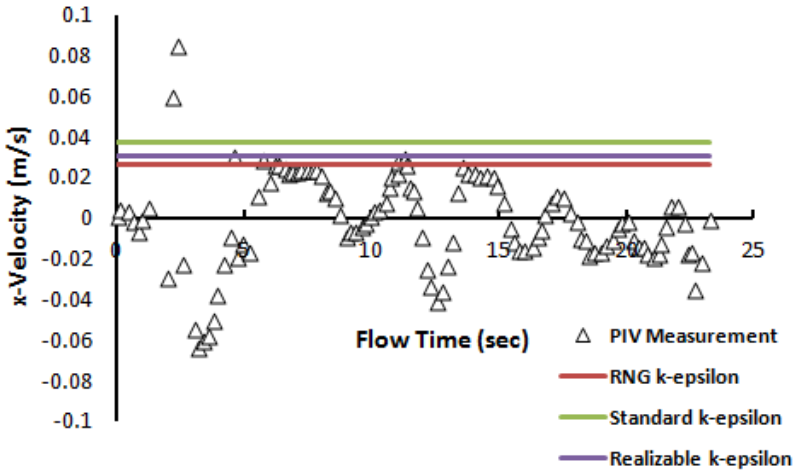

Fig. 9 Comparison of the steady RANS predictions for the x-component of velocity data with the corresponding time dependent PIV data [14] at location 3 of PIV measuring window.

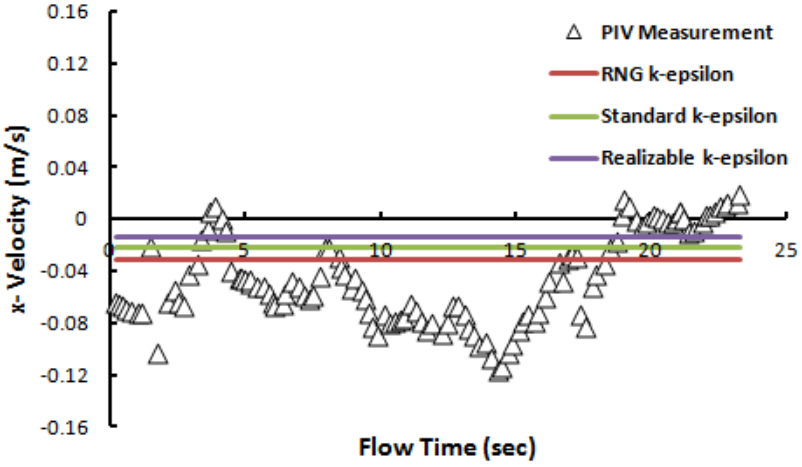

Fig. 10 Comparison of the steady RANS predictions for the x-component of velocity data

with the corresponding time dependent PIV data [14] at location 5 of PIV measuring window.

b. Airflow Simulations in Cabin with Half-Height Nozzle

This section presents the study of flow characteristics when the cabin nozzle height is reduced to one-half of its original size. As the flow rate of the incoming air to the cabin remains the same, by halving the nozzle height, the magnitude of the airflow velocity at the inlet is doubled. So it is expected that the magnitude of each airflow velocity component in the cabin experiences an increase. Figures 11 and 12 compare the PIV measurements [14] with the LES predictions from this study for the airflow x and y velocity components in locations 1 and 3 of the PIV measuring windows (The predictions and measurements corresponding to locations 2 and 5 are also well compared similar to location 1). As explained previously, the comparisons for z-component of velocity data is not presented here. The sampling frequency in PIV measurements is 7.5 Hz. A structured grid consisting of 2,225,000 hexahedral mesh cells with the grid spacing in the range of 4η-43η is used in LES simulations for this part of study. Similar to the simulations done for the cabin with full-height nozzle, the time-step size of 0.05 s is used in LES simulations for the cabin with half-height nozzle as well. The comparisons indicate that, except for the location 3 of the PIV measuring windows, LES predicts the range of flow velocity variations fairly well. In location 3, however, due to the complexities associated with the flow in this region, the agreement between the LES predictions and PIV measurements is not as good for all flow times. For example, in Fig. 12, for the times between ~12 s to ~30 s and also greater than ~35 s there is not an acceptable agreement between LES and PIV data. It seems in order to get better predictions for such regions in which the airflow patterns are more complicated, local grid refinements are needed.

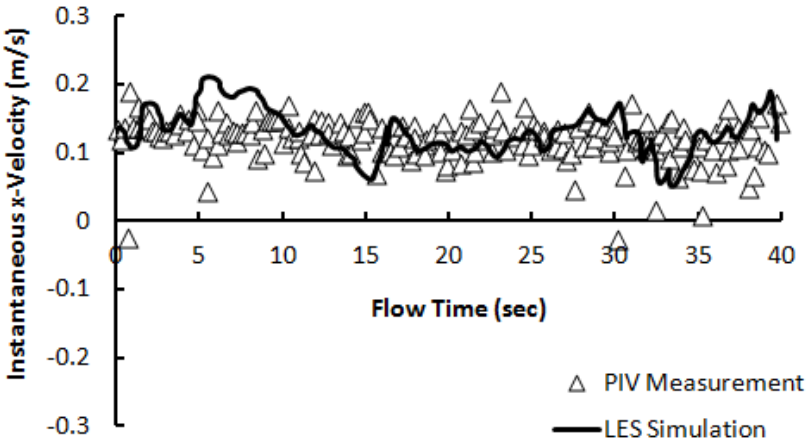

(a) x-component of velocity data

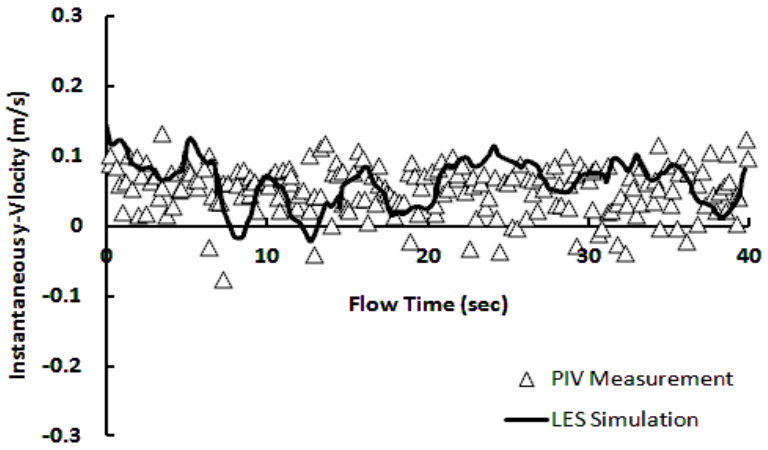

(b) y-component of velocity data

Fig. 11 Comparison of the LES predictions and PIV measurements [14] for the x-component of velocity data corresponding to the location 1 of the cabin with half-height nozzle.

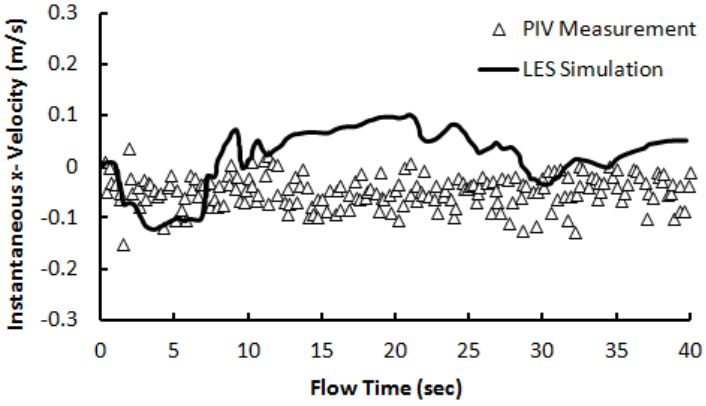

(a) x-component of velocity data

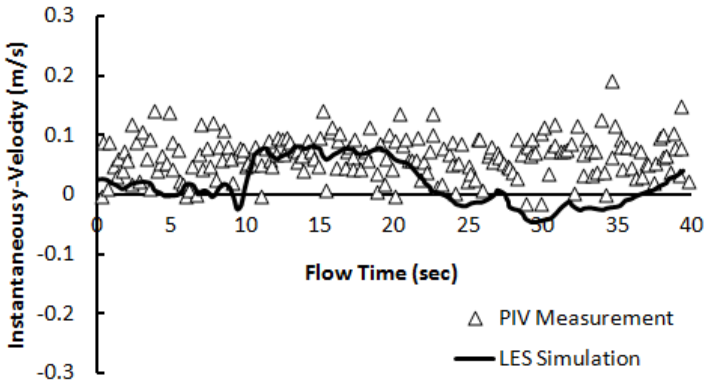

(b) y-component of velocity data

Fig. 12 Comparison of the LES predictions and PIV measurements [14] for velocity data corresponding to the location 3 of the cabin with half-height nozzle.

Comparisons of the velocity data between the full and half-height nozzle cases indicate that by halving the nozzle height, the mean value of the predicted as well as measured flow velocity data corresponding to locations 1 and 2 of the PIV measuring windows are approximately doubled (compare Fig. 7 with Fig. 11). However for the locations 4 and 5, the expected increase in the velocity is slight and not as much as that experienced in the locations 1 and 2 (Fig. 13). In addition, comparison of the PIV measurements for the velocity data corresponding to the location 3 (as shown in Fig. 14) implies that by halving the nozzle height and consequently doubling the inlet airflow velocity, the flow in the location 3, which used to be almost stationary in the full-height nozzle case, takes the tendency of moving to the upper left corner of the cabin.

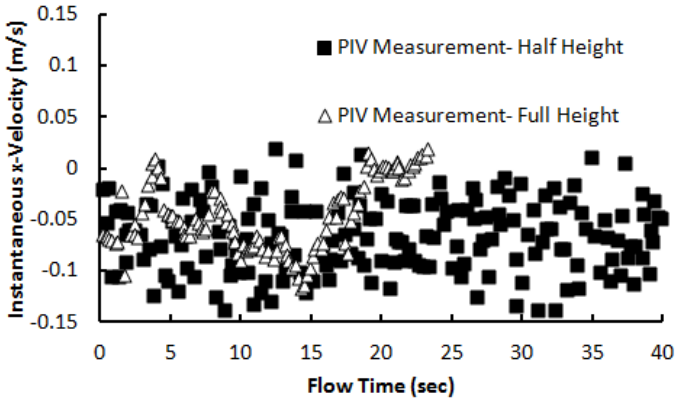

(a): x-component of velocity data

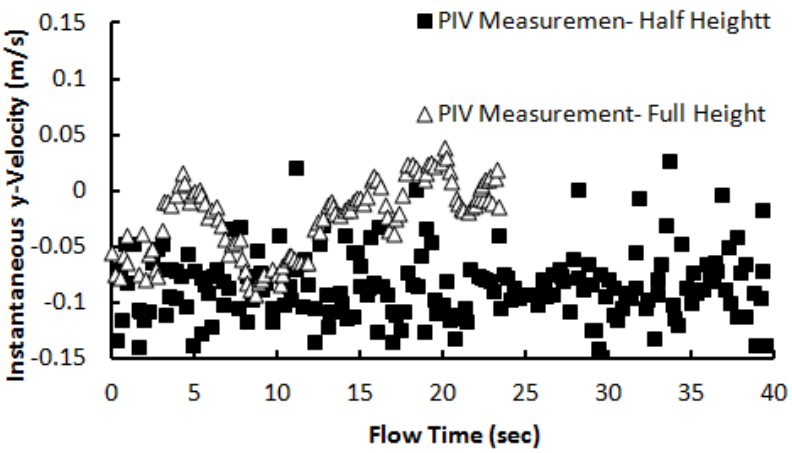

(b): y-component of velocity data

Fig. 13 Study the effect of decreasing the cabin nozzle height through a comparison between the PIV measured velocity data [14] corresponding to the location 5 of the PIV measuring windows for two cases of full and half-heigh nozzle.

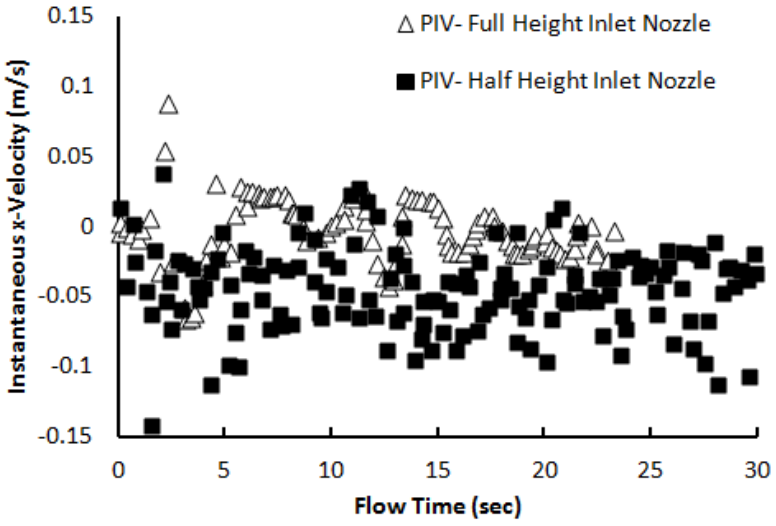

(a): x-component of velocity data

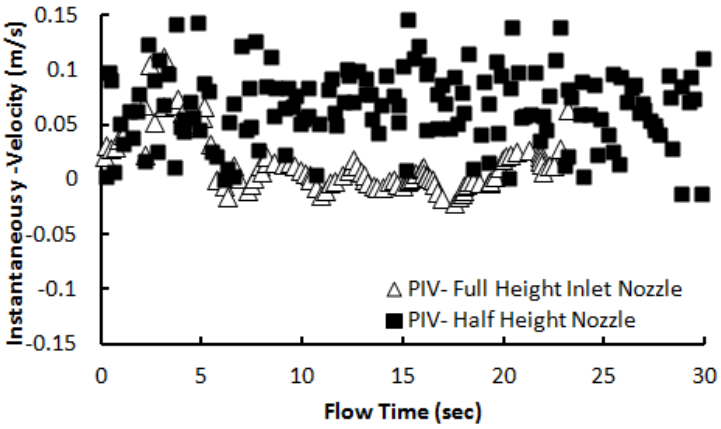

(b): y-component of velocity data

Fig. 14 Study the effect of decreasing the cabin nozzle height through a comparison between the PIV measured velocity data [14] corresponding to the location 3 of the PIV measuring windows for two cases of full and half-height nozzle.

Study of the Tracer Gas Diffusion in the Cabin with Half-Height Nozzle

After the turbulent flow of the air-CO_2 mixture reached quasi-steady conditions, the measurement of the time-dependent values of carbon dioxide concentration at specified sampling points, as shown in Fig. 3, was started and continued for about 10 minutes. The measured data, denoted by C(t), were non-dimensionalized using the concentration of CO_2 at the inlet of the cabin and the average value of the CO_2 concentrations at the outlet between two times: at the beginning of the measurement and at the end of the measurement through the following equation:

$$y(t) = \frac{C(t) - \bar{C}_{inlet}}{\bar{C}_{outlet} - \bar{C}_{inlet}} \tag{9}$$

where; t (s) is time $y(t)$ is the dimensionless concentration of carbon dioxide, C (ppm) is the CO_2 concentration at different sampling points, $\bar{C}_{inlet}$ (ppm) is the CO_2 concentration at the inlet measured one time and assumed to be constant during the experiment. $\bar{C}_{outlet}$ (ppm) is the average of the two measured values for the CO_2 concentration at the outlet (the measured values are corresponded to the beginning and the end of measurement duration).The generated grid for the tracer gas simulations is unstructured and contains 1,728,000 mesh elements of tetrahedral, hexahedral and wedge shapes. A schematic of this grid is shown in Fig. 15.

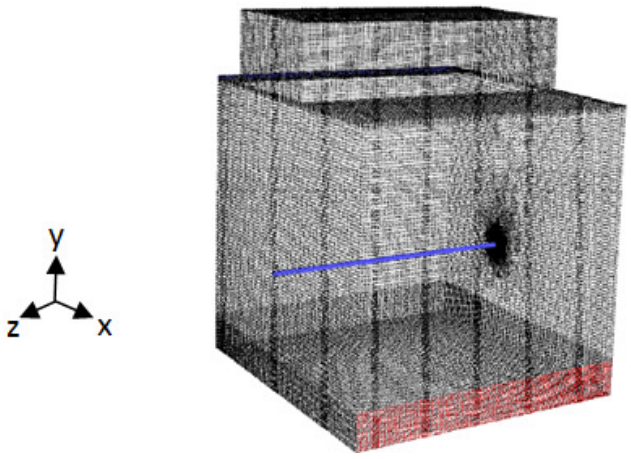

Fig. 15 3-D schematic of the unstructured grid (for the generic cabin with the injection tube) used in CFD simulation of the carbon dioxide diffusion in the generic cabin model.

In Fig. 16 and Fig. 17, the time-averaged predicted and measured values of the CO_2 concentration are compared to each other. For the sampling points above the tube (Fig. 16), it is observed that there is an excellent agreement between predictions and measurements at sampling points 3, 5 and 6. However, the agreement for the sampling point 4 is not as good. There is an error between 11-30% in predicting the concentration data for the sampling points 1, 2 and 7.

Figure 17 shows a graphical comparison between the time-averaged predictions and measurements for CO_2 concentration corresponding to the sampling point located along the x- axis below the injection tube. As can be seen, the best agreements have been achieved for point 12 (right below the tube) and point 14. The worst results correspond to the points 8, 9 and 10. The error in computations for this case varies from ~4% (point 12) to ~40% (point 9).

In order to study the effect of grid size on the simulation results, the number of mesh cells was increased from 1,728,000 to 2,630,000. The CO_2 mass fraction at different sampling points computed using two different grids were compared. A comparison of the RMS values of computed data from two different grids is shown in Table 2. As it is seen, by increasing the number of mesh cells, the computed CO_2 concentration data varies between 2% to 16%. Table 3 shows the comparisons between the mean values of computed CO_2 concentration data from two different grid sizes. As it is seen, by increasing the number of mesh cells, the computed CO_2 concentration data varies between 2% to 17%.

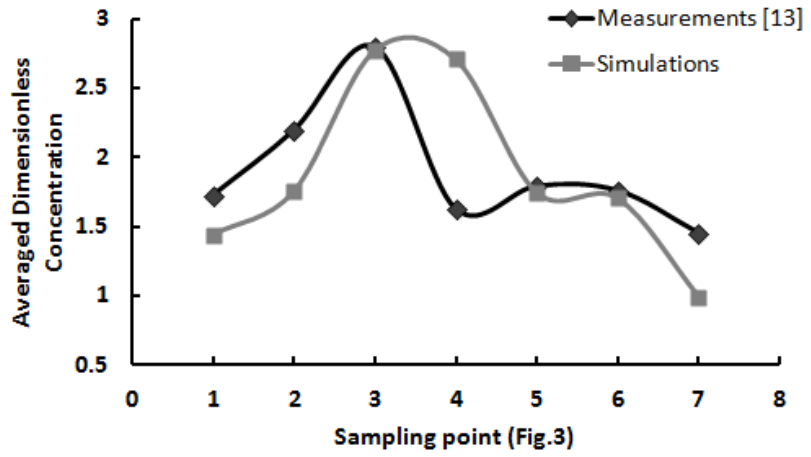

Fig. 16 Comparison between the time-averaged predictions and measurement of dimensionless CO_2 concentration data [14] for the sampling points located along the x-axis above the injection tube.

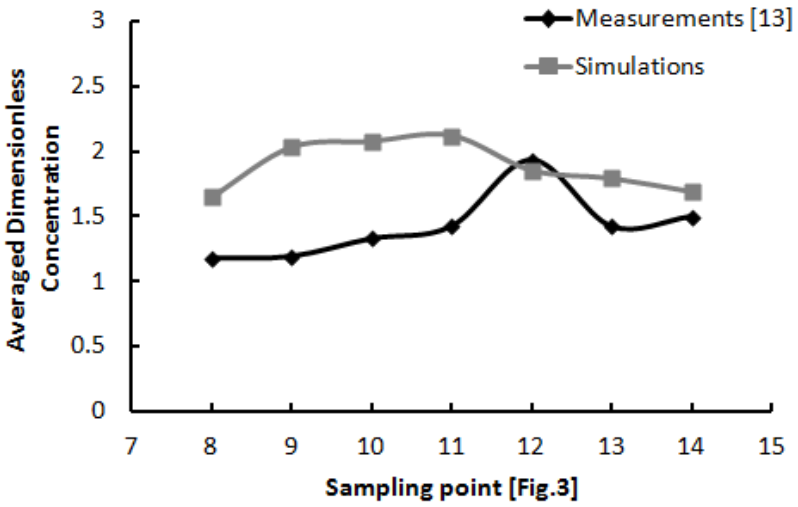

Fig. 17 Comparison between the time-averaged predictions and measurement of dimensionless CO_2 concentration data [14] for the sampling points located along the x-axis below the injection tube.

From the comparison of Tables 2 and 3 it can be seen that the deviation between the predicted CO_2 concentration data using two grid sizes is greater for the sampling points located in the upper right of the injection tube. In order to explain the reason for this behavior, recall the study of the airflow in the cabin presented earlier in this paper. It was

observed that the airflow in the location 3 of the PIV windows (Fig. 2) demonstrates more complexity than other locations. Since the sampling points located in the upper right of the injection tube are very close to that region, changing the grid size has a considerable effect on computational accuracy. Therefore, one expects higher computational uncertainties for the sampling points located in regions with more complex airflow structure.

Table 2. Comparison of RMS values for computed CO_2 concentrations using two different grid sizes.

Sampling point Number	2,630,000 mesh cells	1,728,000 Mesh cells	Deviation (%)
1	0.0114	0.0116	2.38
2	0.0151	0.0155	2.87
3	0.0117	0.0114	2.85
4	0.0111	0.0116	4.16
5	0.0097	0.0088	10.22
6	0.0095	0.0082	16.06
7	0.0079	0.0094	15.9

Table 3. Comparison of mean values for computed CO_2 concentrations using two different grid sizes.

Sampling point Number	2,630,000 mesh cells	1,728,000 Mesh cells	Deviation %
1	0.0113	0.0116	2.08
2	0.0155	0.0151	2.89
3	0.0115	0.0112	2.85
4	0.0109	0.0114	4.86
5	0.0083	0.0092	9.78
6	0.0095	0.0082	17.1
7	0.0078	0.0093	16.13

CONCLUSION

In this study, the capability of a CFD commercial software in simulating turbulent airflow as well as tracer gas diffusion in a generic half-cabin was evaluated. Two different types of turbulence models were used to find the turbulent viscosity in the governing equations: unsteady Large Eddy Simulation (LES) and steady Reynolds Averaged Navier Stokes (RANS) models. While LES predicts the temporal variations of airflow velocity, the steady RANS method predicts a steady value for the velocity. Through the comparisons, it was concluded that the LES at least is able to predict the range of velocity variations fairly well. Examining the three different k-ε (standard, RNG and Realizable) models indicated that, as expected, the errors associated with the RANS method are much more than that of LES. It was also recognized that among the above mentioned k-ε models, the RNG k-ε leads to the most accurate predictions.

In order to monitor the velocity data in PIV measuring windows, two different approaches were employed. The first approach used velocity data at the center points of the PIV windows and the second approach used the area-averaged velocity values of the PIV windows. The comparisons indicated that the area-averaged velocity value decreased the fluctuations in the velocity but the general behavior of predicted velocities did not change. Comparisons with the experimental data showed that the center point values had a better agreement with experimental measurements.

The effect of halving the cabin inlet nozzle height with the same airflow rate was studied. It was observed that although LES method gave a good estimation of the velocity data in the locations 1, 2, 4 and 5 of measuring windows, the agreement between the simulations and measurements was not as good in location 3 at the middle of the cabin. A local refinement in grid size is recommended to get more accurate results in this region in the future study. Comparing to the cabin with the full-height nozzle, it was seen that by halving the nozzle height and consequently doubling the inlet velocity, the magnitude of flow velocities in locations 1 and 4 increased dramatically (by 100%). However, in locations 2 and 5, the increase in the velocity value was slight and not as much. It was also realized that the airflow located in location 3 that used to be almost stationary in the full-height nozzle case had the tendency of moving to the upper left corner of the cabin model.

In the second part of this study, the capability of commercial CFD software with LES in simulating the tracer gas diffusion in the generic cabin model was examined. Using LES, the temporal variations in tracer gas concentration in the specified sampling points were predicted. Following the same procedure as used in the experiments the predicted values were non-dimensionalized and compared with the experimental data. Although excellent agreement was observed in some sampling points, the predictions had an average error of 23%.

ACKNOWLEDGMENT

The authors would like to express their gratitude to Dr. C.H. Lin from Boeing Company for his valuable input in CFD simulations, and to Dr. P. A. Lebbin from the National Research Council of Canada for his kind assistance in analyzing the experimental data and test procedures.

The authors also would like to thank Dr. J. Bennett from the National Institute for Occupational Safety and Health (NIOSH) for his technical assistance. The research was funded, in part, by the Kansas State University Targeted Excellence Program.

NOMENCLATURE

Capital Letters

C concentration of species at sampling point, ppm

C_μ empirical constant

D molecular diffusion coefficient, m^2/s

D_H hydraulic diameter, m

I turbulence intensity

Re_{DH} Reynolds number based on the hydraulic diameter

U average velocity at inlet, m/s

Y species mass fraction

Lowercase Letters

g_i gravitational acceleration in i direction, m/s^2

k turbulent kinetic energy, m^2/s^2

p pressure, Pa

t time, s

u_i flow velocity in i direction, m

u_j flow velocity in j direction, m

x_i position along i direction, m

x_i position along i direction, m

x_j position along j direction, m

Greek Symbols

ρ density, kg/m^3

μ dynamic viscosity, Pa.s

τ Kolmogorov time scale, s

η Kolomgorov length scale, m

ℓ Turbulence length scale, m

ε turbulent dissipation rate, m^2/s^3

Subscripts

i, j coordinate system directions

Superscript

$\bar{}$ averaged value over time

REFERENCES

[1] Occupational Outlook Handbook, Bureau of Labor Statistics, 2010-11 Edition (http://www.bls.gov/oco/ocos107.htm, visited June 10, 2011).

[2] National Transportation Statistics, Bureau of Transportation, (http://www.bts.gov, visited June 10, 2011).

[3] Garner, R.P., Wong, K. L., Ericson, S.C., Baker, A.J, Orzechowaki, J.A., 2004, "CFD Validation for Contaminant Transport in Aircraft Cabin Ventilation Fields," Report No. DOT/FAA/AM-04/7, U.S. Department of Transportation and Federal Aviation Administration, Office of Aerospace Medicine, Washington DC.

[4] Lin, C.H., Horstman, R.H., Ahlers, M. F., Sedgwick, LM., Dunn, K.H., Topmiller, J.L, Bennett, J.S., Wirogo, S., 2005, "Numerical Simulation of Airflow and Airborne Pathogen Transport in Aircraft Cabins- Part I: Numerical Simulation of the Flow Field," ASHRAE Transactions, **111**, pp: 755-763.

[5] Lin, C.H., Horstman, R.H., Ahlers, M. F., Sedgwick, LM., Dunn, K.H., Topmiller, J.L, Bennett, J.S., Wirogo, 2005, "Numerical Simulation of Airflow and Airborne Pathogen Transport in Aircraft Cabins- Part II: Numerical Simulation of Airborne Pathogen Transport," ASHRAE Transactions, **111**, pp: 764-768.

[6] Lin, C.H., Horstman, R.H., Lebbin, P.A., Hosni, M.H., Jones, B.W, Beck, B.T., 2006, "Comparison of Large Eddy Simulation Predictions with Particle Image Velocimetry Data for the Airflow in a Generic Cabin," HVAC&R Special Issue, **12**(3c), pp: 935-951.

[7] Tang, Y., Ratko, D., Wang, X., 2009, "3D Numerical Simulation of Contaminant Distribution in an Aircraft", *Proceedings of the ASME 2009 International Mechanical Engineering Congress & Exposition*, Lake Buena Vista, Florida, pp: 31-36.

[8] Yan, W., Zhang, Y., Sun, Y., Li, D., 2009, "Experimental and CFD Study of Unsteady Airborne Pollutant Transport within an Aircraft Cabin Mock-up", J. Building and Environment, **44**, pp:34-43.

[9] Su, M., Chen, Q., Chiang, C.M., 2001. "Comparison of Different Sub-Grid-Scale Models of Large Eddy Simulation for Indoor Airflow Modeling", J. Fluids Eng.-Trans. ASME, **123**, pp: 628-639.

[10] Zhao, B., Li, X., Yan, Q., 2003, "A Simplified System for Indoor Airflow Simulation", J. Building and Environment, **38**, pp: 543-552.

[11] Zhang, T., Chen, Q., 2007, "Novel Air Distribution Systems for Commercial Aircraft Cabins", J. Building and Environment, **42**, pp. 1675-1684.

[12] Liu, W., Zhang, Z., Poussou, B. S., Liu, J., Lin, C. H., Chen, Q., 2012, "State-of-the-Art Methods for Studying Air Distribution in Commercial Airliner Cabins", To appear in J. Building and Environment

[13] Abdilghanie, A. M., Collins, L. R., Caughey, D. A., 2009, "Comparison of Turbulence Modeling Strategies for Indoor Flows", J. Fluids Eng.-Trans. ASME, **131**, pp.051402-1:051402-18.

[14] Lebbin, P.A., 2006, "Experimental and Numerical Analysis of Air, Tracer Gas and Particulate Movement in a Large Eddy Simulation Chamber", PhD dissertation, Kansas State University. Manhattan, Kansas.

[15] Padilla, A.M., 2008, "Experimental Analysis of Particulate Movement in a Large Eddy Simulation Chamber", MS Thesis, Kansas State University. Manhattan, Kansas.

[16] Smagorinsky, J., 1963, "General Circulation Experiments with the Primitive Equations: I. The Basic Experiment", Monthly Weather Review, **91**, pp: 99-164.

[17] Lilly, D.K, 1966, "*On the Application of the Eddy Viscosity Concept in the Internal Sub-range of Turbulences*", National Center for Atmospheric Research, Manuscript No.123.

[18] Werner. H., Wengle, H., 1991, "Large Eddy Simulation of Turbulent Flow Over and Around a Cube in a Plate Channel", *8th Symposium on Turbulent Shear Flows*, Munich, Germany.

[19] Bird, B.R., Steward, W.E., Lightfoot, E.N., 2001, "*Transport Phenomena*", 2nd Edition, John Wiley and Sons, NY.

[20] Launder, B.E., Spalding, D.B., 1972,"*Lectures in Mathematical Models of Turbulence*," Academic Press, London, England.

[21] Yakhot, V., Orszag., S.A., 1986,"Renormalization Group Analysis of Turbulence: I. Basic Theory", J. Scientific Computing, **1**(1), pp: 1-51.

[22] Shih, T.H., Lieu, W.W., Shabbir, A., Yang, Z., Zhu, J., 1995, "A New k-ε Eddy-Viscosity Model for High Reynolds Number Turbulent Flows - Model Development and Validation" J. Computers & Fluids, **24**(3), pp: 227-238.

[23] Fluent 6.3 User's Manual Guide (http:/my.fit.edu/itresources/manuals/fluent6.3, visited Nov. 12, 2011).

[24] Landahl, M.T. , Mollo-Christensen, M., 1992, *Turbulence and Random Processes in Fluid Mechanics*, 2nd Edition, Cambridge, UK.

Figure Captions List

Fig. 1 Full scale generic aircraft half-cabin mockup model [14].

Fig. 2 Dimensions of the generic cabin model and the location of PIV monitoring windows on the cabin central plane (units in mm) [15].

Fig. 3 A schematic view of the experimental setup for tracer gas measurements. The xy view of the setup shows the tracer gas sampling points above and below the injection tube.

Fig. 4 The results of uncertainty study for the cabin with full-height nozzle when x component of velocity data are predicted for the location 5 of the PIV measuring windows. The PIV data were produced by Lebbin [14].

Fig. 5 The converging behavior of x-component of velocity deviations with respect to the corresponding prediction from the finest grid for the location 5 of PIV measuring windows.

Fig. 6 The converging behavior of x-component of velocity deviations with respect to the corresponding prediction from the finest grid from steady RANS solution for all the PIV measuring windows.

Fig. 7 Comparison of the predicted values (this study), PIV measurements [14] and predictions produced by Lin et al. [6] for the airflow velocity data corresponding to the location 1 of the cabin with full-height nozzle.

Fig. 7 Comparison of the predicted values (this study), PIV measurements [14] and predictions produced by Lin et al. [6] for the airflow velocity data corresponding to the location 4 of the cabin with full-height nozzle.

Fig. 8 Study the effect of choosing monitoring surface on the predicted velocities, corresponding to location 2 of the cabin with full height nozzle, through comparison with PIV measurements [14].

Fig. 9 Comparison of the steady RANS predictions for the x-component of velocity data with the corresponding time dependent PIV data [14] at location 3 of PIV measuring window.

Fig. 10 Comparison of the steady RANS predictions for the x-component of velocity data with the corresponding time dependent PIV data [14] at location 5 of PIV measuring window.

Fig. 11 Comparison of the LES predictions and PIV measurements [14] for the x component of velocity data corresponding to the location 1 of the cabin with half-height nozzle.

Fig. 12 Comparison of the LES prediction and PIV measurements [14] for velocity data corresponding to the location 3 of the cabin with half- height nozzle.

Fig. 13 Study the effect of decreasing the cabin nozzle height through a comparison between the PIV measured velocity data [14] corresponding to the location 5 of the PIV measuring windows for two cases of full and half-height nozzle.

Fig. 14 Study the effect of decreasing the cabin nozzle height through a comparison between the PIV measured velocity data [14] corresponding to the location 3 of the PIV measuring windows for two cases of full and half-height nozzle.

Fig. 15 3-D schematic of the unstructured grid (for the generic cabin with the injection tube) used in CFD simulation of the carbon dioxide diffusion in the generic cabin model.

Fig. 16 Comparison between the times averaged predictions and measurement of dimensionless CO_2 concentration data [14] for the sampling points located along the x-axis above the injection tube.

Fig. 17 Comparison between the times averaged predictions and measurement of dimensionless CO_2 concentration data [14] for the sampling points located along the x-axis below the injection tube.

Table Caption List

Table 1 Comparison between the important parameters in the simulations.

Table 2 Comparison of RMS values for computed CO_2 concentrations using two different grid sizes.

Table 3 Comparison of mean values for computed CO_2 concentrations using two different grid sizes.

Appendix B – Published Articles

Proceeding of ASME 2011 International Mechanical Engineering Congress & Exposition

November 11-17, Denver, Colorado, USA

IMECE2011-64183

SIMULATION OF THE TURBULENT DISPERSION OF 10 MICRON PARTICLES IN A GENERIC HALF-CABIN MODEL

Khosrow Ebrahimi
Mechanical and Nuclear Engineering
Kansas State University
Manhattan, KS 66506
khe1976@ksu.edu

Zhongquan C. Zheng
Aerospace Engineering Department
University of Kansas
Lawrence, KS 66045
zzheng@ku.edu

Mohammad H. Hosni
Mechanical and Nuclear Engineering
Kansas State University
Manhattan, KS 66506
hosni@ksu.edu

ABSTRACT

Study of particle dispersion in ventilated indoor environments is a very useful and effective way to understand the mechanism for disease transmission in an enclosed environment. In this investigation, a computational approach is adopted in order to gain more knowledge about the transport of particulate materials in a simplified half cabin model of a Boeing 767. The simulations are performed using a commercial Computational Fluid Dynamics (CFD) software and are validated through comparing the predictions with the corresponding experimental measurements. The Lagrange-Euler approach is invoked in the simulations. In this approach, while the air is considered as the continuous first phase, the particles are treated as the discrete second phase. By solving the particles equation of motion, the trajectory of particles is computed. The discrete phase equation of motion is coupled with the continuous phase governing equations through the calculation of drag and buoyancy forces acting on particles. The continuous phase flow is turbulent and Reynolds Averaged Navier Stokes (RANS) is employed in the calculation of continuous phase velocity field. A complete study on grid dependence of RANS simulation is performed through a controllable local mesh refinement scheme. The grid dependence study shows that using unstructured grid with tetrahedral and hybrid elements in the refinement region are more efficient than using structured grid with hexahedral elements. The effect of turbulence on particle dispersion is taken into account by using a stochastic tracking method (random walk model). Through the comparison of computational predictions with corresponding experimental measurements the capability of Discrete Phase Model (DPM) in predicting the behavior of particles is studied.

INTRODUCTION

During the past decades, the aviation industry has experienced a dramatic increase in both the number of people traveling by commercial airplanes as well as the number of long distance commercial flights. According to the Bureau of Labor Statistics (2011), the number of commercial airline passengers experienced an average growth of 340% between the years 1970 and 2008. Also the statistics published by the Bureau of Transportation indicates 650-800 million passengers travel by aircrafts each year in the United States, around 20% of those are international passengers. The close proximity of this huge number of commercial airline passengers especially in long distance flights has increased the risk of spreading biological contaminants and diseases between passengers. This potential threat to passengers health is the primary reason for funding of this research project and study of air quality in commercial aircraft cabins.

Study of air quality requires the study of different transport phenomena: transport of mass, momentum, and energy. Due to advances in computer technologies which have enabled researchers to solve the required governing partial differential

equations numerically, with relatively high degree of accuracy, in a cost and time effective manner, the use of computational methods in this field of research has increased considerably in recent decades.

Since biological contaminants and/or viruses may spread among aircraft passengers in the form of fine particulates, the primary attention is focused on the understanding of the particle dispersion patterns in such enclosures. There are a number of relevant research articles in the literature that use the computational methods in order to study the particle dispersions in indoor environments.

Zhao et al. (2003) investigated the air movement and aerosol particle concentration and deposition in a ventilated room numerically. Two different ventilation systems were considered: displacement and mixing. In order to simulate airflow and particle dispersion, the Lagrange-Euler approach was adopted. This study showed the strong effect of the room ventilation type on the airflow pattern, the particle concentration, and deposition rate. It was found that under the same air supply rate and particle property conditions, using the displacement ventilation type leads to smaller deposition rate and a larger particle removal rate than the mixing type ventilation. However the average particle concentration is higher in a displacement type ventilation system.

In another study by Zhao et al. (2004), an Euler-Euler approach was used to study the effects of air ventilation type and particle size on the behavior of particle dispersion in a ventilated room. A three dimensional drift flux model was used combined with deposition boundary conditions for the wall surfaces. Through this computational research it was found that the deposited particle mass or flux is strongly dependent on the ventilation type. More particle depositions were observed in the mixing ventilated room for a certain size of particles.

In 2009, Zhao et al. developed their drift flux model by considering the effects of both thermal and gravitational forces in calculating the particles slippage velocity for non-isothermal cases. After an experimental validation of the modified model, it was used to study the effect of the indoor ventilation type and particle size on dispersion pattern of ultrafine (particles with sub-100nm diameter) particles in a test room. Through this study, it was determined that although using mixing ventilation type leads to lower concentration of micron particles in the zone below one meter high, it will cause higher concentration of ultrafine particles in the mixing zone in comparison to the displacement ventilation type. It was also concluded that both ventilation types are not sensitive to the particle size when the diameters are in the range of 0.01 to 0.1 micron.

Zhang et al. (2010) used an Euler-Euler approach to study the deposition of particles of tens of microns size. The particles were created due to aggregation of nano-particles injected through an injection port to the test chamber. The transient deposition of particles caused by the gravitational settling was simulated. For this purpose the mass conservation equation for the discrete phase was modified to include the gravitational settling effect as well as convection and diffusion effects. The simulations were verified through the comparisons between predictions and measurements for the particles deposition-rate data. The comparisons indicated best agreement between experimental measurements and computational predictions for the intermediate particle-size range.

This study is a continuation of the previous research conducted by the authors of this paper in the numerical investigation of the turbulent airflow and tracer gas diffusion in a generic cabin model (The generic cabin model resembles one-half of a twin-aisle Boeing 767 aircraft cabin neglecting the curves in the corners and the walls). However, in this paper, the airflow pattern is different from what was studied previously, because the injection of particles in this case is accompanied with the high flow-rate injected air. A steady RANS method is used to simulate the turbulent airflow behavior. Using the steady RANS to calculate the airflow velocity data, a comprehensive grid dependency study is performed by concentrating on regional refinement using both structured and unstructured grids. The effectiveness of both grid refining schemes in producing the converged velocity data is investigated and discussed. The optimum mesh size and type is then used to simulate the dispersion of 10 micron size particles by applying a Discrete Phase Model (DPM). The particles are made of Di-Octyle Phthalate (DOP)[1] and injected continuously into the cabin through a vertical tube installed on the cabin's floor. The computational model is verified through the comparison of the predicted particles concentration data with the corresponding experimental measurement conducted by Padilla (2008). Another feature of this study is the investigation of the effect of the number of tries on the accuracy of results. Subsequently, the optimum number of tries to obtain the most accurate predictions for the particle dispersion data is determined.

GOVERNING EQUATIONS AND NUMERICAL SOLUTION METHOD

In the Lagrange-Euler approach, which is also called Discrete Phase Model (DPM), the discrete phase computations are performed in a Lagrangian frame (calculation of particles trajectories). The continuous gas phase, however, is dealt with in an Eulerian frame and does interact with the discrete phase through the exchange of momentum, heat and mass. In this approach, the interaction between particles is not taken into account. In order to have negligible interactions between particles, the discrete phase needs to be sufficiently dilute. For this reason the application of DPM is recommended only for the two-phase flows that have low volume fraction of discrete phase.

[1] Chemical Formula: $C_{24}H_{38}O_4$

In order to simulate the dispersion of particles, using DPM, the following assumptions have been adopted:

1. The continuous phase flow is incompressible.
2. The heat transfer is neglected in the cabin. The temperature is assumed to be constant at 27°C.
3. The particles are not cooled, heated or evaporated (inert particles).
4. The particles neither coagulate nor break.
5. The effects of buoyancy are taken into account.
6. No chemical reaction takes place between discrete and continuous phases.
7. Steady RANS model is used to solve the continuous phase governing equations.
8. Except the drag and gravity forces, other forces are assumed to be zero.
9. The particles are assumed to be trapped on the walls when they collide with the walls.

Discrete Phase Equation of Motion

The trajectory of particles is computed through integrating the governing equation for the particles motion:

$$\frac{du_i^p}{dt} = \frac{F_i}{m_p} \tag{1}$$

where m_p(kg) is the mass of particle, u^p(m/s) is the velocity of particle in i direction. F_i (N) denotes all the forces acting on the particle which is a combination of viscous, pressure drags, and buoyancy force (Clayton et al. , 1998):

$$F_i = \frac{1}{2}\rho \cdot A \cdot C_D \cdot (u_i - u_i^p)\left|u_i - u_i^p\right| + m_p g_i \frac{\rho_p - \rho}{\rho_p} \tag{2}$$

where ρ and ρ_p (kg/m^3) are the densities of the continuous phase (air) and particles, respectively, C_D is the drag coefficient for the spherical particle, A (m^2) is the projected area for the particle, u_i (m/s) is the instantaneous velocity of continuous phase in i direction, and finally g_i (m/s^2) is the gravitational acceleration in i direction.

Equations (1) and (2) indicate that the continuous phase affects the trajectory of particles through the drag and buoyancy forces.

Continuous Phase Governing Equations

The governing equations for the continuous phase are:

Continuity:

$$\frac{\partial u_i}{\partial x_i} = 0 \tag{3}$$

Momentum (Navier-Stokes):

$$\frac{\partial u_i}{\partial t} + u_j \frac{\partial u_i}{\partial x_j} = -\frac{1}{\rho}\frac{\partial p}{\partial x_i} + \frac{1}{\rho}\frac{\partial}{\partial x_j}\left(\mu \frac{\partial u_i}{\partial x_j}\right) + g_i - \frac{F_i}{m_p} \tag{4}$$

where μ(kg/m.s) is the continuous phase viscosity, p (Pa), is the continuous phase pressure and F_i/m_p (N/kg) is the force acting on the continuous phase exerted by the discrete phase (the reaction of drag and buoyancy forces acting on the particles).

In coupled (2-way coupling) approach, the effect of discrete phase on the continuous phase calculations is taken into account by keeping the last term in Eq. (4). However, in uncoupled approach (1-way coupling) the effect of discrete phase on the continuous phase is neglected by dropping the last term of Eq. (4).

Solution Method

The simulation begins with the quasi-steady solution of the continuous phase governing equations, i.e. Eqs. (3) and (4). At the beginning, the value of the last term in Eq. (4) is considered as zero. Therefore the number of unknowns (three velocity components and one pressure) matches with the number of equations (one continuity and three momentum equations). After the first 5 iterations of the continuous phase computations, using the calculated velocity data (for the continuous phase) from the last iteration, the trajectory of particles is calculated by solving Eqs. (1) and (2). By calculating the particles trajectory, the last term in Eq. (4) will not be zero for the next 5 iterations of the continuous phase computations. After every 5 iterations of the continuous phase calculations, the last term of Eq.4 is updated by solving Eqs. (1) and (2) simultaneously. This computational scheme is continued until the convergence criteria (10^{-7} for velocity components as well as k and ε and 10^{-6} for continuity) for the continuous phase governing equations are satisfied.

Turbulence model

In solving Eqs. (3) and (4), which govern the instantaneous velocity field of the continuous phase (airflow), Reynolds Averaged Navier Stokes (RANS) is applied. In this study, for steady RANS:

$$\frac{\partial \overline{u}_i}{\partial x_i} = 0 \tag{5}$$

$$\frac{\partial \overline{u}_j \overline{u}_i}{\partial x_j} = \frac{\partial}{\partial x_j}\left(-\overline{p}\delta_{ij} + (\mu + \mu_t)\left(\frac{\partial \overline{u}_i}{\partial x_j} + \frac{\partial \overline{u}_j}{\partial x_i}\right)\right) + \rho g_i - \frac{F_i}{m_p} \tag{6}$$

Using the standard k-ε turbulence model, the turbulent viscosity is calculated through the following equation:

$$\mu_t = \frac{C_\mu \rho k^2}{\varepsilon} \tag{7}$$

where C_u is an empirical constant which is equal to 0.09 (Launder and Spalding, 1972).

Particle-Turbulence Interactions

The major issue in the Lagrange-Euler approach, or the Lagrangian particle tracking, is calculating the effect of turbulence on particles trajectory (Dehbi, 2008). As explained before, the trajectory of particles is computed by integrating the equation of motion (Newton's second law) of the particles. By combining Eq. (1) and (2) the following equation is derived for the spherical particles Integrating this equation determines the path of particles.

$$\frac{du_i^2}{dt} = \frac{3C_D\rho}{8r\rho_p}(u_i - u_i^2)\left|u_i - u_i^2\right| + g_i\frac{(\rho_p - \rho)}{\rho_p} \tag{8}$$

In the equation above r (m/s) denotes the particle radius and as RANS method is used, the instantaneous velocity, u_i, consists of a time-averaged or mean component ($\overline{u}_i$) and a fluctuating component (u'). The continuous phase mean velocity data is computed from the RANS method. The turbulence affected the trajectory of particles through the fluctuating velocity (u').

In this study, in order to calculate the effect of turbulence on trajectory of particles, the Discrete Random Walk (DRW) model is used. The main idea of this model is the interaction between the particles and turbulent eddies. In other words, in this model, it is assumed that the particle is trapped by an eddy during an eddy life time. The eddy life time (τ_e) is calculated using the equation below:

$$\tau_e = 2C_L\frac{k}{\varepsilon} \tag{9}$$

The value of C_L in Eq. (9) does depend on the employed turbulence model. For the k-ε model, $C_L \approx 0.15$. During lifetime of the eddy, the continuous phase velocity fluctuations are randomly distributed Gaussian variables whose Root Mean Squared (RMS) values are equal and deduced from the turbulent kinetic energy:

$$u_i' = \lambda_i\sqrt{\overline{u_i^2}} \tag{10}$$

$$\sqrt{\overline{u_i^2}} = \sqrt{2k/3} \tag{11}$$

In equations above, λ's are Gaussian random variables with the mean value of 0 and the standard deviation of 1. In the simulations, in order to calculate the random effects of turbulence on the discrete phase dispersion, it is required to pick a sufficient number of representative particles which is called the number of tries (Dehbi, 2008 and the ANSYS FLUENT 12.0 Manual, 2009). The effect of number of tries will be discussed in the next section.

Particle Tracking Parameters

In order to take the integration of Eq. (8), two parameters should be specified: The time step size and the maximum number of time steps. The time step size can be calculated using the following equation:

$$\Delta t = \frac{L}{\left\|\vec{u}_p\right\| + \left|\vec{u}\right|} \tag{12}$$

where L (m) is the length scale, $\left|\vec{u}_p\right|$ (m/s), is the magnitude of particle velocity and $\left\|\vec{u}\right\|$ (m/s), is the magnitude of continuous phase velocity. In this study the length scale, which is the length traveled by particle between two successive particle tracking updates, is assumed to be constant and equal to 0.01m. The maximum value of Δt is such that the cell is traversed in one step. Smaller time steps leads to more accurate results. The maximum number of steps should be equal to the number of grid cells that particles traverse in a computational domain (ANSYS FLUENT 12.0 Manual, 2009).

Numerical Scheme

In the RANS method, the second order upwind scheme is used to discretize spatial derivatives in the governing continuity and momentum equations. Also the standard wall function is used as the near wall treatment. In calculating the particle trajectories, which is performed through the integration of Eq. (8), an automated tracking algorithm is employed. This algorithm switches between the numerically stable lower order and higher order schemes, depending on whether or not the particle is close to the hydrodynamic equilibrium (ANSYS FLUENT Manual, 2009). In this study, the trapezoidal integration is used in higher order scheme however for the lower order scheme an implicit Euler integration is applied.

EXPERIMENTAL PROCEDURE: MEASUREMENT AND INJECTION LOCATIONS

Particles are injected continuously through an injection tube located at x=1447 mm, y=595 mm, and z=0 (see Fig.1). The injection tube, which installed vertically on the cabin's floor, is made of stainless steel and has the inner diameter of 22.1 mm (Figures 1 and 2). The injection port is the upper end of the injection tube which has 595 mm height (Padilla, 2008).

Figure 1 shows the generic cabin with the particles injection tube inside it. Also, the measurement locations are shown in this schematic. It should be mentioned that for the five measurement locations on the cabin central plane, the Aerodynamic Particle Sizer (APS) is used to measure the concentration of the discrete phase (particles). However, for the nine measurement locations at the cabin outlet, Optical Particle Counter (OPC) is used for the concentration measurements. The measurement locations at the outlet have the height of 51mm.

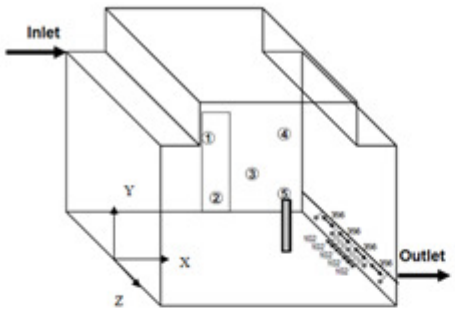

Figure 1: Schematic of the generic cabin, injection tube and measurement locations (units in mm). (Padilla, 2008)

Using the dimensions shown in Fig.2, the coordinates of the five measurement location on the cabin central plane can be determined. This figure also presents information about the inlet volumetric airflow rate as well as the volumetric flow rate of carrying air injected into the cabin through the particle injection tube. Particles are produced by the Vibrating Orifice Aerosol Generator (VOAG) as shown in this figure. VOAG was set to a vibrating frequency of ~49 Hz that yields a theoretical concentration of 54 particles/cm^3. Particles are made of Di-Octyl Phthalate (DOP oil).

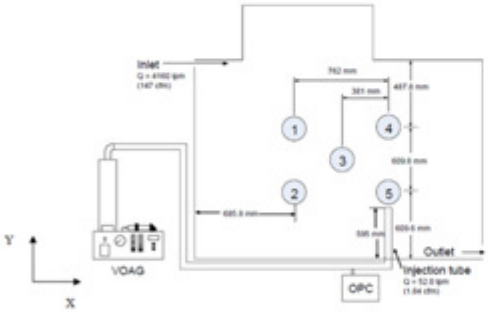

Figure 2: XY View of the test configuration for the straight tube injection (units in mm). (Padilla, 2008)

In each experiment, the measurement of particles concentration was started when the air flow inside the cabin reached a quasi-steady state condition. Initially 15 minutes and later 30 minutes time was considered as the warm-up time for the system in order to reach the steady state conditions. The particle measurements were carried out continuously at each sampling location over the period of 60 minutes. The experimental data were presented in terms of normalized particle concentration data. The normalized particle concentration data were calculated using the following equation (Padilla, 2008):

$$C = \frac{C_m \times Q_{sup}}{C_I \times Q_I} \tag{13}$$

where C_m is the measured sample concentration corrected for the particle loss in the sampling tube, C_I is the calibrated injected concentration, Q_{sup} is the supply flow (inlet and injected), and Q_I is the injected flow of the carrying air.

RESULTS AND DISCUSSIONS

Part 1- Simulation of Turbulent Airflow and the Grid Dependency Study

In the experiments, the average airflow rate coming into the cabin was maintained at the constant value of 4.2 m^3/min, resulting in an average inlet velocity of 0.64 m/s. The corresponding Reynolds number based on the hydraulic diameter of nozzle inlet was calculated as 4,200. At the outlet of the 22.1 mm particle injection tube, the airflow rate injected into the cabin was held at a constant rate of 0.05 m^3/min, resulting in an average airflow velocity of 2.27 m/s. The corresponding Reynolds number based on the injection tube diameter was 3300.

The XY view of the grid is shown in Fig.3. This figure also shows the region where the grid refinement is focused. Figure 4 shows the 3D view of the cabin as well as the refinement region. The volume of the refinement region is less than 3% of the whole volume of the generic cabin model. The refinement region, as shown in Fig.4, consists of two sub-volumes. Locations 1, 2 and 3 are located on the interface between these two sub-volumes. At the beginning , a pseudo-structured coarse mesh is generated for the cabin. This mesh is used as the base grid for the next refinements. Two approaches are followed in the refinements. In the first approach, it is tried to keep the grid inside the refinement region structured with orthogonal hexahedral mesh elements, however in the second approach, unstructured grid with different types of mesh elements (hexahedral, tetrahedral, wedges) is used for the refining purposes. In both of the approaches the grid in other regions and sub-volumes are kept structured.

In order to check the grid independency, the velocity data calculated using different grid sizes are compared with the corresponding results from the finest grid. If this difference(deviation) experiences decreasing as the number of mesh cells increased then the solution would meet the grid independency criteria.

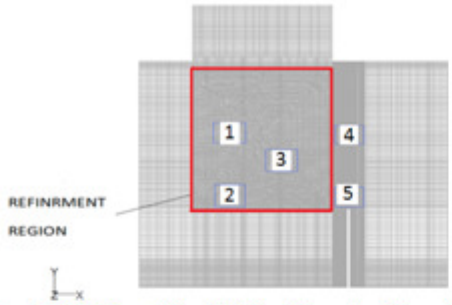

Figure 3: XY View of the grid. The refinement region and APS measurement locations

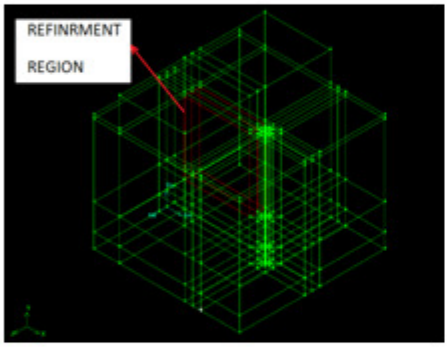

Figure 4: 3D View of the cabin and the sub-volumes in order to create the grid. The refinement region is also marked by red edges

Figures 5-9 show the behavior of the results as the both approaches explained above are used in grid refining. In each figure, there are four tables and graphs. The tables and graphs in the left side of each figure show the effect of grid refinement when the structured grid refining is followed however the tables and graphs in the right side show the uncertainty study results when the grid is refined in the refinement region using an unstructured scheme. Each table has four columns. The first column shows the total number of mesh elements in the whole geometry. The second column shows the number of mesh cells in the refinement region. The third column shows the calculated velocity data for each grid size. And finally, the last column is the corresponding deviation percentage for each grid size which is calculated using the following equation:

$$Deviation\% = 100 \times \frac{V_{cal} - V_{cal,\,finest}}{V_{cal,\,finest}} \qquad (14)$$

In the equation above, V_{cal} (m/s) is the calculated velocity for a specified grid size and $V_{cal,finest}$ (m/s) is the corresponding velocity calculated from the finest grid.

Figure 5 shows the effect of grid refinement on the behavior of x and y components of calculated velocity data corresponding to the location 1 of the APS measurement locations. It is seen that the velocity data are converged using either structured or unstructured refining scheme however unstructured grid refinement resulted in converged velocity data for grids with less number of mesh cells comparing to structured refining approach.

Figure 6 shows the effect of grid refinement on the behavior of calculated x and y velocity data corresponding to the APS location 2. Similar to the APS location 1, it is observed that unstructured grid refining scheme is more efficient in reaching converged velocity data.

Figure 7 shows the effect of mesh refinement on the velocity calculations for the APS location 3. It is seen that the behavior of velocity data for this location is different from what was observed in the APS locations 1 and 2. Indeed the convergence criteria are not met for the velocities calculated for this location. In order to find a physical reason for this behavior, a special attention should be paid to the position of the APS location 3 in the cabin model (Figure 1, 2 and 3). In this location, which is almost in the middle of the cabin, the flow is almost stationary and it is seen from the tables presented in Figs. 9 and 10 that the magnitude of both x and y velocity data are very close to zero. Therefore the deviations for this location are much higher than those calculated for the locations 1 and 2.

Although the mesh refinement is focused on the refinement region that contains the APS locations 1, 2 and 3, the grid in other regions are also refined due to the mesh refinement in the refinement region. However the refinement in other regions is not as much as that happens in the refinement region. Therefore the calculated velocity data in the APS locations 4 and 5 are also affected by the consecutive grid refinements. Figure 8 indicates the effect of mesh refinement on the behavior of velocity data in the APS location 4. It is seen that although this location is outside of the refinement region, using the unstructured refining scheme for the refinement region leads to reach converged velocity data for grids with less mesh element comparing to the case when the structured grid refining is used.

Figure 9 indicates that using unstructured grid refining in the refinement region has a very significant improvement in the convergence of the calculated x-velocity data in the APS location 5. However for y-velocity data in location 5, it shows that using either structured or unstructured grid gives results with acceptable convergence behavior.

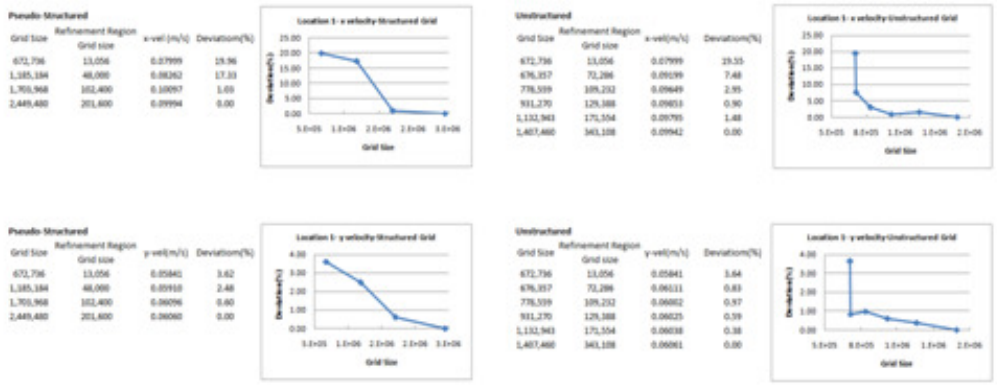

Figure 5: The effect of grid size on the calculated x and y components of airflow velocity corresponding to the location 1 of the APS measurement location

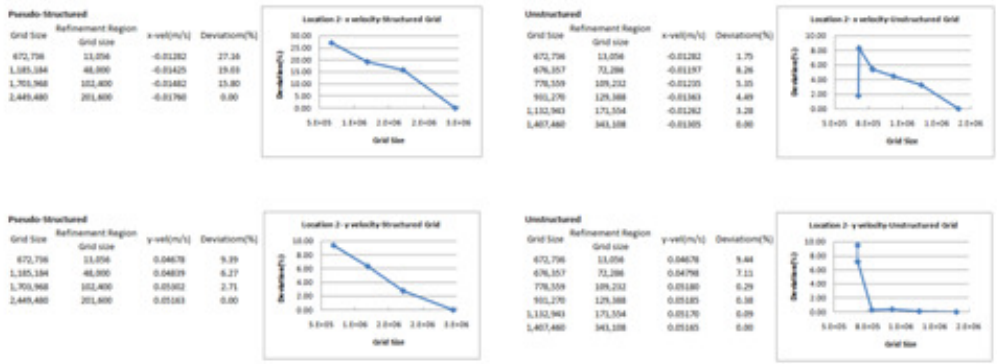

Figure 6: The effect of grid size on the calculated x and y components of airflow velocity corresponding to the location 2 of the APS measurement location

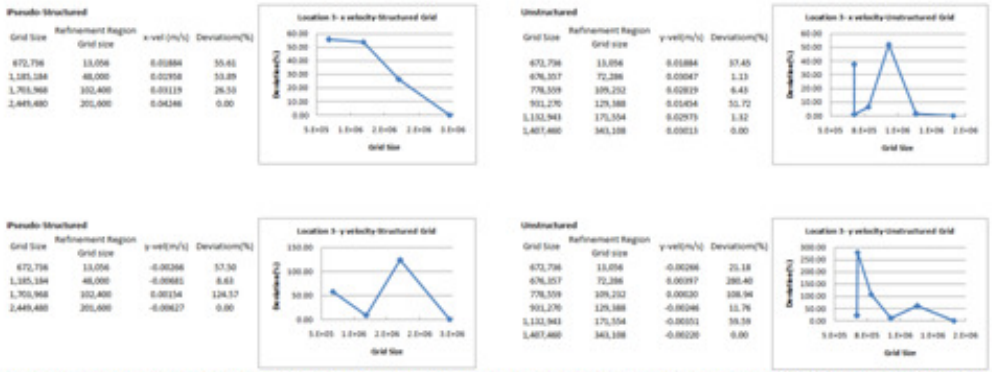

Figure 7: The effect of grid size on the calculated x and y components of airflow velocity corresponding to the location 3 of the APS measurement location

Figure 8: The effect of grid size on the calculated x and y components of airflow velocity corresponding to the location 4 of the APS measurement location

Figure 9: The effect of grid size on the calculated x and y components of airflow velocity corresponding to the location 5 of the APS measurement location

All the APS measurement locations are located on the central plane of the cabin (z=0). Due to the symmetry of the geometry as well as the boundary conditions respect to the central plane, the z-component of velocity data for the points on this plane are expected to be very close to zero and of course the computational results confirmed this expectation. Because of the very small values of z component of velocity data for the APS locations 1-5, the behavior of z-velocity data don't show a converging trend and the deviations are much larger than what were calculated for x and y components of velocity data.

From the graphs and tables presented through Fig. 5-9, the significant advantages of using the unstructured grid refining approach comparing to the structured one is revealed. As shown in the above mentioned figures, in the structured grid refining approach, by 1400% increase in the number of mesh elements in the refinement region, from 13,056 to 201, 600, the total number of mesh elements for the whole geometry is increased by 250% i.e., from 672,736 to 2,449,480. However, in the unstructured grid refining approach, the total number of mesh elements is less sensitive and by 2528% increase in the number of mesh cells in the refinement region from 13,056 to 343,108, the total number of mesh elements experiences just a 109% growth i.e., from 672,736 to1,407,460. In the other word, the unstructured mesh refinement scheme enables us to make a high resolution grid in the refinement region with the minimum increase in the total number of mesh elements for the whole geometry. Especially when the better converging behavior of results from the unstructured grid refinement is taken into

account, it can be concluded that using unstructured grid for the local refinement purposes, not only leads to the more accurate and reliable results , but also it would be considerably more computational time and cost effective comparing to the structured mesh refinement.

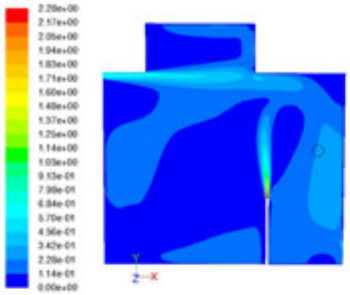

Figure 10: Airflow velocity magnitude contours on the central plane (z=0) of the generic cabin model

Part 2- DPM Simulation Results for the Particles Concentration Data- Study the Effect of Number of Tries

As explained earlier, the inert DOP[1] spherical particles with 10 micron diameter are injected continuously through the top end surface of the particle injection tube (surface injection). The vertically upward velocity of the injected particles, at the injection surface, is uniform and equals to 2.27 m/s. The concentration of particles at the injection port is 54 particle/cm^3. There are three sets of experimental measurements, entitled with: test 2-APS, test 3-APS, and test 5-APS, used in order to evaluate the simulations. The uncertainty of the experimental data is around 39%. Because of some deficiencies in measuring the particles injection at the APS location 5, the comparison between the computations and measurements does not include this location and just made for the locations 1, 2, 3, and 4. The finest unstructured grid with 1,407,460 mesh elements (which discussed earlier in grid independency study) is picked to be used in the simulations. Figure 11 shows an evaluation of the explained computational simulation by comparing the model predictions with the corresponding experimental measurements for the APS locations on the central plane of the cabin (see Fig.1). In this figure the concentration data were normalized using Eq. (14). As discussed previously in the particle-turbulence interaction section, the accuracy of results depends on the number of tries. The number of tries for the simulation results shown in Fig. 11 is 175. Considering the uncertainty bars for the experimental data, it is seen the model gives results with acceptable accuracies at least for APS location 3 and 4.

[1] Di-Octyle Pirthalate

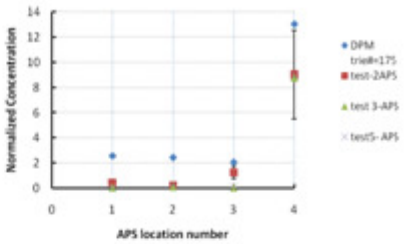

Figure 11: Comparisons between the computational predictions (when the number of tries is 175) and the corresponding experimental measurements for the APS location on the cabin central plane.

Table 1 shows the tabular outcomes of the investigation about the effect of number of tries on the accuracy of predicted particle concentration for the APS locations on the cabin's central plane. It is seen that there is not a unique optimum value for the number of tries to lead the most accurate results for the all APS location on the central plane.

Table 1: Effect of number of tries on the accuracy of predicted particle concentration data for the APS locations on the cabin central plane

APS location Number	The reference Experimental Test Title	The Number of Tries corresponding to the Minimum Errors	Minimum Error(%)
1	test 2-APS	100	223
2	test 2-APS	175	83
3	test 2-APS	175	57
4	test 2-APS	120	7

If for each selected number of tries, the arithmetic average of errors for the APS locations on the central plane (except of location 5) are calculated and compared to the corresponding average errors calculated for other numbers of tries, then the optimum number of tries which leads to the minimum average errors can be found. Such a comparison is shown in Fig.12. As implied from this figure, selecting 175 as the numbers of tries gives the most accurate prediction rather than other number of tries. The average error corresponding to this number of tries is 340%.

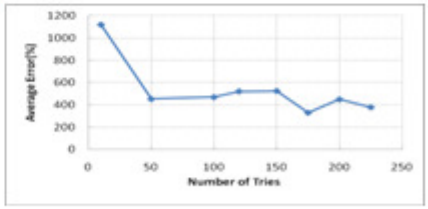

Figure 12: Comparisons between the arithmetic average errors for the predicted particle concentration data corresponding to the APS locations 1, 2, 3, and 4 when different numbers of tries are examined. Eight different numbers of tries were examined in this comparison: 10, 50, 100, 120, 150, 175, 200, 225.

Another evaluation of DPM simulations are presented in Fig.13. In this figure, the predicted results for the particle concentration data for the sampling points located at the cabin outlet (which are also called OPC[1] locations) are compared to the corresponding experimental data measure by Optical Particle Counter. Figure 13 indicates that how increasing the number of tries from 10 to 150 affects the average accuracy of the predictions. Figure 14 shows the relationship between the number of tries and the average accuracy. As it is indicated in this figure, amongst the examined number of tries(i.e. 10, 50, 100, 120, 150, 175, 200, and 225), the least average error is achieved when 150 is selected as the number of tries. The average error correspond to this number of tries is 169%. It is needed to mention that similar to what was observed for the sampling points on the cabin central plane, the optimum number that leads to the most accurate prediction for each of the sampling points located at the cabin outlet is not necessarily equal to the optimum number was found to have the least average errors for all the OPC locations. It is also implied from Fig.14 that the simulation results are closer to the measurements for the OPC sampling points located in z>0 region.

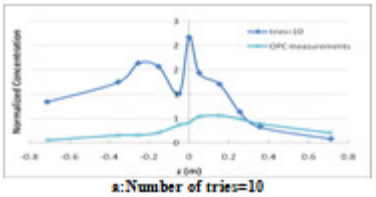

a:Number of tries=10

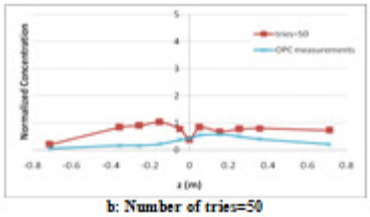

b: Number of tries=50

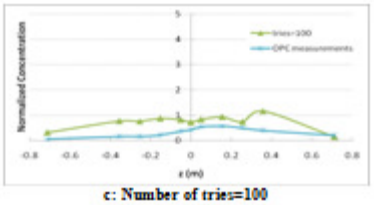

c: Number of tries=100

[1] Optical Particle Counter

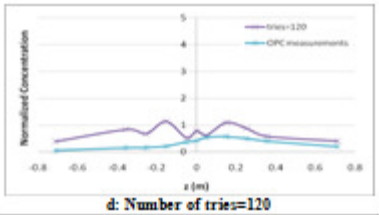

d: Number of tries=120

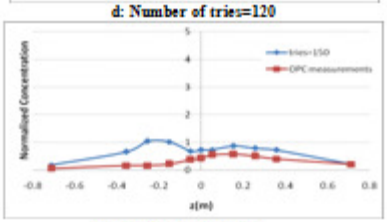

e: Number of tries=150

Figure 13: Comparisons between the computational predictions (when different number of tries are examined) and the corresponding experimental measurements for the OPC location at the cabin outlet.

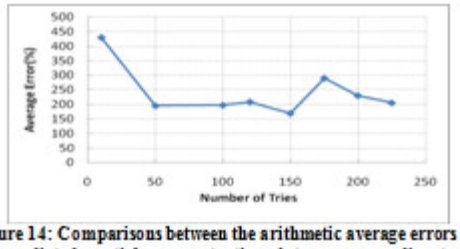

Figure 14: Comparisons between the arithmetic average errors for the predicted particle concentration data corresponding to the OPC locations at the cabin outlet when different numbers of tries are examined. Five different numbers of tries were examined in this comparison: 10, 50, 100, 120, 150.

CONCLUSIONS

In this study, the research about the capabilities of computational approaches in investigating different transport phenomena in aircraft cabins was continued by simulating the turbulent airflow and dispersion of inert spherical particles injected into a generic half cabin model. In order to simulate the turbulent airflow a steady RANS scheme was applied using standard k-ε model. A detailed comprehensive grid dependency analysis was conducted and based on its results the optimum grid was selected to perform DPM simulation of particle dispersion in the cabin. In the DPM simulations, the effect of motion of particles on the continuous phase was taken into account by using a 2-way coupling approach. The effect of turbulence on the particles motion was simulated by employing

the Discrete Random Walk (DRW) Model. The effect of number of tries on the accuracy of predictions was also studied in details.

From the grid dependency, the benefits associated with the regional mesh refinement was revealed. Based on the structure of the flow, it is not necessary to do the refinement in all of the flow regions. In this study, the refinement was focused on a region in which the flow was more complicated. Using the regional refinement, enabled us to have more control on the number and the type of the mesh elements. The other benefit of using regional refinement was preventing to be encountered with non-useful excessive number of mesh elements that increases the computational costs and time dramatically.

Although the initial generated coarse mesh was structured, two approaches were used in refining the mesh in the selected refinement region. After several tests, it can be concluded that unstructured local grid refinement not only leads to the more accurate and reliable results , but also it is considerably more computational time and cost effective rather than the structured local grid refinement.

Comparison of the Steady RANS-Steady Particle Tracking (DPM) simulation results with the corresponding experimental data revealed that, considering the measurements uncertainty, there is a good agreement between the predictions and measurements at least for the APS locations 3, and 4 (on the cabin central plane). Because of the experimental deficiencies in measuring the correct value of particles concentration at the APS location 5, the simulations were not verified by comparing the predictions and measurements corresponding to the this location. For the APS locations 1 and 2 , since the value of experimental measurements are very small, achieving predictions with good accuracy for these locations are difficult.

A detailed study about the effect of the number of tries on the accuracy of predicted particle concentration data was also performed. The investigation showed that although increasing the number of tries may have a positive effect on improving the average accuracy, beyond a specific number of tries (which is called as the optimum number of tries in which the average error has its minimum value), any increasing in the number of tries does not have considerable effect in improving the average accuracy.

ACKNOWLEDGEMENT

The authors would like to express their gratitude to Dr. C. H. Lin from Boeing Company for his valuable input in CFD simulations, and to Dr. P. A. Lebbin from the National Research Council of Canada and Ms. A. Padilla from the Stanford University for their kind assistant in analyzing the experimental data and test procedures. The authors also would like to thank Dr. J. Bennett from the National Institute for Occupational Safety and Health (NIOSH) for his technical assistance. The research was funded, in part, by the Kansas State University Targeted Excellence Program.

REFERENCES

ANSYS FLUENT 12.0 Manual, April 2009, ANSYS Inc.

Clayton. C, Sommerfeld. M, Tsuji. Y, 1998, "Multiphase Flows", CRC Press, USA

Dehbi. A, 2008, " A CFD model for particle dispersion in turbulent boundary layer flows", *Nuclear Engineering and Design*, Vol. 238, Issue 3, pp: 707-715

Launder, B.E., and D.B. Spalding, 1972,"Lectures in Mathematical Models of Turbulence," Academic Press, London, England.

Occupational Outlook Handbook, Bureau of Labor Statistics, 2010-11 Edition (http://www.bls.gov/oco/ocos107.htm, visited June 10, 2011)

Padilla, A., 2008, "Experimental Analysis of Particulate Movement in a Large Eddy Simulation Chamber," MSc dissertation, Kansas State University. Manhattan, Kansas

Zhao. B, Li. X, and Yan. Q, 2003, "A simplified airflow simulatiom", *Building and Environment*, Vol. 38, , pp: 543-552.

Zhao. B, Li. X, and Zhang. Z, 2004, "Numerical Study of Particle Deposition in Two Differently Ventilated Rooms", *Indoor and Built Environment*, Vol. 13, , pp: 443-451.

Zhang. N, Zheng. Z.C, Glasgow. L, and Braley. B, 2010, "Simulation of particle deposition at the bottom surface in a room-scale chamber with particle injection", *Advanced Powder Technology*, Vol. 21, , pp: 256-267.

Proceeding of ASME 2010-3rd Joint US-European Fluids Engineering Summer Meeting and

8th International Conference on Nanochannels, Microchannels, and Minichannels

FEDSM-ICNMM2010-30552

LES AND RANS SIMULATION OF TURBULENT AIRFLOW AND TRACER GAS INJECTION IN A GENERIC AIRCRAFT CABIN MODEL

Khosrow Ebrahimi
Mechanical and Nuclear Engineering
Kansas State University
khe1976@ksu.edu

Zhongquan C. Zheng
Mechanical and Nuclear Engineering
Kansas State University
zzheng@ksu.edu

Mohammad H. Hosni
Mechanical and Nuclear Engineering
Kansas State University
hosni@ksu.edu

ABSTRACT

This study is a continuation of a previous research in numerical simulation of a turbulent airflow in a generic aircraft cabin model. Specifically, the primary objective of this project is to use Computational Fluid Dynamics (CFD) to simulate transport of a tracer gas injected into the generic aircraft cabin. The research work reported herein is composed of three parts.

First, both Large Eddy Simulation (LES) and Reynolds averaged Navier Stokes (RANS) methods are used to simulate airflow from a full-height nozzle and corresponding airflow characteristics within the mockup aircraft cabin. The computational results are validated by comparing them with Particle Image Velocity (PIV) data and published CFD predictions available in the literature. Through these comparisons, the potential for using the CFD methods to predict unsteady as well as time-averaged velocity for a generic aircraft cabin model is examined.

Second, airflow characteristics are studied by reducing the inlet nozzle height to one-half of its original size but keeping the total volumetric airflow rate the same as that of the full-height nozzle. Accuracy of the LES approach in predicting airflow in the half-height nozzle is evaluated by comparing prediction results with the PIV measurement data for the mockup cabin.

Third, simulation of a tracer gas injection through the injecting tube placed in different locations in the half-height nozzle cabin is investigated. In this part, carbon dioxide (CO_2) is chosen as the tracer gas. The LES method is used to solve the equations of motion and the unsteady species transport equation for tracer gas concentration. The predictions are compared with the average measurement data for CO_2-concentration in various locations in the cabin.

INTRODUCTION

Computational Fluid Dynamics has been used for a few decades to evaluate the performance of air conditioning systems through the simulation of fluid flow and heat transfer for the indoor environments. Due to the advances in the computer technology and in turbulence models, use of CFD as a powerful and economical design tool for improving the efficiency and performance of air conditioning systems has been increased. In aircraft industry, CFD models are used to investigate the effect of air ventilation system on the passenger comfort as well as the dispersion of particulates and gases as part of understanding the possible spread of contaminants within an aircraft cabin (Lebbin, 2006).

There are a number of research articles in the literature that discuss the use of CFD approaches to study the airflow and contaminants transport in aircraft cabins. Garner et al. (2004) presented a CFD model which was developed to simulate the airflow field characteristics in a Boeing 747 aircraft cabin. The applied CFD model is described by the unsteady, time-accurate, buoyant ventilation flow field in an aircraft cabin at cruise conditions. The simulation was conducted using a finite element implementation of an augmented laminar Taylor stabilized finite turbulent kinetic energy (TKE) model.

Lin et al. (2005) performed a numerical simulation of airflow and airborne pathogen transport in a commercial aircraft

cabin (Boeing 767). Two different turbulence models were used in that study; Large Eddy Simulation (LES) and Reynolds Averaged Navier Stokes (RANS) models. It was observed while RANS simulation substantially under-predicted turbulent intensity, the LES predicted values were in good agreement with the test data. Based on the LES results, the k-ε equations in the RANS model were modified and then used in simulating the disease transmission using less than 1/100 of computing resources required for the equivalent LES simulation of particle transport in the same cabin.

Lin et al. (2006) performed another study in which the CFD predicted velocity data for turbulent airflow in a generic cabin model were compared with corresponding Particle Image Velocimetry (PIV) experimental data. The main focus of that study was using LES simulation to compare the temporal variations in the experimental data. The good agreement between the simulation results and measured data validated the LES predictions. Also it was observed that energy-spectrum function calculated from the LES velocity prediction had excellent correlation with the Kolmogrov spectrum law in the universal equilibrium range.

The present study is designed to simulate the turbulent airflow and tracer gas diffusion in the same generic cabin as used in Lin et al. (2006) research. A commercial CFD software is used for simulations presented herein. In the first part of this study which deals with airflow characteristics in the cabin, two widely used turbulence models are employed: LES and RANS. The LES method provides the temporal velocity variations and the RANS procedure gives time-independent velocity data. The predictions from both the LES and RANS models are compared with the PIV measured data for five monitoring areas along the cabin center plane parallel to the bulk airflow direction (Lebbin, 2006). Through these comparisons the capability of the two aforementioned turbulence models in predicting the airflow velocities is discussed and compared to each other.

In the second part of this study, the effect of reducing the inlet nozzle height to one-half of its original size on turbulence level and airflow velocities is studied, while maintaining the same Reynolds number for inlet airflow. In this part the predictions are validated by comparing them with the corresponding experimental PIV measurements. In the third part of this study, the tracer gas (CO2) injection is simulated using the LES model for solving the governing mass, momentum and transport species equations. The simulation results are validated through the comparison of time-averaged predicted concentrations of the tracer gas in specified locations in the cabin with the corresponding experimental measurements.

GOVERNING EQUATIONS AND NUMERICAL SOLUTION METHOD

In this study the following assumptions are employed for numerical simulation of turbulent airflow and tracer gas injection in the cabin. Theses assumptions conform to the experimental conditions. The assumptions are:

1. The airflow field is 3-dimensional.
2. In the LES model, the flow is considered unsteady while in the RANS model, the flow is assumed to be at steady state conditions.
3. In both cases of pure airflow and air-CO_2 mixture, the fluid is assumed to be incompressible.
4. The heat transfer in the cabin is neglected. The inlet airflow is at the temperature of 27°C. In simulating the carbon dioxide diffusion, the temperature of injected CO_2 is also considered to be at 27°C.
5. In simulating the tracer gas injection, the effects of buoyancy are taken into account.
6. No chemical reaction takes place in tracer gas diffusion.

The governing equations of turbulent airflow in the cabin are listed as follows:

Continuity:

$$\frac{\partial u_i}{\partial x_i} = 0 \qquad (1)$$

Momentum (Navier-Stokes equations):

$$\frac{\partial u_i}{\partial t} + u_j \frac{\partial u_i}{\partial x_j} = -\frac{1}{\rho}\frac{\partial p}{\partial x_i} + \frac{1}{\rho}\frac{\partial}{\partial x_j}\left(\mu \frac{\partial u_i}{\partial x_j}\right) + g_i \qquad (2)$$

In solving the above equations using LES, just the large scale motions of the flow are solved by filtering out the small and universal eddies. In other words, in this approach the velocity field is separated into resolved and sub-grid domains. The resolved domain of the velocity field represents the large eddies which are dependent on the geometry while the sub-grid domain represents the small scale eddies which are not dependent on the geometry of flow and have a universal behavior such that their effect on the resolved domain is included through the sub-grid scale (SGS) model. So, in this method the instantaneous velocity is considered as the summation of resolvable scale velocity ($\tilde{u}_i$) and sub-grid scale velocity (u_i''):

$$u_i = \tilde{u}_i + u_i'' \qquad (3)$$

It should be mentioned that in the most commercial CFD packages, the grid size is used to filter out sub-grid scale eddies. Substituting the decomposition forms of u_i (as indicated by Equation-3) and p ($p = \tilde{p} + p''$) in the instantaneous governing continuity and Navier-Stokes equations, and then filtering the resulting equations, gives the following filtered equations of continuity and motion:

$$\frac{\partial \tilde{u}_i}{\partial x_i} = 0 \quad (4)$$

$$\frac{\partial \tilde{u}_i}{\partial t} + \tilde{u}_j \frac{\partial \tilde{u}_i}{\partial x_j} = -\frac{1}{\rho}\frac{\partial \tilde{p}}{\partial x_i} + \frac{1}{\rho}\frac{\partial}{\partial x_j}\left([\mu + \mu_t]\frac{\partial \tilde{u}_i}{\partial x_j}\right) + g_i \quad (5)$$

where μ_t in Equation (5) is the sub-grid scale turbulent viscosity. In this study, the Smagorinsky-Lilly SGS model (Smagorinsky, 1963 and Lilly, 1966) is used to calculate μ_t:

$$\mu_t = \frac{\rho}{\sqrt{2}}(C_s\Delta)^2\left|\frac{\partial \tilde{u}_i}{\partial x_j} + \frac{\partial \tilde{u}_j}{\partial x_i}\right| \quad (6)$$

where Δ is the filter width and can be calculated using the following equation:

$$\Delta = (\text{Volume of the grid element})^{1/3} \quad (7)$$

and C_s is the Smagorinsky constant which varies between 0.1 and 0.2. In this study the selected value for C_s is 0.14.

As was mentioned earlier, the heat transfer is negligible in the cabin so that the energy or heat equation is not needed. Needless to say, the governing equations are second order with respect to space and first order with respect to time, so that in solving the governing equations we need to have two boundary conditions in each direction and one initial condition.

When the RANS models are used to simulate the turbulent airflow in the cabin, the instantaneous flow variables are decomposed into the mean value (time-averaged) and fluctuating components:

$$u_i = \overline{u}_i + u_i' \quad (8)$$

where $\overline{u}_i$ and u_i' denote the mean and fluctuating components of the flow velocity, respectively. Substituting the decomposed form of flow variables in the instantaneous governing equations (2) and (3) and taking a time average of those equations gives the following time-averaged governing equations for the steady state incompressible flow:

$$\frac{\partial \overline{u}_i}{\partial x_i} = 0 \quad (9)$$

$$\frac{\partial \overline{u}_j \overline{u}_i}{\partial x_i} = \frac{\partial}{\partial x_i}\left(-\overline{p}\delta_{ij} + (\mu + \mu_t)\left(\frac{\partial \overline{u}_i}{\partial x_j} + \frac{\partial \overline{u}_j}{\partial x_i}\right)\right) + \rho g_i \quad (10)$$

where μ_t is the turbulent or eddy viscosity and using the Boussinesq hypothesis, is defined as:

$$\mu_t = \frac{-\rho\overline{u_i'u_j'}}{\frac{\partial \overline{u}_i}{\partial x_j} + \frac{\partial \overline{u}_j}{\partial x_i}} \quad (11)$$

In this study, in order to calculate the above defined turbulent viscosity, the $k-\varepsilon$ model which is a typical two equation turbulence model is employed. Using this model, the turbulent viscosity is calculated through the following equation (Tu et al., 2008):

$$\mu_t = \frac{C_\mu \rho k^2}{\varepsilon} \quad (12)$$

where $C_\mu = 0.09$ is an empirical constant, k and ε denote the turbulent kinetic energy and turbulent dissipation. Therefore, in addition to the time-averaged governing equations, two additional differential transport equations are solved (along with required boundary conditions) at the same time to find k and ε.

To simulate the carbon dioxide diffusion in the cabin, the LES is used as the turbulence model. In this part of study, not only the geometry of the cabin is changed due to locating the carbon dioxide injection tube in the cabin, but also the equation for transport of species is added to the governing equations:

$$\frac{\partial(\rho\tilde{Y})}{\partial t} + \frac{\partial}{\partial x_i}\left(\rho\tilde{u}_i\tilde{Y}\right) = -\frac{\partial}{\partial x_i}\left(-(\rho D + \frac{\mu_t}{Sc_t})\frac{\partial \tilde{Y}}{\partial x_i}\right) \quad (13)$$

In the above equation, $\tilde{Y}$ is the carbon dioxide mass fraction in the resolved domain of eddies in the air-CO_2 mixture, D is the diffusion coefficient of carbon dioxide in the air-CO_2 mixture. In this study, it is assumed that the estimated value for $D = 1.57\times10^{-5} m^2/s$ is constant throughout the simulations (Bird el al., 2001). The turbulent Schmidt number is defined as $Sc_t = \frac{\mu_t}{\rho D_t}$, where D_t is the turbulent diffusion coefficient. In the simulations we selected Sc_t=0.7. Since Eq. (13), in terms of $\tilde{Y}$, is second order with respect to space and first order with respect to time, we need to determine two boundary conditions for $\tilde{Y}$ in each direction and one initial condition.

Another important point is that the viscosity and density of the air-carbon dioxide mixture are not uniformly constant in the cabin and their values in each location in the cabin are dependent on the concentration of constituents at that location. There are a number of methods in the commercial software to calculate the density and viscosity in a mixture. In this study the "volumetric-weighted mixing law" and "mass weighted mixing law" are used to calculate the mixture density and viscosity, respectively, as presented below:

Volumetric Weighted Mixing law:

$$\frac{1}{\rho_{mixture}} = \frac{\tilde{Y}}{\rho_{CO_2}} + \frac{1-\tilde{Y}}{\rho_{air}} \quad (14)$$

Mass Weighted Mixing law:

$$\mu_{mixture} = \tilde{Y}\mu_{CO_2} + (1-\tilde{Y})\mu_{air} \qquad (15)$$

So it can be seen that in order to simulate the tracer gas diffusion in the cabin, Equations (4-6) and (13-15) are solved simultaneously with the determined boundary and initial conditions.

To solve the above governing equations using LES method, the second order central differencing as well as the second order implicit schemes are used to discretize spatial and temporal derivatives, respectively. Also in this method, Werner-Wengle wall function (Werner and Wengle, 1991) is used as the near wall approach. The reason for using Werner-Wengle wall function for the near wall treatment, as explained elaborately by Werner and Wengle (1991), is its simplicity as well as its more accuracy in comparison with the other wall functions. While other functions are multi-domain functions based on non-dimensionalized velocity and distance from the wall, Werner-Wengle wall function defines unique relationships between shear stress and velocity that enhances accuracy and reduces the computational time. In the RANS method, the second order upwind scheme is used to discretize spatial derivatives in the governing equations. Two different wall approaches are selected: the enhanced wall treatment and non-equilibrium wall function, for the near wall treatment in the RANS method.

RESULTS AND DISCUSSIONS

Part 1- Study of airflow in cabin with full height nozzle

This section starts with the Large Eddy Simulation of turbulent airflow in the generic cabin with the full-height nozzle. The geometry of the cabin as well as the location of PIV measuring windows are shown in Fig. 1:

The generic cabin model has the key features of one-half of a twin-aisle aircraft cabin. The upper left and upper right corners represent the overhead bins. The slit right below the upper left corner represents the nozzle port through which the fresh conditioned air comes into the cabin and the slit in the lower right corner represents the outlet port for exiting exhaust air.

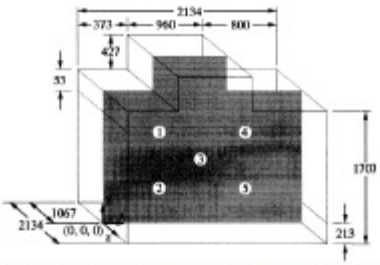

Figure 1: Simplified generic cabin model and the location of PIV monitoring windows on the cabin central plane (units in mm). (Lebbin, 2006)

In the experiment, the adiabatic condition was assumed for the cabin and the measurements were taken at five measurement locations when the airflow inside the cabin was fully developed (Lebbin, 2006), as shown in Fig. 2.

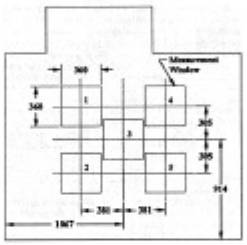

Figure 2: The exact locations of five PIV measurement windows on the central plane (units in mm). (Lin et al., 2006)

In the experiments, the average airflow rate coming into the cabin was maintained at the constant value of 4.2 m^3/min. The Reynolds number at the inlet was held constant at 2,226. In LES, the spacing of the mesh has a very important role in the quality and the accuracy of simulation predictions not only because of using that in discretizing the governing equations but also because it is used in filtering the instantaneous governing equations. Another important parameter affecting the accuracy of simulations is the size of the time steps. Knowing the Reynolds number at the inlet, the Kolmogrov length (η) and time (τ) scales are calculated as 0.928 mm and 0.0589 sec., respectively. Although the Kolmogrov length and time scales are used as a basis in the grid and time spacing, making a decision on the grid and time spacing requires a compromise between the solution accuracy, the computation time and cost as well as the existing restrictions in the computing resources. The CFD grid used in this part of study consists of 2,340,000 hexahedral cells with the grid spacing varied in the range of 7η - 34η. Also the time step size of 0.05 sec is used in all Large Eddy Simulations presented in this paper.

Figure 3 shows the turbulent airflow patterns in the cabin at four different time levels predicted using LES. This sequence

also shows the development of the flow field inside the cabin, such as formation of boundary layers and large eddies.

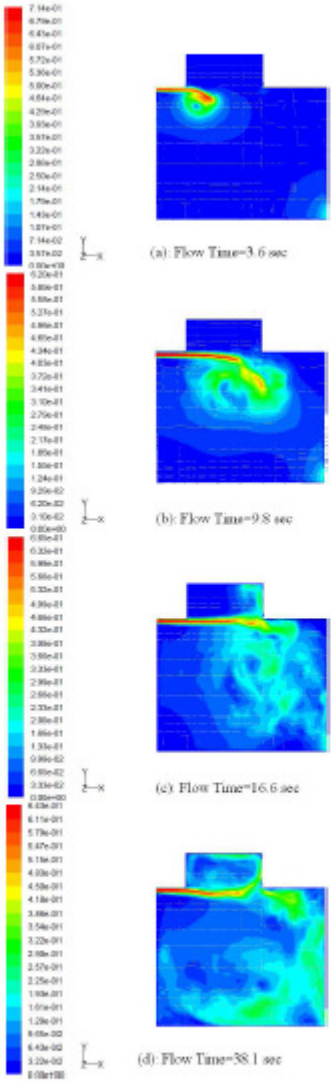

Figure 3: The turbulent airflow patterns (The contour representations of airflow velocity magnitudes) predicted by LES at different flow times: (a) flow time=3.6 s, (b) flow time=9.8 s, (c) flow time=16.579 s and (d) flow time=38.1 s (units in m/s).

In order to validate the simulation, the LES predictions are compared with the PIV measurement data as well as the CFD predictions by Lin et al. (2006) at each of the five PIV measuring areas. The PIV measurements were taken when the airflow inside the cabin reached quasi-steady conditions. The time interval between each two succeeding PIV sampling data was 0.2 sec (Lebbin, 2006). A comparison between the corresponding LES parameters used in this study and those used in Lin et al. (2006) is listed in Table 1.

We first consider the value of velocity at the center point of each PIV measuring windows as the measured value of velocity in that window, as assumed by Lin et al. (2006). The predicted temporal histories of velocity components at these points are compared with the PIV data obtained with a sampling frequency of 5 Hz, as well as the CFD predictions by Lin et al (2006) that had a sampling frequency of 20 Hz. Figures 4-6 show some of those comparisons for the locations 1 and 4. Since the values of z-component of airflow velocities in the central cutting plane (z=0) is so small, just the comparisons for x and y components of airflow velocities are presented here.

Table 1: Comparison between the important parameters in the simulations

LES CODE	Lin et al. (2006) (Using Commercial CODE)	Lin et al. (2006) (Using Fire Dynamic Simulator)	This Study (Using Commercial Software)
Mesh size (# of cells)	2,535,744	2,580,480	2,340,000
Cell Type	All hexahedral cells, unstructured mesh	All hexahedral cells, Cartesian Mesh	All hexahedral cells, Structured mesh
Grid Spacing(cm)	5-20	5-20	7-34
Time Step(seconds)	0.05	0.01 ± 0.002	0.05
SGS model	Smagorinsky Lilly	Smagorinsky Lilly	Smagorinsky Lilly
Smagorinsky constant, C_s	0.14	0.14	0.14
Near Wall Treatment	Law of the wall approach	Standard Wall function	Werner-Wengle
Numerical Scheme	Spatial: Second order central differencing Temporal: Implicit second order predictor corrector scheme	Spatial: Second order central differencing Temporal: Implicit second order predictor corrector scheme	Spatial: Second order central differencing Temporal: Implicit second order predictor corrector scheme

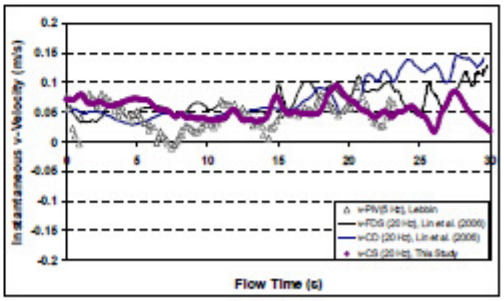

(a): x-component of velocity data

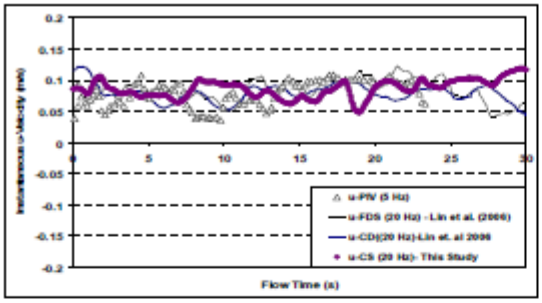

(b): y-component of velocity data

Figure 4: Comparison of the predicted values (this study), PIV measurements (Lebbin, 2006) and Lin et al (2006) predictions (using FDS and a commercial software) for the airflow velocity data corresponding to the location 1 of the cabin with full height nozzle.

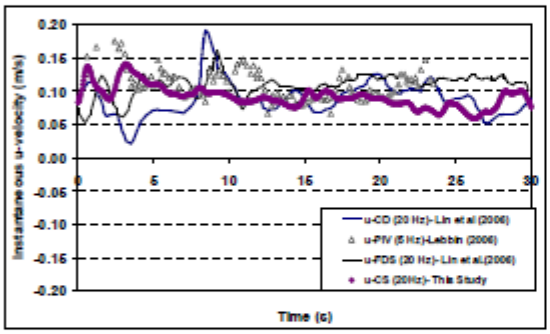

(a): x-component of velocity data

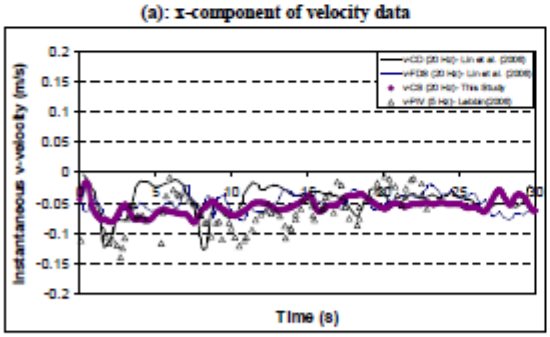

(b): y-component of velocity data

Figure 5: Comparison of the predicted values (this study), PIV measurements (Lebbin, 2006) and Lin et al (2006) predictions (using FDS and a commercial software) for the airflow velocity data corresponding to the location 4 of the cabin with full height nozzle.

As can be seen from Figs. 4-6, there is a good agreement among the simulation results of this study, PIV measurements, and Lin et al (2006) CFD predictions. Especially, the comparisons indicate that the simulations predict the ranges of variations of instantaneous velocities fairly close to the variation ranges of the measurements.

In the above comparison, the predicted velocity values were selected at the center of each PIV measuring window. However in the experiments, the PIV velocity data were averaged over the area of each measuring window. In order to study the effect of changing the prediction velocity from the center point value to the area average value of the PIV measuring windows, the simulation results were reprocessed based on the area weighted average values of velocities over the measuring windows areas. Figure 6 shows the comparisons between the predictions from two differently processed velocity values and the corresponding experimental data for location 2 of the PIV window.

In Fig. 6, it is observed that although the mean temporal behaviors of the predictions are almost the same between the two different simulation data sets, the area-averaged data set shows a smoother curve, which means the area-averaged velocity experiences less fluctuations than the local velocity at the center point of the window.

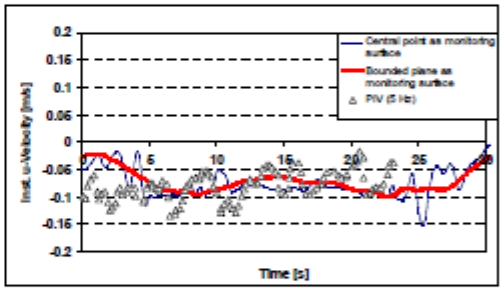

(a) x- component of velocity data

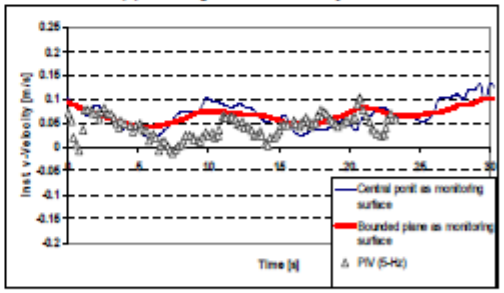

(b) y- component of velocity data

Figure 6: Study the effect of choosing monitoring surface on the predicted velocities, corresponding to location 2 of the cabin with full height nozzle, through comparison with PIV measurements.

Figures 7 and 8 present the comparisons between the predictions from the steady-state RANS simulations using three

variations of the k-ε turbulence models for the x-component of velocity in locations 3 and 5 of the PIV windows and the corresponding time-dependent PIV data. Although the accuracy of RANS predictions is considerably less than LES, the computation time and cost associated with LES simulations are much more than RANS.

Among the three examined RANS models, the standard $k-\varepsilon$ (Launder and Spalding, 1972), the re-normalization group (RNG) $k-\varepsilon$ (Yakhot and Orszag, 1986) and the realizable $k-\varepsilon$ (Shin et al., 1995), the RNG predicted value is closer to the mean value of the experimental data. The standard $k-\varepsilon$ predicted value is less than the measured mean value; however, the RNG and realizable $k-\varepsilon$ predicted values are greater than measured mean values. Based on the simulations performed in this study, the RNG is the most accurate model.

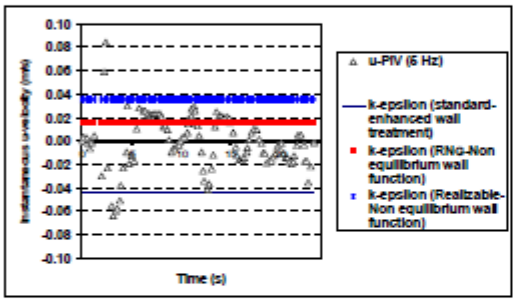

Figure 7: Comparison between the RANS predictions of time independent x-component velocity data in location 3 of measuring windows and corresponding time dependent PIV data.

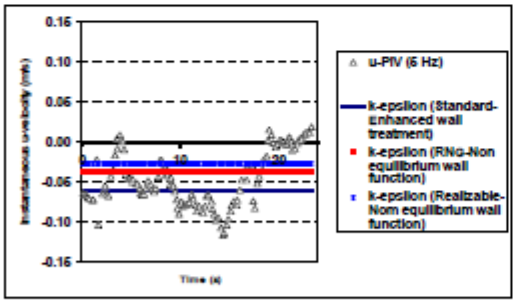

Figure 8: Comparison between the RANS predictions of time independent x-component velocity data in location 5 of measuring windows and corresponding time dependent PIV data.

Part 2- Study of the airflow in cabin with half height nozzle:

This section presents the study of flow characteristics when the cabin nozzle height is reduced to one half of its previous size. As the flow rate of the incoming air to the cabin still remains the same, by halving the nozzle height, the magnitude of the airflow velocity at the inlet is doubled. So it is expected that the magnitude of each airflow velocity component in the cabin experience an increase. Figures 9-12 compare the PIV measurements (Lebbin, 2006) with the LES predictions from this study for the airflow velocity components in location 1, 2, 3 and 5 of the PIV measuring windows. The sampling frequency in PIV measurements is 7.5 Hz. A structured grid consisting of 2,225,000 hexahedral mesh cells with the grid spacing in the range of 4η-43η was used in the LES simulations for this part of study. Similar to the simulations done for the cabin with full height nozzle, the time-step size of 0.05 sec was used in simulating the airflow in the cabin with half-height nozzle as well. As can be seen from the comparison, except for the location 3 of the measuring windows, LES predicts the range of flow velocity variations fairly well. In location 3, due to the complexity of flow in this region, the agreement between the LES predictions and PIV measurements is not as good for all flow times. For example, in Fig. 11, for the times between ~12 sec to ~30 sec and greater than ~35 sec there is not an acceptable agreement between LES and PIV. It seems in order to get better predictions for such regions in which the airflow patterns are more complicated, local grid refinements are needed.

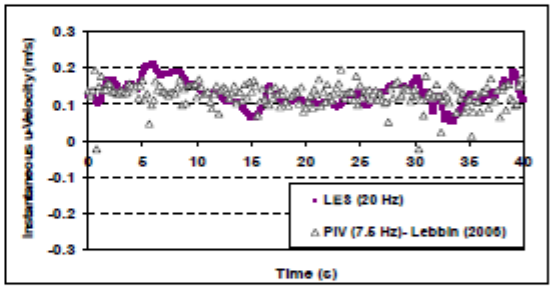

(a): x-component of velocity data

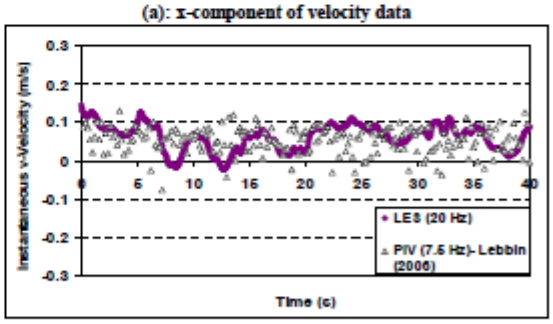

(b): y-component of velocity data

Figure 9: Comparison of the LES prediction and PIV measurements (Lebbin, 2006) for velocity data corresponding to the location 1 of the cabin with half height nozzle.

Comparisons of velocity data between the full and half height nozzle cases indicate that by halving the nozzle height,

the mean value of the predicted as well as measured flow velocity data corresponding to locations 1 and 2 of the PIV measuring windows are approximately doubled. However for the locations 4 and 5, the expected increase in the velocity is slight and not as much as that experienced in the locations 1 and 2. In addition, comparison of the PIV measurements for the velocity data corresponding to the location 3 (Fig. 13) implies that by halving the nozzle height and consequently doubling the inlet airflow velocity, the flow in the location 3, which used to be almost stationary in the full height nozzle case, takes the tendency of moving to the upper left corner of the cabin.

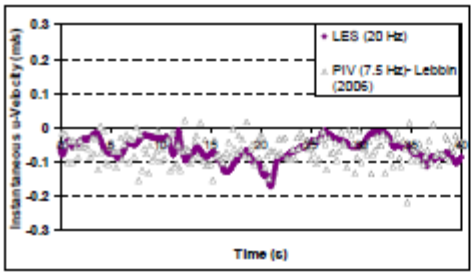

(a): x-component of velocity data

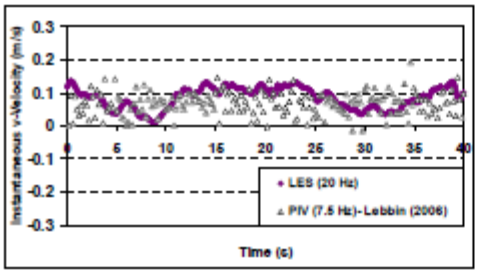

(b): y-component of velocity data

Figure 10: Comparison of the LES prediction and PIV measurements (Lebbin, 2006) for velocity data corresponding to the location 2 of the cabin with half height nozzle.

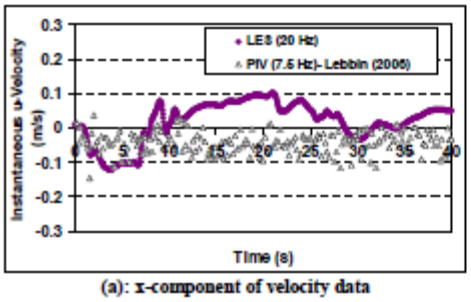

(a): x-component of velocity data

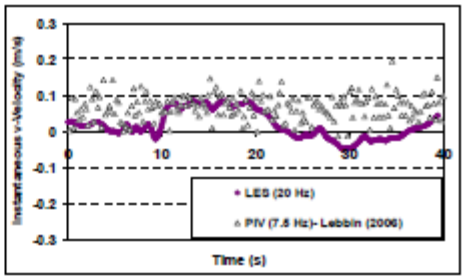

(b): y-component of velocity data

Figure 11: Comparison of the LES prediction and PIV measurements (Lebbin, 2006) for velocity data corresponding to the location 3 of the cabin with half height nozzle.

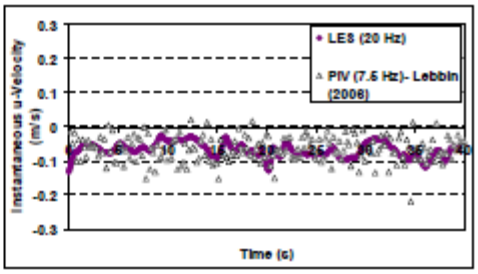

(a): x-component of velocity data

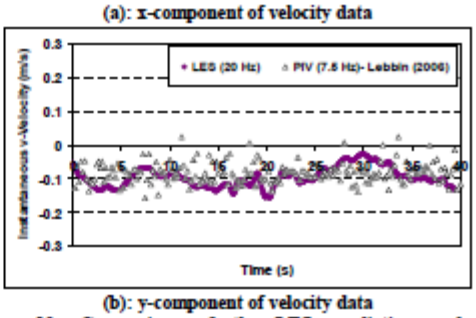

(b): y-component of velocity data

Figure 12: Comparison of the LES prediction and PIV measurements (Lebbin, 2006) for velocity data corresponding to the location 5 of the cabin with half height nozzle.

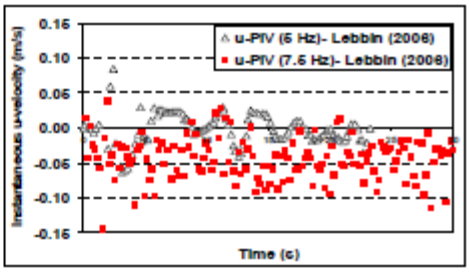

(a): x-component of velocity data

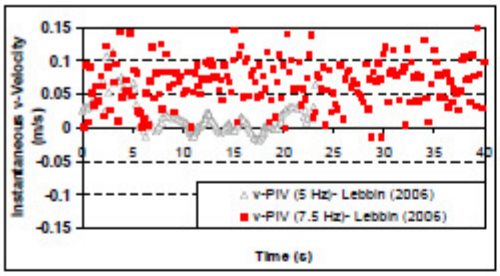

(b): y-component of velocity data

Figure 13: Study the effect of decreasing the cabin nozzle height through a comparison between the PIV measured velocity data (Lebbin, 2006) corresponding to the location 3 of the PIV measuring windows for two cases of full (PIV-5 Hz) and half nozzle height (PIV-7.5 Hz).

Part 3-Study of the tracer gas diffusion in the cabin with half height nozzle

This section is devoted to the study and understanding of the patterns of pollutants diffusion in a mockup aircraft cabin and its impact on the cabin indoor environment. In the experiments performed by Lebbin (2006), a 12.7 mm schedule-40 porous polythene tube was installed horizontally inside the cabin perpendicular to the x-y plane. One end of the tube was connected to a CO_2 tank through the back wall (corresponding to z=-1.067m) of the cabin while the other end was caped and positioned 134 mm from the opposite wall. The tube passed through the central point of the location 2 of the PIV measuring windows as identified in Figure 2. A pressurized CO_2 tank (p~800 psi containing CO_2 with the purity of more than 99.6%) was used to supply the carbon dioxide required for the experiments. By passing through an expansion valve, the pressure of carbon dioxide was regulated down from ~800 psi to an atmospheric pressure. Since the density of CO_2 at the atmospheric pressure is higher than the air density at the same pressure and temperature, in order to maintain the neutral buoyancy condition, before flowing into the injection tube, CO2 was blended with Nitrogen such that the density of the diluted CO_2 in the injection tube reached approximately the density of air. Carbon dioxide was injected through small holes uniformly distributed over the circumferential surface of the injection tube.

Figure 14 shows a rough graphical representation of the generic cabin model with the installed injection tube. In specifying the boundary conditions required for the numerical solution of the transport species equation, the concentration of the carbon dioxide in the incoming air, which is in the range of ~300 ppm to ~400 ppm, should be taken into consideration. In the experiments, the CO_2 was injected after quasi steady conditions were achieved for the turbulent airflow in the cabin. Also the measurement of the carbon dioxide concentration was performed when the flow of air-CO2 mixture reached quasi steady state conditions.

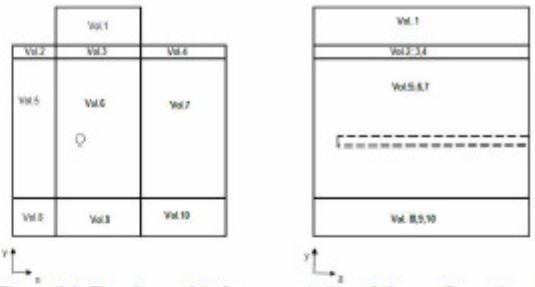

Figure 14: Rough graphical representation of the configuration of the generic cabin model and installed injection tube. (The numbered volumes indicated in the above sketch where used in grid generation for the geometry of the generic cabin model and the injection tube.

After the turbulent flow of the air-CO_2 mixture reached quasi-steady state conditions, the measurement of the time-dependent values of carbon dioxide concentration at specified sampling points, as shown in Fig.15, was started and continued for about 10 minutes. The measured data, denoted by C(t), were non-dimensionalized using the concentration of CO_2 at the inlet of the cabin and the average value of the CO_2 concentrations at the outlet between two times: at the beginning of the measurement and at the end of the measurement through the following equation:

$$y(t) = \frac{C(t) - \overline{C}_{inlet}}{\overline{C}_{outlet} - \overline{C}_{inlet}} \qquad (16)$$

where;

$y(t)$: dimensionless concentration of carbon dioxide

$C(t)$: temporal data of CO_2 concentration at different sampling points

$\overline{C}_{inlet}$: the CO_2 concentration at the inlet measured one time and assumed to be constant during the experiment

$\overline{C}_{outlet}$: the average of the two measured values for the CO_2 concentration at the outlet (the measured values are corresponded to the beginning and the end of measurement duration).

The grid generation for this geometry was performed by dividing the whole volume of the cabin model into 10 sub-volumes, as shown in Fig. 14, and producing grid for the each of theses 10 sub-volumes separately. The generated grid is unstructured and contains 1,728,000 mesh elements of tetrahedral, hexahedral and wedge shapes. A schematic of this grid is shown in Fig. 16.

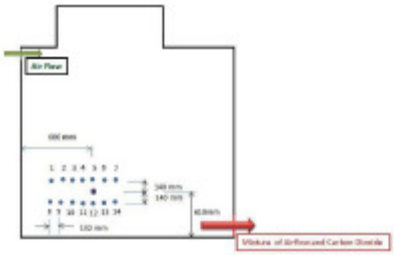

Figure 15: Points 1-14 are the sampling points above and below the injection tube. The concentration values of CO_2 are predicted using LES at these points and compared with the corresponding experimental data for CFD validation purposes.

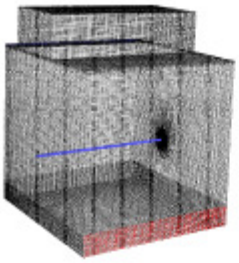

Figure 16: A 3-D schematic of the unstructured grid (for the generic cabin with the injection tube) used in CFD simulation of the carbon dioxide diffusion in the generic cabin model.

Figures 17 and 18 show comparisons between the LES predicted values for the time dependent concentration data and the corresponding time-averaged experimental measurement for the sampling points above and below the injection tube, respectively.

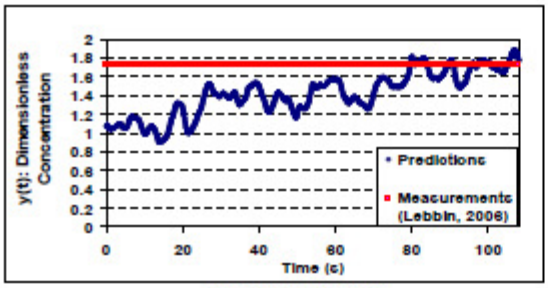

(a) Sampling point 1

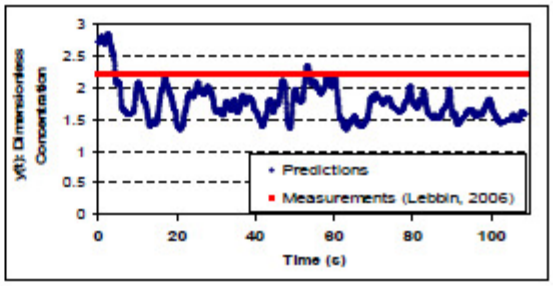

(b): Sampling point 2

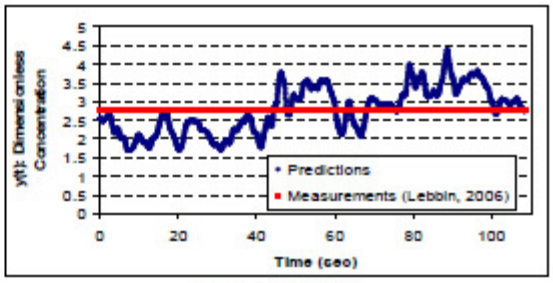

(c): Sampling point 3

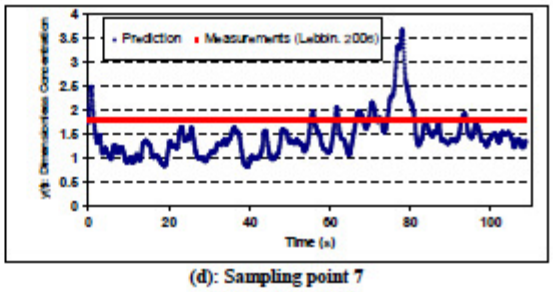

(d): Sampling point 7

Figure 17: Comparison between the time dependent predictions and time-averaged measurement for the dimensionless CO_2 concentration data at some sampling points above the injection tube (arbitrary selected).

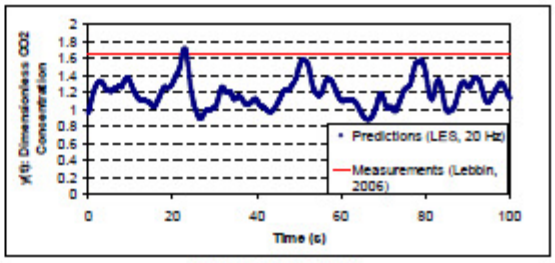

(a) Sampling point 8

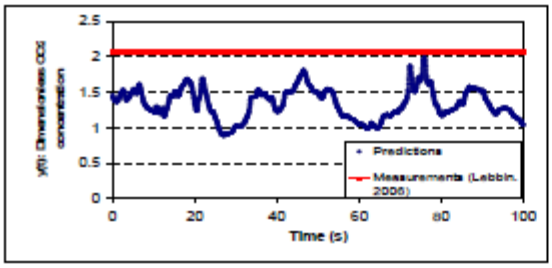

(b) Sampling point 10

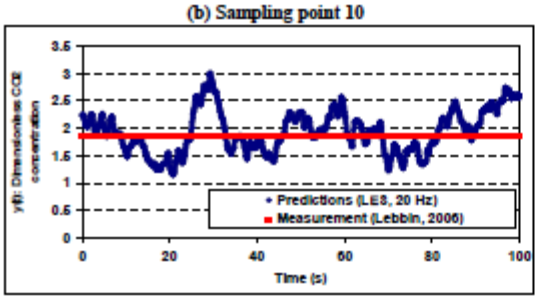

(c) Sampling point 12

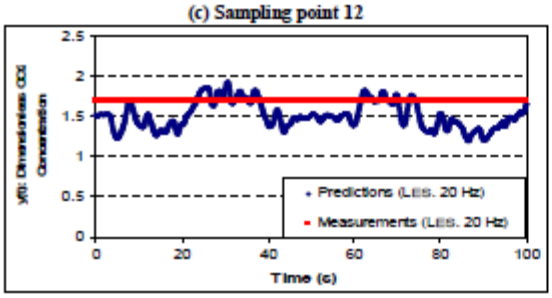

(d) Sampling point 14

Figure 18: Comparison between the time dependent predictions and time-averaged measurement for the dimensionless CO_2 concentration data at some sampling points above the injection tube (arbitrary selected)

In Figs 19 and 20, the time-averaged predicted and measured values of the CO_2 concentration are compared to each other. For the sampling points above the tube, it is observed that there is an excellent agreement between predictions and measurements at sampling points 3, 5 and 6 above the injection tube. However, the agreement for the sampling point 4 is not as good. There is an error between 11-30% in predicting the concentration data for the sampling points 1, 2 and 7 (Fig. 19)

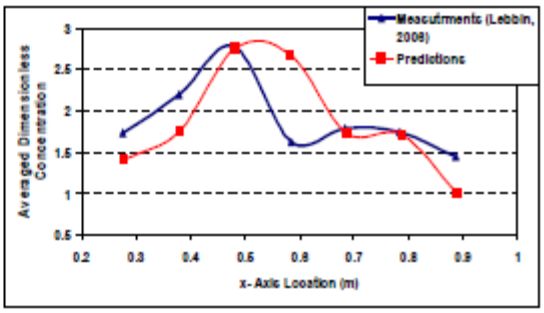

Figure 19: Comparison between the times averaged predictions and measurement of dimensionless CO_2 concentration data for the sampling points located along the x-axis above the injection tube.

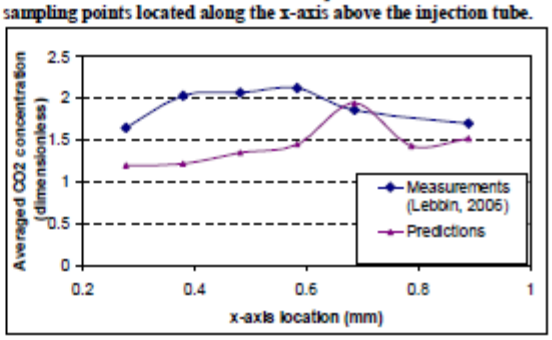

Figure 20: Comparison between the times averaged predictions and measurement of dimensionless CO_2 concentration data for the sampling points located along the x-axis above the injection tube

Figure 20 presents a graphical comparison between the time-averaged predictions and measurements for CO_2 concentration corresponding to the sampling point located along the x- axis below the injection tube. As can be seen, the best agreements have been achieved for point 12 (right below the tube) and point 14. The worst results correspond to points 8, 9 and 10. The error in computations for this case varies from ~4% (point 12) to ~40% (point 9).

Uncertainty (mesh error) study

In order to study the effect of grid size on the simulation results, the number of mesh cells was increased from 1,728,000 to 2,630,000. The CO_2 mass fraction at different sampling points computed using two different grid sizes were compared. Figure 21 shows this comparison for the sampling points above the injection tube, points 1-7 as shown in Fig. 15.

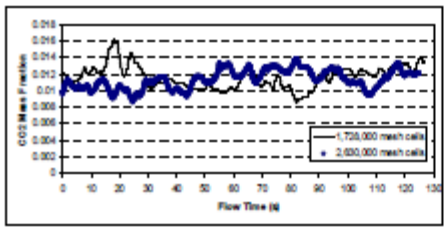

(a) Sampling point 1

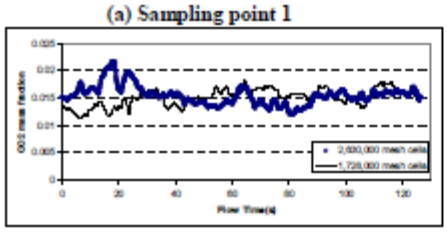

(b) Sampling point 2

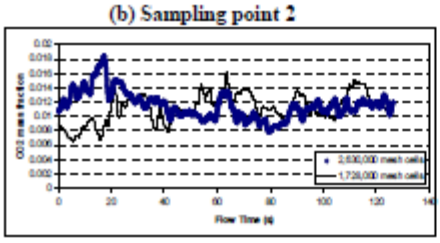

(c) Sampling point 3

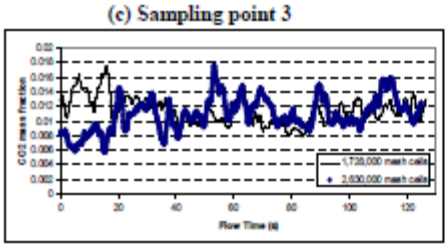

(d) Sampling point 4

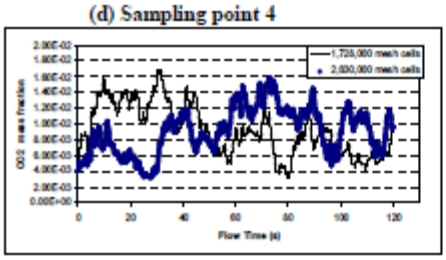

(e) Sampling point 5

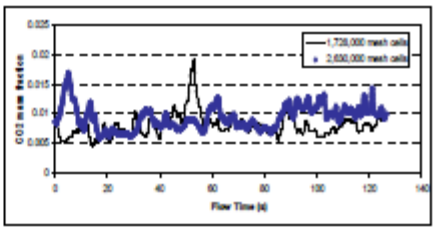

(f) Sampling point 6

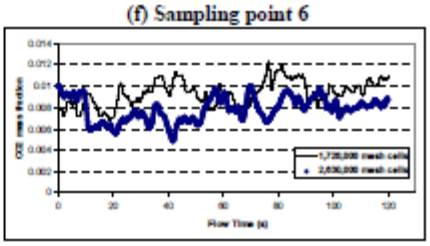

(g) Sampling point 7

Figure 21: Uncertainty (mesh error) study for simulating tracer gas injection through monitoring the CO_2 concentration at different sampling points above the injection tube.

A comparison of the root-mean-squared (RMS) values of computed data from two different grid sizes is shown in Table 2. As it is seen, by increasing the number of mesh cells, the computed CO_2 concentration data varies between 1% to 16%.

Table 2: Comparison of RMS values for computed CO_2 concentrations using two different grid sizes

Sampling point Number (Fig.15)	2,630,000 mesh cells	1,728,000 Mesh cells	Relative difference (%)
1	0.0114	0.0116	2.38
2	0.0151	0.0155	2.87
3	0.0117	0.0114	2.85
4	0.0111	0.0116	4.16
5	0.0097	0.0088	10.22
6	0.0095	0.0082	16.06
7	0.0079	0.0094	15.9

Table 3 shows comparisons between the mean values of computed data from two different grid sizes. As it is seen, by increasing the number of mesh cells, the computed CO_2 concentration data varies between 2% to 17%.

Table 3: Comparison of mean values for computed CO_2 concentrations using two different grid sizes

Sampling point Number (Fig.15)	2,630,000 mesh cells	1,728,000 Mesh cells	Relative difference %
1	0.0113	0.0116	2.08
2	0.0155	0.0151	2.89
3	0.0115	0.0112	2.85
4	0.0109	0.0114	4.86
5	0.0083	0.0092	9.78
6	0.0095	0.0082	17.1
7	0.0078	0.0093	16.13

As seen from the prediction data presented in Tables 2 and 3, the relative difference between the predicted CO_2 concentration data using two grid sizes is greater for the sampling points located in the upper right of the injection tube. In order to explain the reason for this behavior, recall the study of the airflow in the cabin presented earlier in this paper. It was observed that the airflow in the location 3 of the PIV windows (see Fig. 1) demonstrates more complexity than other locations. Since the sampling points located in the upper right of the injection tube are very close to that region, changing the grid size has a considerable effect on computational accuracy. Therefore, one expects higher computational uncertainties for the sampling points located in regions with more complex airflow structure.

CONCLUSIONS

In this study, the capability of a CFD commercial software in simulating turbulent airflow as well as tracer gas diffusion in a generic half cabin was evaluated. Two different types of turbulence models were used to find the turbulent viscosity in the governing equations: unsteady Large Eddy Simulation (LES) and steady-state Reynolds Averaged Navier Stokes (RANS) methods. While LES predicts the temporal variations of airflow velocity, the steady-state RANS method predicts a steady-state value for the velocity. Through the comparisons, it was concluded that the LES at least is able to predict the range of velocity variations fairly well. Examining the three different $k-\varepsilon$ (standard, RNG and Realizable) indicated that, as expected, the errors associated with the RANS method are much more than that of LES. It was also recognized that among the above mentioned $k-\varepsilon$ model, the standard $k-\varepsilon$ underestimated the velocity value, and the RNG and realizable models overestimated the velocity data. The most accurate predictions among the three RANS models were achieved using the RNG model.

In order to monitor the velocity data in PIV measuring windows, two different approaches were employed. The first approach used velocity data at the center points of the PIV windows and the second method used the area-averaged velocity values of the PIV windows. The comparisons indicated that the area-averaged velocity value decreased the fluctuations in the velocity but the general behavior of predicted velocities did not change. Comparisons with the experimental data showed that the center point values had a better agreement with experimental measurements.

In the second part of this study, the effect of halving the cabin inlet nozzle height with the same airflow rate was studied. It was observed that although LES method gave a good estimation of the velocity data in the locations 1, 2, 4 and 5 of measuring windows, the agreement between the simulations and measurements was not as good in the other locations. A local refinement in grid size is recommended to get more accurate results in this region in the future study. Comparing to the cabin with the full-height nozzle, it was seen that by halving the nozzle height and consequently doubling the inlet velocity, the magnitude of flow velocities in locations 1 and 4 increased dramatically (by 100%). However, in locations 2 and 5, the increase in the velocity value was slight and almost negligible. It was also realized that the airflow located in location 3 that used to be almost stationary in the full-height nozzle case had the tendency of moving to the upper left corner of the cabin model.

In the last part of this study, the capability of commercial CFD software in simulating the tracer gas diffusion in the generic cabin model was examined. In the corresponding simulations, LES was used to solve the Navier Stokes equations. Using LES, the temporal variations in tracer gas concentration in the specified sampling points were predicted. Following the same procedure as used in experiments the predicted values were non-dimensionalized and compared with experimental data. Although excellent agreement was observed in some sampling points, the predictions had an average error of 23%.

ACKNOWLEDGEMENT

The authors would like to express their gratitude to Dr. C. H. Lin from Boeing Company for his valuable input in CFD simulations, and to Dr. P. A. Lebbin from the National Research Council of Canada for his kind assistant in analyzing the experimental data and test procedures. The authors also would like to thank Dr. J. Bennett from the National Institute for Occupational Safety and Health (NIOSH) for his technical assistance. The research was funded, in part, by the Kansas State University Targeted Excellence Program.

REFERENCES

Bird, B.R., W.E. Steward, E.N Lightfoot, 2001, "Transport Phenomena", 2nd Edition, John Wiley and Sons, NY.

Fluent 6.3 User's Manual Guide (http:/my.fit.edu/itresources/manuals/fluent6.3, visited April 12, 2010).

Garner, R.P., K.L. Wong, S.C. Ericson, A.J. Baker, J.A. Orzechowaki, 2004, "CFD Validation for Contaminant Transport in Aircraft Cabin Ventilation Fields," Report No. DOT/FAA/AM-04/7, U.S. Department of Transportation and Federal Aviation Administration, Office of Aerospace Medicine, Washington DC.

Launder, B.E., and D.B. Spalding, 1972,"Lectures in Mathematical Models of Turbulence," Academic Press, London, England.

Lebbin, P., 2006, "Experimental and Numerical Analysis of Air, Tracer Gas and Particulate Movement in a Large Eddy Simulation Chamber," PhD dissertation, Kansas State University. Manhattan, Kansas.

Lilly, D.K, 1966, "On the application of the eddy viscosity conceptin the internal subrange of turbulences," NCAR Manuscrip123.

Lin, C.H., R.H. Horstman, M.F. Ahlers, L.M. Sedgwick, K.H. Dunn, J.L. Topmiller, J.S. Bennett, and S. Wirogo, 2005a, "Numerical simulation of airflow and airborne pathogen transport in aircraft cabins - Part 1: Numerical simulation of the flow field," *ASHRAE Transactions,* Vol.111, pp:755-763.

Lin, C.H., R.H. Hortsman, M.F. Ahlers, L.M. Sedgwick, K.H. Dunn, J.L. Topmiller, J.S. Bennett, S. Wirogo, 2005, "Numerical Simulation of Airflow and Airborne Pathogen Transport in Aircraft Cabins- Part II: Numerical Simulation of Airborne Pathogen Transport," *ASHRAE Transactions*, Vol.111, pp: 764-768.

Lin, C.H., R.H. Hortsman, P.A. Lebbin, M.H. Hosni, B.W. Jones, B.T. Beck, 2006, "Comparison of Large Eddy Simulation Predictions with Particle Image Velocimetry Data for the Airflow in a Generic Cabin," *HVAC&R Special Issue*, Vol. 12, Number 3c. pp: 935-951.

Shih, T.H., W.W. Liou, A. Shabbir, Z. Yang, and J. Zhu., 1995, "A New $k-\varepsilon$ Eddy-Viscosity Model for High Reynolds Number Turbulent Flows - Model Development and Validation. *Computers Fluids*, Vol. 24, No.3, pp: 227-238.

Smagorinsky, J., 1963, "General circulation experiments with the primitive equations: I. The Basic Experiment,". Monthly *Weather Review,* Vol. 91, pp: 99-164.

Tu, J., G.H. Yeoh, C. Liu, 2008, "Computational Fluid Dynamics- A Practical Approach,", pp: 102-106, Butterworth-Heinemann, USA.

V. Yakhot and S.A. Orszag., 1986,"Renormalization Group Analysis of Turbulence: I. Basic Theory," *Journal of Scientific Computing*, Vol.1, No.1, pp: 1-51.

Werner. H. and H. Wengle, 1991, "Large Eddy Simulation of Turbulent Flow Over and Around a Cube in a Plate Channel," 8th *Symposium on Turbulent Shear Flows*, Munich, Germany, 1991.